

THE SYNTHESIS AND EVALUATION OF NEW RADIOPHARMACEUTICALS  
AND MULTIMODAL IMAGING PROBES

THE SYNTHESIS, EVALUATION AND MECHANISTIC STUDY OF NEW  $^{99m}\text{Tc(I)}$ -  
TETRAZINES FOR THE DEVELOPMENT OF NEW RADIOPHARMACEUTICALS  
AND MULTIMODAL IMAGING PROBES

By

Holly Bilton, B.Sc.

A Thesis

Submitted to the School of Graduate Studies

In Partial Fulfillment of the Requirements

For the Degree

Doctor of Philosophy

McMaster University

© Copyright by Holly Bilton, August 2019

Ph.D. Thesis – H. Bilton; McMaster University – Chemistry and Chemical Biology

DOCTOR OF PHILOSOPHY (2019)

McMaster University

Chemical Biology

Hamilton, Ontario

TITLE:        The Synthesis, Evaluation and Mechanistic Study of New  $^{99m}\text{Tc}$ -  
Tetrazines for the Development of New Radiopharmaceuticals and Multimodal  
Imaging Probes

AUTHOR: Holly Bilton, B.Sc. (Wilfrid Laurier University)

SUPERVISOR: Professor John Fitzmaurice Valliant

Number of Pages: XXXIV, 235

## Abstract

Technetium-99m ( $^{99m}\text{Tc}$ ) radiopharmaceuticals are widely used for diagnostic imaging of heart, kidney, and liver disease, and cancer. Evolution from perfusion type tracers to targeted agents however has proven difficult.  $^{99m}\text{Tc}$  labeled antibodies for imaging specific disease biomarkers would be of great interest, however the disparity between the isotopes half-life (6 hours) and the long circulation time of most antibodies (multiple days) has been a significant barrier. Furthermore, the conjugation of bifunctional  $^{99m}\text{Tc}$ -chelate complexes to small molecules often has a detrimental impact on targeting. The use of bioorthogonal chemistry derived from tetrazines and trans-cyclooctene derivatives, along with pretargeting has the potential to overcome these issues and create a new generation of targeted  $^{99m}\text{Tc}$  radiopharmaceuticals.

Initially, the synthesis of three generations of imidazole based tridentate chelates linked to a tetrazine was completed. These new ligands were labeled with  $^{99m}\text{Tc}$  under mild conditions (60 °C, 20 min, pH 3.5) with modest to good radiochemical yields ranging from 31 to 83%. Biodistribution studies revealed that compound **14**, which contains a polyethylene glycol 5 (PEG<sub>5</sub>) linker had the best clearance from non-target tissues. Compound **14** was also used successfully in a pretargeting strategy along with a trans-cyclooctene (TCO) derivative of the bone targeting bisphosphonate, alendronate (ALN). One hour following the administration of TCO-ALN to BALB/c mice, compound **14** was injected intravenously where uptake at sites of high calcium turn over (i.e. the joints) was



observed. At 6 hours post injection, for example, uptake reached as high as  $20.1 \pm 4.91$  and  $16.1 \pm 4.84$  %ID/g in the knee and shoulder, respectively.

Pretargeted imaging studies were performed subsequently with a TCO-functionalized huA33 antibody in mice bearing SW122 xenografts. The TCO-huA33 antibody was injected 24 hours before the administration of two radiolabeled tetrazines at high and low specific activities. At 6 hours post injection tumour uptake was minimal, with tumour: blood ratios  $<1$  in all cases. Blood clearance studies determined that the tetrazines were being cleared rapidly, with a blood residence half-life of 1.3-2.1 minutes. The hypothesis is that the low concentration of the antibody (owing to its high molecular weight), combined with the rapid clearance of the tetrazine and significant off-target uptake resulted in unfavorable kinetics and low tumor binding.

Studies of the clearance pathway of **14** were investigated with clinically approved hepatobiliary transport inhibitors to help understand the mechanism of clearance, which could in turn be used to optimize the pharmacokinetics of the tetrazine ligands. A range of different inhibitors of key clearance pathways were evaluated with limited success. However, co-administration of **14** with ALN resulted in a 75% decrease in gall bladder uptake of **14** ( $216 \pm 75.9$  to  $33.6 \pm 3.93$  %ID/g). Pretargeting studies of **14** with TCO-ALN in the presence of excess ALN revealed that ALN did not hinder the uptake of TCO-ALN in the bone, with all organs and tissues having the same uptake with TCO-ALN or TCO-ALN + ALN

(knee:  $20.1 \pm 4.91$  and  $14.9 \pm 2.43$  %ID/g, respectively). There was also a concomitant decrease in gall bladder uptake ( $91.5 \pm 17.1$  to  $28.8 \pm 2.63$  %ID/g).

Further work on improving the distribution of the tetrazine ligands involved investigating the effect of the chelate. The core chelate found in **14** without the tetrazine moiety (compound **11a**) was labeled with  $^{99m}\text{Tc}$  to produce **11b** in a 31% radiochemical yield. Biodistribution studies of **11b** and **14** at 6 hours post injection demonstrated that the imidazole-based  $^{99m}\text{Tc}$ -chelate was a major factor in the rapid and significant uptake and retention in the liver and gallbladder. A new triazole based chelate with optimal clearance from Kluba and coworkers was synthesized in 45% yield and successfully labeled with  $^{99m}\text{Tc}$  (compound **23a**). Biodistribution studies were performed where at 6 hours post injection, **23a** had five times lower uptake in all non-target organs compared to **11b**. The synthesis of a tetrazine derivative of **23a** (compound **32**) unfortunately demonstrated high hepatobiliary uptake compared to the original triazole chelate (gall bladder:  $228 \pm 251$  and  $8.77 \pm 0.73$  %ID/g, large intestine:  $85.5 \pm 83.5$  and  $6.88 \pm 0.30$  %ID/g, respectively). This particular derivative had a lipophilic linker as a result of the synthetic challenges faced during the preparation of a more hydrophilic triazole-tetrazine derivative.

In addition to pretargeting applications, the  $^{99m}\text{Tc}$ -tetrazine was used as a reagent to create multimodal imaging agents. Nanoscale gas vesicle (GV) ultrasound contrast agents were functionalized with TCO via an amide coupling to lysine residues. TCO-GVs were then radiolabeled by adding compound **6** where

the desired product, a new multimodal probe, was obtained in 59% radiochemical yield. SPECT imaging and biodistribution studies in mice were completed where the labeled GV's showed uptake in the gall bladder ( $120 \pm 29.1$  %ID/g), liver ( $16.8 \pm 7.50$  %ID/g), lungs ( $3.26 \pm 1.53$  %ID/g), small intestines ( $14.5 \pm 5.30$  %ID/g), and spleen ( $5.47 \pm 2.71$  %ID/g) at 120 min post injection. In addition to radiolabelling, the TCO-GVs were also functionalized with a near IR-tetrazine dye to produce a multimodal ultrasound/photoacoustic (US/PA) imaging agent in a 68% yield.

## **Acknowledgements**

First of all, I would like to thank my supervisor, Dr. John Valliant for providing guidance, encouragement and advice throughout my time as a graduate student. Your passion, kindness, and generosity are something that I am incredibly grateful for. You have given your students opportunities that many students do not get to experience in their lifetime, and have opened up so many doors in terms of future endeavors. I look forward to working with you in this exciting field for years to come.

I would also like to thank my committee members, Dr. William Leigh and Dr. Jose Moran-Mirabal for the advice and support throughout the years, pushing my boundaries of knowledge, and for aiding me in becoming a better scientist.

Next, I would like to thank the past and present members of the Valliant research group for the support and friendship throughout the years. I would like to thank Dr. A-man Zlitni (holla!) for being an amazing mentor and friend. Thank you to Nancy, Amber and Shannon for teaching me all that there is to know about biology, and for always being there to listen to my crazy ramblings. Thanks to Dr. Afaf Genady for all of the help over the years, whether it be fixing equipment, or trying to make it through an extra stubborn reaction. Thank you to Little Z for being by my side since day one, and for sharing all of the laughter, tears, and adventures together. I am going to miss seeing your face everyday! Thank you Sam for being such a good friend and for being on this journey with me since we were little first year undergraduate babies. Who knew that one day we would be

kicking butt and taking names as doctors!? Thank you Steph, Natalie, Rowan, Zoya, Leanne, Kevin and George for being such an amazing group to work with.

I would like to thank the department of Chemistry and Chemical biology, especially Tammy for the tremendous support throughout the years. I would also like to thank everyone in the department who have become close friends, whether it be through MCGSS, softball, or other social outings, you have all made graduate school a very enjoyable experience.

Finally, I would like to thank my incredible husband, Mike. First off, thanks for marrying me – that was pretty cool. Second, thank you for keeping me sane (or you trying to) during these past 5 years, all while completing a PhD yourself. I can honestly say that without your love, support, and strength, I would not be where I am today. I am so unbelievably proud of how far we have come, from being completely clueless in first year of undergrad labs, to crushing it all the way to double doctor status! You are my best friend, and I cannot wait to see where life takes us. Love ya boo!

## **Dedication**

I would like to dedicate this dissertation to my amazing parents, Sonia and Duane. You have both worked your entire lives with the purpose of bettering the lives of your children. I am so unbelievably proud of your resiliency, work ethic, and selflessness. I love both of you with my entire heart, and I hope that Mike and I can grow to be half of the parents that you are.

## **Publications**

### ***Peer reviewed journal articles***

#### **Preparation and Evaluation of $^{99m}\text{Tc}$ -labeled Tridentate Chelates for Pretargeting Using Bioorthogonal Chemistry.**

**Holly A. Bilton**,\* Zainab Ahmad\*, Nancy Janzen, Shannon Czorny, John F. Valliant. Journal of Visualized Experiments 2017; 120: e55188. DOI: 10.3791/55188.

\*Co-authors

#### **A Bone-Seeking trans-Cyclooctene for Pretargeting and Bioorthogonal Chemistry: A Proof of Concept Study Using $^{99m}\text{Tc}$ - and $^{177}\text{Lu}$ -Labeled Tetrazines.**

Abdolreza Yazdani, **Holly Bilton**, Alyssa Vito, Afaf R. Genady, Stephanie M. Rathmann, Zainab Ahmad, Nancy Janzen, Shannon Czorny, Brian M. Zeglis, Lynn C. Francesconi, John F. Valliant. Journal of Medicinal Chemistry 2016; 59(20): 9381-89.

#### ***In Vivo* Biodistribution of Radiolabeled Acoustic Protein Nanostructures.**

Johann Le'Floch, Aimen Zlitni, **Holly A. Bilton**, Melissa Yin, Arash Farhadi, Nancy R. Janzen, Mikhail G. Shapiro, John F. Valliant, Stuart F. Foster. Molecular Imaging and Biology 2018; 20(2): 230-39.

### ***Published meeting abstracts***

#### **Preparation and *in vivo* testing of $^{99m}\text{Tc}(\text{I})$ -tetrazines for pretargeted imaging.**

Ph.D. Thesis – H. Bilton; McMaster University – Chemistry and Chemical Biology

**Holly A. Bilton**, Zainab Ahmad, Nancy Janzen, Shannon Czorny, Dalya Abdel-Atti, Kimberly Edwards, Lynn C. Francesconi, Brian M. Zeglis, Jason S. Lewis, John F. Valliant. *J. Label. Compd. Radiopharm.* 2017; 60: S92.

**Radiolabeled nanoscale gas vesicles using bioorthogonal chemistry for multimodal SPECT and ultrasound imaging.**

**Holly A. Bilton**, Aimen Zlitni, Johann Le Floc'h, Melissa Yin, Alyssa Vito, Stuart F. Foster, Mikhail G. Shapiro, John F. Valliant. *J. Label. Compd. Radiopharm.* 2017; 60: S281.

**Imidazole-Based, Tetrazine Functionalized,  $^{99m}\text{Tc(I)}$  Tridentate Chelates for Bioorthogonal Chemistry.**

**Holly A. Bilton**, John F. Valliant. *J. Labelled Compd. Rad.* 2015; 58: S61.

**Synthesis, Characterization and Imaging of a  $^{99m}\text{Tc(I)}$ -Tetrazine Tridentate Ligand Complex for Bioorthogonal Chemistry.**

Zainab Ahmad, Megan Blacker, Aimen Zlitni, **Holly Bilton**, John Valliant. *J. Label. Compd. Radiopharm.* 2015; 58: S138.

### ***Textbook Chapter Publications***

**The Radiopharmaceutical Chemistry of Technetium-99m.**

Stephanie M. Rathmann, Zainab Ahmad, Samantha Slikboer, **Holly A. Bilton**, Denis P. Snider, John F. Valliant. In *Radiopharmaceutical Chemistry*; Lewis, J. S., Windhorst, A. D., Zeglis, B. M., Eds.; SpringerLink, 2019; pp 311–333.

## Table of Contents

<b>Abstract .....</b>	<b>iv</b>
<b>Acknowledgements .....</b>	<b>viii</b>
<b>Dedication .....</b>	<b>ix</b>
<b>Publications .....</b>	<b>x</b>
<b>List of Figures .....</b>	<b>xvii</b>
<b>List of Supporting Figures .....</b>	<b>xxvi</b>
<b>List of Tables .....</b>	<b>xxix</b>
<b>List of Supporting Tables .....</b>	<b>xxx</b>
<b>List of Abbreviations .....</b>	<b>xxxi</b>
 Chapter 1: Introduction	 1
<b>1.1 Molecular imaging .....</b>	<b>1</b>
<b>1.2 Molecular imaging probes .....</b>	<b>2</b>
<b>1.3 Nuclear imaging .....</b>	<b>3</b>
1.3.1 Single Photon Emission Computed Tomography.....	3
1.3.2 Technetium-99m .....	4
1.3.3 Technetium-99m(I) Chelates .....	6
1.3.4 Isostructural Rhenium Complexes .....	8
1.3.5 Challenges in preparing targeted <sup>99m</sup> Tc radiopharmaceuticals .....	8
<b>1.4 Bioorthogonal Chemistry and Pretargeted Imaging.....</b>	<b>9</b>
<b>1.5 Thesis Overview.....</b>	<b>12</b>
<b>1.6 References.....</b>	<b>14</b>
 Chapter 2: Preparation and evaluation of <sup>99m</sup> Tc-labeled tridentate chelates for pretargeting using bioorthogonal chemistry	 19



<b>2.1</b>	<b>Introduction .....</b>	<b>19</b>
<b>2.2</b>	<b>Protocol .....</b>	<b>22</b>
2.2.1	Radiolabeling of tetrazine-tridentate ligands with $^{99m}\text{Tc}$ .....	22
2.2.2	Radiolabeling of tetrazine-tridentate ligands with $^{99m}\text{Tc}$ .....	24
<b>2.3</b>	<b>Results and discussion .....</b>	<b>27</b>
<b>2.4</b>	<b>Conclusion and Future Work .....</b>	<b>35</b>
<b>2.5</b>	<b>Acknowledgements .....</b>	<b>35</b>
<b>2.6</b>	<b>References .....</b>	<b>36</b>
Chapter 3: Evaluation of $^{99m}\text{Tc}$ -tetrazines for pretargeted imaging with trans-cyclooctene functionalized antibodies 38		
<b>3.1</b>	<b>Introduction .....</b>	<b>38</b>
<b>3.2</b>	<b>Materials and Methods .....</b>	<b>43</b>
3.2.1	General materials and instruments .....	43
3.2.2	Animal models and biodistribution studies .....	44
3.2.3	Preparation of TCO-modified antiVEGFR2 antibody (TCO-antiVEGFR2).....	44
3.2.4	Labeling of TCO-antiVEGFR2 with 6 .....	45
3.2.5	Flow Chamber Cell Adhesion Assay .....	45
3.2.6	Preparation of TCO-modified huA33 antibody (TCO-huA33).....	46
3.2.7	Labeling of TCO-huA33 with 6 .....	47
3.2.8	Pretargeted SPECT Imaging Studies .....	47
3.2.9	Biodistribution Studies .....	48
3.2.10	Blood clearance studies .....	48
<b>3.3</b>	<b>Results and Discussion .....</b>	<b>49</b>
3.3.1	Preparation and labeling of TCO-antiVEGFR2 antibody with 6 .....	49
3.3.2	Flow Chamber Cell Adhesion Assay .....	51
3.3.3	Preparation and labeling of TCO-huA33 antibody with 10 .....	53

3.3.4	Pretargeted imaging and biodistribution of 6 .....	55
3.3.5	Pretargeted imaging and biodistribution of 10 .....	57
3.3.6	Cysteine and histidine stability studies .....	60
3.3.7	Blood clearance studies .....	62
3.3.8	Comparing pretargeting with TCO-huA33 antibody and TCO-ALN... ..	66
<b>3.5</b>	<b>Conclusion and Future Work .....</b>	<b>67</b>
<b>3.6</b>	<b>References .....</b>	<b>68</b>
Chapter 4: Towards the optimization of the pharmacokinetics of <sup>99m</sup> Tc(I) labeled tetrazines. Investigation of the mechanism of clearance 71		
<b>4.1</b>	<b>Introduction .....</b>	<b>71</b>
<b>4.2</b>	<b>Materials and Methods .....</b>	<b>76</b>
4.2.1	General materials and instruments .....	76
4.2.2	Cells and culture protocols .....	78
4.2.3	Cell assay protocols .....	78
4.2.4	Flow cytometry assay protocol .....	79
4.2.5	Fluorescence cell imaging .....	79
4.2.6	Animal models and biodistribution studies .....	80
<b>4.3</b>	<b>Results and Discussion .....</b>	<b>81</b>
4.3.1	Evaluation of nitrogen containing bisphosphonates as mevalonate pathway inhibitors .....	81
4.3.2	Biodistribution studies in the presence of taurine .....	87
4.3.3	<i>In vitro</i> and <i>in vivo</i> evaluation of P-glycoprotein/Multi-drug resistance protein inhibitors .....	90
4.3.4	<i>In vivo</i> evaluation of OATP inhibitors .....	97
4.3.5	<i>In vivo</i> evaluation of OAT inhibitors .....	99
4.3.6	<i>In vivo</i> evaluation of MRP inhibitors .....	100
<b>4.4</b>	<b>Conclusions and Future Work .....</b>	<b>105</b>
<b>4.5</b>	<b>References .....</b>	<b>106</b>

<b>4.6 Supplemental Information.....</b>	<b>110</b>
Chapter 5: Towards a new <sup>99m</sup> Tc-labeled tetrazine-chelate derivative with improved pharmacokinetics 113	
<b>5.1 Introduction .....</b>	<b>113</b>
<b>5.2 Materials and Methods .....</b>	<b>114</b>
5.2.1 General materials and instruments .....	114
5.2.2 Synthesis of compounds 22-23b, 26-27, and 30-32.....	115
<b>5.2.3 Animal models and biodistribution studies .....</b>	<b>115</b>
<b>5.3 Results and Discussion .....</b>	<b>116</b>
5.3.1 Effect of chelates on distribution .....	116
5.3.3 Alternative synthesis of a triazole based chelate .....	126
<b>5.4 Conclusion .....</b>	<b>130</b>
<b>5.5 References.....</b>	<b>131</b>
Chapter 6: <sup>99m</sup> Tc-labeled tetrazines for the development of multimodal imaging probes 132	
<b>6.1 <i>In vivo</i> biodistribution of radiolabeled acoustic protein nanostructures<sup>‡</sup> .....</b>	<b>132</b>
6.1.1 Introduction.....	133
6.1.2 Results .....	136
6.1.3 Discussion .....	148
6.1.4 Conclusion.....	151
6.1.5 Experimental .....	152
<b>6.2 The development of a nanoscale multimodal ultrasound-photoacoustic dual imaging agent <sup>§</sup> .....</b>	<b>158</b>
6.2.1 Introduction.....	159
6.2.2 Results and Discussion .....	161

6.2.3	Conclusion and Future Work.....	167
6.2.4	General Methods.....	168
6.2.5	Experimental .....	168
<b>6.3</b>	<b>References.....</b>	<b>170</b>
<b>6.4</b>	<b>Supplemental Information.....</b>	<b>175</b>
<b>7</b>	<b>Summary and Future Work</b>	<b>178</b>
<b>7.1</b>	<b>Summary.....</b>	<b>178</b>
<b>7.2</b>	<b>Future Work.....</b>	<b>181</b>
7.2.1	Development of a more hydrophilic triazole ligand.....	181
7.2.3	The development of a <sup>188</sup> Re-tetrazine derivative for therapeutic applications .....	184
7.2.4	The development of a targeted PA/US contrast agent for tumour imaging .....	185
<b>7.3</b>	<b>References.....</b>	<b>189</b>
APPENDIX I		192
	<b>Supporting Information for Chapter 2 .....</b>	<b>192</b>
APPENDIX II		231
	<b>Supplemental Information for Chapter 5.....</b>	<b>231</b>

## List of Figures

Figure 1.1 Schematic showing the key components of a MI probe.....	3
Figure 1.2 Schematic of a $^{99}\text{Mo}/^{99\text{m}}\text{Tc}$ generator.....	5
Figure 1.3 Single amino acid chelate (SAAC)-derived ligand (MIP-1404) that is currently in phase 3 clinical trials for imaging prostate cancer.....	7
Figure 1.4 A) Pretargeting approach using a TCO-antibody and a radiolabeled tetrazine at the tumour site. <sup>59</sup> B) SPECT/CT image (postmortem, maximum intensity projection) of CC49-TCO pretargeted mouse bearing LS174T xenografts, 3 h after injection of a $^{111}\text{In}$ -tetrazine.....	12
Figure 2.1 The bioorthogonal IEDDA reaction between tetrazine and TCO.....	20
Figure 2.2 $^{99\text{m}}\text{Tc}$ -complexes 6, 10, 14, 16, and 18 were produced using different linkers (Y) and donor groups (X) as shown (bottom). All compounds were radiolabeled with $^{99\text{m}}\text{Tc}[\text{Tc}(\text{CO})_3(\text{OH})_2]_3^+$ using the same reaction conditions (top), with the exception of 16, which did not require step (ii).....	27
Figure 2.3 Stability test results using compound 10. $\gamma$ -HPLC traces of 10 incubated in PBS at 37 °C for 1, 4 and 6 h.....	28
Figure 2.4 Biodistribution results for $^{99\text{m}}\text{Tc}$ -tetrazines 6, 10, 14, 16, 18 (bars indicated). Data shown were obtained from selected tissues and fluids taken 6 h post injection of the radiolabeled derivatives, and activity was normalized to tissue or fluid weight, as mean percent injected dose per gram of tissue or fluid (%ID/g) $\pm$ SEM. Bone targets are indicated by •. NOTE: All remaining tissues not shown had mean %ID/g that was less than 1%.....	29
Figure 2.5 Biodistribution results for control study using $^{99\text{m}}\text{Tc}$ -tetrazine (6) without prior injection of TCO-ALN. Data shown were obtained from selected tissues and fluids taken from 3 mice at 0.5, 1, 4, and 6 h post injection of 6. Activity was normalized to tissue or fluid weight, as mean percent injected dose per gram of tissue or fluid (%ID/g) $\pm$ SEM.....	30

Figure 3.1 Tumour-to-organ ratios for CC49-TCO-pretargeted <sup>177</sup> Lu-tetrazine in mice bearing LS174T colon carcinoma xenografts. <sup>6</sup> This research was originally published in JNM. Rossin, R. <i>et al.</i> J Nucl Med. 2013; 54(11): 1989-1995. © SNMMI.....	38
Figure 3.2 Pretargeted PET imaging using <sup>64</sup> Cu-Tz-SarAr with 48 h (A) and 120 h (B) accumulation intervals. The coronal slices (left) intersect the center of the tumour (white arrow). Maximum intensity projections (MIP) collected at 24 h post-injection are also displayed (right); (C) Activity concentration in the tumour as a function of both time post-injection and accumulation interval for pretargeting with <sup>64</sup> Cu-Tz-SarAr; (D) Activity concentration in the blood as a function of both time post injection and accumulation interval pretargeting with <sup>64</sup> Cu-Tz-SarAr; (E) Tumour-to-blood activity concentration ratios as a function of both time post injection and accumulation interval pretargeting with <sup>64</sup> Cu-Tz-SarAr; (F) Tumour-to-muscle activity concentration ratios as a function of both time post injection and accumulation interval pretargeting with <sup>64</sup> Cu-Tz-SarAr. Reprinted (adapted) with permission from Zeglis, B.M <i>et al.</i> Mol. Pharm. 2015, 12(10), 3575-3587. Copyright 2019 American Chemical Society.....	39
Figure 3.3 MALDI-TOF analysis of antiVEGFR2 (left) and TCO-antiVEGFR2 (right) showing an average of 4.3 TCO groups per antibody.....	48
Figure 3.4 Radio-iTLCs of 6 (left) and 6 following the addition of TCO-antiVEGFR2 (right). Note: baseline is set at 50 mm.....	49
Figure 3.5 A graphical representation showing the amount of 6 binding to H520 cells when (a) H520 cells pre-treated with TCO-antiVEGFR2 for 30 min before introducing 6 and (b) untreated cells. The binding of 6 was 12 times higher in TCO-tagged cells (a) compared to untreated cells (b) (P <0.001). Data is expressed as counts per minute (CPM) per µg of protein found in each sample (n= 5). *Statistical analysis was done using a one-way ANOVA relative to (b).....	50

Figure 3.6 iTLC analysis of 10 (left) and 10 after incubation with TCO-huA33 (right).....	52
Figure 3.7 SPECT-CT images of pretargeting approach at 1,4 and 6 hours (left to right) post-injection with 6 containing the Re complex 5.....	53
Figure 3.8 Biodistribution data for pretargeting studies with TCO-huA33 and compounds 5 and 6. Compounds 5 and 6 were co-administered (approximately 37 MBq of 6, 0.75 mM of 5) to athymic nude mice (n=4 per compound) 24 hours after the injection of TCO-huA33. Mice were sacrificed 6 hours post injection of 5 and 6. Data is expressed as the mean injected dose per gram (%ID/g) $\pm$ SEM.....	54
Figure 3.9 SPECT-CT images of pretargeting approach at 1, 4, and 6 hours (left to right) post-injection of 10.....	56
Figure 3.10 SPECT-CT images of pretargeting approach at 1, 4, and 6 hours (left to right) post-injection with 10 containing the Re complex 9.....	56
Figure 3.11 Biodistribution of pretargeting studies with TCO-huA33 and compound 10 (dark grey bars), or 9 + 10 (light grey bars). Compound 10 was administered (approximately 37 MBq) to Athymic nude mice (n=4 per compound) 24 hours post injection of TCO-huA33. Mice were sacrificed 6 hours post injection of 10. Data is expressed as the mean injected dose per gram (%ID/g) $\pm$ SEM.....	57
Figure 3.12 Gamma HPLC traces of 6 upon incubation at 37 °C with 2 mM L-cysteine for 1, 3 and 6 h (Method 1, 1 mL/min).....	59
Figure 3.13 Gamma HPLC traces of 6 upon incubation at 37 °C with 100 mM histidine for 1, 3 and 6 h (Method 1, 1 mL/min).....	60
Figure 3.14 iTLC of 10 in an eluent of 1:1 v/v (H <sub>2</sub> O: ACN) + 0.1% TFA. A) Control of 10 in PBS + 0.5% BSA + 0.01% tween80. B) Control of 10 in PBS + 0.5% BSA + 0.01% polysorbate-80 incubated with excess TCO-antiVEGFR2 for 10 minutes at 37 °C. C) Compound 10 isolated from blood taken at 15 minutes post-injection. D) The sample from C incubated with excess TCO-antiVEGFR2 for 10 minutes at 37 °C.....	61

Figure 3.15 Plot of %ID/g of 10 at 15, 25, 30, 60, and 120 minutes post-injection.

The inset shows the time where activity levels in the blood reach 50 %ID/g, indicated by an arrow.....63

Figure 4.1 Human hepatocyte transporters. Transporters on the sinusoidal membrane include sodium/ taurocholate co-transporting peptide (NTCP); three members of the OATP family (OATP1B1, OATP1B3 and OATP2B1); two members of the organic anion transporter family (OAT2 and OAT7); and OCT1. Efflux pumps in the hepatocyte basolateral membrane include MRP3, MRP4 and MRP6. Apical efflux pumps of the hepatocyte comprise P-gp; bile-salt export pump (BSEP); BCRP and MRP2. In addition, multidrug and toxin extrusion protein 1 (MATE1) is located in the apical hepatocyte membrane.<sup>14</sup> Reprinted with permission from Nature: Giacomini, K. M. *et al.* Nat. Rev. Drug Discov. 2010, 9, 215–236. Copyright 2010.....70

Figure 4.2 Inhibition of Mevalonate pathway by Bisphosphonates and Statins.....72

Figure 4.3 Structure of compound 14.....79

Figure 4.4 Biodistribution of compound 14 alone (light grey) and 14 with alendronate (dark grey) (300 µg). BALB/c mice (n=3 per compound) were injected with approximately 740 kBq of 14 and sacrificed 6 hours post injection. Data is expressed as the mean injected dose per gram (%ID/g) ± SEM. Organs and tissues with uptake less than 1 %ID/g are not presented. \*p < 0.05.....80

Figure 4.5 Biodistribution data from pretargeting studies with compound 14 and TCO-ALN, or compound 14 and TCO-ALN + ALN. Compound 14 was administered (approximately 740 kBq) to BALB/c mice (n=3 per compound) 1 hour post injection of TCO-ALN. Mice were sacrificed 6 hours post injection of 14. Data is expressed as the mean injected dose per gram (%ID/g) ± SEM. Organs and tissues with uptake less than 1 %ID/g are not presented. \*p < 0.05.....82



Figure 4.6 Biodistribution of compound 14 alone, 14 with alendronate (300 $\mu$ g), and 14 with zoledronate (135 $\mu$ g). BALB/c mice were administered approximately 740 kBq of 14 and sacrificed 6 hours post injection. Data is expressed as the mean injected dose per gram (%ID/g) $\pm$ SEM. Organs and tissues with uptake less than 1 %ID/g are not presented. *p < 0.05.....	84
Figure 4.7 Biodistribution of compound 14 alone, 14 with alendronate (300 $\mu$ g), and 14 with taurine (300 $\mu$ g). BALB/c mice were administered approximately 740 kBq of 14 and sacrificed 6 hours post injection. Data is expressed as the mean injected dose per gram (%ID/g) $\pm$ SEM. Organs and tissues with uptake less than 1 %ID/g are not presented. *p < 0.05.....	86
Figure 4.8 Percent binding of $^{99m}\text{Tc}$ -Sestamibi in Caco-2 (P-gp positive, dark bars) and MCF7 (P-gp negative, light bars) cell lines in the absence or presence of known P-gp inhibitors (10 $\mu$ M).....	89
Figure 4.9 Percent binding of compound 14 to Caco-2 (P-gp positive, dark bars) and MCF7 (P-gp negative, light bars) cells in the absence or presence of known P-gp inhibitors (10 $\mu$ M).....	90
Figure 4.10 Biodistribution data for $^{99m}\text{Tc}$ -Sestamibi alone and $^{99m}\text{Tc}$ -Sestamibi with Elacridar (62.4 mg/kg p.o.). BALB/c mice were administered approximately 740 kBq of $^{99m}\text{Tc}$ -Sestamibi and sacrificed 1 hour post injection. Data is expressed as the mean injected dose per gram (%ID/g) $\pm$ SEM. Organs and tissues with uptake less than 5 %ID/g are not presented. *p < 0.05, **p < 0.01, ***p < 0.001, ****p < 0.0001.....	91
Figure 4.11 Biodistribution data for compound 14 alone and 14 with Elacridar (62.4 mg/kg p.o.). BALB/c mice were administered approximately 740 kBq of 14 and sacrificed 1 hour post injection. Data is expressed as the mean injected dose per gram (%ID/g) $\pm$ SEM. Organs and tissues with uptake less than 1 %ID/g are not presented.....	93

Figure 4.12 Structures of key pathway inhibitors. A) Alendronate B) Taurine C) Zoledronate D) Indomethacin E) Indocyanine green F) Rifampicin G) Pantoprazole H) Elacridar I) Montelukast and J) Cyclosporin A.....99

Figure 4.13 Biodistribution data for compound 14 alone, and 14 with indocyanine green (300  $\mu$ g), alendronate (300  $\mu$ g), zoledronate (135  $\mu$ g), indomethacin (15  $\mu$ g), rifampicin (300  $\mu$ g), and Montelukast (375  $\mu$ g). Compound 14 (approximately 740 kBq) or 14 with each formulation additive were administered to healthy BALB/c mice (n=3 per compound). Biodistribution studies were conducted 6 hours post injection. Data is expressed as the mean injected dose per gram (%ID/g)  $\pm$  SEM. Organs and tissues with uptake less than 1 %ID/g are not presented. \*p < 0.05.....100

Figure 5.1 Labeling of 11a with  $^{99m}\text{Tc}$  to produce 11b. Experimental details are provided in Appendix II.....111

Figure 5.2 Structure of compound 14.....112

Figure 5.3 Biodistribution data of 11b (light bars) and 14 (dark bars). BALB/c mice (n=3 per compound) were injected with approximately 0.74 MBq of 11b or 14 and sacrificed 1 hour post injection. Data is expressed as the mean injected dose per gram (%ID/g)  $\pm$  SEM. Note: large error bars are due to the variability associated with clearance organs.....113

Figure 5.4 Synthesis of 22 from 19.....115

Figure 5.5 Synthesis of 23a from 22 .....115

Figure 5.6 HPLC traces of the reaction involving the treatment of 23a with  $^{99m}\text{Tc}[\text{Tc}(\text{CO})_3(\text{OH}_2)_3]^+$  (UV – top, Gamma – bottom). (Method 1, 1 mL/min).....116

Figure 5.7 Biodistribution of 11b (light bars) and 23a (dark bars). BALB/c mice (n=3 per compound) were injected with approximately 0.74 MBq of 11 or 23a and sacrificed 1 hour post injection. Data are expressed as the mean

injected dose per gram (%ID/g) $\pm$ SEM. Organs and tissues containing <1% ID/g were excluded from the graph.....	117
Figure 5.8 Synthesis of compound 27.....	118
Figure 5.9 Proposed amide coupling of 22 and 27.....	119
Figure 5.10 Attempted coupling of 23b with a commercially available active ester, Boc-HYNIC-NHS.....	120
Figure 5.11 Synthesis of 31.....	121
Figure 5.12 $^{99m}\text{Tc}$ labeling of 31 to produce 32.....	122
Figure 5.13 Biodistribution of 23a (solid bars) and 32 (patterned bars). BALB/c mice (n=3 per compound) were injected with approximately 0.74 MBq of 23a or 32 and sacrificed 1 and 6 hours post injection. Data is expressed as the mean injected dose per gram (%ID/g) $\pm$ SEM. Organs with less than 5 %ID/g were excluded from the graph.....	123
Figure 6.1 Radiolabeling methodology and processes. A) Synthesis of [ $^{99m}\text{Tc}$ ]Tz complex 6. (1) PyBOP, DIPEA, DMF, ((4- tetrazine-3-yl)phenyl)methanamine hydrochloride, rt., 12 h (2) (i) $^{99m}\text{Tc}[\text{Tc}(\text{CO})_3(\text{OH}_2)_3]^+$ , MeOH, saline, 60 °C (MW), 20 min. (ii) TFA, DCM, 60 °C (MW), 6 min. B) Representation of the chemistry used to prepare TCO conjugated GVs. TCO-GVs were purified by dialysis and concentrated to an optical density (OD <sub>500nm</sub> ) of 40. C) Chemistry used to label TCO-GVs with compound 6. [ $^{99m}\text{Tc}$ ]Tz (6) was added to TCO-GVs in PBS for 30 min and the [ $^{99m}\text{Tc}$ ]GVs purified by centrifugal flotation.....	132
Figure 6.2 Quantitative <i>ex vivo</i> tissue counting biodistribution data for [ $^{99m}\text{Tc}$ ]GVs and [ $^{99m}\text{Tc}$ ]Tz (6). Groups of mice (n = 3/ time point) were euthanized at 5, 20, 60, and 120 min ([ $^{99m}\text{Tc}$ ]GVs) or at 30, 60, 240, and 360 min ([ $^{99m}\text{Tc}$ ]Tz). Tissues and fluids were then collected and activity counted. A) The uptake of [ $^{99m}\text{Tc}$ ]GVs was mainly found in the gall bladder, liver, lungs, small intestine, spleen, and bladder. B) In contrast, [ $^{99m}\text{Tc}$ ]Tz was mainly found in the gall bladder, small intestine, large intestine and cecum, and	

- bladder. Data are reported in % injected dose (%ID/g)  $\pm$  SEM.....134
- Figure 6.3 Maximum intensity projection (MIP) of SPECT images following [ $^{99m}\text{Tc}$ ]GVs injection. Rapid uptake of [ $^{99m}\text{Tc}$ ]GVs is shown in the lungs (white stars, Lg), gall bladder (GB) and liver (L), followed by duodenum (D) and small intestines over time.....135
- Figure 6.4 *Ex vivo* tissue counting and SPECT biodistribution. A) Comparison of both biodistribution data reporting the uptake of [ $^{99m}\text{Tc}$ ]GVs in major organ/tissues 20 min following injection. B) [ $^{99m}\text{Tc}$ ]GVs uptake in the duodenum (SPECT) and small intestine (*ex vivo* tissue counting) showing a similar increase at corresponding time points (4 time points,  $n = 3$  per time point). Each SPECT reported values were calculated using the segmentation results multiplied by the volume of the corresponding segmented organ. Data are reported in %ID/organ  $\pm$  SEM (*Ex vivo* counting data is not normalized for weight, 4 time points,  $n = 3$  per time point, SPECT  $n = 23, 55, 31,$  and  $8$  at  $5, 20, 60,$  and  $120$  min, respectively).....136
- Figure 6.5 MIP, 3D segmentation, and time activity curves (TACs) of segmented organs. A) MIP of SPECT data and associated 3D segmentation of individual organs at 120 min (lungs in green (Lg), liver in brown (L), gall bladder (GB) in light orange, spleen (S) in yellow, duodenum in light blue (D), and bladder in light brown (B)). B) TACs showed the uptake of [ $^{99m}\text{Tc}$ ]GVs in segmented organs. TACs are reported in percent injected dose per volume of tissue (%ID/cm<sup>3</sup>) by averaging together data acquired within a time periods of 10 min to yield the mean and associated standard error of the mean (SEM). The inset shows the number of observations ( $n$ ) for each time point. Significant statistical differences are only shown for the gall bladder and duodenum for each data point between 10 and 60 min (\* $p \leq 0.05$ , \*\* $p \leq 0.01$ , \*\*\*\* $p \leq 0.0001$ ).....138
- Figure 6.6 Fluorescence imaging of the liver and spleen tissues. Native GV in A)

the liver and in C) the spleen tissues showing only autofluorescence. Alexa 488 fluorophore tagged GVs in B) the liver and D) spleen tissues showing an increase green signal intensity. White arrows show clustering of Alexa488-GVs in both tissues. Scale bar is 100 $\mu\text{m}$ (a–c) and 50 $\mu\text{m}$ (d). Magnification: $\times 20$ (a, c) and $\times 10$ (b, d).....	139
Figure 6.7 Schematic of ultrasound and photoacoustic imaging systems.....	152
Figure 6.8 Synthesis of IR-GVs.....	154
Figure 6.9 Absorbance spectra of IR-Tz (green), TCO-GV (red), and IR-GV (blue) in PBS.....	155
Figure 6.10 Photoacoustic average threshold. Intact TCO-GVs (blue), popped TCO-GVs (purple), intact IR-GVs (red), and popped IR-GVs (orange).....	156
Figure 6.11 Average absorbance (n=3) vs. wavelength for the loading study, with increasing amounts of IR-Tz added to 30 OD of TCO-GVs.....	157
Figure 6.12 PA average signal of loading study samples, with increasing amounts of IR-Tz added to 30 OD of TCO-GVs.....	157
Figure 6.13 Unmixing of IR-GVs at various concentrations from whole blood. (green = IR-GVs, red = oxy hemoglobin, blue = deoxy hemoglobin). From left to right: 30 OD, 15 OD, blood alone, 3 OD, 0.3 OD.....	158
Figure 7.1 Proposed synthesis of a polar triazole-tetrazine chelate derivative.....	173
Figure 7.2 Alternate synthesis of a more hydrophilic triazole-tetrazine ligand.....	173
Figure 7.3 Example of a theranostic pair of $^{99\text{m}}\text{Tc}$ and $^{188}\text{Re}$ tetrazine derivatives.....	175
Figure 7.4 Amide coupling of a tetrazine-acid to glutamate-urea-lysine.....	177

Figure 7.5 Functionalization of TCO-GVs with a PSMA-tetrazine for prostate cancer imaging.....	178
Figure 7.6 Structure of uPAR targeting peptide <sup>64</sup> Cu-NOTA-AE105.....	179

## List of Supporting Figures

Figure S2.1 Synthesis of 4 from 1. a) DMF, DIPEA, t-butylbromoacetate, 80 °C, 4 h. b) DCE, NaBH(OAc) <sub>3</sub> , 6-aminocaproic acid, 50 °C, 12 h. c) PyBOP, DIPEA, DMF, ((4-tetrazine-3-yl)phenyl)methanamine hydrochloride, rt, 12 h.....	182
Figure S2.2 <sup>1</sup> H NMR (600 MHz, CDCl <sub>3</sub> ) of 2.....	183
Figure S2.3 <sup>13</sup> C NMR (150 MHz, CDCl <sub>3</sub> ) of 2.....	184
Figure S2.4 <sup>1</sup> H NMR (600 MHz, CDCl <sub>3</sub> ) of 6-(Bis((1-(2-( <i>tert</i> -butoxy)-2-oxoethyl)-1 <i>H</i> -imidazol-2-yl)methyl)amino)hexanoic acid (3).....	185
Figure S2.5 <sup>13</sup> C NMR (150 MHz, CDCl <sub>3</sub> ) of 6-(Bis((1-(2-( <i>tert</i> -butoxy)-2-oxoethyl)-1 <i>H</i> -imidazol-2-yl)methyl)amino)hexanoic acid (3).....	186
Figure S2.6 <sup>1</sup> H NMR (600 MHz, CDCl <sub>3</sub> ) of <i>tert</i> -Butyl {2-[(1-( <i>tert</i> -butoxycarbonylmethyl)-1 <i>H</i> -imidazol-2-yl)methyl][6-oxo-6-([ <i>p</i> -(1,2,4,5-tetrazin-3-yl)phenyl)methyl]amino)hexyl]amino)methyl]-1 <i>H</i> -imidazol-1-yl}acetate (4).....	188
Figure S2.7 <sup>13</sup> C NMR (150 MHz, CDCl <sub>3</sub> ) of <i>tert</i> -Butyl {2-[(1-( <i>tert</i> -butoxycarbonylmethyl)-1 <i>H</i> -imidazol-2-yl)methyl][6-oxo-6-([ <i>p</i> -(1,2,4,5-tetrazin-3-yl)phenyl)methyl]amino)hexyl]amino)methyl]-1 <i>H</i> -imidazol-1-yl}acetate (4).....	189
Figure S2.8 Synthesis of 5 from 4. a) Re(CO) <sub>3</sub> (H <sub>2</sub> O) <sub>3</sub> Br, ACN, MW, 60 °C, 20 min. b) DCM, TFA, MW, 60 °C, 6 min.....	189
Figure S2.9 <sup>1</sup> H NMR (600 MHz, MeOD) of <i>tert</i> -Butyl {2-[(1-( <i>tert</i> -butoxycarbonylmethyl)-1 <i>H</i> -imidazol-2-yl)methyl][6-oxo-6-([ <i>p</i> -(1,2,4,5-tetrazin-3-yl)phenyl)methyl]amino)hexyl]amino)methyl]-1 <i>H</i> -imidazol-1-yl}acetate rhenium tricarbonyl complex (5).....	191

Figure S2.10 $^{13}\text{C}$ NMR (150 MHz, MeOD) of <i>tert</i> -Butyl {2-[[[1-( <i>tert</i> -butoxycarbonylmethyl)-1 <i>H</i> -imidazol-2-yl]methyl][6-oxo-6-([ <i>p</i> -(1,2,4,5-tetrazin-3-yl)phenyl]methyl)amino)hexyl]amino)methyl]-1 <i>H</i> -imidazol-1-yl}acetate rhenium tricarbonyl complex (5).....	192
Figure S2.11 Synthesis of 6 from 4. a) $^{99\text{m}}\text{Tc}(\text{CO})_3(\text{OH}_2)_3^+$ , MeOH, Saline (0.9%), MW, 60 °C, 20 min. b) DCM, TFA, MW, 60 °C, 6 min.....	193
Figure S2.12 Gamma HPLC traces of reaction between 6 and TCO.....	194
Figure S2.13 Gamma HPLC traces of 6 after incubation in PBS for 1 and 3 hours.....	195
Figure S2.14 Gamma HPLC traces of 6 upon incubation at 37 °C with 100 mM L-cysteine for 1, 3 and 6 hours.....	196
Figure S2.15 Gamma HPLC traces of 6 upon incubation at 37 °C with 100 mM histidine for 1, 3 and 6 hours.....	196
Figure S2.16 Gamma HPLC traces of 6 upon incubation at 37 °C in PBS for 1, 3 and 6 hours.....	197
Figure S2.17 HPLC chromatograms (UV and $\gamma$ ) of compound 5 (UV) (top) co-injected with compound 6 ( $\gamma$ )(bottom).....	198
Figure S2.18 Synthesis of Compound 8 from Compound 2. a) DMF, DIPEA, <i>t</i> -butylbromoacetate, 80 °C, 4 h. b) DCE, $\text{NaBH}(\text{OAc})_3$ , $\text{NH}_2\text{-PEG}_{10}\text{-CH}_2\text{CH}_2\text{COOH}$ , 50 °C, 12 h. c) PyBOP, DIPEA, DMF, ((4-tetrazine-3-yl)phenyl)methanamine hydrochloride, rt, 12 h.....	199
Figure S2.19 $^1\text{H}$ NMR (600 MHz, $\text{CDCl}_3$ ) of 7.....	200
Figure S2.20 $^{13}\text{C}$ NMR (150 MHz, $\text{CDCl}_3$ ) of 7.....	201
Figure S2.21 $^1\text{H}$ NMR (600 MHz, $\text{CDCl}_3$ ) of 8.....	203
Figure S2.22 $^{13}\text{C}$ NMR (150 MHz, $\text{CDCl}_3$ ) of 8.....	204
Figure S2.23 Synthesis of compound 9 from 8. a) $\text{Re}(\text{CO})_3(\text{OH}_2)_3\text{Br}$ , ACN, MW, 60 °C, 20 min. b) DCM, TFA, MW, 60 °C, 6 min.....	204
Figure S2.24 $^1\text{H}$ NMR (600 MHz, MeOD) of 9.....	206
Figure S2.25 $^{13}\text{C}$ NMR (150 MHz, MeOD) of 9.....	207

Figure S2.26 Synthesis of 10 from 8. a) $^{99m}\text{Tc}(\text{CO})_3(\text{OH}_2)_3^+$ , MeOH, Saline (0.9%), MW, 60 °C, 20 min. b) DCM, TFA, MW, 60 °C, 6 min.....	208
Figure S2.27 Co-injection of 9 (UV) (top) with 10 (bottom) (gamma).....	209
Figure S2.28 Stability of 10 in PBS at 1 (top), 4 (middle) and 6 hours (bottom).....	210
Figure S2.29 Synthesis of 12 from 2. a) DMF, DIPEA, t-butylbromoacetate, 80 °C, 4 h. b) DCE, $\text{NaBH}(\text{OAc})_3$ , $\text{NH}_2\text{-PEG}_5\text{-CH}_2\text{COOH}$ , 50 °C, 12 h. c) PyBOP, DIPEA, DMF, ((4-tetrazine-3-yl)phenyl)methanamine hydrochloride, rt, 12 h.....	211
Figure S2.30 $^1\text{H}$ NMR (600 MHz, $\text{CDCl}_3$ ) of 11a.....	212
Figure S 2.31 $^{13}\text{C}$ NMR (150 MHz, $\text{CDCl}_3$ ) of 11a.....	213
Figure S2.32 $^1\text{H}$ NMR (600 MHz, $\text{CDCl}_3$ ) of 12.....	215
Figure S2.33 $^{13}\text{C}$ NMR (150 MHz, $\text{CDCl}_3$ ) of 12.....	216
Figure S2.34 Synthesis of 13 from 12. a) $\text{Re}(\text{CO})_3(\text{OH}_2)_3\text{Br}$ , ACN, 60 °C, 20 min. b) DCM, TFA, 60 °C, 6 min.....	216
Figure S2.35 Synthesis of 14 from 12. a) $^{99m}\text{Tc}(\text{CO})_3(\text{OH}_2)_3^+$ , MeOH, Saline (0.9%), MW, 60 °C, 20 min. b) DCM, TFA, 60 °C, 6 min.....	218
Figure S2.36 HPLC chromatograms (UV and gamma) of compound 13 (UV - top) co-injected with compound 14 (gamma - bottom).....	219
Figure S3.1 Bright field image (left) and fluorescent image (right) of P-gp (+) Caco-2 cells stained with FITC Mouse Anti-Human P-glycoprotein (CD243) Clone 17F9.....	106
Figure S5.1 Gamma HPLC trace of $^{99m}\text{Tc}$ labeling of 11b.....	220
Figure S5.2 $^1\text{H}$ NMR (600 MHz, Acetone- $\text{d}_6$ ) of 21.....	222
Figure S5.3 $^{13}\text{C}$ NMR (150 MHz, Acetone- $\text{d}_6$ ) of 21.....	223
Figure S5.4 HPLC trace of $^{99m}\text{Tc}$ labeling of 23a (UV – top, Gamma – bottom).....	225
Figure S5.5 Gamma HPLC traces of 23a upon incubation at 37 °C in PBS for 1 and 6 hours.....	226
Figure S5.6 $^1\text{H}$ NMR (600 MHz, $\text{CD}_3\text{OD}$ ) of 26.....	227



Figure S5.7 $^{13}\text{C}$ NMR (150 MHz, $\text{CD}_3\text{OD}$ ) of 26.....	228
Figure S5.8 $^1\text{H}$ NMR (600 MHz, $\text{CDCl}_3$ ) of 27.....	229
Figure S5.9 $^{13}\text{C}$ NMR (150 MHz, $\text{CDCl}_3$ ) of 27.....	230
Figure S5.10 $^1\text{H}$ NMR (600 MHz, $\text{CDCl}_3$ ) of 30.....	231
Figure S5.11 $^{13}\text{C}$ NMR (150 MHz, $\text{CDCl}_3$ ) of 30.....	232
Figure S5.12 $^1\text{H}$ NMR (600 MHz, $\text{CD}_3\text{OD}$ ) of 31.....	233
Figure S5.13 $^{13}\text{C}$ NMR (150 MHz, $\text{CD}_3\text{OD}$ ) of 31.....	234
Figure S5.14 Purified gamma HPLC trace of 32.....	235
Figure S6.1 Size exclusion HPLC chromatograms (gamma detection). A) Chromatogram of the reaction mixture containing both [ $^{99\text{m}}\text{Tc}$ ]GVs and free [ $^{99\text{m}}\text{Tc}$ ]Tz (6). B) Purified [ $^{99\text{m}}\text{Tc}$ ]GVs showing no residual [ $^{99\text{m}}\text{Tc}$ ]Tz.....	166
Figure S6.2 Radio-TLC analysis of [ $^{99\text{m}}\text{Tc}$ ]Tz (Top-left). Radio-TLC analysis of [ $^{99\text{m}}\text{Tc}$ ]GVs incubated at 37 °C in plasma at the indicated time points. Radio-TLC was eluted with 75% methanol and 25% water.....	167

## List of Tables

Table 1.1 Key features of major molecular imaging modalities. Cost of systems: \$ = <\$100,000; \$\$ = \$100,000-300,000; \$\$\$ = >\$300,000 (figures in USD).....	2
Table 1.2 Bioorthogonal pairs and their second order reaction rates.....	10
Table 2.1 Bone: blood ratios determined from biodistribution studies.....	31
Table 4.1 Inhibitors of specific hepatobiliary transport pathways and their dose (i.v. = intravenous, p.o. = per os).....	98
Table 5.1 List of reaction conditions of 22 with 27.....	119

## List of Supporting Tables

Table S6.1 Stability in plasma. Table reports the stability of [ $^{99m}\text{Tc}$ ]GVs in plasma at 37 °C for up to 120 minutes.....	167
Table S6.2 Activity in plasma layers. Table reports the % Activity in the GV and plasma layers after centrifugal flotation at 60 and 120 minutes.....	168
Table S6.3 3D Segmentation quantification. Table reports the mean and SEM of the volume of segmented organs.....	168
Table S6.4 Dynamic Uptake quantification. Table reports the mean and SEM of the uptake rate constants. Rate constants were calculated using a linear regression for all organs using the 0-10 min range except for the duodenum for which the 30-60 min range was used.....	168

## List of Abbreviations

### A

7AAD:	7-aminoactinomycin D
ACN:	Acetonitrile
ALN:	Alendronate
AREB:	Animal Ethics Research Board
a.u.	Arbitrary unit

### B

Boc:	tert-butoxycarbonyl
BSA:	Bovine serum albumin

### C

CAF:	McMaster central animal facility
CCAC:	Canadian council on animal care
CDCl <sub>3</sub> :	Deuterated chloroform
CD <sub>3</sub> OD:	Deuterated methanol
CEUS:	Contrast enhanced ultrasound
Ci:	Curie
CPM:	Counts per minute
CT:	Computed tomography
δ:	Chemical shift (NMR)

### D

DCM:	Dichloromethane
------	-----------------

DI: Deionized  
DIPEA: Diisopropylethylamine  
DMF: Dimethylformamide  
DMSO: Dimethyl sulfoxide

## **E**

EDC: 1-ethyl-3-(3-dimethylaminopropyl)carbodiimide  
ESI-MS: Electrospray ionization-mass spectrometry  
EtOH: Ethanol

## **F**

FITC: Fluorescein isothiocyanate  
FITC-Ab: FITC-tagged P-glycoprotein mouse anti-human antibody  
Fmoc: Fluorenylmethyloxycarbonyl

## **G**

Glu: Glutamic acid  
GBq: Gigabequerel  
GVs: Gas vesicles  
 $\gamma$ : Gamma

## **H**

HBTU: 2-(1*H*-benzotriazol-1-yl)-1,1,3,3 tetramethyluronium  
hexafluorophosphate  
HCl: Hydrochloric acid  
HPLC: High performance liquid chromatography

hr: Hour(s)

HRMS: High-resolution mass spectrometry

## **I**

ICG: Indocyanine green

%ID/g: Percent injected dose per gram

IEDDA: Inverse electron demand Diels-Alder reaction

IgG: Immunoglobulin G

IR: Infrared

iTLC: Instant thin layer chromatography

i.v. Intravenous

## **K**

kBq: Kilobecquerel

K<sub>d</sub>: Dissociation constant

kD: Kilodalton

## **L**

Lys: Lysine

## **M**

mAb: Monoclonal antibody

MDR: Multidrug resistance gene

MeOH: Methanol

MI: Molecular imaging

min: Minute(s)

MRP: Multidrug resistance-associated protein

## **N**

NHS: N-hydroxysuccinimide

NMR: Nuclear magnetic resonance

## **O**

OATP: Organic anion transport polypeptide

OAT: Organic anion transporter

OD: Optical density

## **P**

PBS: Phosphate buffered saline

PEG: Polyethylene glycol

PET: Positron emission tomography

P-gp: P-glycoprotein

p.o. Per Os (oral administration)

ppm: Parts per million

PSMA: Prostate specific membrane antigen

PyBOP: benzotriazol-1-yl-oxytripyrrolidinophosphoniumhexafluorophosphate

## **R**

Rcf: Relative centrifugal field

RCP: Radiochemical purity

RCY: Radiochemical yield

RES: Reticuloendothelial system

Rt: Retention time

## **S**

SAAC: Single amino acid chelate

Sec: Second(s)

SEM: Standard error of the mean

SPECT: Single photon emission computed tomography

## **T**

tBu: Tertiary-butyl

t-BuOH: Tert-butanol

TCO: Trans-cyclooctene

TCO-ALN: Trans-cyclooctene functionalized alendronate

TEA: Triethylamine

TFA: Trifluoroacetic acid

TFP: 2,3,5,6-tetrafluorophenyl trifluoroacetate

TLC: Thin layer chromatography

Tz: Tetrazine

$t_{1/2}$ : Half-life

## **U**

US: Ultrasound

UV: Ultraviolet

## **V**

VEGFR2: Vascular endothelial growth factor receptor 2

## **Chapter 1: Introduction**

### **1.1 Molecular imaging**

Molecular Imaging (MI) is a non-invasive technique that is used to image biochemical processes at the cellular level, without perturbing the system under study.<sup>1-3</sup> MI not only has the ability to identify the location of disease, but can also characterize specific molecular markers simultaneously. Furthermore, in oncology, MI has the ability to provide information across the entire disease burden, rather than a subset of tissue which is a known limitation of pathology done on biopsy samples.<sup>4</sup> The ability of MI to characterize tumours and identify the presence of specific targets is becoming an increasingly important tool to use in conjunction with the increasing availability of targeted therapies. For patients, this results in better outcomes, fewer complications and shorter hospital stays.<sup>5</sup>

There are several different MI modalities including magnetic resonance imaging (MRI), ultrasound (US), positron emission tomography (PET), and single photon emission computed tomography (SPECT). When selecting a MI modality, several factors have to be considered such as the spatial resolution required, level of sensitivity needed, if whole body imaging is necessary, and the depth of penetration required. Select features of the most widely used (clinically) MI modalities are summarized in Table 1.1.



**Table 1.1** Key features of major molecular imaging modalities. Cost of systems: \$ = <\$100,000; \$\$ = \$100,000-300,000; \$\$\$ = >\$300,000 (figures in USD).<sup>6</sup>

Imaging Modality	Resolution	Depth of Penetration	Time	Cost
<b>MRI</b>	10-100 $\mu\text{m}$	Whole body	Minutes-hours	\$\$\$
<b>US</b>	50 $\mu\text{m}$	Millimeters	Minutes	\$\$
<b>PET</b>	1-2 mm	Whole body	Minutes	\$\$\$
<b>SPECT</b>	1-2 mm	Whole body	Minutes	\$\$

## 1.2 Molecular imaging probes

MI probes are used with certain imaging modalities to help visualize specific biochemical targets and pathways, and are typically comprised of three main components. The first is a signaling component, which makes the probe observable by external detectors (paramagnetic metal complexes for MRI, ionizing radiation for PET and SPECT, fluorescent molecules for optical imaging, etc.). The second component is a targeting vector. A targeting vector must be highly selective for its target, and accumulate at the area of interest with substantially less uptake in other tissues. There are many different targeting vectors used in literature, ranging from small molecules, to peptides, to antibodies.<sup>7-16</sup> The third component of a MI probe system is a linker, which is responsible for tethering the targeting vector and signaling component. The linker

can also be used to modify the hydrophilicity of the probe through the addition of different functional groups.

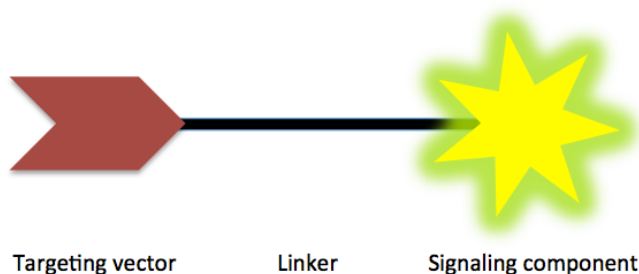


**Figure 1.1** Schematic showing the key components of a MI probe.

### 1.3 Nuclear imaging

Nuclear imaging is a subset of MI that utilizes radioisotopes as a signaling component to image disease. Nuclear imaging works by detecting ionizing radiation (gamma rays) emitted from radioactive isotopes and converting that into a visual representation of distribution. Under the umbrella of nuclear imaging, there are two main imaging modalities: positron emission tomography (PET), and single photon emission computed tomography (SPECT). PET relies on isotopes that decay through the release of positrons, while SPECT relies on isotopes that decay through the emission of gamma rays.

#### 1.3.1 Single Photon Emission Computed Tomography

Although PET scans have higher sensitivity than SPECT, the latter is more readily available, where gamma cameras and/or SPECT scanners can be found

Ph.D. Thesis – H. Bilton; McMaster University – Chemistry and Chemical Biology

in almost every major hospital.<sup>17</sup> This is due to the lower capital cost of gamma cameras versus PET cameras, and historically lower cost of SPECT isotopes compared to those for PET.<sup>5</sup> Furthermore, many SPECT isotopes such as indium-111 (<sup>111</sup>In), technetium-99m (<sup>99m</sup>Tc), and iodine-123 (<sup>123</sup>I) have longer half-lives than the most commonly used PET isotopes (2.8 days, 6 hours, and 13.2 hours respectively), making it easier to synthesize, purify, and distribute imaging agents beyond the facility in which they are produced.

### 1.3.2 Technetium-99m

For SPECT, <sup>99m</sup>Tc remains the predominant radioisotope for imaging.<sup>18</sup> <sup>99m</sup>Tc has nearly ideal nuclear properties ( $t_{1/2} = 6$  h, 140 keV, 89% abundance),<sup>9,18,19</sup> and is widely available from <sup>99</sup>Mo/<sup>99m</sup>Tc generators at a low cost.<sup>20</sup> Developed by Lebowitz and Richards in 1974, the <sup>99</sup>Mo/<sup>99m</sup>Tc generator is comprised of an aluminum oxide column loaded with <sup>99</sup>Mo in the form of molybdate (<sup>99</sup>Mo[MoO<sub>4</sub><sup>2-</sup>]).<sup>21</sup> Upon the decay of <sup>99</sup>Mo ( $\beta^-$  decay,  $t_{1/2} = 66$  h) to <sup>99m</sup>Tc, pertechnetate (<sup>99m</sup>Tc[TcO<sub>4</sub><sup>-</sup>]) is formed. The free <sup>99m</sup>Tc[TcO<sub>4</sub><sup>-</sup>] can then be eluted from the generator using saline due to its mono-anionic charge. This is achieved by attaching a vial of saline to the generator paired with an evacuated collection vial on the opposite end of the alumina column (Figure 1.2).

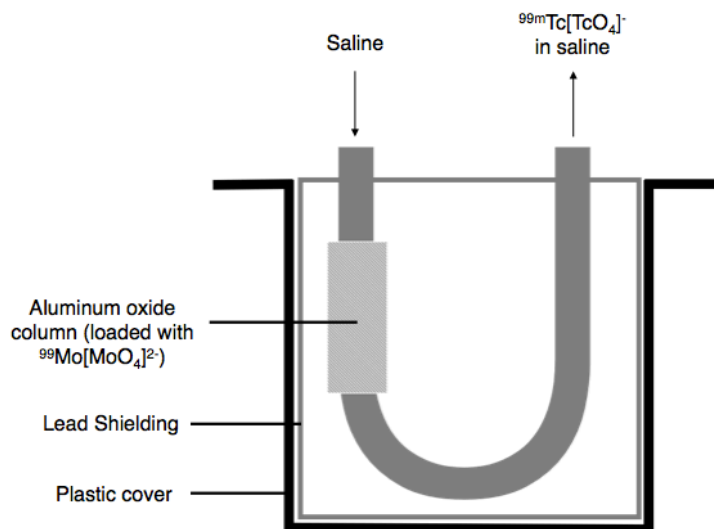


**Figure 1.2** Schematic of a  $^{99}\text{Mo}/^{99\text{m}}\text{Tc}$  generator.<sup>20</sup>

Tc is a group 7 transition metal that forms complexes in a variety of oxidation states ranging from -1 to +7. When  $^{99\text{m}}\text{Tc}$  is eluted from a  $^{99}\text{Mo}/^{99\text{m}}\text{Tc}$  generator,  $[\text{Na}]^{99\text{m}}\text{Tc}[\text{TcO}_4]$  has an oxidation state of +7.<sup>21</sup> To label a molecule with  $^{99\text{m}}\text{Tc}$ , sodium pertechnetate must first be reduced to a lower oxidation state in the presence of a suitable ligand. This is often performed using reducing agents such as tin(II) chloride or sodium borohydride. Most commonly,  $^{99\text{m}}\text{Tc}$  is used in the +1, +3 and +5 oxidation states for radiopharmaceutical applications. The relatively recent development of a method to produce  $^{99\text{m}}\text{Tc}[\text{Tc}(\text{CO})_3(\text{OH}_2)_3]^+$  in water has created the opportunity to develop novel SPECT agents through substitution of the labile water molecules. The associated  $^{99\text{m}}\text{Tc}(\text{I})$  complexes have increased stability compared to earlier  $^{99\text{m}}\text{Tc}(\text{V})$  metal complexes,<sup>22</sup> where the strong field CO ligands with the right chelate form robust  $^{99\text{m}}\text{Tc}(\text{I})$  complexes that can be readily linked to targeting molecules.

To simplify the preparation of  $^{99m}\text{Tc}[\text{Tc}(\text{CO})_3]^+$  complexes, Alberto and coworkers developed a facile single-step instant kit method for the production of  $^{99m}\text{Tc}[\text{Tc}(\text{CO})_3(\text{OH}_2)_3]^+$ . This chemistry employs potassium boranocarbonate ( $\text{K}_2[\text{H}_3\text{BCO}_2]$ ) as a reducing agent and solid source of CO. In the presence of elevated temperatures in water,  $\text{K}_2[\text{H}_3\text{BCO}_2]$  decomposes to produce formate ( $\text{HCOO}^-$ ), carbon monoxide (CO), hydrogen ( $\text{H}_2$ ), and tetrahydroxyborate  $[\text{B}(\text{OH})_4]^-$ . The kits typically contain a buffer such as sodium tetraborate, and sodium tartrate as a complexing agent to stabilize intermediate oxidation states of  $^{99m}\text{Tc}$  formed during the reduction process.

### 1.3.3 Technetium-99m(I) Chelates

$^{99m}\text{Tc}[\text{Tc}(\text{CO})_3(\text{OH}_2)_3]^+$  if administered alone shows widespread distribution with persistent uptake seen in the kidneys ( $13.5 \pm 2.9$  %ID/g), liver ( $10.2 \pm 2.3$  %ID/g), lungs ( $7.9 \pm 6.5$  %ID/g), and blood ( $3.6 \pm 0.8$  %ID/g) at 24 hours post injection.<sup>23</sup> Therefore, as a means of creating targeted  $^{99m}\text{Tc}$  agents derived from the  $^{99m}\text{Tc}[\text{Tc}(\text{CO})_3]^+$  core, several bifunctional bidentate and tridentate  $^{99m}\text{Tc}(\text{I})$  chelates have been developed. Such chelates have been prepared with a mixture of N, O, and S donor atoms that often include heterocycles such as pyridines, imidazoles, triazoles, and quinolines. Owing to their stabilities *in vitro* and *in vivo*, tridentate chelates are preferred when preparing targeted radiopharmaceuticals.<sup>22</sup>

Although many of the early tridentate chelates demonstrated excellent stability, results *in vivo* showed slow clearance from non-target tissues, with

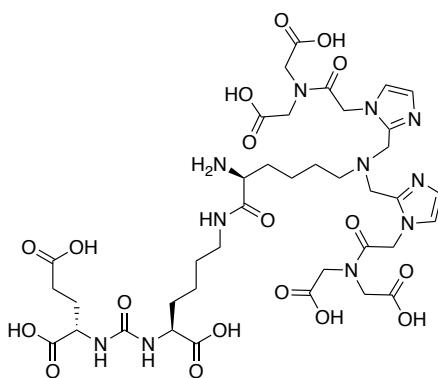


**Figure 1.3** Single amino acid chelate (SAAC)-derived ligand (MIP-1404) that is currently in phase 3 clinical trials for imaging prostate cancer.<sup>14,27–29</sup>

#### 1.3.4 Isostructural Rhenium Complexes

Since technetium does not possess a non-radioactive isotope, it is difficult to characterize new  $^{99m}\text{Tc}$ -complexes using conventional analytical methods, due to the nanomolar quantities of product produced. For this reason, non-radioactive rhenium (Re) complexes are often used as a surrogate to facilitate characterization. Re is a group 7 transition metal that has a similar atomic radius to  $^{99m}\text{Tc}$  due to the lanthanide contraction.<sup>30</sup> As a result, Tc and Re complexes often form nearly identical (isostructural) complexes where the Re-complexes can be made in large quantities, making characterization using standard techniques (X-ray, NMR, etc.) possible. To confirm the identity of the corresponding  $^{99m}\text{Tc}$ -complex, the two metal complexes are co-injected on an HPLC fitted with both a radiation and UV detector, where the corresponding peaks should co-elute and have comparable retention times.

#### 1.3.5 Challenges in preparing targeted $^{99m}\text{Tc}$ radiopharmaceuticals

When developing targeted  $^{99m}\text{Tc}$  radiopharmaceuticals, there are several factors that need to be considered, such as the clinical need, expression of the target in relation to the disease or injury, and normal tissue distribution. In addition, one must also consider the nature of the chelate, and the targeting vector of choice. There are many different types of targeting vectors that have been used to create radiopharmaceuticals including monoclonal antibodies (mAbs), peptides, and small molecules.<sup>8,10,31–34</sup> Of these, mAbs have unmatched

affinity and specificity for disease specific cellular targets.<sup>35</sup> Although  $^{99m}\text{Tc}$  is a very desirable isotope for imaging, previous attempts to prepare and use  $^{99m}\text{Tc}$ -labeled antibodies have proven to be troublesome. This is due in large part to the long circulation time associated with mAbs, and subsequent slow tumour uptake, which can take upwards of 7-14 days, surpassing the 6 hour half-life of  $^{99m}\text{Tc}$ .<sup>36</sup> Given the increasing availability of humanized antibodies, their specificity, and high affinity for important molecular targets, a means of generating  $^{99m}\text{Tc}$ -antibodies would be highly desirable. However, to overcome the shortfalls of directly labeled  $^{99m}\text{Tc}$ -antibodies, a new radiopharmaceutical development and radiolabeling approach is needed.

## 1.4 Bioorthogonal Chemistry and Pretargeted Imaging

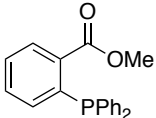
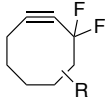
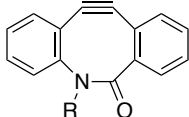
Bioorthogonal chemistry is defined as a chemical reaction that occurs in a living system without disrupting any endogenous biochemical process or partaking in competing side reactions.<sup>37,38</sup> Furthermore, a bioorthogonal reaction must proceed in aqueous media, at physiological temperature and pH.<sup>38</sup> Shortly after coining the term in 2003, Bertozzi and coworkers reported the first bioorthogonal reaction *in vivo* between an azide and functionalized phosphine.<sup>38</sup> Since this discovery, many bioorthogonal pairs have been developed, with the aim of increasing reaction kinetics (Table 1.2). Preliminary attempts focused on strain promoted azide-alkyne reactions. Such reactions increased reaction rates

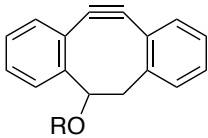
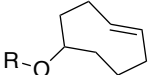
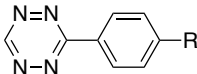
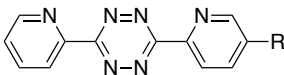


and could be performed without the need for a cytotoxic copper catalyst. Furthermore, adding electron-withdrawing fluorine atoms, as well as additional ring strain in the form of cyclooctyne groups further improved reaction kinetics.<sup>39,40</sup> Ultimately, Bertozzi and coworkers reported the development of a biarylzaaoctynone (BARAC), which had an order of magnitude higher second order reaction kinetics than previously developed agents ( $k_2 = 0.96 \text{ M}^{-1} \text{ s}^{-1}$ ).<sup>41</sup>

In 2008, Fox and coworkers as well as Hilderbrand and coworkers, reported two different bioorthogonal reactions based on the inverse electron demand Diels-Alder reaction (IEDDA).<sup>42,43</sup> These reaction pairs presented rapid second order kinetics, exceeding alkyne-azide reactions by three orders of magnitude.<sup>42</sup> More specifically, the tetrazine and transcyclooctene (TCO) pair reported by Fox and coworkers had the highest reaction kinetics ( $k_2 = 2000 \text{ M}^{-1} \text{ s}^{-1}$ ), and showed promise as a new way to target molecules *in vivo* (Table 1.2).<sup>42</sup>

**Table 1.2** Bioorthogonal pairs and their second order reaction rates.

Bioorthogonal components		Second order rate constant ( $\text{M}^{-1} \text{s}^{-1}$ )
	$\text{N}_3\text{-R}$	$0.002^{38}$
	$\text{N}_3\text{-R}$	$0.76^{44}$
	$\text{N}_3\text{-R}$	$0.96^{41}$

	$N_3-R$	0.057 <sup>45</sup>
		6000 <sup>46</sup>
		3000-32000 <sup>47-50</sup>

The first application of IEDDA bioorthogonal chemistry *in vivo* was demonstrated by Rossin and coworkers, for the purpose of pretargeted nuclear imaging.<sup>49</sup> This pretargeted imaging approach was based on a two-component system. First, a CC49-antibody with high affinity for the tumour-associated glycoprotein 72 (TAG72) receptor was functionalized with TCO, and administered to mice bearing LS174T xenografts. After allowing time for the TCO-targeting vector to accumulate at the site of interest and clear from non-target tissues, a <sup>111</sup>In radiolabeled tetrazine was injected.<sup>19</sup> The tetrazine coupled rapidly and irreversibly with the TCO-antibody at the tumour site, generating a high contrast image with high target to non-target ratios (Figure 1.4).

Since the work by Rossin and coworkers was published, several radiolabeled tetrazines have been reported for SPECT and PET imaging.<sup>47,51-58</sup> The pretargeting approach offers a way to overcome the disparity between using short-lived isotopes for imaging with long circulating targeting vectors

(antibodies). Despite the diversity of reported radiolabeled tetrazines, there has been a notable absence of  $^{99m}\text{Tc}$ -labelled tetrazines, even with the use of  $^{99m}\text{Tc}$  being so widespread.

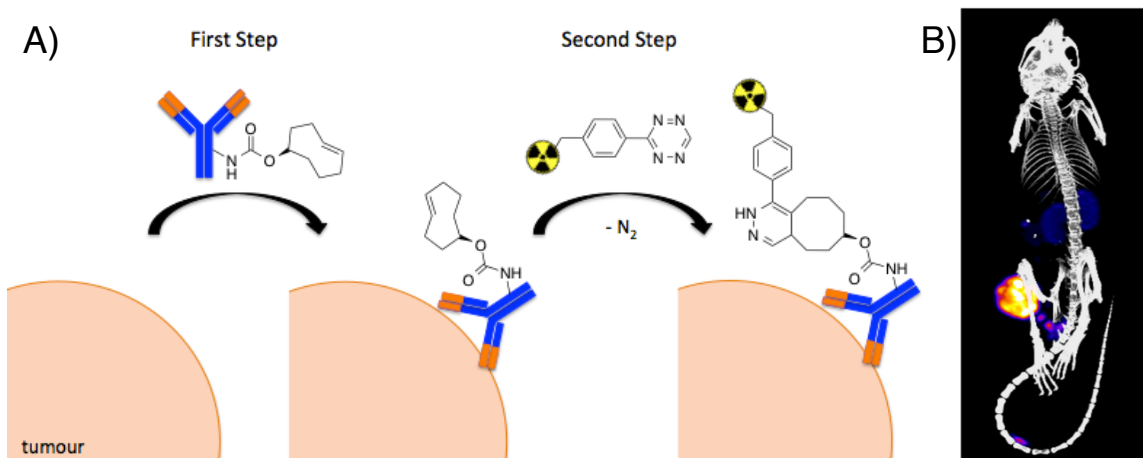


**Figure 1.4** A) Pretargeting approach using a TCO-antibody and a radiolabeled tetrazine at the tumour site.<sup>59</sup> B) SPECT/CT image (postmortem, maximum intensity projection) of CC49-TCO pretargeted mouse bearing LS174T xenografts, 3 h after injection of a  $^{111}\text{In}$ -tetrazine.<sup>49</sup>

## 1.5 Thesis Overview

The goal of this thesis was to develop the means to use bioorthogonal chemistry to create targeted  $^{99m}\text{Tc}$ -radiopharmaceuticals. It was hypothesized that the IEDDA reaction between tetrazines and transcyclooctene could overcome the

shortcomings of directly labeled imaging probes through the use of pretargeted imaging. This approach involved synthesizing and characterizing a family of tetrazine-derived chelates and developing ways to label them with  $^{99m}\text{Tc(I)}$ . The reactivity of the  $^{99m}\text{Tc}$ -tetrazines were evaluated *in vitro* and *in vivo*, and pretargeting explored using TCO-functionalized small molecules and antibodies (Chapter 2). Next, the clearance mechanism of the lead  $^{99m}\text{Tc}$ -tetrazine was investigated through the study of hepatobiliary transport proteins using specific inhibitors (Chapter 3). The effect of the  $^{99m}\text{Tc}$  chelate on compound distribution was also evaluated, where a second generation of  $^{99m}\text{Tc}$ -complexes were synthesized, characterized, and evaluated *in vivo* (Chapter 4).

In addition, other applications of the bioorthogonal chemical reaction between tetrazines, including the  $^{99m}\text{Tc(I)}$  chelate developed in chapter 2, and TCO were investigated. Using this chemistry, a platform was developed for the facile synthesis of several multimodal imaging probes using a TCO-functionalized nanoscale ultrasound contrast agent. These nanoscale gas vesicles were functionalized with both SPECT and photoacoustic (PA) imaging agents on their surface. The feasibility of both agents to perform as dual-imaging probes were evaluated *in vitro* and *in vivo* (Chapter 5).

## 1.6 References

- (1) Weissleder, R. *Radiology* **1999**, 212 (3), 609–614.
- (2) Weissleder, R. *Science*. **2006**, 312, 1168.
- (3) Massoud, F.; Gambhir, S. *Genes Dev.* **2003**, 17 (5), 545–580.
- (4) Silberman, S.; Philip, B.; Butzbach, A. *J. Clin. Stud.* **2008**, 4 (3), 22–2.
- (5) Bartholomä, M.; Valliant, J.; Maresca, K. P.; Babich, J.; Zubieta, J. *Chem. Commun.* **2009**, 5, 493–512.
- (6) Rudin, M.; Weissleder, R. *Nat. Rev. Drug Discov.* **2003**, 2 (2), 123–131.
- (7) Lupetti, A.; Welling, M. M.; Pauwels, E. K. J.; Nibbering, P. H. *Lancet Infect. Dis.* **2003**, 3 (4), 223–229.
- (8) Lewis, J. S.; Lewis, M. R.; Srinivasan, A.; Schmidt, M. A.; Wang, J.; Anderson, C. J. *J. Med. Chem.* **1999**, 42 (8), 1341–1347.
- (9) Maresca, K. P.; Marquis, J. C.; Hillier, S. M.; Lu, G.; Femia, F. J.; Zimmerman, C. N.; Eckelman, W. C.; Joyal, J. L.; Babich, J. W. *Bioconjugate Chem.* **2010**, 21, 1032–1042.
- (10) Olafsen, T.; Wu, A. M. *Semin. Nucl. Med.* **2010**, 40 (3), 167–181.
- (11) Carrasquillo, J. A.; Pandit-Taskar, N.; O'Donoghue, J. A.; Humm, J. L.; Zanzonico, P.; Smith-Jones, P. M.; Divgi, C. R.; Pryma, D. A.; Ruan, S.; Kemeny, N. E.; Fong, Y.; Wong, D.; Jaggi, J. S.; Scheinberg, D. A.; Gonen, M.; Panageas, K. S.; Ritter, G.; Jungbluth, A. A.; Old, L. J.; Larson, S. M. *J. Nucl. Med.* **2011**, 52 (8), 1173–1180.
- (12) Zeglis, B. M.; Mohindra, P.; Weissmann, G. I.; Divilov, V.; Hilderbrand, S. A.; Weissleder, R.; Lewis, J. S. *Bioconjugate Chem.* **2011**, 22 (10), 2048–2059.
- (13) Wu, A. M. *Methods* **2014**, 65 (1), 139–147.
- (14) Barrett, J. A.; Coleman, R. E.; Goldsmith, S. J.; Vallabhajosula, S.; Petry, N. A.; Cho, S.; Armor, T.; Stubbs, J. B.; Maresca, K. P.; Stabin, M. G.; Joyal, J. L.; Eckelman, W. C.; Babich, J. W. *J. Nucl. Med.* **2013**, 54 (3), 380–387.

- (15) Jurisson, S. S.; Lydon, J. D. *Chem. Rev.* **1999**, *99* (9), 2205–2218.
- (16) Hillier, S. M.; Maresca, K. P.; Lu, G. L.; Merkin, R. D.; Marquis, J. C.; Zimmerman, C. N.; Eckelman, W. C.; Joyal, J. L.; Babich, J. W. *J. Nucl. Med.* **2013**, *54* (8), 1369–1376.
- (17) Lu, G.; Maresca, K. P.; Hillier, S. M.; Zimmerman, C. N.; Eckelman, W. C.; Joyal, J. L.; Babich, J. W. *Bioorg. Med. Chem. Lett.* **2013**, *23*, 1557–1563.
- (18) Kluba, C. A.; Mindt, T. L. *Molecules* **2013**, *18*, 3206–3226.
- (19) Coogan, M. P.; Doyle, R. P.; Valliant, J. F.; Babich, J. W.; Zubieta, J. J. *Label. Compd. Radiopharm.* **2014**, *57*, 255–261.
- (20) Rathmann, S. M.; Ahmad, Z.; Slikboer, S.; Bilton, H. A.; Snider, D. P.; Valliant, J. F. In *Radiopharmaceutical Chemistry*; Lewis, J. S., Windhorst, A. D., Zeglis, B. M., Eds.; SpringerLink, 2019; pp 311–333.
- (21) Lebowitz, E.; Richards, P. *Semin. Nucl. Med.* **1974**, *4* (3), 257–268.
- (22) Alberto, R.; Pak, J. K.; van Staveren, D.; Mundwiler, S.; Benny, P. *Biopolymers* **2004**, *76* (4), 324–333.
- (23) Egli, A.; Alberto, R.; Tannahill, L.; Schibli, R.; Abram, U.; Schaffland, A.; Waibel, R.; Tourwé, D.; Jeannin, L.; Iterbeke, K.; Schubiger, P. A. *J. Nucl. Med.* **1999**, *40* (11), 1913–1917.
- (24) Banerjee, S. R.; Pullambhatla, M.; Foss, C. A.; Falk, A.; Byun, Y.; Nimmagadda, S.; Mease, R. C.; Pomper, M. G. *J. Med. Chem.* **2013**, No. 3, 6108–6121.
- (25) Jiang, H.; Kasten, B. B.; Liu, H.; Qi, S.; Liu, Y.; Tian, M.; Barnes, C. L.; Zhang, H.; Cheng, Z.; Benny, P. D. *Bioconjugate Chem.* **2012**, *23* (11), 2300–2312.
- (26) Schibli, R.; La Bella, R.; Alberto, R.; Garcia-Garayoa, E.; Ortner, K.; Abram, U.; Schubiger, P. A. *Bioconjugate Chem.* **2000**, *11* (3), 345–351.
- (27) Schmidkonz, C.; Hollweg, C.; Beck, M.; Reinfelder, J.; Goetz, T. I.; Sanders, J. C.; Schmidt, D.; Prante, O.; Bäuerle, T.; Cavallaro, A.; Uder, M.; Wullich, B.; Goebell, P.; Kuwert, T.; Ritt, P. *Prostate* **2018**, *78* (1), 54–63.

- (28) Ellis, W. J.; Donnelly, B. J.; Gorin, M. A.; Pouliot, F.; Nguyen, H. G.; Carroll, P. R.; Scherr, D.; Probst, S.; Saperstein, L.; Fleshner, N.; Maroni, P.; Shah, K.; Stambler, N.; DiPippo, V. A.; Strack, T.; Mahmood, S.; Jensen, J.; Wong, V.; Allaf, M. *J. Urol.* **2019**, *201* (4), 2019.
- (29) Mulvagh, S. L.; Rakowski, H.; Vannan, M. A.; Abdelmoneim, S. S.; Becher, H.; Bierig, S. M.; Burns, P. N.; Castello, R.; Coon, P. D.; Hagen, M. E.; Jollis, J. G.; Kimball, T. R.; Kitzman, D. W.; Kronzon, I.; Labovitz, A. J.; Lang, R. M.; Mathew, J.; Moir, W. S.; Nagueh, S. F.; Pearlman, A. S.; Perez, J. E.; Porter, T. R.; Rosenbloom, J.; Strachan, G. M.; Thanigaraj, S.; Wei, K.; Woo, A.; Yu, E. H. C.; Zoghbi, W. A. *J. Am. Soc. Echocardiogr.* **2008**, *21* (11), 1179–1201.
- (30) Cotton, S. A.; Hart, F. A. *The Heavy Transition Elements*; Macmillan Chemistry Text, 1975.
- (31) Christiansen, J. P.; Lindner, J. R. *Proc. IEEE* **2005**, *93* (4), 809–818.
- (32) Fischer, C. R.; Groehn, V.; Reber, J.; Schibli, R.; Ametamey, S. M.; Müller, C. *Mol. Imaging Biol.* **2013**, *15* (6), 649–654.
- (33) Stephenson, K. A.; Banerjee, S. R.; Sogbein, O. O.; Levadala, M. K.; McFarlane, N.; Boreham, D. R.; Maresca, K. P.; Babich, J. W.; Zubietta, J.; Valliant, J. F. *Bioconjugate Chem.* **2005**, *16* (5), 1189–1195.
- (34) Banerjee, S. R.; Pullambhatla, M.; Byun, Y.; Nimmagadda, S.; Foss, C. A.; Green, G.; Fox, J. J.; Lupold, S. E.; Mease, R. C.; Pomper, M. G. *Angew. Chemie Int. Ed.* **2011**, *50*, 9167–9170.
- (35) Kaur, S.; Venktaraman, G.; Jain, M.; Senapati, S.; Garg, P. K.; Batra, S. K. *Cancer Lett.* **2012**, *315* (2), 97–111.
- (36) Price, E. W.; Orvig, C. *Chem. Soc. Rev.* **2014**, *43*, 260–290.
- (37) Bertozzi, C. R. *Acc. Chem. Res.* **2011**, *44* (9), 651–653.
- (38) Prescher, J. A.; Dube, D. H.; Bertozzi, C. R. *Nature* **2004**, *430* (19), 873–878.
- (39) Ning, X.; Guo, J.; Wolfert, M. A.; Boons, G. J. *Angew. Chemie Int. Ed.* **2008**, *47* (12), 2253–2255.

- (40) Baskin, J. M.; Prescher, J. A.; Laughlin, S. T.; Agard, N. J.; Chang, P. V.; Miller, I. A.; Lo, A.; Codelli, J. A.; Bertozzi, C. R. *Proc. Natl. Acad. Sci. U. S. A.* **2007**, *104* (43), 16793–16797.
- (41) Jewett, J. C.; Sletten, E. M.; Bertozzi, C. R. *J. Am. Chem. Soc.* **2010**, *132* (11), 3688–3690.
- (42) Blackman, M. L.; Royzen, M.; Fox, J. M. *J. Am. Chem. Soc.* **2008**, *130* (41), 13518–13519.
- (43) Devaraj, N. K.; Weissleder, R.; Hilderbrand, S. A. *Bioconjugate Chem.* **2008**, *19* (12), 2297–2299.
- (44) Chang, P. V.; Prescher, J. A.; Sletten, E. M.; Baskin, J. M.; Miller, I. A.; Agard, N. J.; Lo, A.; Bertozzi, C. R. *Proc. Natl. Acad. Sci.* **2010**, *107* (5), 1821–1826.
- (45) Van den Bosch, S. M.; Rossin, R.; Renart Verkerk, P.; Ten Hoeve, W.; Janssen, H. M.; Lub, J.; Robillard, M. S. *Nucl. Med. Biol.* **2013**, *40*, 415–423.
- (46) Devaraj, N. K.; Thurber, G. M.; Keliher, E. J.; Marinelli, B.; Weissleder, R. *Proc. Natl. Acad. Sci. USA* **2012**, *109* (13), 4762–4767.
- (47) Rossin, R.; Verkerk, P. R.; van den Bosch, S. M.; Vulders, R. C. M.; Verel, I.; Lub, J.; Robillard, M. S. *Angew. Chemie Int. Ed.* **2010**, *49*, 3375–3378.
- (48) Rossin, R.; van den Bosch, S. M.; Ten Hoeve, W.; Carvelli, M.; Versteegen, R. M.; Lub, J.; Robillard, M. S. *Bioconjugate Chem.* **2013**, *24*, 1210–1217.
- (49) Rossin, R.; Läppchen, T.; van den Bosch, S. M.; Laforest, R.; Robillard, M. S. *J. Nucl. Med.* **2013**, *54* (11), 1989–1995.
- (50) Rossin, R.; Duijnhoven, S. M. J. van; Läppchen, T.; Bosch, S. M. van den; Robillard, M. S. *Mol. Pharm.* **2014**, *11* (9), 3090–3096.
- (51) Yazdani, A.; Bilton, H.; Vito, A.; Genady, A. R.; Rathmann, S. M.; Ahmad, Z.; Janzen, N.; Czorny, S.; Zeglis, B. M.; Francesconi, L. C.; Valliant, J. F. *J. Med. Chem.* **2016**, *59* (20), 9381–9389.
- (52) Bilton, H.; Ahmad, Z.; Valliant, J. *J. Label. Compd. Radiopharm.* **2015**, *58*, S61.



- (53) Zeglis, B. M.; Brand, C.; Abdel-Atti, D.; Carnazza, K. E.; Cook, B. E.; Carlin, S.; Reiner, T.; Lewis, J. S. *Mol. Pharm.* **2015**, *12* (10), 3575–3587.
- (54) Albu, S. A.; Al-karmi, S. A.; Patel, R. M.; Capretta, A.; Valliant, J. F. *Bioconjugate Chem.* **2016**, *27* (1), 207–216.
- (55) Li, Z.; Cai, H.; Hassink, M.; Blackman, M. L.; Brown, R. C. D.; Conti, P. S.; Fox, J. M. *Chem. Commun.* **2010**, *46*, 8043–8045.
- (56) Herth, M. M.; Andersen, V. L.; Lehel, S.; Madsen, J.; Knudsen, G. M.; Kristensen, J. L. *Chem. Commun.* **2013**, *49* (36), 3805–3807.
- (57) Van Duijnhoven, S. M. J.; Rossin, R.; van den Bosch, S. M.; Wheatcroft, M. P.; Hudson, P. J.; Robillard, M. S. *J. Nucl. Med.* **2015**, *56* (9), 1422–1428.
- (58) García, M. F.; Zhang, X.; Shah, M.; Newton-Northup, J.; Cabral, P.; Cerecetto, H.; Quinn, T. *Bioorg. Med. Chem.* **2016**, *24* (6), 1209–1215.
- (59) Rossin, R.; Renart Verkerk, P.; van den Bosch, S. M.; Vulders, R. C. M.; Verel, I.; Lub, J.; Robillard, M. S. *Angew. Chemie Int. Ed.* **2010**, *49* (19), 3375–3378.

## **Chapter 2: Preparation and evaluation of $^{99m}\text{Tc}$ -labeled tridentate chelates for pretargeting using bioorthogonal chemistry**

Section 2.1 of the following chapter was published in the Journal of Visualized Experiments, under the citation:

H.A. Bilton\*, Z. Ahmad\*, N. Janzen, S. Czorny, J.F. Valliant. J. Vis. Exp. **2017**, *120*, e55188. DOI: 10.3791/55188.

With respect to this publication, I was responsible for the synthesis, characterization, and labeling optimization of compounds **6**, **10** and **14**. Zainab Ahmad was responsible for the synthesis, characterization and labeling optimization of compounds **16** and **18**. Zainab and I were responsible for the preparation and execution of biodistribution studies, where Nancy Janzen and Shannon Czorny were also responsible for the animal preparation and necropsy work. Prof. John Valliant was the PI.

### **2.1 Introduction**

$^{99m}\text{Tc}$  remains the dominant radioisotope used in diagnostic nuclear medicine, with over 25 million imaging procedures conducted per year worldwide.<sup>1–4</sup> The majority of  $^{99m}\text{Tc}$  agents used clinically are perfusion type radiopharmaceuticals. There are a limited number of actively targeted compounds

in which  $^{99m}\text{Tc}$  is directed to bind a specific biomarker through ligation to a targeting agent. The creation of targeted  $^{99m}\text{Tc}$  radiopharmaceuticals is often hindered by the steric and electronic influence of  $^{99m}\text{Tc}$ -ligand complexes, which can prevent targeting molecules from binding the biomarker of interest. Furthermore, the isotope's half-life is not long enough for use with higher molecular weight biomolecules such as antibodies. Antibodies typically require circulation times of several days before images are acquired in order for the biomolecule to clear from non-target tissues. Pretargeting offers an alternative approach that has the potential to circumvent these challenges.

As noted in Chapter 1, pretargeting combined with bioorthogonal chemistry has been shown to be an effective way to develop new molecular imaging probes for both fluorescence and radio-imaging.<sup>5–9</sup> The inverse electron demand Diels-Alder (IEDDA) reaction between 1,2,4,5-tetrazines and trans-cyclooctene (TCO) derivatives, as shown in Figure 2.1, has been particularly effective.<sup>7</sup> The IEDDA reaction with these components can exhibit fast kinetics in PBS ( $k_2 \approx 6,000 \text{ M}^{-1}\text{s}^{-1}$ ) and high selectivity, making it almost ideal for *in vivo* pretargeting applications.<sup>10,11</sup>

The most common approach used involves administering a TCO-derived targeting vector and, following a sufficient delay period, a radiolabeled tetrazine. Several radiolabeled tetrazines based on carbon-11 ( $^{11}\text{C}$ ), fluorine-18 ( $^{18}\text{F}$ ), copper-64 ( $^{64}\text{Cu}$ ), zirconium-89 ( $^{89}\text{Zr}$ ), and indium-111 ( $^{111}\text{In}$ ) have been reported.<sup>12–16</sup> In contrast, there are only two reports of  $^{99m}\text{Tc}$ -labeled tetrazines,

which were prepared using hydrazinonicotinic acid (HYNIC)-based ligands requiring the use of co-ligands to prevent protein binding and degradation *in vivo*.<sup>17,18</sup> As an alternative, we report here the synthesis of  $^{99m}\text{Tc(I)}$  labeled tetrazines using a family of ligands which form stable tridentate complexes with the  $^{99m}\text{Tc}[\text{Tc}(\text{CO})_3]^+$  core.

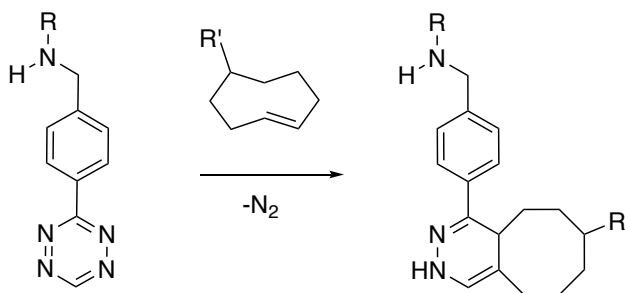


**Figure 2.1** The bioorthogonal IEDDA reaction between tetrazine and TCO.

The family of ligands prepared contain tridentate chelates that vary in polarity and the nature of the linker group between the metal binding region and the tetrazine (Figure 2.2). The goal was to identify a  $^{99m}\text{Tc}$ -tetrazine construct that could effectively localize and react with TCO-labeled sites *in vivo* and rapidly clear when not bound, in order to yield high target to non-target ratios. To test the ligands, a TCO derivative of a bisphosphonate, alendronate (TCO-ALN) was used.<sup>19</sup> We have shown previously that TCO-ALN localizes to areas of active bone metabolism and can react with radiolabeled tetrazines *in vivo*.<sup>20</sup> It is a convenient reagent to test new tetrazines, as it can be prepared in a single step

Ph.D. Thesis – H. Bilton; McMaster University – Chemistry and Chemical Biology

and experiments can be performed in normal mice where localization occurs primarily in the joints (knees and shoulders).

## 2.2 Protocol

Note that the following format is from the paper: H.A. Bilton, Z. Ahmad, N. Janzen, S. Czorny, J.F. Valliant. J. Vis. Exp. 2017, 120, e55188. DOI: 10.3791/55188.

### 2.2.1 Radiolabeling of tetrazine-tridentate ligands with $^{99m}\text{Tc}$

#### 2.2.1.1 *Synthesis of $^{99m}\text{Tc}[\text{Tc}(\text{CO})_3(\text{OH}_2)_3]^+$* <sup>21,22</sup>

1. In a microwave vial, combine 8 mg  $\text{K}_2[\text{BH}_3\text{CO}_2]$ , 15 mg  $\text{Na}_2\text{CO}_3$ , 20 mg  $\text{Na}_2\text{B}_4\text{O}_7 \cdot 10\text{H}_2\text{O}$ , and 25 mg  $\text{KOCO}[\text{CH}(\text{OH})_2\text{COONa} \cdot 4\text{H}_2\text{O}]$ . Purge the vial for 10 min with argon gas.
2. Add 4 mL of  $^{99m}\text{Tc}[\text{TcO}_4^-]$  (~1,100 MBq, ~30 mCi) in 0.9% saline to the vial.
3. Heat the reaction in a microwave for 3.5 min at 110 °C after 10 sec of stirring to ensure thorough mixing of reagents.
4. Adjust the pH of the solution to 3.5-4 using ~400  $\mu\text{L}$  of 1 M HCl. Verify using pH paper.

#### 2.2.1.2 *Radiolabeling of tetrazine ligands 4, 8, 12, 15, and 16*

1. Dissolve 2 mg of each ligand (compounds **4**, **8**, **12**, **15**, **16**) in 250  $\mu\text{L}$  MeOH.<sup>23</sup>
2. Add 250  $\mu\text{L}$  of  $^{99m}\text{Tc}[\text{Tc}(\text{CO})_3(\text{OH}_2)_3]^+$  (~74 MBq, ~2 mCi) to each solution.

3. Heat the reaction mixture using a microwave for 20 min at 60 °C. NOTE:  
This step was identical for all 5 tetrazines.
4. For compounds **4**, **8**, **12**, and **16**, evaporate the solvent and re-dissolve the resulting products in 1 mL of 1:1 v/v DCM: TFA.
5. Heat the dissolved reaction products (**4**, **8**, **12**, and **16**) at 60 °C in a microwave for 6 min (**4**, **8**, **12**, **16**) or 10 min (**15**).
6. After cooling to room temperature, evaporate the solvent using an evaporator (36 °C, 8 mbar, 3 min, 6,000 rpm) and dissolve the dried compound in 1:1 ACN:H<sub>2</sub>O or 1:1 MeOH:H<sub>2</sub>O, prior to HPLC purification.
7. Purify the <sup>99m</sup>Tc-labeled compounds (**6**, **10**, **14**, **16**, and **18**), including separating the labeled product from unlabeled tetrazine ligand, using HPLC (C18 reversed-phase). Typically, use an elution gradient of 30:70 ACN: H<sub>2</sub>O (both with 0.1% TFA) to 40:60 ACN:H<sub>2</sub>O over 20 min (18 min) and a C18 analytical 4.6 x 100 mm column. Use both UV (254 nm) and gamma detection.
8. Take a small sample of each labeled product and compare its HPLC retention time to that of a co-injected, non-radioactive, rhenium (Re)-labeled standard (0.125 mg in 20% MeOH/H<sub>2</sub>O). The Re-labeled standard is identified in the UV HPLC trace, and will elute at the same time as the <sup>99m</sup>Tc-labeled compound in the γ-HPLC trace. This co-injection shows peaks at comparable retention times, confirming the identity of the <sup>99m</sup>Tc-labeled compound.

9. Evaporate the solvent from HPLC fractions using an evaporator (36 °C, 8 mbar, 3 min, 6,000 rpm).
10. Formulate the purified compound at a concentration of 7.4 kBq/μL in PBS, containing 0.5% BSA and 0.01% polysorbate-80.
11. To ensure the labeled compounds are stable, perform an *in vitro* stability study. Incubate the formulated compound at 37 °C for 1, 4 and 6 h, injecting a small amount (3.7 MBq) of the mixture on the HPLC at each time point to assess stability.

## **2.2.2 Radiolabeling of tetrazine-tridentate ligands with <sup>99m</sup>Tc**

### **2.2.2.1 Preparation of animals**

1. Using 7-9 week old, female BALB/c mice (n=3), administer TCO-ALN formulated in saline (20 mg/kg) (5 μg/μL), via tail-vein injection.
2. Place mouse in physical restraint device, and identify the veins located on the lateral surfaces of the tail and wipe with an alcohol swab. At approximately 2 cm from the end of the tail, insert a 30-gauge needle at a shallow angle, parallel to the vein. Slowly depress the plunger to inject, remove needle and apply clean gauze sponge at injection site with slight pressure until bleeding stops.
3. At 1 h post injection of TCO-ALN, administer ~0.74 MBq (20 μCi) of <sup>99m</sup>Tc-tetrazine formulated in 100 μL of 0.5% BSA, 0.01% Tween-80 in PBS, via tail-vein injection.

#### **2.2.2.2 Biodistribution studies**

1. At the desired time point ( $t = 6$  h), anaesthetize the mice using 3% isoflurane and 2% oxygen gas mixture. Demonstrate a toe pinch withdrawal on the anesthetized mouse to ensure they are under surgical plane of anesthesia.
2. Collect blood (1 mL) via cardiac puncture using a syringe pre-treated with heparin. Place mouse on its back with nose in the nose cone for continued anesthesia and locate the xiphoid process on the animal. Insert a 25 G needle, slightly to the left of the animal's midline under the xiphoid process, at a  $20^\circ$  angle. Fully insert the needle, and slowly pull back on the plunger to see blood in the needle hub if the heart was punctured. Slightly readjust the needle while holding the plunger if necessary, to puncture the heart. Slowly draw blood into the syringe.
3. Euthanize the animal by cervical dislocation, while under anesthesia.
4. Place each animal in a plastic bag and use a dose calibrator ( $^{99m}\text{Tc}$  setting) to measure the whole body activity level.
5. Collect the following tissues and fluids in pre-weighed counting tubes: blood, bone (knee and shoulder), gall bladder, kidneys, liver, stomach (with contents), small intestines (with contents), large intestines and caecum (with contents), thyroid and trachea, urinary bladder with urine, and tail.
6. Rinse appropriate tissues (excluding blood, gall bladder, and urinary bladder) in PBS to remove blood and blot dry before placing the tissues in



appropriate counting tubes.

7. Place animal carcass in a plastic bag and measure residual whole body activity using a dose calibrator.
8. Weigh each tube containing a tissue sample. Subtract initial weight of the tube to obtain mass of the tissue.
9. Use a dose calibrator ( $^{99m}\text{Tc}$  setting) to measure the amount of activity in a test sample (100  $\mu\text{L}$ ) at the time of injection for each mouse. NOTE: This test sample is equal to the injection volume, thus giving the activity count at the time of injection.
10. At the time of tissue measurement, aliquot 5  $\mu\text{L}$  of the test sample used previously. Use a multi-detector gamma counter ( $^{99m}\text{Tc}$  setting) and count to obtain the count per minute (CPM) for the 5  $\mu\text{L}$  test sample.
11. Use the two values obtained in 2.2.9 and 2.2.10 to calculate the activity and CPM relationship using equation 1 to obtain a conversion factor (CPM  $\mu\text{Ci}^{-1}$ ).

$$\frac{\text{Standard CPM} \times \left( \frac{\text{dose cal volume}}{\text{gamma counter volume}} \right)}{\mu\text{Ci in Standard at time of injection}} \quad (1)$$

12. Use the gamma counter to measure the amount of radioactivity in each tissue or fluid sample.
13. Use equation 1 to calculate the amount of activity in each tissue or fluid at the time of measurement relative to the total injected dose. This value is then normalized by organ weight and reported as percent injected dose per

gram (i.e., %ID/g) of tissue.

14. Follow steps 2.1.2 to 2.2.13 to conduct a negative control experiment using the  $^{99m}\text{Tc}$ -labeled tetrazine ligands in the absence of TCO-ALN. Sacrifice mice ( $n = 3$ ) at 0.5, 1, 4 and 6 h post injection and obtain tissue or fluid as described above.

## 2.3 Results and discussion

The ligands were synthesized using different linkers and chelators via a simple reductive amination strategy (Figure 2.2), followed by coupling of the product to a commercially available tetrazine.<sup>24,25</sup> Radiolabeling was performed using the same method for all compounds and was highly reproducible. The process was optimized by varying the pH, amount of ligand, reaction time and temperature whereupon the  $^{99m}\text{Tc}$ -radiolabeled compounds **6**, **10**, **14**, **16** and **18** were obtained in moderate to high radiochemical yield: 45% (**6**), 42% (**10**), 31% (**14**), 83% (**16**), and 54% (**18**). Following HPLC purification from unreacted ligand and evaporation using a Biotage V-10 evaporator, the compounds were formulated in PBS containing 0.5% BSA and 0.01% polysorbate 80 prior to injection. The specific activity of the purified  $^{99m}\text{Tc}$ -labeled tetrazine was  $\sim 1.48$  MBq/ $\mu\text{g}$ . Studies were conducted to assess the stability of the  $^{99m}\text{Tc}$ -labeled tetrazine ligands prior to *in vivo* studies. The stability was monitored by HPLC at 1, 4 and 6 h with no visible degradation over 6 h ( $R_t = 14$  min), as seen in Figure 2.3 for compound **10** as an example.

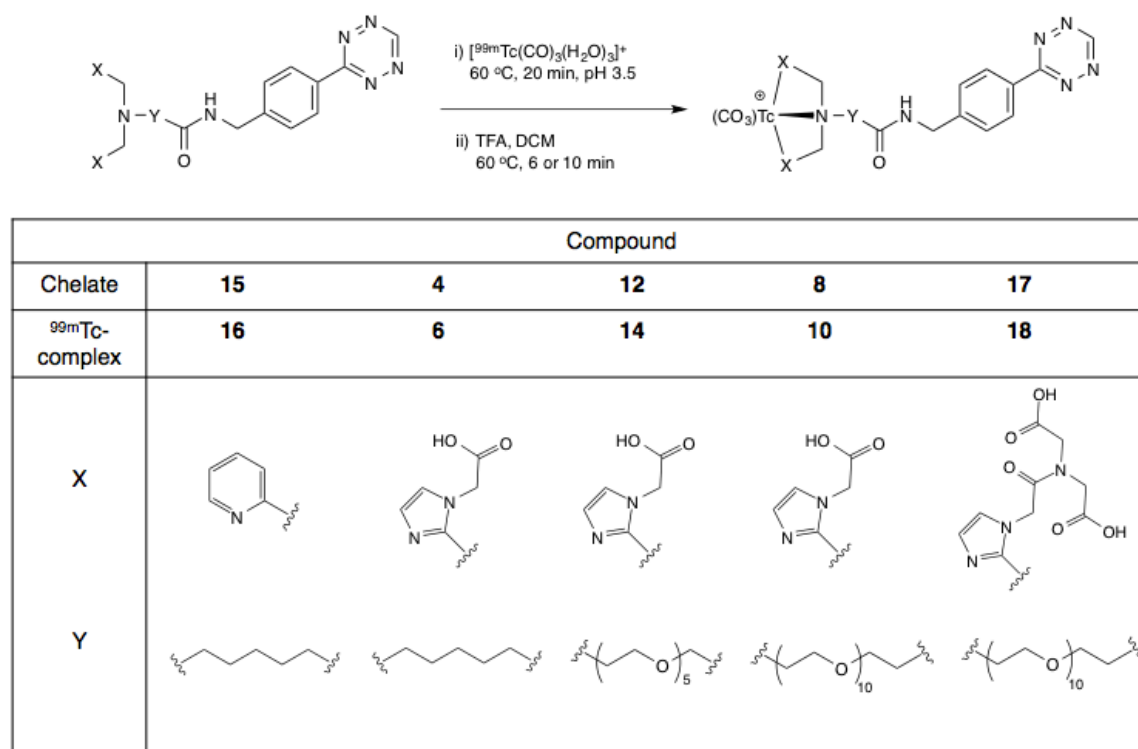


**Figure 2.2** <sup>99m</sup>Tc-complexes **6**, **10**, **14**, **16**, and **18** were produced using different linkers (Y) and donor groups (X) as shown (bottom). All compounds were radiolabeled with <sup>99m</sup>Tc[Tc(CO)<sub>3</sub>(OH<sub>2</sub>)<sub>3</sub>]<sup>+</sup> using the same reaction conditions (top), with the exception of **16**, which did not require step (ii).

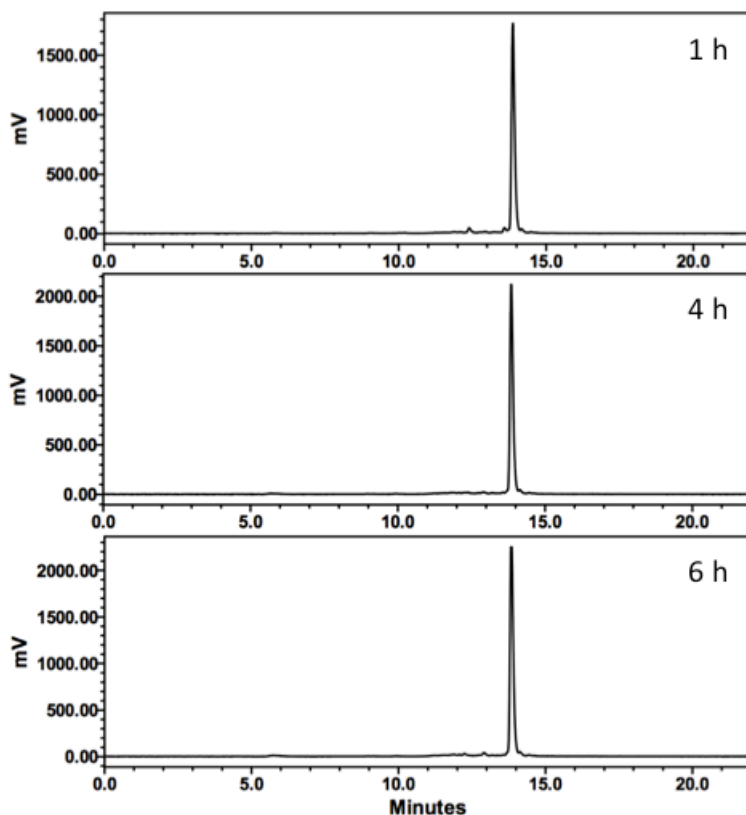


**Figure 2.3** Stability test results using compound **10**.  $\gamma$ -HPLC traces of **10** incubated in PBS at 37 °C for 1, 4 and 6 h.

For *in vivo* testing, healthy BALB/c mice were used. Briefly, for each compound, groups of mice ( $n = 3$ ) were injected with TCO-ALN (100  $\mu$ L, 20 mg/kg), which was followed by administration of the  $^{99m}\text{Tc}$ -labeled compounds 1 h later. At 6 h post-injection of the  $^{99m}\text{Tc}$  complexes, the animals were sacrificed and the activity concentrations in various tissues and fluids determined. The resulting data is reported as percent injected dose per gram tissue (%ID/g) and is shown in Figure 2.4. Representative ratios of bone (knee or shoulder) to blood for

each of the five  $^{99m}\text{Tc}$ -labeled tetrazine compounds are shown on Table 2.1. These data indicate clearly that compound **14** provided optimal targeting combined with clearance from blood, and that there was substantial variation among the  $^{99m}\text{Tc}$ -tetrazines in regards to off-target tissue localization. A negative control study using CD1 mice ( $n = 3$ ) was conducted; where mice were injected with  $^{99m}\text{Tc}$ -tetrazine ligands in the absence of TCO-ALN. Mice were sacrificed at 0.5, 1, 4 and 6 h and %ID/g was determined for all tissues and fluids. For all compounds tested, where data for compound **6** is presented in Figure 2.5, no significant uptake was seen in bone or other tissues (heart, lungs, spleen, skeletal muscle) not shown in Figure 2.4.

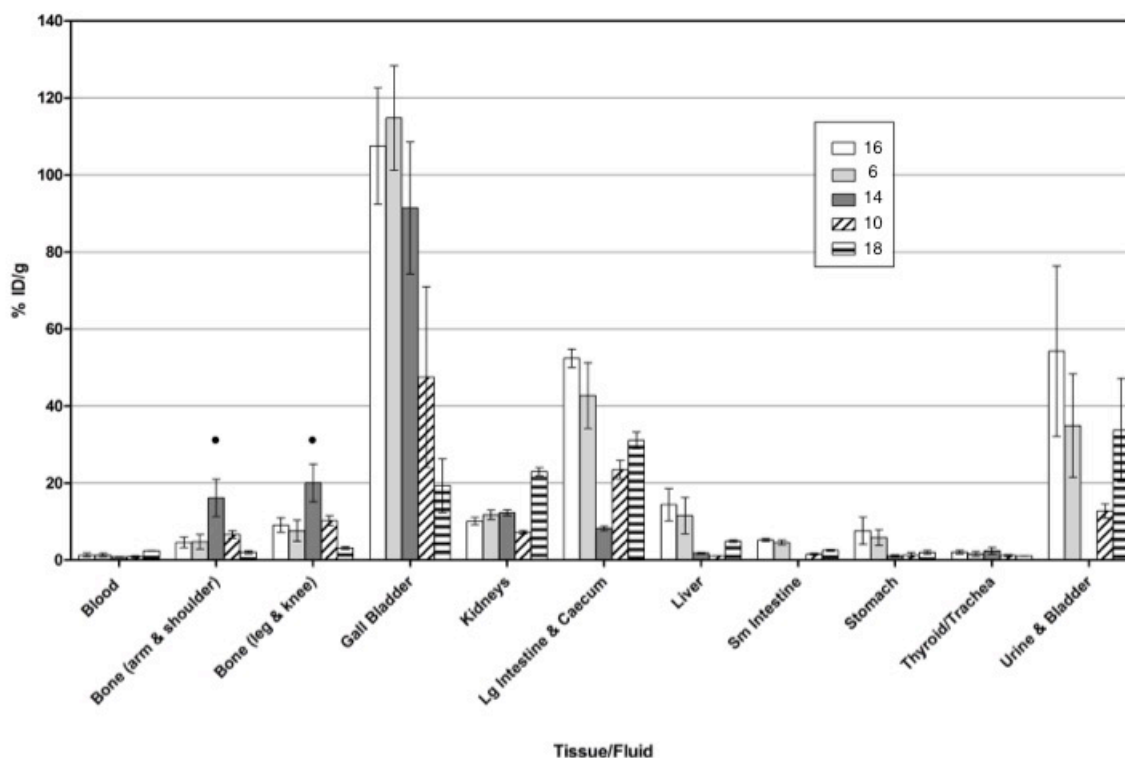


**Figure 2.4** Biodistribution results for  $^{99m}\text{Tc}$ -tetrazines **6**, **10**, **14**, **16**, **18** (bars indicated). Data shown were obtained from selected tissues and fluids taken 6 h post injection of the radiolabeled derivatives, and activity was normalized to tissue or fluid weight, as mean percent injected dose per gram of tissue or fluid (%ID/g)  $\pm$  SEM. Bone targets are indicated by •. NOTE: All remaining tissues not shown had mean %ID/g that was less than 1%.

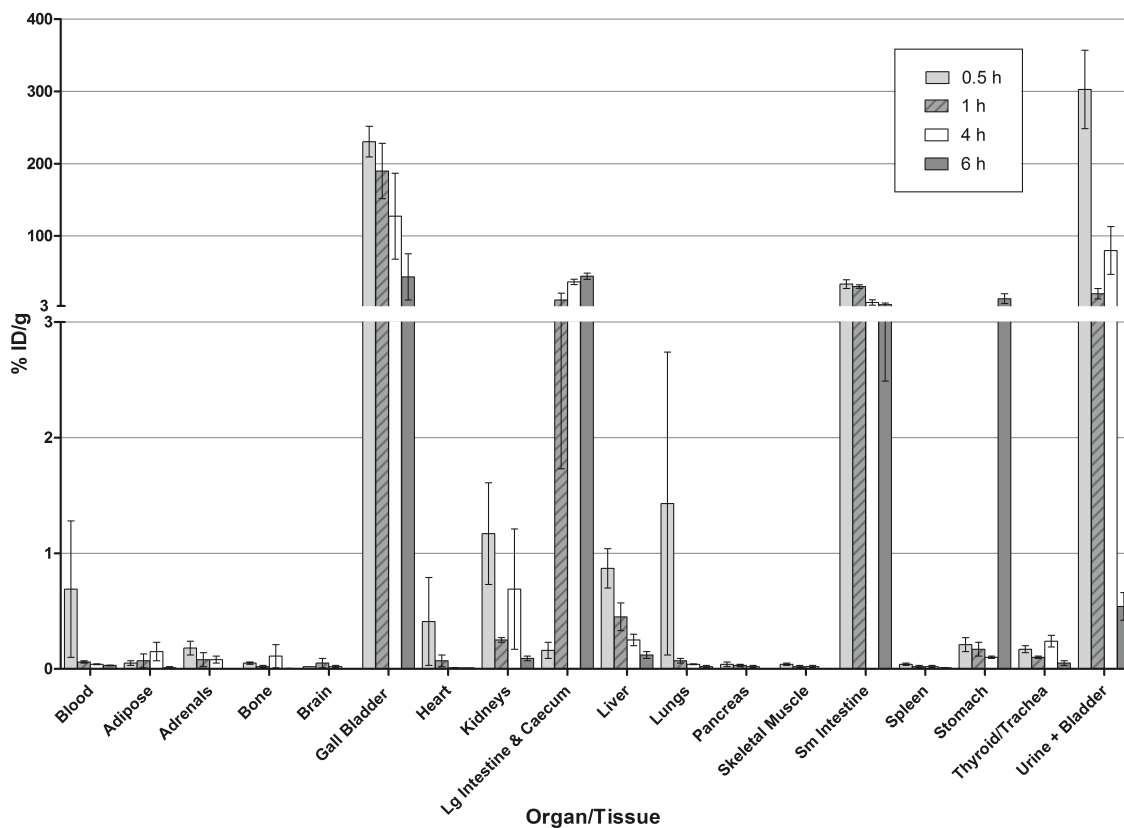


**Figure 2.5** Biodistribution results for control study using  $^{99m}\text{Tc}$ -tetrazine (**6**) without prior injection of TCO-ALN. Data shown were obtained from selected tissues and fluids taken from 3 mice at 0.5, 1, 4, and 6 h post injection of **6**.

Activity was normalized to tissue or fluid weight, as mean percent injected dose per gram of tissue or fluid (%ID/g)  $\pm$  SEM.

**Table 2.1** Bone: blood ratios determined from biodistribution studies.

Compound No.	<b>6</b>	<b>10</b>	<b>14</b>	<b>16</b>	<b>18</b>
Shoulder : Blood	3.5 : 1	7.8 : 1	21 : 1	3.5 : 1	0.8 : 1
Knee : Blood	5.6 : 1	12 : 1	26 : 1	6.9 : 1	1.3 : 1

A collection of tetrazine-linked tridentate chelates of varying polarities were prepared, and the utility of their  $^{99m}\text{Tc}$  complexes in the IEDDA reaction with a TCO derivative was assessed *in vivo*. An effective and reproducible  $^{99m}\text{Tc}$  labeling method was developed for five tetrazine chelates, where the ligand concentration was  $10^{-3}$  M. The labeling step was followed by deprotection of t-butyl groups (for compounds **6**, **10**, **14** and **18**). The high concentration of ligand was used to improve the radiochemical yield and reduce reaction times which minimized degradation of the tetrazine.<sup>23</sup> The product was isolated and separated from unlabeled ligand and any radiochemical impurities by HPLC, resulting in radiochemical yields ranging from 31-83%, with all having >99% radiochemical purity and a high specific activity of  $\sim 1.48$  MBq/ $\mu\text{g}$ . All compounds were shown to be stable in PBS containing 0.5% BSA and 0.01% polysorbate-80 for up to 6 h (Figure 2.3).

Bisphosphonate compounds, like TCO-ALN, localize to regions of active

bone metabolism or injury, which include knee and shoulder joints in mice. TCO-ALN therefore provides a simple means to assess the effectiveness of new radiolabeled tetrazines to deliver isotopes *in vivo*. Evaluation of the biodistribution of all five  $^{99m}\text{Tc}$ -tetrazines showed uptake in knee and shoulder joints 6 h post injection, demonstrating successful pretargeting to bone *in vivo* (Figure 2.4). Previous studies confirmed that radiolabeled TCO-ALN accumulates at the bone,<sup>20</sup> whereas the  $^{99m}\text{Tc}$ -tetrazine construct (**6**) given alone does not (Figure 2.5). This allows one to conclude that bone uptake was due to the IEDDA reaction.

The more lipophilic constructs **6** and **16** had similar distribution data including high uptake in the knee ( $9.1 \pm 1.9$  and  $7.6 \pm 2.7$  %ID/g, respectively) and the shoulder ( $4.6 \pm 1.4$  and  $4.8 \pm 1.9$  %ID/g, respectively). High radioactivity concentrations were also seen in the gall bladder, liver and intestines, which is consistent with the distribution of the lipophilic  $^{99m}\text{Tc}$ -tetrazine compound **6** in the absence of TCO-ALN (Figure 2.5). Other non-target tissues and organs such as the skeletal muscle and spleen did not show any significant uptake (<1%) when biodistribution studies were performed on the  $^{99m}\text{Tc}$ -tetrazines in the absence of the TCO-ALN (Figure 2.5), so these organs were not taken for the pretargeting experiments. Additionally, biodistribution experiments with the  $^{99m}\text{Tc}$ -tetrazines alone revealed good clearance from non-target tissues at 6 h post injection. Consequently, this time point, which is within one half-life of the isotope, was selected as the time point for comparing the different radiolabeled tetrazine



ligands.

The more polar  $^{99m}\text{Tc}$ -tetrazine compound **14** bearing a polyethylene glycol 5 (PEG<sub>5</sub>) linker showed very high knee and shoulder uptake ( $16.2 \pm 4.8$  and  $20.7 \pm 4.9$  respectively). There was also lower activity observed in the liver and intestines. The corresponding PEG<sub>10</sub> derivative also showed binding to the bone and reduced uptake in the liver compared to compounds **16** and **6**. The most polar derivative **18** showed lower bone binding than all other constructs, which is likely due to its rapid clearance.

The high bone uptake and bone: blood ratios (Table 2.1) particularly for compounds **10** and **14** demonstrate that pretargeting and the IEDDA reaction can be used to localize  $^{99m}\text{Tc}$ -labeled compounds *in vivo*. The methods reported here can be used to evaluate any radiolabeled tetrazine including next generation of  $^{99m}\text{Tc(I)}$ -tetrazine ligands. It should be noted that for the class of ligands that were used in this study, the structures can be readily varied by changing the nature of the donor groups and linkers between the metal complex and the tetrazine, without significantly altering the ligand synthesis method.<sup>23</sup> Once a lead molecule is identified, an instant kit labeling method, which will likely include solid phase purification methods, can be developed to support clinical translation.

The  $^{99m}\text{Tc(I)}$  complexes reported here create the opportunity to prepare new  $^{99m}\text{Tc}$  radiopharmaceuticals using a wide array of different TCO-derived targeting molecules including antibodies. Antibodies, despite their excellent targeting properties prior to the creation of technetium labeled tetrazines, would

not typically be used with  $^{99m}\text{Tc}$  because of their slow clearance (days), which is much longer than the half-life of the isotope ( $\sim 6$  h). An additional application is that the same class of ligands can be prepared with the beta emitting radionuclides  $^{186}\text{Re}$  and  $^{188}\text{Re}$ . The isostructural  $\text{Re(I)}$  analogues of the  $^{99m}\text{Tc(I)}$  agents when combined with the tumor seeking properties of TCO-ALN can be used to treat bone metastases.

## 2.4 Conclusion and Future Work

In conclusion, five different  $^{99m}\text{Tc}$ -tetrazines were synthesized, characterized and evaluated *in vivo* for pretargeted imaging. Furthermore, successful pretargeting with TCO-ALN for bone targeting was demonstrated. The next step involves testing the ability of the lead  $^{99m}\text{Tc}$ -tetrazines to couple to a TCO-antibody using a pretargeting strategy.

## 2.5 Acknowledgements

This work supported by research grant funding from the Natural Sciences and Engineering Research Council (NSERC) of Canada, the Ontario Institute for Cancer Research (OICR, #P.SI.015.8), and the Canadian Cancer Society (CCS, #703857). The authors acknowledge the contributions of Dr. Denis Snider who provided assistance in preparing the manuscript.

## 2.6 References

- (1) Boschi, A.; Uccelli, L.; Martini, P. *Appl. Sci.* **2019**, *9* (2526), 1–16.
- (2) Jurisson, S. S.; Lydon, J. D. *Chem. Rev.* **1999**, *99* (9), 2205–2218.
- (3) Kluba, C. A.; Mindt, T. L. *Molecules* **2013**, *18*, 3206–3226.
- (4) Amato, I. *Chem. Eng. News.* **2009**, *87* (36), 58–70.
- (5) Hnatowich, D. J.; Virzi, F.; Rusckowski, M. *J. Nucl. Med.* **1987**, *28* (8), 1294–1302.
- (6) Blackman, M. L.; Royzen, M.; Fox, J. M. *J. Am. Chem. Soc.* **2008**, *130*, 13518–13519.
- (7) Devaraj, N. K.; Weissleder, R.; Hilderbrand, S. A. *Bioconjugate Chem.* **2008**, *19* (12), 2297–2299.
- (8) Rossin, R.; Verkerk, P. R.; van den Bosch, S. M.; Volders, R. C. M.; Verel, I.; Lub, J.; Robillard, M. S. *Angew. Chemie Int. Ed.* **2010**, *49*, 3375–3378.
- (9) Zeglis, B. M.; Brand, C.; Abdel-Atti, D.; Carnazza, K. E.; Cook, B. E.; Carlin, S.; Reiner, T.; Lewis, J. S. *Mol. Pharm.* **2015**, *12* (10), 3575–3587.
- (10) Rossin, R.; van den Bosch, S. M.; Ten Hoeve, W.; Carvelli, M.; Versteegen, R. M.; Lub, J.; Robillard, M. S. *Bioconjugate Chem.* **2013**, *24*, 1210–1217.
- (11) Rossin, R.; Robillard, M. S. *Curr. Opin. Chem. Biol.* **2014**, *21*, 161–169.
- (12) Denk, C.; Svatunek, D.; Filip, T.; Wanek, T.; Lumpi, D.; Fröhlich, J.; Kuntner, C.; Mikula, H. *Angew. Chemie Int. Ed.* **2014**, *53* (36), 9655–9659.
- (13) Herth, M. M.; Andersen, V. L.; Lehel, S.; Madsen, J.; Knudsen, G. M.; Kristensen, J. L. *Chem. Commun.* **2013**, *49* (36), 3805–3807.
- (14) Li, Z.; Cai, H.; Hassink, M.; Blackman, M. L.; Brown, R. C. D.; Conti, P. S.; Fox, J. M. *Chem. Commun.* **2010**, *46* (42), 8043.
- (15) Nichols, B.; Qin, Z.; Yang, J.; Vera, D. R.; Devaraj, N. K. *Chem. Commun.* **2014**, *50* (40), 5215–5217.

- (16) Zeglis, B. M.; Sevak, K. K.; Reiner, T.; Mohindra, P.; Carlin, S. D.; Zanzonico, P.; Weissleder, R.; Lewis, J. S. *J. Nucl. Med.* **2013**, *54* (8), 1389–1396.
- (17) García, M. F.; Zhang, X.; Shah, M.; Newton-Northup, J.; Cabral, P.; Cerecetto, H.; Quinn, T. *Bioorg. Med. Chem.* **2016**, *24* (6), 1209–1215.
- (18) García, M. F.; Gallazzi, F.; Junqueira, M. D. S.; Fernández, M.; Camacho, X.; Mororó, J. D. S.; Faria, D.; Carneiro, C. D. G.; Couto, M.; Carrión, F.; Pritsch, O.; Chammas, R.; Quinn, T.; Cabral, P.; Cerecetto, H. *Org. Biomol. Chem.* **2018**, *16* (29), 5275–5285.
- (19) Russell, R. G. G. *Bone* **2011**, *49* (1), 2–19.
- (20) Yazdani, A.; Bilton, H.; Vito, A.; Genady, A. R.; Rathmann, S. M.; Ahmad, Z.; Janzen, N.; Czorny, S.; Zeglis, B. M.; Francesconi, L. C.; Valliant, J. F. *J. Med. Chem.* **2016**, *59* (20), 9381–9389.
- (21) Alberto, R.; Schibli, R.; Egli, A.; Schubiger, A. P.; Abram, U.; Kaden, T. A. *J. Am. Chem. Soc.* **1998**, *120* (31), 7987–7988.
- (22) Alberto, R.; Ortner, K.; Wheatley, N.; Schibli, R.; Schubiger, A. P. *J. Am. Chem. Soc.* **2001**, *123* (13), 3135–3136.
- (23) Lu, G.; Maresca, K. P.; Hillier, S. M.; Zimmerman, C. N.; Eckelman, W. C.; Joyal, J. L.; Babich, J. W. *Bioorg. Med. Chem. Lett.* **2013**, *23*, 1557–1563.
- (24) Maresca, K. P.; Hillier, S. M.; Lu, G.; Marquis, J. C.; Zimmerman, C. N.; Eckelman, W. C.; Joyal, J. L.; Babich, J. W. *Inorganica Chim. Acta* **2012**, *389*, 168–175.
- (25) Bartholomä, M. D.; Vortherms, A. R.; Hillier, S.; Ploier, B.; Joyal, J.; Babich, J.; Doyle, R. P.; Zubieta, J. *ChemMedChem* **2010**, *5* (9), 1513–1529.

## **Chapter 3: Evaluation of $^{99m}\text{Tc}$ -tetrazines for pretargeted imaging with trans-cyclooctene functionalized antibodies**

### **3.1 Introduction**

Antibodies have been widely studied in the field of radioimaging and radiotherapy due to their high specificity for disease-specific cellular targets.<sup>1</sup> In oncology, there has been a notable increase in the number of clinically approved antibodies and antibody drug conjugates.<sup>2</sup> There has been a concomitant increase in interest in developing antibody-based diagnostics particularly for patient selection and therapeutic monitoring. As mentioned previously, the long circulation times of antibodies does not align with the short half-lives of the most widely used medical isotopes like  $^{99m}\text{Tc}$ . However, there is the potential to address this issue through pretargeting and bioorthogonal chemistry.

Pretargeted imaging with several TCO-functionalized antibodies and radiolabeled tetrazines has been demonstrated in the literature. Rossin and coworkers were the first to demonstrate successful *in vivo* pretargeted imaging, using  $^{111}\text{In}$  and  $^{177}\text{Lu}$  labeled tetrazines. These radiolabeled tetrazines were paired with a TCO-derived CC49 antibody, which targets the tumour-associated glycoprotein 72 (TAG72), a glycoprotein expressed on the surface of many cancers such as colorectal, ovarian, and breast.<sup>3–5</sup> In this study, tumour uptake in

LS174T colon carcinoma xenografts reached  $5.38 \pm 0.48$  %ID/g at 3 hours post injection, but what was more impressive was the tumor to background ratios:  $196 \pm 13$  (tumour: blood),  $31 \pm 3$  (tumour: liver),  $3 \pm 0$  (tumour: kidney),  $141 \pm 67$  (tumour: muscle), and  $95 \pm 86$  (tumour: bone) at 3 hours post injection (Figure 3.1).<sup>6</sup>

Organ	1 h	3 h	6 h	1 d	2 d	4 d	7 d
Blood	$13 \pm 6$	$196 \pm 13$	$206 \pm 75$	$307 \pm 90$	$410 \pm 270$	$446 \pm 82$	$540 \pm 169^*$
Liver	$17 \pm 6$	$31 \pm 3$	$30 \pm 9$	$30 \pm 8$	$30 \pm 18$	$14 \pm 4$	$8 \pm 1$
Kidney	$2 \pm 1$	$3 \pm 0$	$4 \pm 1$	$4 \pm 1$	$7 \pm 3$	$6 \pm 2$	$6 \pm 2$
Bladder	$3 \pm 2$	$8 \pm 4$	$25 \pm 10$	$20 \pm 7$	$33 \pm 16$	$15 \pm 3$	$7 \pm 2$
Muscle	$31 \pm 18$	$141 \pm 67$	$245 \pm 108$	$257 \pm 75$	$229 \pm 145$	$203 \pm 100$	$225 \pm 152$
Bone	$23 \pm 20^*$	$95 \pm 86$	$162 \pm 46$	$159 \pm 69$	$149 \pm 78$	$114 \pm 61$	$76 \pm 25$

\* $n = 3$

Data are mean  $\pm$  SD ( $n = 4$ )

**Figure 3.1** Tumour-to-organ ratios for CC49-TCO-pretargeted  $^{177}\text{Lu}$ -tetrazine in mice bearing LS174T colon carcinoma xenografts.<sup>6</sup> This research was originally published in JNM. Rossin, R. *et al.* J Nucl Med. 2013; 54(11): 1989-1995. © SNMMI.

Zeglis and coworkers developed several  $^{64}\text{Cu}$ -labeled tetrazines to be used with a TCO-huA33 antibody,<sup>7</sup> which targets the A33 antigen expressed on the surface of 95% of colorectal cancers.<sup>8</sup> Biodistribution studies in SW122 human

colorectal cancer xenografts showed uptake values for a  $^{64}\text{Cu}$ -SarAr-tetrazine reaching as high as  $7.38 \pm 2.02$  %ID/g at 24 hours post injection (Figure 3.2).<sup>9</sup>

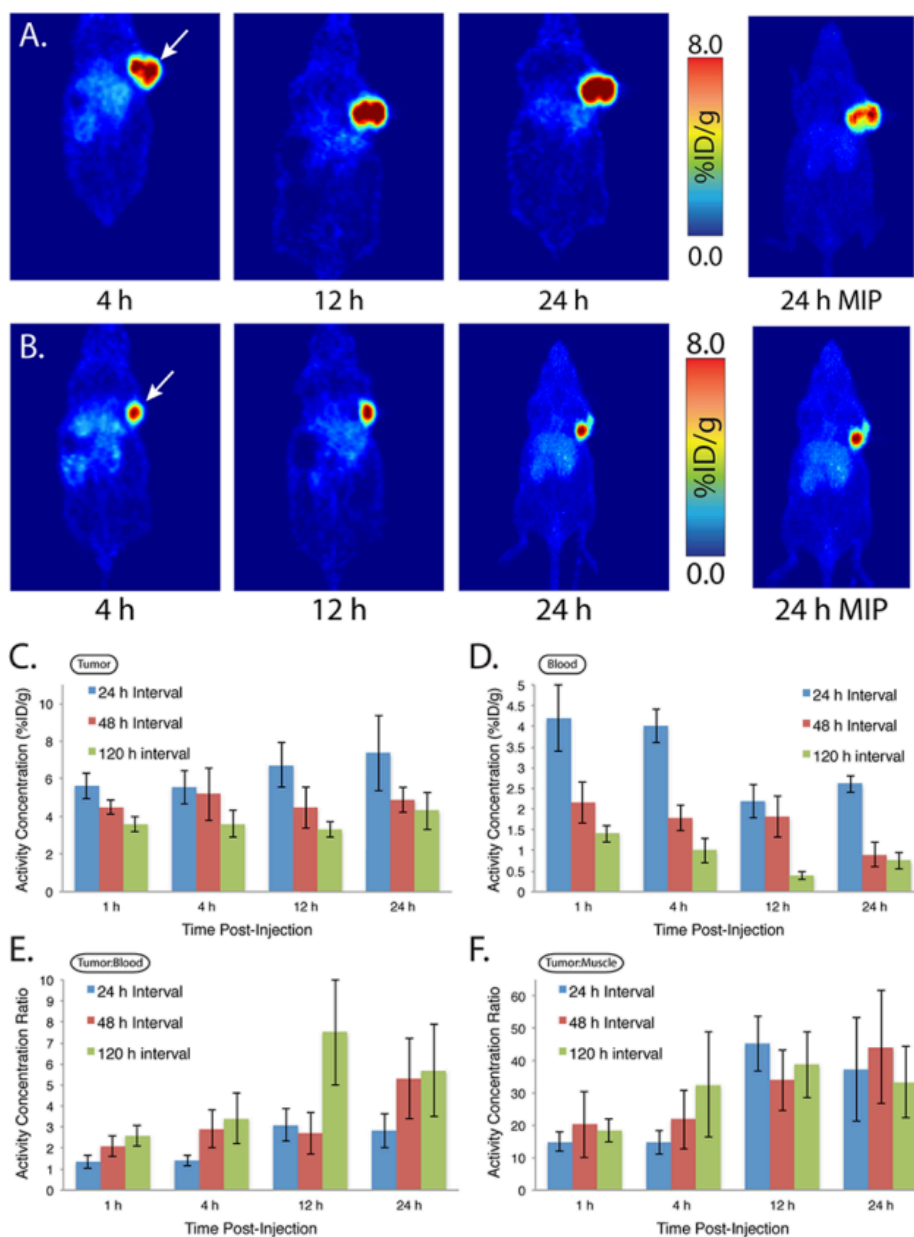


**Figure 3.2** Pretargeted PET imaging using  $^{64}\text{Cu}$ -Tz-SarAr with 48 h (A) and 120 h (B) accumulation intervals. The coronal slices (left) intersect the center of the tumour (white arrow). Maximum intensity projections (MIP) collected at 24 h post-

injection are also displayed (right); (C) Activity concentration in the tumour as a function of both time post-injection and accumulation interval for pretargeting with  $^{64}\text{Cu}$ -Tz-SarAr; (D) Activity concentration in the blood as a function of both time post injection and accumulation interval pretargeting with  $^{64}\text{Cu}$ -Tz-SarAr; (E) Tumour-to-blood activity concentration ratios as a function of both time post injection and accumulation interval pretargeting with  $^{64}\text{Cu}$ -Tz-SarAr; (F) Tumour-to-muscle activity concentration ratios as a function of both time post injection and accumulation interval pretargeting with  $^{64}\text{Cu}$ -Tz-SarAr. Reprinted (adapted) with permission from Zeglis, B.M *et al.* Mol. Pharm. 2015, 12(10), 3575-3587. Copyright 2019 American Chemical Society.

In addition to the results from  $^{111}\text{In}$  and  $^{64}\text{Cu}$  labeled tetrazines, several other radiolabeled tetrazines have been reported with some of the most widely used isotopes. Lewis and coworkers developed several  $^{18}\text{F}$ -labeled tetrazines for pretargeted PET imaging with a variety of TCO-functionalized antibodies.<sup>10,11</sup> Of these studies, pretargeted imaging was successful with an  $^{18}\text{F}$ -tetrazine and a TCO-hu5b1 antibody, which targets carbohydrate antigen 19.9 (CA19.9) overexpressed in pancreatic ductal adenocarcinomas.<sup>12,13</sup> Biodistribution studies resulted in tumour uptake as high as  $5.6 \pm 0.85$  %ID/g at 4 hours post injection in BxPC3 pancreatic cancer xenografts, with tumour: blood ratios  $>3$ .

Aboagye and coworkers developed a  $^{68}\text{Ga}$ -labeled tetrazine to be used with a TCO-Cetuximab derivative to target epidermal growth factor receptors



(EGFR) expressed on the surface of many cancers.<sup>14</sup> Pretargeted PET imaging in A431 xenografts revealed modest tumour uptake values of ~2 %ID/g at 1 hour post injection, however off target uptake remained prevalent, with many tumour: non-tumour ratios being <1.

Garcia and coworkers reported the first <sup>99m</sup>Tc-labeled tetrazine, where pretargeting studies were performed with a previously mentioned TCO-CC49 antibody.<sup>15</sup> Biodistribution studies in LS174T xenografts showed uptake values of the <sup>99m</sup>Tc-tetrazine reaching  $1.39 \pm 0.42$  %ID/g at 2 hours post injection. However, off-target uptake was still observed, with tumour: blood ratios <1, supporting the need for further improvement.

With the demonstration of successful pretargeting between several TCO-antibodies and radiolabeled tetrazines in literature, and the lack of effective <sup>99m</sup>Tc-labeled tetrazines, it was of interest to test the pretargeting ability of the <sup>99m</sup>Tc-tetrazines reported in chapter 2 with a TCO-functionalized antibody. Specifically, *in vitro* tests were completed using a TCO-functionalized antiVEGFR2 antibody, while *in vivo* studies were performed using the aforementioned TCO-functionalized huA33 antibody in conjunction with compounds **6** and **10**.<sup>7</sup>

## 3.2 Materials and Methods

### 3.2.1 General materials and instruments

All reagents were purchased from Sigma Aldrich unless otherwise stated. (E)-Cyclooct-4-enyl-2,5-dioxopyrrolidin-1-yl carbonate (TCO-NHS) and 4-(1,2,4,5-tetrazin-3-yl)phenylmethanamine hydrochloride was purchased from Conju-Probe (San Diego, CA). All cell media, and antiVEGFR2 antibody were purchased from ThermoFisher scientific. Sodium pertechnetate was provided by Mallinckrodt Pharmaceuticals from an Ultra-Technekow generator.

A MALDI-TOF MS analysis was performed on a MALDI Bruker UltrafleXtreme Spectrometer. Radio TLC imaging was performed on a BIOSCAN AR-2000 radio-TLC imaging scanner. High performance liquid chromatography (HPLC) of radioactive compounds were performed on a Waters 1525 Binary (Midford, MA, USA) monitored simultaneously with 2998 photodiode array detector at 220/254 nm and in line radioactivity Bioscan gamma detector with NaI (T1) scintillator using the Empower software package. Analytical HPLC of all other compounds were performed on a Varian Prostar 230 monitored simultaneously with a Prostar 335 PDA detector. HPLC method: Phenomenex C-18 analytical column (250 mm × 4.6 mm × 5 µm) operating at a flow rate of 1.0 mL/min (analytical) was used. The following solvent gradient was employed (Method 1): (solvent A = H<sub>2</sub>O + 0.1% TFA, solvent B = ACN + 0.1% TFA): 0-2 min 20% B, 2-19 min 20-80% B, 19-21 min 100% B, 21-27 min 20% B. Preclinical imaging

Ph.D. Thesis – H. Bilton; McMaster University – Chemistry and Chemical Biology

system SPECT-CT experiments were conducted on an X-SPECT (Gamma Medica, Northridge, CA).

### **3.2.2 Animal models and biodistribution studies**

Animal studies were either approved by the Animal Research Ethics Board at McMaster University in accordance with Canadian Council on Animal Care (CCAC) guidelines, or performed under an Institutional Animal Care and Use Committee-approved protocol, and the experiments followed institutional guidelines for the proper and humane use of animals in research (Memorial Sloan Kettering Cancer Center, New York, NY, USA). Biodistribution studies were performed using either female BALB/c mice or Athymic nude female mice (Charles River Laboratories, Kingston, NY) at the indicated time points. For Athymic nude mice, SW1222 tumors were induced on the right shoulder by subcutaneous injection of  $5.0 \times 10^6$  cells in a 200  $\mu$ L cell suspension at approximately nine weeks of age.

### **3.2.3 Preparation of TCO-modified antiVEGFR2 antibody (TCO-antiVEGFR2)**

The preparation of TCO-modified antiVEGFR2 antibody was adapted from a literature procedure reported by Zlitni *et al.*<sup>16</sup> The pH of the solution containing anti-VEGFR2 (eBioscience, 14-5821) (1 mL, 500  $\mu$ g, 3.34 nmol) was adjusted to 9-9.5 by adding 5  $\mu$ L of 1 M  $\text{Na}_2\text{CO}_3$ (aq). In the dark, a solution of TCO-NHS (35.6  $\mu$ g, 133.6 nmol) in DMSO (18  $\mu$ L) was prepared and added to antiVEGFR2.

The mixture was left on a shaker overnight at 4 °C. The conjugated antibody was purified from excess TCO-NHS using an Amicon Ultra-0.5 Centrifugal filter (30,000 Da) and washing with PBS three times.

### 3.2.4 Labeling of TCO-antiVEGFR2 with **6**

Compound **6** (25  $\mu$ L, 2.2 MBq) was incubated with TCO-antiVEGFR2 in the dark. 1  $\mu$ L of the mixture (~37 kBq) was spotted on iTLC (VARIAN, SGI0001) glass microfiber chromatography paper impregnated with silica gel and the elution step run using a mixture of 75:25 v/v MeOH: 0.1 M HCl. As a reference standard, a mixture of **6** (25  $\mu$ L, 60  $\mu$ Ci) with PBS (25  $\mu$ L) was also prepared and a sample was run on iTLC under the same conditions. Both iTLCs were then scanned on a BIOSCAN AR-2000 radio-TLC imaging scanner.

### 3.2.5 Flow Chamber Cell Adhesion Assay

The chamber cell adhesion assay was performed following a modified method published by Zlitni *et al.*<sup>16</sup> One day prior to assay,  $16 \times 10^5$  of VEGFR2-expressing cells (H520) were plated. The binding of **6** (0.296 MBq) to the H520 cells was assessed under flow conditions (0.164 mL/min) with and without pre-incubation with TCO-antiVEGFR2 (10  $\mu$ g). Furthermore, the binding of **6** to H520 cells treated with TCO-antiVEGFR2 (30  $\mu$ g) for 30 min before the assay was also assessed. To decrease any non-specific binding, the mounted parallel-plate flow chamber (Glycotech, Rockville, Md.) was inverted. A syringe pump (PhD 2000, Harvard Apparatus, Holliston, USA) was used to first wash the cells with PBS (1

mL), followed by **6** (0.296 MBq/mL), and finally washed with PBS (1 mL). After the assay, cells were lysed using a 1% Triton-X100 (1 mL) solution at 37 °C for 30 min. From each cell lysate, two samples were taken; one to measure the amount of activity using a dose calibrator while the other to assess its protein levels using a Pierce BCA Protein assay kit (Thermo Scientific, 23225). The counts per minute (CPM) normalized by the amount of protein ( $\mu\text{g}$ ) was plotted for both the untreated cells, and cells treated with TCO-antiVEGFR2.

### **3.2.6 Preparation of TCO-modified huA33 antibody (TCO-huA33)**

The TCO modified huA33 antibody was prepared according to literature.<sup>17</sup> The pH of the solution containing huA33 antibody (210  $\mu\text{L}$ , 2 mg, 13.3  $\mu\text{mol}$ ) was adjusted to 9 by adding 30  $\mu\text{L}$  of 0.1 M  $\text{Na}_2\text{CO}_{3(\text{aq})}$ . A solution of (E)-cyclooct-4-enyl-2,5-dioxopyrrolidin-1-yl carbonate (TCO-NHS, 50  $\mu\text{g}$ , 0.33 nmol) in DMSO (2  $\mu\text{L}$ ) was prepared and added to huA33 antibody. The mixture was placed on a shaker at room temperature for one hr. The conjugated antibody was purified from excess TCO-NHS using an Amicon-Ultra Centrifugal filter with a 50,000 kDa cut off, followed by washing with 25 mL of PBS. The purified conjugated antibody was concentrated in 1mL from the centrifugal filter. Analysis using spectrophotometry at 280 nm showed a concentration of 1.71 mg/mL.

### 3.2.7 Labeling of TCO-huA33 with **6**

Compound **6** (100  $\mu$ L, 11.1 MBq) was incubated with TCO-huA33 (11  $\mu$ L, 100  $\mu$ g) in the dark. 1  $\mu$ L of the mixture ( $\sim$ 111 kBq) was spotted on iTLC C-18 silica TLC plates, with an eluent of 1:1 ( $\text{H}_2\text{O}$  + 0.1% TFA : ACN + 0.1% TFA). As a reference standard, a mixture of **6** (1  $\mu$ L,  $\sim$ 111 kBq) with PBS was also prepared and a sample was run on iTLC under the same conditions. Both iTLCs were then scanned on a BIOSCAN AR-2000.

### 3.2.8 Pretargeted SPECT Imaging Studies

Mice bearing subcutaneous SW1222 xenografts (100-150 mm; 18-21 days post inoculation) in the shoulder were administered TCO-huA33 (100 mg in 200  $\mu$ L of 0.9% sterile saline) via tail vein injection. After 24 hours, mice were administered a solution of **6** (37 MBq in 200  $\mu$ L of PBS + 1% BSA), or **5** (0.66 nM) and **6** (37 MBq in 200  $\mu$ L of PBS + 1% BSA), **10** (37 MBq in 200  $\mu$ L of PBS + 1% BSA), or **9** (0.66 nM) and **10** (37 MBq in 200  $\mu$ L of PBS + 1% BSA). Approximately 5 min before SPECT imaging, mice were anesthetized by inhalation of 2% isoflurane (Baxter healthcare): oxygen gas mixture and placed on the scanner bed. Anesthesia was maintained during the scans using 2% isoflurane: oxygen gas mixture. SPECT-CT data was collected at 1, 4 and 6 hours post injection the radiotracer.

### **3.2.9 Biodistribution Studies**

Animals (n = 4) were euthanized 6 hr post injection after SPECT-CT imaging was complete by CO<sub>2</sub>(g) asphyxiation. After exsanguination, tissues, organs and fluids (including tumor) were removed, washed with water where relevant, dried, weighed, and counted in a gamma counter calibrated for <sup>99m</sup>Tc. Gamma counts were repeated 12 hours post-organ excision. Counts were converted to activity using a calibration curve produced from known standards.

### **3.2.10 Blood clearance studies**

A solution of **6** (37 MBq) in 100 µL PBS + 0.5% BSA + 0.01% tween 80 was injected intravenously in healthy CD1 mice. At 0.5, 5, 15, 25, 30, 60 and 120 min post injection, anaesthetized mice were sacrificed (n=2) and blood drawn by cardiac puncture, followed by cervical dislocation. Blood samples were heparinized and split into two fractions. The first fraction was placed into pre-weighed gamma tubes to be counted on the gamma counter to determine %ID/g in the blood at each time point. The second fraction of blood was centrifuged at 10,000 rpm for 10 min to remove leukocytes and erythrocytes. Plasma supernatant was removed after centrifugation and transferred to a separate eppendorf tube. Radioactivity measurements were taken of the plasma and the erythrocyte/leukocyte layer. Next, 250 µL of ice cold ACN was added to the plasma, vortexed briefly, and centrifuged for another 10 min at 10,000 rpm. The plasma layer was removed from the resulting protein pellet, and radioactivity

Ph.D. Thesis – H. Bilton; McMaster University – Chemistry and Chemical Biology

measurements were taken. Centrifuging and separation from any remaining protein pellet was repeated. Finally, the purified plasma was then spotted onto iTLC plates and run with an eluent of 1:1 H<sub>2</sub>O + 0.1% TFA and ACN + 0.1% TFA. The remaining portions of the purified plasma were incubated with excess TCO-antiVEGFR2 (40x excess) at 37 °C for 10 min. The mixture was then spotted on iTLC and run using the same eluent.

### **3.3 Results and Discussion**

#### **3.3.1 Preparation and labeling of TCO-antiVEGFR2 antibody with 6**

Prior to *in vivo* studies, the ability of the <sup>99m</sup>Tc-tetrazines to bind TCO-antibody conjugates was tested *in vitro* using a well-established antibody and assay system. The synthesis of the TCO-antiVEGFR2 antibody was adapted from a literature procedure.<sup>16</sup> TCO-NHS was added to a solution of anti-VEGFR2 at a pH of 9-9.5 and shaken overnight at 4 °C. The TCO-antiVEGFR2 antibody was purified using a centrifugal filter (30 kDa) and washing with PBS. The purified antibody was characterized using MALDI-TOF MS analysis. Comparing the results of the MALDI-TOF MS analysis for the TCO-antiVEGFR2 and non-conjugated antiVEGFR2, it was determined that the TCO-antiVEGFR2 had an average of 4.3 TCO groups per antibody (Figure 3.3).



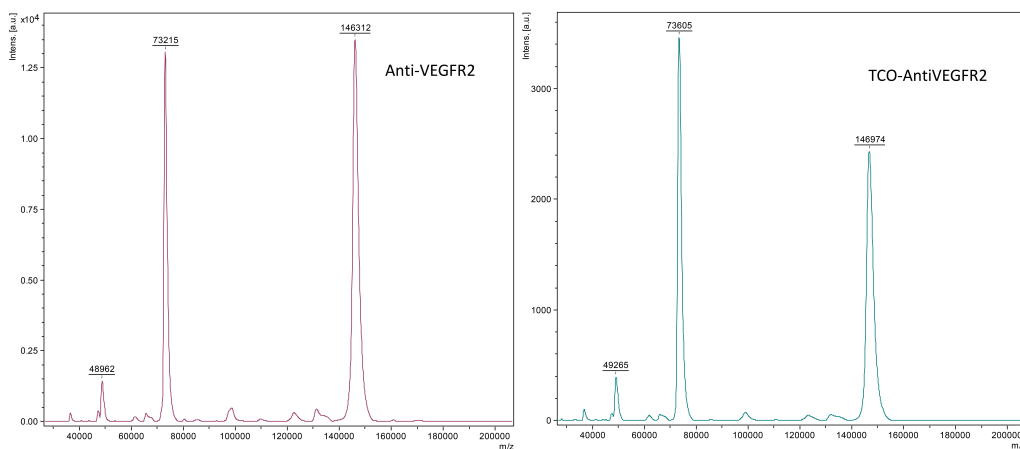


**Figure 3.3** MALDI-TOF analysis of antiVEGFR2 (left) and TCO-antiVEGFR2 (right) showing an average of 4.3 TCO groups per antibody.

Once the TCO-antiVEGFR2 antibody was prepared and characterized, the next step was to evaluate the coupling reaction with a  $^{99\text{m}}\text{Tc}$ -labeled tetrazine. To this end, compound **6** was incubated with TCO-antiVEGFR2 in the dark at room temperature for 30 minutes. To monitor reaction progression, an aliquot of the reaction mixture was spotted on an iTLC glass microfiber chromatography paper using an eluent consisting of a mixture of 75:25 v/v MeOH: 0.1 M HCl (Figure 3.4). In parallel, an iTLC of compound **6** alone was run as a reference standard. Results from the reference standard showed that compound **6** eluted approximately 50 mm from the baseline (note baseline is set at 50 mm) (Figure 3.4, left) where in the reaction mixture, almost all the radioactivity remained on the baseline, which is consistent with successful ligation of **6** to the TCO-antiVEGFR2 antibody (Figure 3.4, right).

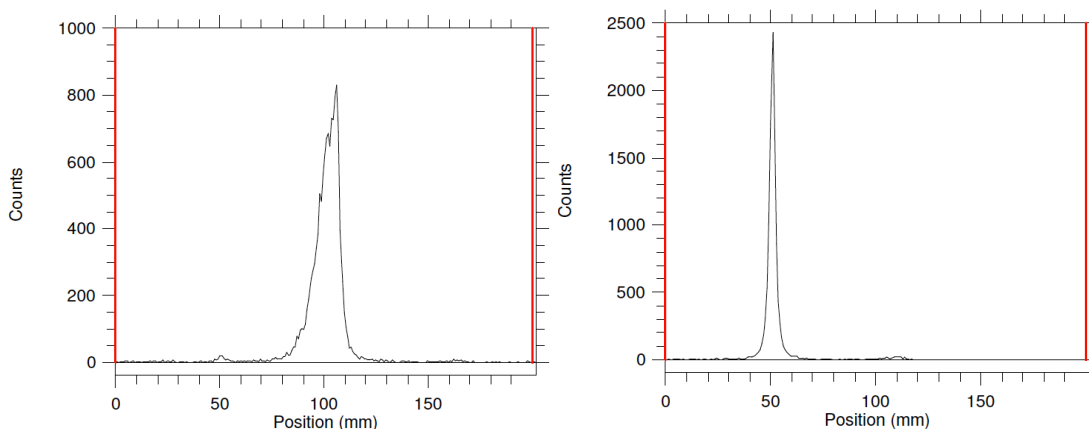


**Figure 3.4** Radio-iTLCs of **6** (left) and **6** following the addition of TCO-antiVEGFR2 (right). Note: baseline is set at 50 mm.

### 3.3.2 Flow Chamber Cell Adhesion Assay

Next, the ability of **6** to couple with TCO-antiVEGFR2 bound to cells under conditions designed to mimic the dynamic flow found in tumour capillaries was evaluated.<sup>18</sup> A flow chamber cell adhesion assay was performed following a procedure developed by Zlitni *et al*, where the binding of **6** to TCO-antiVEGFR2 was assessed at the shear flow rate of 0.164 mL/min.<sup>16</sup> First, H520 cells (VEGFR2+) grown in a tissue culture dish were fitted onto the flow chamber apparatus. Cells were then incubated with TCO-antiVEGFR2 for 30 minutes, followed by a wash step to remove any unbound antibody. Next, the cells were inverted before performing the assay to reduce any non-specific binding. A solution of **6** in PBS (296 kBq/mL) was then “flowed over” the cells, followed by a second wash with PBS. As a negative control, the experiment was repeated,

where **6** was passed over cells that were not pre-incubated with TCO-antiVEGFR2. After the assay, cells were lysed and radioactivity measurements were taken of the lysates. Protein concentrations of the cells were also determined using a BCA protein assay kit. After normalizing the counts per minute (CPM) by amount of protein, it was found that the binding of **6** was 12 times higher in cells pretreated with TCO-antiVEGFR2, than cells alone (Figure 3.5). This confirmed that under dynamic flow conditions similar to that found *in vivo*, the reaction between TCO-antiVEGFR2 and a radiolabeled tetrazine is rapid enough to see appreciable binding.

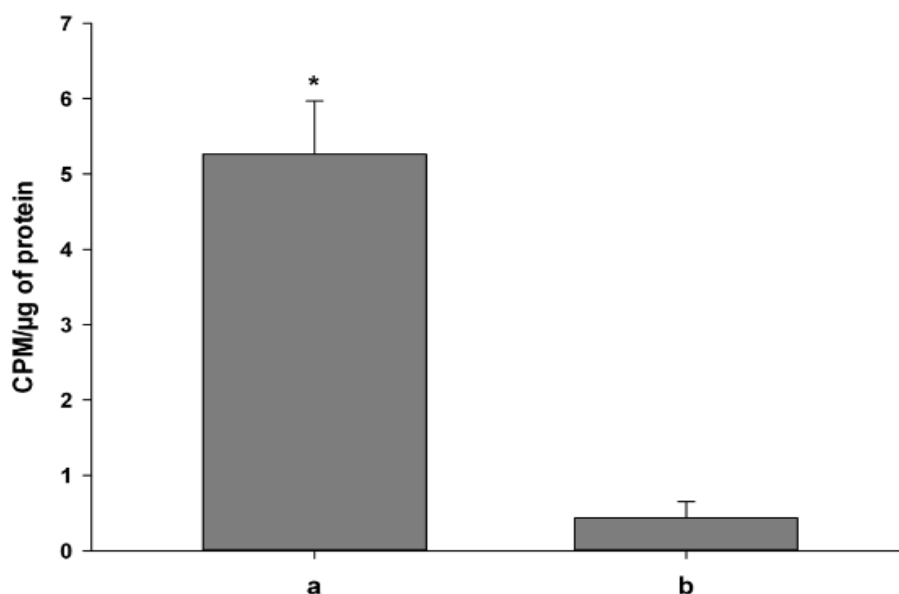


**Figure 3.5** A graphical representation showing the amount of **6** binding to H520 cells when (a) H520 cells pre-treated with TCO-antiVEGFR2 for 30 min before introducing **6** and (b) untreated cells. The binding of **6** was 12 times higher in

TCO-tagged cells (a) compared to untreated cells (b) ( $P < 0.001$ ). Data is expressed as counts per minute (CPM) per  $\mu\text{g}$  of protein found in each sample ( $n = 5$ ). \*Statistical analysis was done using a one-way ANOVA relative to (b).

### 3.3.3 Preparation and labeling of TCO-huA33 antibody with 10

With *in vitro* studies showing promise, translation toward *in vivo* studies was carried out. While TCO-antiVEGFR2 had proven to be an effective tool for *in vitro* screening, it had not been used *in vivo* previously with radiolabeled tetrazines. Therefore, a collaboration with the Zeglis group at Hunter College- was initiated to utilize a humanized TCO-huA33 antibody. The huA33 antibody binds the A33 antigen, a transmembrane glycoprotein that is overexpressed in 95% of colorectal cancers.<sup>19</sup> When bound, the huA33 antibody has little to no internalization into cells, making it an optimal targeting vector for pretargeting studies.<sup>20</sup> The Zeglis and Lewis groups have demonstrated successful pretargeting using the TCO-huA33 antibody and several radiolabeled tetrazines, making it a promising targeting vector for pretargeting studies with our  $^{99\text{m}}\text{Tc}$ -tetrazines.<sup>9,17</sup>

The synthesis of the TCO-huA33 was performed following a literature procedure.<sup>17</sup> TCO-NHS was added to a solution of huA33 antibody at a pH of 9.0. The solution was incubated at room temperature for 30 minutes with gentle

shaking. The resulting TCO-huA33 was purified using a centrifugal filter (50 kDa) and washed with PBS.

To verify the reactivity of the TCO group, compound **10** was incubated with the purified TCO-huA33 for 10 minutes in the dark with gentle shaking. The mixture was then spotted on an iTLC plate and run in an eluent of 1:1 v/v H<sub>2</sub>O and ACN containing 0.1% TFA. As a reference standard, **10** in PBS + 0.5% BSA + 0.01% tween 80 was prepared, spotted and run under the same conditions. As shown in Figure 3.6 below, the reference standard moved approximately 30 mm off the baseline (marked in red), whereas the mixture of **10** with TCO-huA33 remained on the baseline. This shift in retention time is consistent with a reaction between the <sup>99m</sup>Tc-tetrazine (**10**) and TCO-huA33.

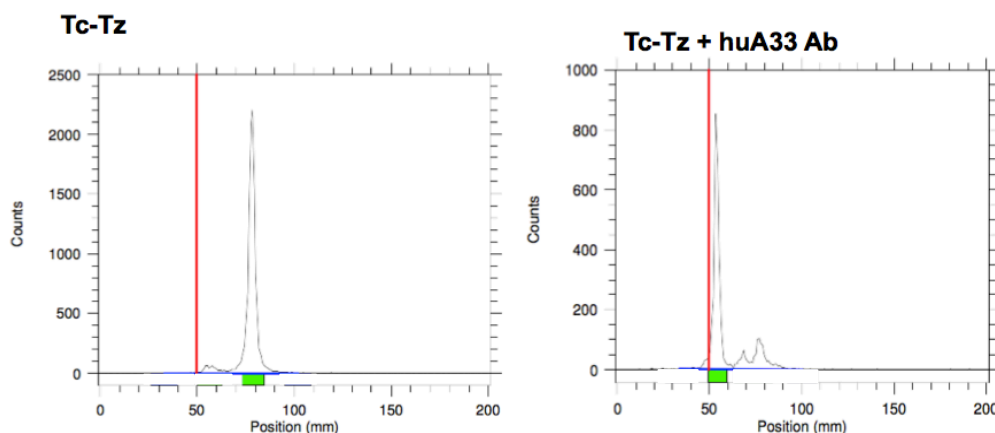


**Figure 3.6** iTLC analysis of **10** (left) and **10** after incubation with TCO-huA33 (right).

### 3.3.4 Pretargeted imaging and biodistribution of **6**

With the successful coupling of **10** and TCO-huA33, *in vivo* experiments were initiated in tumour bearing mice. SW122 tumour bearing mice were administered TCO-huA33 antibody 24 hours prior to the imaging study. It has been shown in literature that for pretargeting studies, administering a compound with lower effective specific activity has increased the uptake in the tumour.<sup>21</sup> For this reason, a mixture of **5** and **6** was administered at a concentration of 0.75 mM per mouse, and SPECT/CT images were taken at 1, 4 and 6 hours post injection (Figure 3.7). After the 6 hour imaging time point, mice were sacrificed and organs excised, weighed, and radioactivity levels counted. Biodistribution data plotted as percent injected dose per gram (%ID/g) is displayed in Figure 3.8 below.

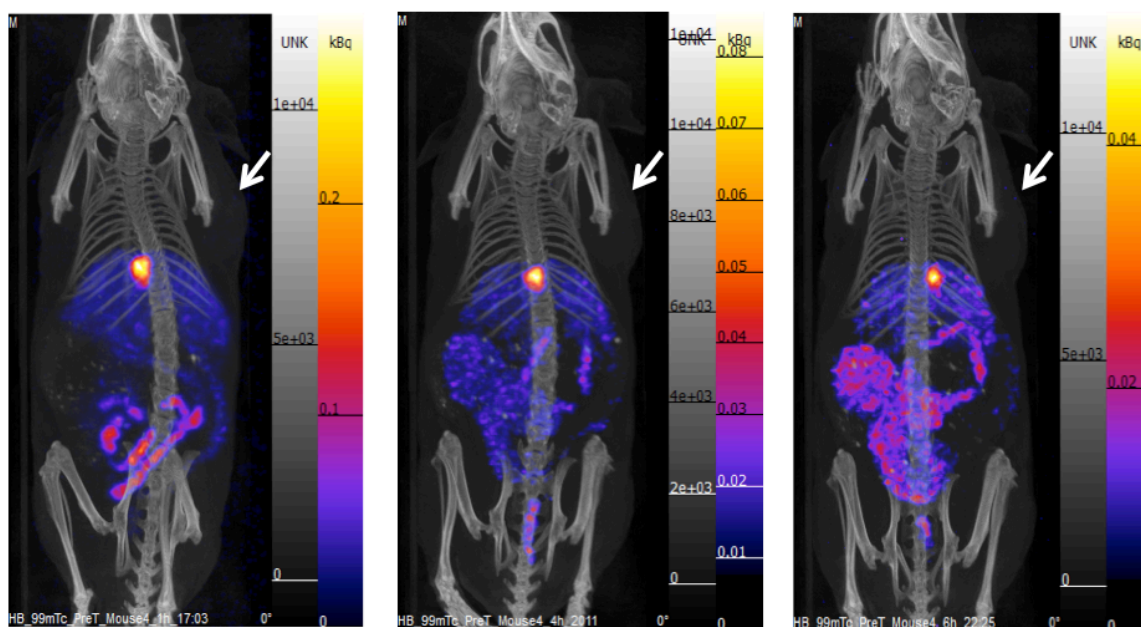


**Figure 3.7** SPECT-CT images of pretargeting approach at 1,4 and 6 hours (left to right) post-injection with **6** containing the Re complex **5**. White arrows indicate location of the tumor on the right shoulder.

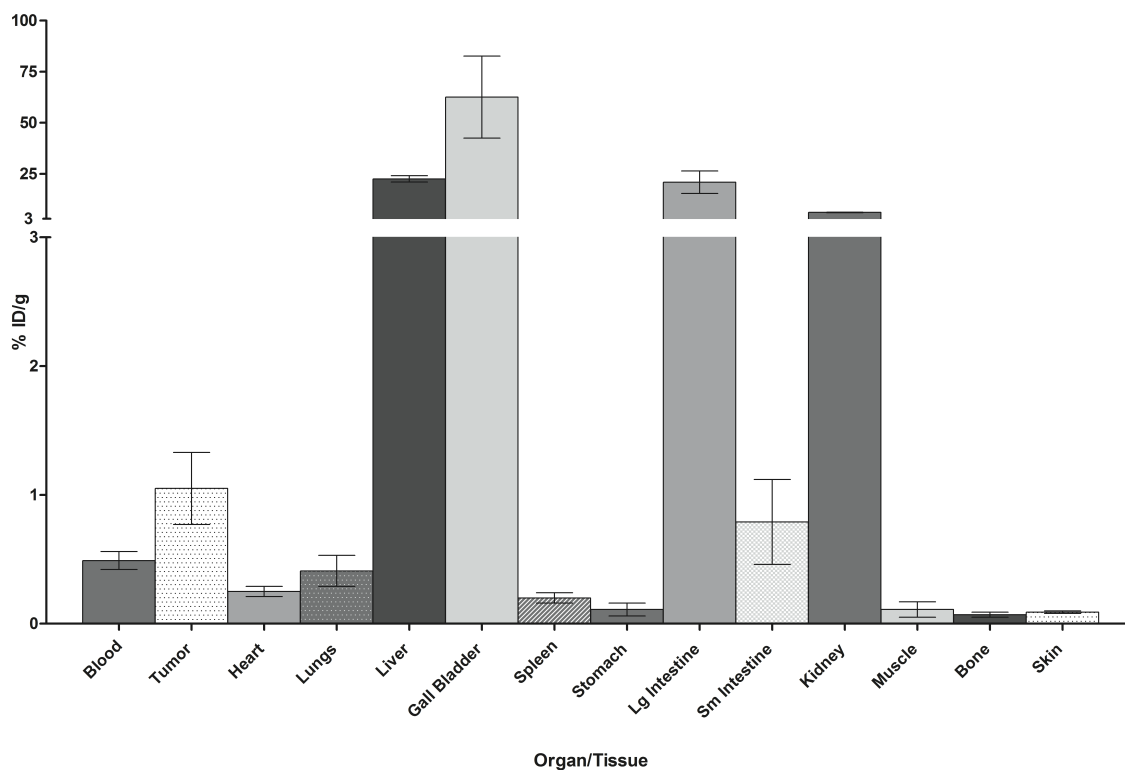


**Figure 3.8** Biodistribution data for pretargeting studies with TCO-huA33 and compounds **5** and **6**. Compounds **5** and **6** were co-administered (approximately 37 MBq of **6**, 0.75 mM of **5**) to athymic nude mice (n=4 per compound) 24 hours after the injection of TCO-huA33. Mice were sacrificed 6 hours post injection of **5** and **6**. Data is expressed as the mean injected dose per gram (%ID/g)  $\pm$  SEM.

Based on the SPECT-CT images and quantitative biodistribution data, tumour uptake was low ( $1.05 \pm 0.28$  %ID/g), with tumour: blood ratios  $<1$ . High concentrations of radioactivity were observed in the gall bladder ( $62.6 \pm 20.1$  %ID/g), liver ( $22.5 \pm 1.55$  %ID/g), and large intestine ( $20.9 \pm 5.48$  %ID/g), suggesting that the compound is cleared through the gastrointestinal (GI) tract. Relatively high uptake was also seen in the kidneys ( $6.14 \pm 0.14$  %ID/g), suggesting partial clearance through the renal pathway.

### 3.3.5 Pretargeted imaging and biodistribution of **10**

Given the initial results with compound **6**, the more polar tetrazine **10** was evaluated. Proceeding with *in vivo* studies, both high and low effective specific activities of **10** were examined, to assess the ability of a non-radioactive carrier to help increase tumour uptake. SW122 tumour bearing mice were administered TCO-huA33 24 hours prior to the imaging studies. The day of the imaging study, compound **10** was administered without any of the corresponding Re-complex via tail vein injection ( $n=4$ ). In a parallel study, compound **10** in the presence of **9** (0.75 mM) was administered via tail vein injection, mimicking the low effective specific activity imaging experiments conducted in section 3.3.4. SPECT-CT images were taken at 1, 4 and 6 hours for both studies (Figure 3.9 and 3.10). After the 6 hour imaging time point, mice were sacrificed and organs excised. The



organs were weighed, and radioactivity levels counted. Biodistribution data plotted %ID/g for both studies are displayed in Figure 3.11 below.

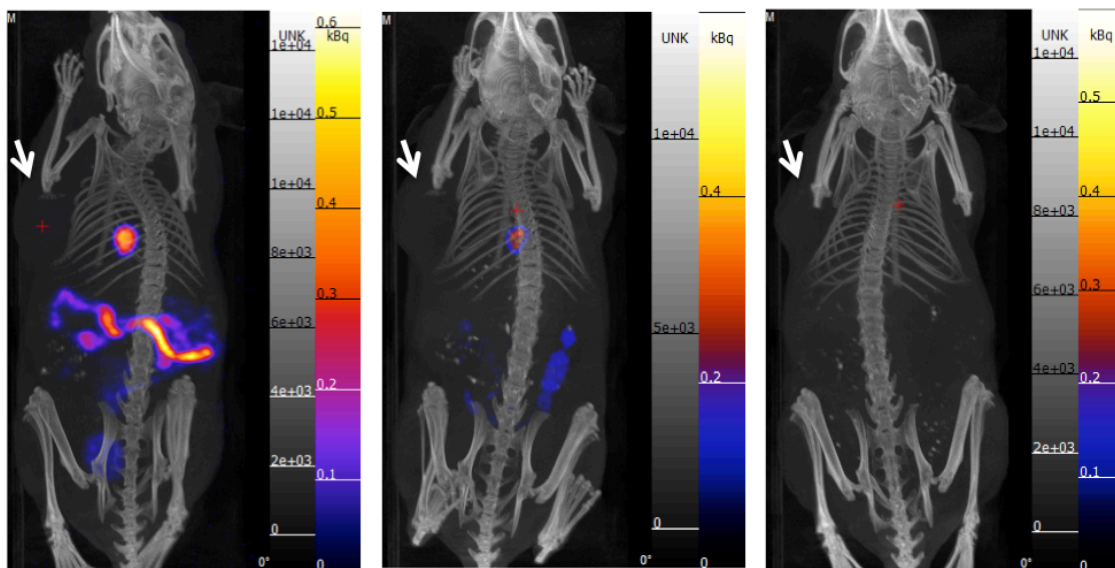


**Figure 3.9** SPECT-CT images of pretargeting approach at 1, 4, and 6 hours (left to right) post-injection of **10**. White arrows indicate location of tumor on the left shoulder.

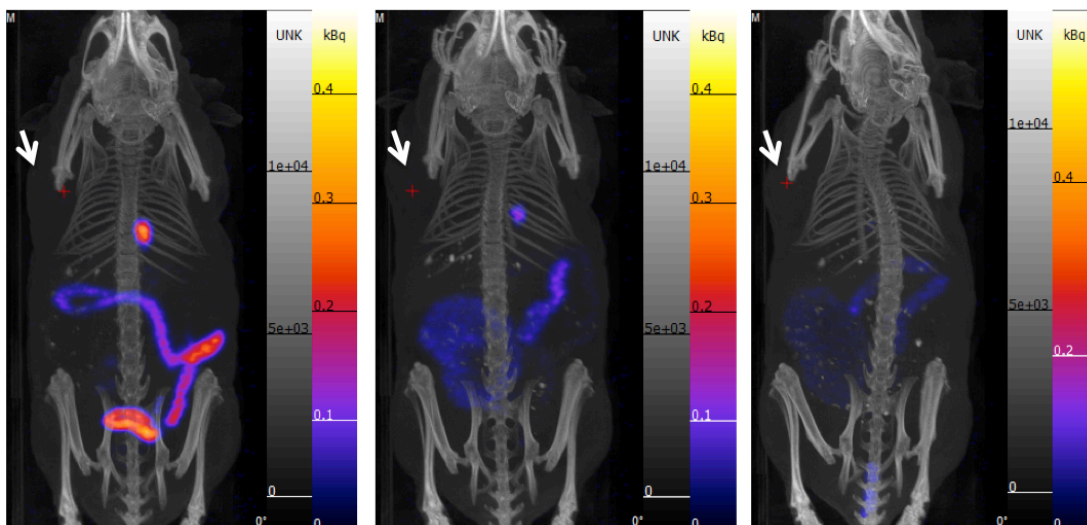


**Figure 3.10** SPECT-CT images of pretargeting approach at 1, 4, and 6 hours (left to right) post-injection with **10** containing the Re complex **9**. White arrows indicate location of tumor on the left shoulder.

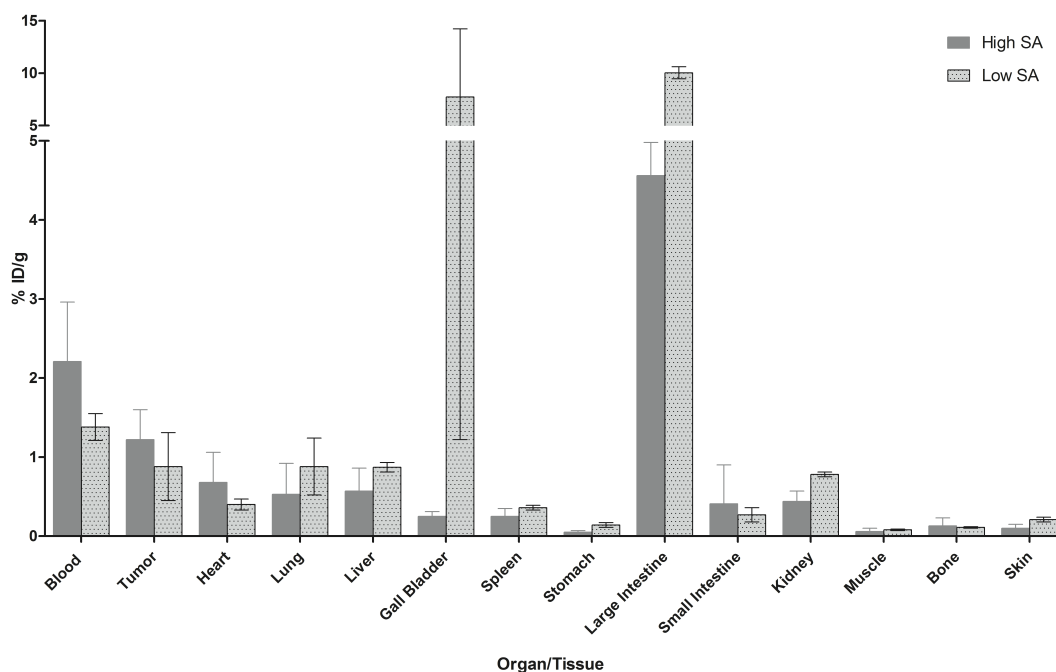


**Figure 3.11** Biodistribution of pretargeting studies with TCO-huA33 and compound **10** (dark grey bars), or **9** + **10** (light grey bars). Compound **10** was administered (approximately 37 MBq) to Athymic nude mice (n=4 per compound) 24 hours post injection of TCO-huA33. Mice were sacrificed 6 hours post injection of **10**. Data is expressed as the mean injected dose per gram (%ID/g)  $\pm$  SEM.

Results shown in figure 3.9 indicate that the clearance of **10** is greater than that of **6** at 6 hours; confirming that the addition of a PEG<sub>10</sub> spacer did help

reduce non-specific uptake. For instance, uptake was significantly reduced in the gall bladder ( $7.72 \pm 6.50$  versus  $62.6 \pm 20.1$  %ID/g), liver ( $0.87 \pm 0.06$  versus  $22.5 \pm 1.55$  %ID/g), large intestine ( $10.0 \pm 0.58$  versus  $20.9 \pm 5.48$  %ID/g) and kidneys ( $0.78 \pm 0.03$  versus  $6.14 \pm 0.14$  %ID/g). Although compound **10** demonstrated an improved clearance profile from **6**, the issue of inadequate tumour uptake persisted. In both of the high and low specific activity studies with compound **10**, little difference was seen in all organs, with minimal uptake in the tumour (~1%), with tumour: blood ratios <1.

### 3.3.6 Cysteine and histidine stability studies

Prior to having the data with TCO-ALN, one potential concern was that the  $^{99m}\text{Tc}$ -tetrazine compounds were degrading in the presence of blood proteins. As a preliminary test, compound **6** was incubated with 2 mM of cysteine in PBS at 37 °C for 1, 3 and 6 hours. This amount exceeds the concentration of cysteine in the blood, which is between 89-107  $\mu\text{M}$ <sup>22</sup>. It was found that there was no interaction between compound **6** and cysteine over 6 hours (Figure 3.12). Similarly, a stability test was run with 100 mM of histidine at 37 °C for 1, 3 and 6 hours. It was found that compound **6** was also stable in the presence of histidine (Figure 3.13).

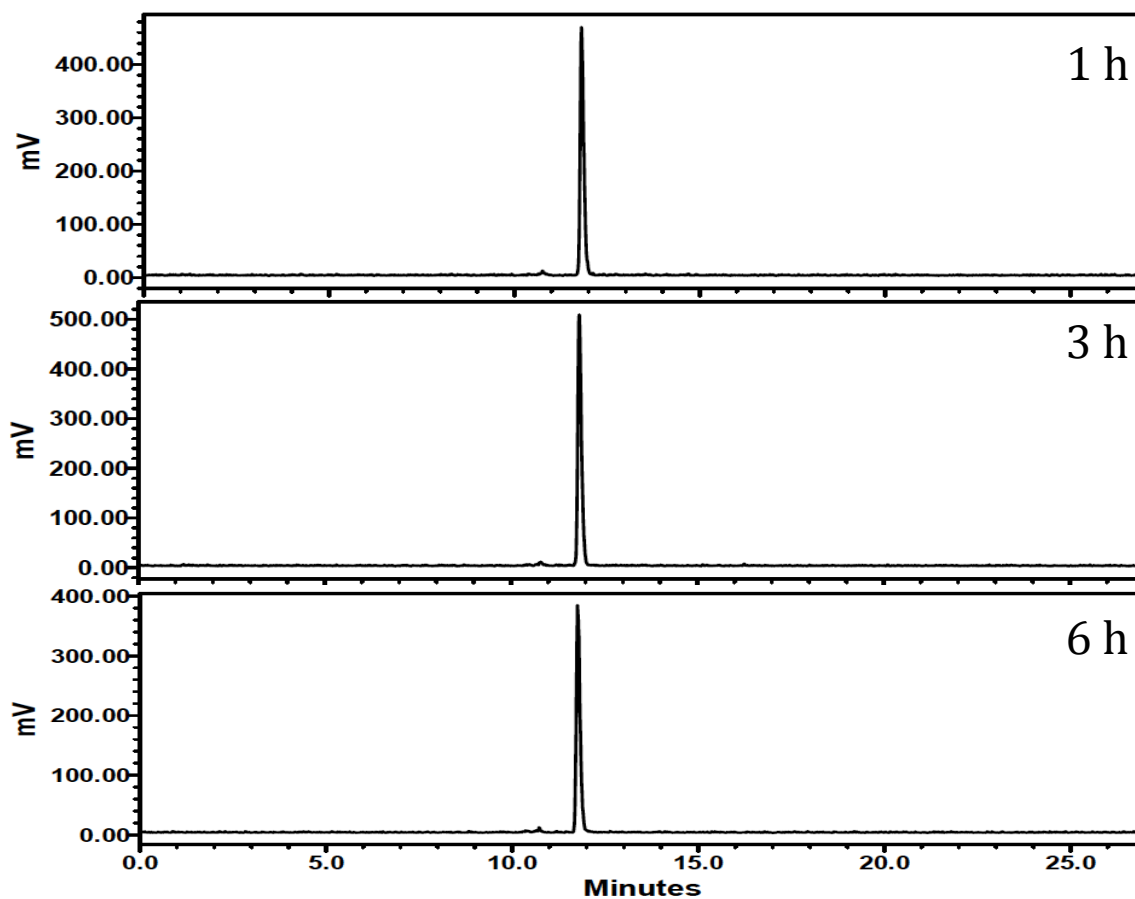


**Figure 3.12** Gamma HPLC traces of **6** upon incubation at 37 °C with 2 mM L-cysteine for 1, 3 and 6 h (Method 1, 1 mL/min).

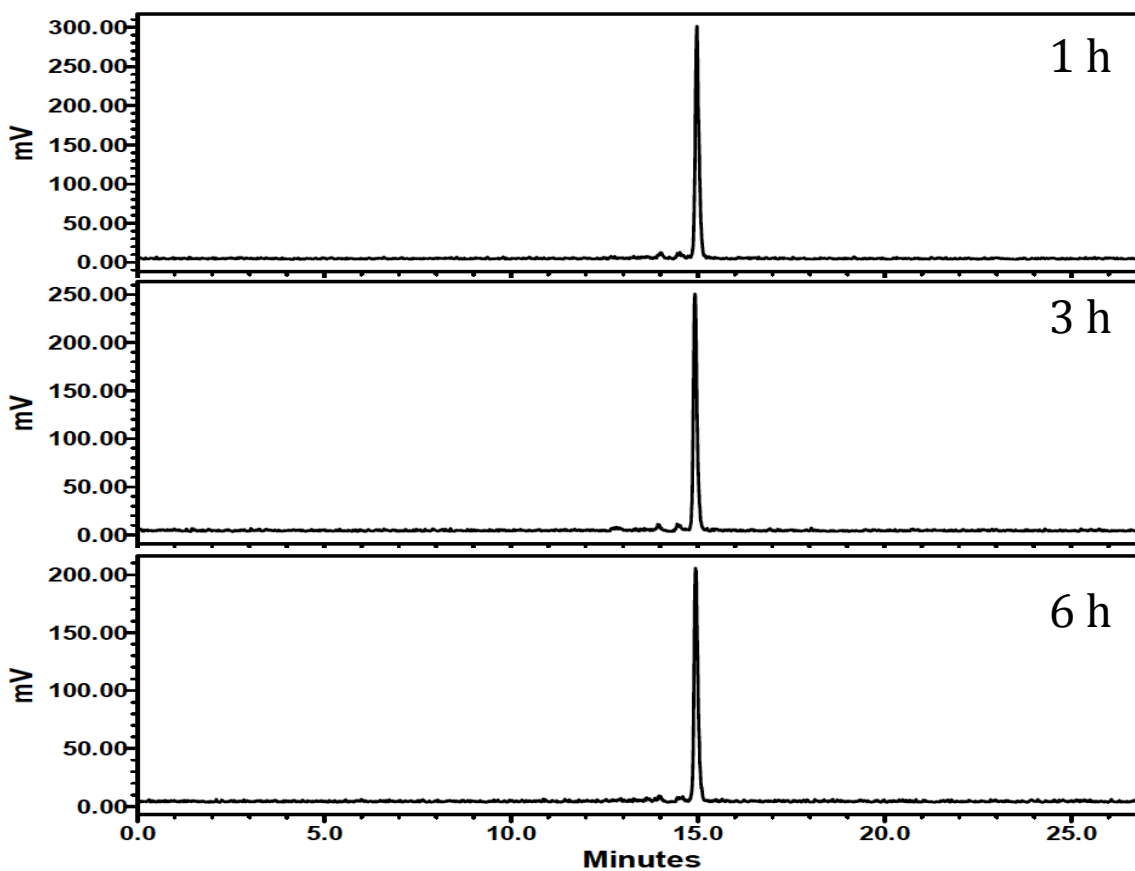


**Figure 3.13** Gamma HPLC traces of **6** upon incubation at 37 °C with 100 mM histidine for 1, 3 and 6 h (Method 1, 1 mL/min).

### 3.3.7 Blood clearance studies

One possible explanation for low tumor uptake was that the  $^{99\text{m}}\text{Tc}$ -tetrazines were clearing from the blood too quickly. If this were the case, the  $^{99\text{m}}\text{Tc}$ -tetrazines would not have sufficient time to react with the tumour-bound TCO-huA33. A second explanation was that the  $^{99\text{m}}\text{Tc}$ -tetrazines were interacting with carrier proteins hindering the reactivity of the tetrazine moiety.

To test these hypotheses, an experiment was conducted where **10** was injected intravenously, and blood draws performed at various time points. Once the blood was drawn, a portion of the blood was used to calculate the concentration of radioactivity reported as the %ID/g. The concentrations in the blood were then plotted as a function of time to determine the blood residence half-life of **10** (Figure 3.15). The remaining blood from the different time points was used to determine the reactivity of the tetrazine (Figure 3.14).

To determine tetrazine reactivity, blood samples were centrifuged to remove erythrocytes, leukocytes and thrombocytes. Radioactivity measurements confirmed that **10** does not interact with any of these blood components. Next, plasma proteins were precipitated by addition of ice-cold acetonitrile, followed by centrifugation. Again, it was determined from radioactivity measurements that **10** did not interact with these proteins. Finally, a portion of the blood plasma containing **10** was incubated with TCO-antiVEGFR2 for 10 minutes at 37 °C. Both the TCO-free plasma fraction and the mixture of plasma and TCO-antiVEGFR2 were spotted on iTLC plates and run with an eluent of 1:1 (H<sub>2</sub>O:ACN) + 0.1% TFA. As a reference standard, **10** in PBS + 0.5% BSA + 0.01% tween 80 was prepared, spotted and run under the same conditions.

The TLC data suggests that **10** is likely still intact in the blood, as it moves the same distance off the baseline as the reference standard (Figure 3.14C). However, the mixture of **10** with TCO-antiVEGFR2 revealed that after circulation for 15 min in the blood, **10** did not react with the TCO-antiVEGFR2 (Figure

3.14D). This suggests that the tetrazine may be decomposing or interacting with something in the blood, preventing the reaction with the TCO-antibody from proceeding. However, it is hard to draw a firm conclusion from this data, as the radioactivity concentrations were extremely low in the blood, resulting in poor iTLC chromatograms with high background signal. The degradation of the tetrazine ligand as a reason for poor tumor localization was ultimately ruled out based on the successful data obtained with TCO-ALN.

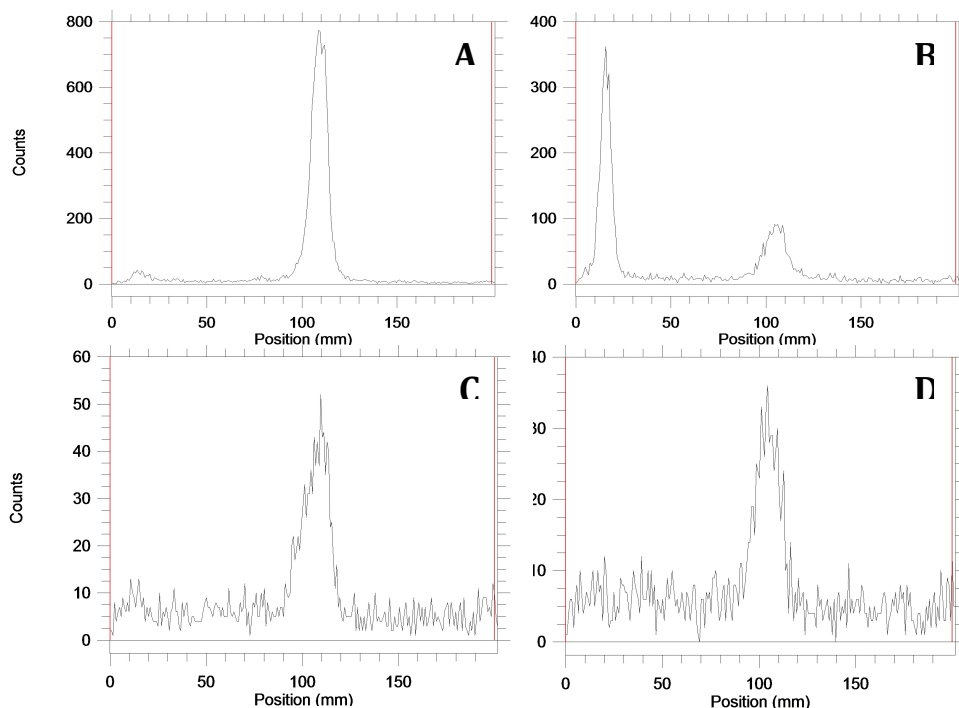


**Figure 3.14** iTLC of **10** in an eluent of 1:1 v/v ( $\text{H}_2\text{O}$ : ACN) + 0.1% TFA. A) Control of **10** in PBS + 0.5% BSA + 0.01% polysorbate-80. B) Control of **10** in PBS + 0.5% BSA + 0.01% polysorbate-80 incubated with excess TCO-antiVEGFR2 for 10 minutes at 37 °C. C) Compound **10** isolated from blood taken at 15 minutes

post-injection. D) The sample from C incubated with excess TCO-antiVEGFR2 for 10 minutes at 37 °C.

After plotting the %ID/g data from the blood draws, it was determined that the blood residence half-life of **10** was between 1.34 and 2.11 minutes (Figure 3.13). This clearance time is extremely fast, far quicker than other radiolabeled tetrazines in literature.<sup>23,24</sup> Such rapid clearance from the blood was likely a key contributor to the low tumour binding seen when using the TCO-huA33 antibody.

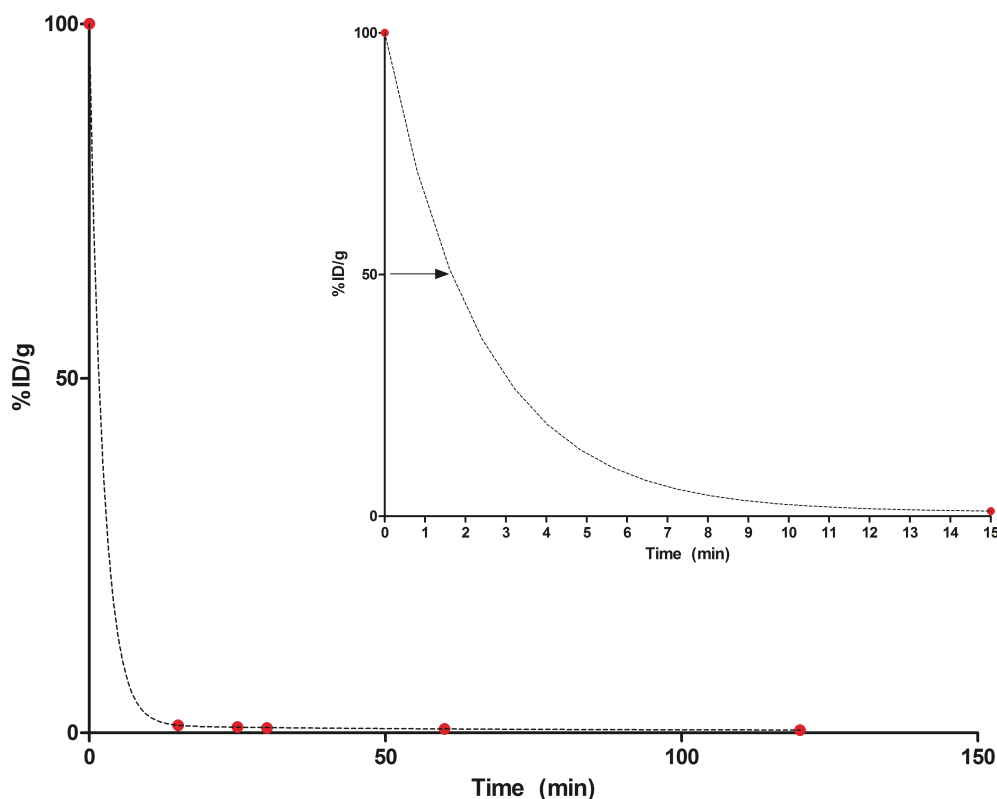




**Figure 3.15** Plot of %ID/g of **10** at 15, 25, 30, 60, and 120 minutes post-injection. The inset shows the time where activity levels in the blood reach 50 %ID/g, indicated by an arrow. Curve fitting according to a two-phase decay performed with GraphPad Prism.

### 3.3.8 Comparing pretargeting with TCO-huA33 antibody and TCO-ALN

In previous studies, *in vivo* pretargeting of **6** and **10** was demonstrated using TCO-ALN. Both compounds showed significant uptake in the knees ( $7.64 \pm 2.72$  and  $10.2 \pm 1.28$  %ID/g, respectively) and shoulder ( $4.77 \pm 1.88$  and  $6.66 \pm 0.96$  %ID/g, respectively), at 1 hour post injection with bone: blood ratios of 4.5 and 10. When considering pretargeting with TCO-ALN, and the successful reactivity of **6** and **10** with TCO-antibodies *in vitro*, the question arises as to why *in vivo* pretargeting with the TCO-huA33 antibody was unsuccessful.

The reasons for the poor tumor localization is likely two-fold. The first factor is the short blood half-life of compound **10**, which was determined to be 1.35 to 2.11 minutes. This clearance is much more rapid than other radiolabeled tetrazines in literature that have demonstrated successful pretargeting with TCO-antibodies.<sup>23,24</sup> This rapid clearance leads to a lower concentration of the tetrazine in the blood, and a slower overall reaction rate. Secondly, since TCO-ALN is a small molecule, a higher amount can be administered ( $75 \mu\text{mol}$ ), resulting in a higher concentration of TCO at the site of interest. Since TCO-huA33 is a protein

(MW = 150 kDa), a much lower amount was injected (0.66 nmol). With the reaction between tetrazine and TCO believed to be second order, the low levels of the two reaction components creates a situation where the kinetics of the coupling reaction are not sufficient to get appreciable concentrations of both reactants at the site of interest.

### 3.5 Conclusion and Future Work

*In vitro* reactivity of **6** and **10** with two different TCO-antibodies were demonstrated. However, *in vivo* translation proved troublesome, with tumour uptake values of approximately 1 %ID/g and tumour: blood ratios <1 observed for both  $^{99m}\text{Tc}$ -tetrazines. Stability studies with cysteine and histidine verified that **6** was not being degraded at physiological concentrations of either compound. Blood clearance studies determined the blood clearance half-life of **10** to be rapid and less than 3 minutes. Since previous *in vivo* pretargeting experiments with TCO-ALN and compound **6** and **10** were successful, the unsuccessful *in vivo* pretargeting with a TCO-huA33 antibody was likely due to a combination of rapid blood clearance of the  $^{99m}\text{Tc}$ -tetrazine, and the low concentration of TCO-antibody injected (0.66 nmol), resulting in both substrates being present in sub-critical concentrations at the tumour site. This is in contrast to the TCO-ALN small molecule, which was administered at a much higher concentration (75  $\mu\text{mol}$ ). Moving forward, two separate approaches were taken to increase the

bioavailability of the  $^{99m}\text{Tc}$ -tetrazines; first through understanding the mechanism behind the rapid blood clearance (Chapter 4), and second through the modification of the tetrazine ligand (Chapter 5).

### 3.6 References

- (1) Kaur, S.; Venktaraman, G.; Jain, M.; Senapati, S.; Garg, P. K.; Batra, S. K. *Cancer Lett.* **2012**, *315* (2), 97–111.
- (2) Dimitrov, D. S.; Marks, J. D. *Therapeutic Antibodies*; 2007; Vol. 4-4.
- (3) Murad, J. P.; Kozłowska, A. K.; Lee, H. J.; Ramamurthy, M.; Chang, W. C.; Yazaki, P.; Colcher, D.; Shively, J.; Cristea, M.; Forman, S. J.; Priceman, S. J. *Front. Immunol.* **2018**, *9*, 1–13.
- (4) Guadagni, F.; Roselli, M.; Cosimelli, M.; Mannella, E.; Tedesco, M.; Cavaliere, F.; Grassi, A.; Abbolito, M. R.; Greiner, J. W.; Schlom, J. *Cancer* **1993**, *72* (7), 2098–2106.
- (5) Pizzi, C.; Sgambato, A.; De Laurentiis, M.; Limite, G.; Panico, L.; Pettinato, G.; Muraro, R.; Tauchmanova, L.; Galiotta, A.; Bianco, A. R.; Mariani-Costantini, R.; Contegiacomo, A. *Oncol. Rep.* **1999**, *6* (6), 1399–1802.
- (6) Rossin, R.; Läppchen, T.; van den Bosch, S. M.; Laforest, R.; Robillard, M. S. *J. Nucl. Med.* **2013**, *54* (11), 1989–1995.
- (7) Zeglis, B. M.; Sevak, K. K.; Reiner, T.; Mohindra, P.; Carlin, S. D.; Zanzonico, P.; Weissleder, R.; Lewis, J. S. *J. Nucl. Med.* **2013**, *54* (8), 1389–1396.
- (8) Sakamoto, J.; Kojima, H.; Kato, J.; Hamashima, H.; Suzuki, H. *Cancer Chemother. Pharmacol.* **2006**, *46*, S27–S32.
- (9) Zeglis, B. M.; Brand, C.; Abdel-Atti, D.; Carnazza, K. E.; Cook, B. E.; Carlin, S.; Reiner, T.; Lewis, J. S. *Mol. Pharm.* **2015**, *12* (10), 3575–3587.
- (10) Meyer, J. P.; Houghton, J. L.; Kozłowski, P.; Abdel-Atti, D.; Reiner, T.; Pillarsetty, N. V. K.; Scholz, W. W.; Zeglis, B. M.; Lewis, J. S. *Bioconjugate Chem.* **2016**, *27* (2), 298–301.

- (11) Keinänen, O.; Fung, K.; Pourat, J.; Jallinoja, V.; Vivier, D.; Pillarsetty, N. V. K.; Airaksinen, A. J.; Lewis, J. S.; Zeglis, B. M.; Sarparanta, M. *EJNMMI Res.* **2017**, 7 (95).
- (12) Viola-Villegas, N. T.; Rice, S. L.; Carlin, S.; Wu, X.; Evans, M. J.; Sevak, K. K.; Drobnjak, M.; Ragupathi, G.; Sawada, R.; Scholz, W. W.; Livingston, P. O.; Lewis, J. S. *J. Nucl. Med.* **2013**, 54 (11), 1876–1882.
- (13) Chan, A.; Prassas, I.; Dimitromanolakis, A.; Brand, R. E.; Serra, S.; Diamandis, E. P.; Blasutig, I. M. *Clin. Cancer Res.* **2014**, 20 (22), 5787–5795.
- (14) Evans, H. L.; Nguyen, Q. D.; Carroll, L. S.; Kaliszczak, M.; Twyman, F. J.; Spivey, A. C.; Aboagye, E. O. *Chem. Commun.* **2014**, 50 (67), 9557–9560.
- (15) García, M. F.; Zhang, X.; Shah, M.; Newton-Northup, J.; Cabral, P.; Cerecetto, H.; Quinn, T. *Bioorg. Med. Chem.* **2016**, 24 (6), 1209–1215.
- (16) Zlitni, A.; Janzen, N.; Foster, S. F.; Valliant, J. F. *Angew. Chemie Int. Ed.* **2014**, 53 (25), 6459–6463.
- (17) Zeglis, B. M.; Sevak, K. K.; Reiner, T.; Mohindra, P.; Carlin, S. D.; Zanzonico, P.; Weissleder, R.; Lewis, J. S. *J. Nucl. Med.* **2013**, 54 (8), 1389–1396.
- (18) Jain, R. K. *Cancer Res.* **1988**, 48 (10), 2641–2658.
- (19) Carrasquillo, J. A.; Pandit-Taskar, N.; O'Donoghue, J. A.; Humm, J. L.; Zanzonico, P.; Smith-Jones, P. M.; Divgi, C. R.; Pryma, D. A.; Ruan, S.; Kemeny, N. E.; Fong, Y.; Wong, D.; Jaggi, J. S.; Scheinberg, D. A.; Gonen, M.; Panageas, K. S.; Ritter, G.; Jungbluth, A. A.; Old, L. J.; Larson, S. M. *J. Nucl. Med.* **2011**, 52 (8), 1173–1180.
- (20) Ackerman, M. E.; Chalouni, C.; Schmidt, M. M.; Raman, V. V.; Ritter, G.; Old, L. J.; Mellman, I.; Wittrup, K. D. *Cancer Immunol. Immunother.* **2008**, 57 (7), 1017–1027.
- (21) Altai, M.; Perols, A.; Tsourma, M.; Mitran, B.; Honarvar, H.; Robillard, M.; Rossin, R.; ten Hoeve, W.; Lubberink, M.; Orlova, A.; Eriksson Karlstrom, A.; Tolmachev, V. *J. Nucl. Med.* **2016**, 57 (3), 431–436.
- (22) Brigham, B. M. P.; Stein, W. H.; Moore, S. *J. Clin. Invest.* **1960**, 39 (11), 1633–1638.

- (23) Altai, M.; Perols, A.; Tsourma, M.; Mitran, B.; Honarvar, H.; Robillard, M.; Rossin, R.; ten Hoeve, W.; Lubberink, M.; Orlova, A.; Eriksson Karlstrom, A.; Tolmachev, V. *J. Nucl. Med.* **2015**.
- (24) Zeglis, B. M.; Brand, C.; Abdel-Atti, D.; Carnazza, K. E.; Cook, B. E.; Carlin, S.; Reiner, T.; Lewis, J. S. *Mol. Pharm.* **2015**, *12* (10), 3575–3587.

## **Chapter 4: Towards the optimization of the pharmacokinetics of $^{99m}\text{Tc(I)}$ labeled tetrazines.**

### **Investigation of the mechanism of clearance**

#### **4.1 Introduction**

When developing a diagnostic or therapeutic radiopharmaceutical, optimizing pharmacokinetics and pharmacodynamics is crucial to minimize off-target uptake and obtain high target to non-target ratios. The traditional approach used to optimize the biodistribution of targeted imaging probes derived from radiometals typically has involved extensive synthetic modification of the chelate and linker. Changes in donor groups and linkers is often employed as a means of reducing off-target uptake and increasing target to non-target ratios.<sup>1-7</sup> An alternative strategy, which has been used less frequently, is to study the specific clearance pathway and use the information to guide compound optimization.

With radiopharmaceuticals and pharmaceuticals alike, exogenous compounds are excreted through several different clearance pathways. Drug excretion occurs primarily through the kidneys, where other routes of clearance can include the liver and bile, saliva, lungs, and breast milk.<sup>8</sup> Within these clearance pathways, there are many different cellular transporters located in organs and tissues that are responsible for the export of drugs from the body.<sup>8,9</sup>

For the tetrazine-derived chelates described in chapter 2, the rapid decrease in blood concentration and significant uptake into the gallbladder warranted investigation into the mechanism(s) of clearance. If it were possible to identify the transporters responsible for the observed clearance, it may become possible to prepare a  $^{99m}\text{Tc}$ -tetrazine derivative with superior pharmacokinetics.

The high gallbladder uptake observed with **14** was believed to be associated with the excretion into the bile, which is preceded by clearance through the liver. Bile is formed in the liver, in the canaliculus between hepatocytes. The bile then drains to the bile ductules, and is then collected in the common hepatic bile duct. From here, the bile is then stored in the gall bladder, and is excreted after a meal to aid in the intestinal digestions of lipids and vitamins.<sup>10–13</sup>

Along with aiding in digestion, bile is also used to clear xenobiotics from the body such as steroids, antibiotics, and lipid lowering medications. In regards to xenobiotic excretion into bile, there are several transporters within liver hepatocytes that are responsible for driving clearance (Figure 4.1 and 4.2), such as organic anion transporting polypeptides (OATP), organic cation transporters (OCT), organic anion transporters (OAT), multidrug resistance-associated proteins (MRP), breast cancer resistance proteins (BCRP), and p-glycoproteins (P-gp).<sup>14</sup> Of these transporters, several are known to transport a wide variety of neutral, cationic, and anionic compounds with varying lipophilicities and molecular

weights, such as Atorvastatin (Lipitor),<sup>15</sup> Cimetidine (Tagamet),<sup>14</sup> and Cidofovir (Vistide).<sup>8</sup>

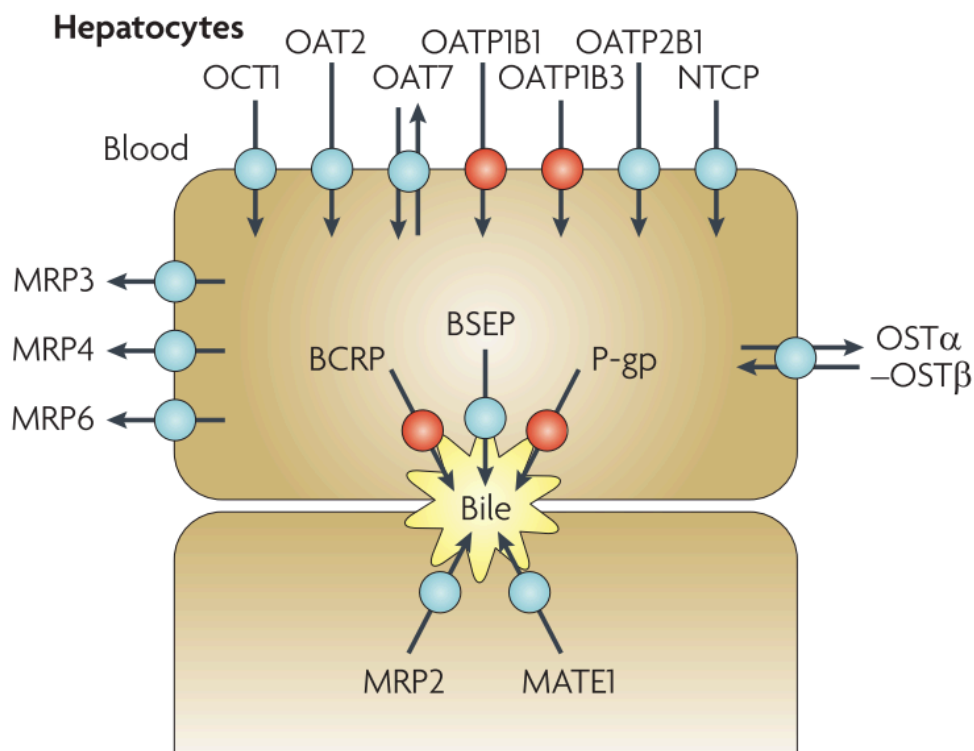


**Figure 4.1** Human hepatocyte transporters. Transporters on the sinusoidal membrane include sodium/ taurocholate co-transporting peptide (NTCP); three members of the OATP family (OATP1B1, OATP1B3 and OATP2B1); two members of the organic anion transporter family (OAT2 and OAT7); and OCT1. Efflux pumps in the hepatocyte basolateral membrane include MRP3, MRP4 and MRP6. Apical efflux pumps of the hepatocyte comprise P-gp; bile-salt export pump (BSEP); BCRP and MRP2. In addition, multidrug and toxin extrusion protein 1 (MATE1) is located in the apical hepatocyte membrane.<sup>14</sup> Reprinted with



permission from Nature: Giacomini, K. M. *et al.* Nat. Rev. Drug Discov. 2010, 9, 215–236. Copyright 2010.

Compounds excreted through the hepatobiliary pathway can either act as a substrate or inhibitor of transporters within hepatocytes. It has been shown that many approved pharmaceuticals are inhibitors of such transporters.<sup>14,16,17</sup> The inhibition of transporters within hepatocytes can elicit changes in the clearance of a drug, and thus change drug efficacy.<sup>18</sup> Recently, this approach has been exploited to increase the efficacy of certain chemotherapeutic drugs, by increasing drug bioavailability and making them more permeable to cancer cells.<sup>19</sup>

In addition to studying clearance pathways, it is also of great interest to investigate the effect of other key pathways in the liver, and their effect on the clearance of xenobiotics. Of particular interest was the mevalonate pathway, which provides cells with essential biomolecules such as cholesterol, lipoproteins, and steroid hormones (Figure 4.2).<sup>20,21</sup> The mevalonate pathway also plays a crucial role in the production of bile, which as mentioned previously, is one of the major routes of clearance for xenobiotics and potentially compounds **6**, **10** and **14** (see chapter 2 for structures).

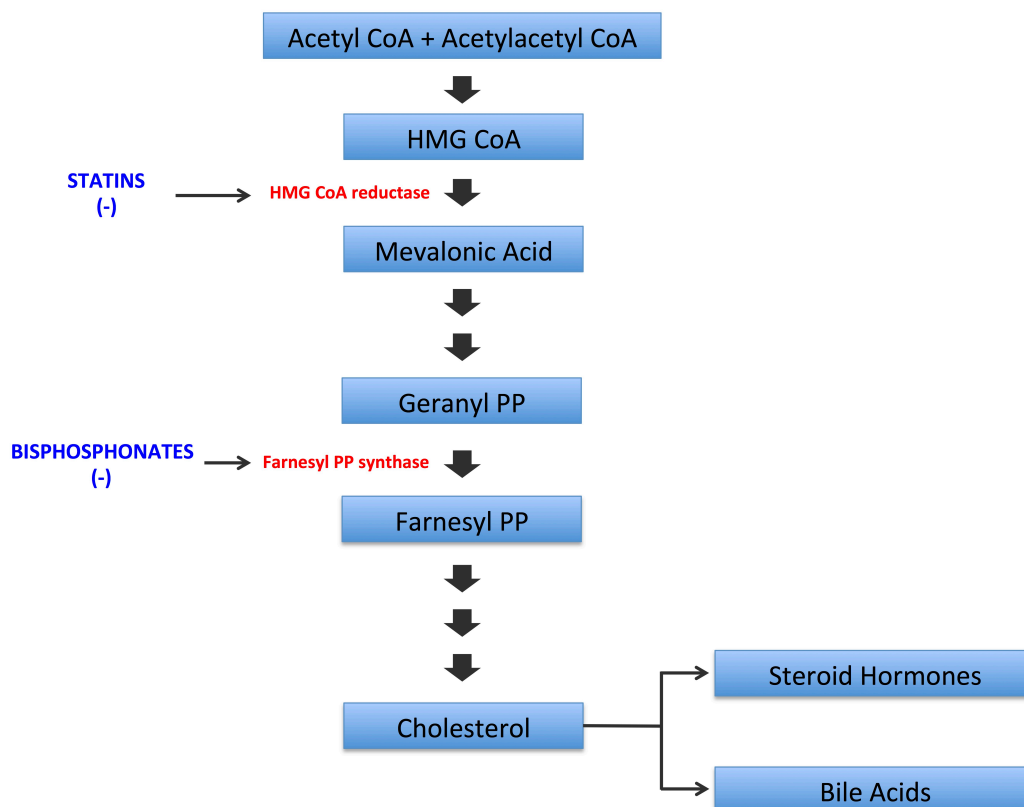


**Figure 4.2** Inhibition of Mevalonate pathway by Bisphosphonates and Statins.

Similar to transport proteins, there are several clinically approved drugs that are known inhibitors of the mevalonate pathway. Statins are a class of drugs commonly prescribed to reduce blood cholesterol levels. Statins work by inhibiting HMG CoA reductase, preventing the production of mevalonic acid and subsequently the production of cholesterol (Figure 4.2).<sup>21</sup> Another well known class of inhibitors for the mevalonate pathway are nitrogen-containing bisphosphonates.<sup>20,22–24</sup> Bisphosphonates are commonly used to treat bone diseases, as they are potent inhibitors of osteoclasts that are involved in bone

absorption.<sup>21,24</sup> It is noteworthy that nitrogen-containing bisphosphonates are also inhibitors of farnesylpyrophosphate synthase in the mevalonate pathway, preventing the formation of farnesylpyrophosphate, and other downstream products of the such as cholesterol and bile acids.<sup>20,21</sup>

With the ability to inhibit several key hepatobiliary transporters and complementary pathways with clinically approved drugs, it was of interest to study these pathways to better understand the clearance of the <sup>99m</sup>Tc-tetrazines developed in chapter 2. The knowledge obtained from these studies can be used to rationally engineer modifications to the chelate, thus improving pharmacokinetics. Herein we describe the effect of several different hepatobiliary transport inhibitors on the distribution of compound **14**. This particular <sup>99m</sup>Tc-tetrazine was selected due to its improved clearance profile from non-target tissues compared to compounds **6** and **10**. Additionally, the high target to non-target ratios when used in pretargeting studies with TCO-ALN makes compound **14** a promising starting point for the development of an optimized <sup>99m</sup>Tc-tetrazine (Figure 4.3).

## **4.2 Materials and Methods**

### **4.2.1 General materials and instruments**

Alendronate, Zoledronate, Indomethacin, Indocyanine green, and Taurine were purchased from Sigma Aldrich. Elacridar, Cyclosporin A, and Pantoprazole

Ph.D. Thesis – H. Bilton; McMaster University – Chemistry and Chemical Biology

were purchased from Cayman Chemical. Rifampicin and Montelukast were provided by the Central Animal Facility (CAF) at McMaster University. FITC-tagged P-glycoprotein mouse anti-human antibody (clone 17F9) was purchased from BD Biosciences. All cell media was purchased from ThermoFisher scientific. Sodium pertechnetate was provided by Mallinckrodt Pharmaceuticals from an Ultra-Technekow generator.  $^{99m}\text{Tc}$ -Sestamibi was provided by Isologic Innovative Radiopharmaceuticals.

High performance liquid chromatography (HPLC) of radioactive compounds were performed on a Waters 1525 Binary (Midford, MA, USA) monitored simultaneously with 2998 photodiode array detector at 220/254 nm and in line radioactivity Bioscan gamma detector with NaI (T1) scintillator using the Empower software package. Analytical HPLC of all other compounds were performed on a Varian Prostar 230 monitored simultaneously with a Prostar 335 PDA detector. HPLC method: Phenomenex C-18 analytical column (250 mm  $\times$  4.6 mm  $\times$  5  $\mu\text{m}$ ) operating at a flow rate of 1.0 mL/min (analytical) was used. The following solvent gradient was employed: (solvent A =  $\text{H}_2\text{O}$  + 0.1% TFA, solvent B = ACN + 0.1% TFA): 0-2 min 20% B, 2-19 min 20-80% B, 19-21 min 100% B, 21-22 min 20% B. Statistical analysis was performed using an unpaired Students t-test.

#### 4.2.2 Cells and culture protocols

Caco-2 cells were purchased from ATCC (Manassas, Virginia). Caco-2 cells were cultured in Eagle's Minimal Essential Medium supplemented with 20% FBS, 1% penicillin-streptomycin and 1% L-glutamine. MCF7 cells were purchased from ATCC (Manassas, Virginia). MCF7 cells were cultured in Dulbecco's Modified Eagle Medium supplemented with 10% FBS and 1% penicillin-streptomycin. Cell lines were grown at 37 °C with 5% CO<sub>2</sub>. For all cell studies, both cell lines were used between passages 20-28.

#### 4.2.3 Cell assay protocols

All cell assays were performed following a modified literature procedure.<sup>25</sup> Cells were plated ( $1.55 \times 10^5$  cells/well for MCF7,  $0.4 \times 10^5$  cells/well for Caco-2) and incubated at 37 °C with 5% CO<sub>2</sub> for 3 days to reach confluency. Cells were then pre-incubated with Pantoprazole, Elacridar, or Cyclosporin A (10  $\mu$ M in media stocks) for 1 hour. Cells were then incubated with 15  $\mu$ L (use repeater pipette) of <sup>99m</sup>Tc-Sestamibi or compound **14** (555 kBq/mL in PBS). Activity uptake was terminated at 60 minutes by washing three times with ice cold PBS + 0.5% BSA and subsequently lysing with RIPA lysis buffer (50 mM Tris, 150 mM NaCl, 0.5% DOC, 1% NP-40, 0.1% SDS, pH 8.0) (300  $\mu$ L/well). Cell media and lysates were collected and counted along with <sup>99m</sup>Tc-Sestamibi and **14** standards of known activity using a gamma counter. Relative cellular accumulation of the <sup>99m</sup>Tc compounds was determined for each well of confluent cells (cpm cells  $\times$  100/cpm

medium). Results were normalized to protein content as determined in the cell lysates using a BCA Assay kit (Thermo Fisher Scientific).

#### **4.2.4 Flow cytometry assay protocol**

The flow cytometry assay was performed as a modified literature procedure.<sup>26</sup> Caco-2 and MCF7 cells were trypsinized and diluted to a concentration of  $1 \times 10^6$  cells/mL. Cells were then centrifuged to remove media, and washed 3 times with PBS + 0.5% BSA. After the final wash, cells were suspended in PBS + 0.5% BSA at a concentration of  $1 \times 10^6$  cells/mL. Cells were then incubated with 10  $\mu$ L of 7AAD, fluorescein isothiocyanate (FITC)-tagged P-glycoprotein mouse anti-human antibody (FITC-Ab) (20  $\mu$ L), both, or neither for 40 minutes on ice in the dark. After staining, cells were washed 3-5 times with ice cold PBS + 0.5 BSA. Cells were then re-suspended in flow buffer and loaded in to flow cytometry tubes. Fluorescence was detected using a FACS calibur flow cytometer equipped with an ultraviolet argon laser (excitation at 466 nm, emission at 535 nm band-pass filters).

#### **4.2.5 Fluorescence cell imaging**

Caco-2 cells were plated at  $0.6 \times 10^5$  cells/well and incubated for 3 days. MCF7 cells were plated at  $1.55 \times 10^5$  cells/well and incubated for 3 days. Media was aspirated from wells, and cells were washed 3 times with ice cold 1 mL of PBS + 0.5% BSA, Wells were then incubated with 500  $\mu$ L of a solution of buffer and FITC-Ab (980  $\mu$ L of PBS + 0.5% BSA and 20  $\mu$ L of FITC-Ab) for 40 minutes

on ice in the dark. Control wells were incubated with 500  $\mu$ L of PBS + 0.5% BSA with no FITC-Ab. Staining buffer was then aspirated from cells and washed 3 times with 1 mL of ice cold PBS + 0.5% BSA. 300  $\mu$ L of ice cold PBS + 0.5% BSA was then added to each well and bright field and fluorescent images taken using an Olympus inverted bright field & fluorescent microscope (Model BX53F) equipped with a FITC filter.

#### **4.2.6 Animal models and biodistribution studies**

Animal studies were approved by the Animal Research Ethics Board at McMaster University in accordance with Canadian Council on Animal Care (CCAC) guidelines. Biodistribution studies were performed using female BALB/c mice (Charles River Laboratories, Kingston, NY) at the indicated time points. The mice were administered the agents via tail vein injection. For all inhibitors that were selected, the dosage of each compound was determined by literature LD<sub>50</sub> values, and in combination with the animal ethics board guidelines at McMaster. In pathway inhibition studies, **14** was added to a solution of alendronate (20 mg/kg), zoledronate (9 mg/kg), rifampin (20 mg/kg), indocyanine green (20 mg/kg), indomethacin (1 mg/kg), Montelukast (25 mg/kg) or taurine (20 mg/kg) in PBS + 0.5% BSA + 0.01% polysorbate 80 to a concentration of 7.4 MBq/mL. For inhibition studies involving Elacridar, Elacridar was dissolved to a concentration of 62.4 mg/kg in PBS + 5% polysorbate 80 + 10% DMSO, and given orally by gavage 2 hours prior to injection of **14**. For solutions containing Montelukast,

indomethacin, indocyanine green, and rifampin, 10% ethanol was also added to aid in solubility.

### **4.3 Results and Discussion**

#### **4.3.1 Evaluation of nitrogen containing bisphosphonates as mevalonate pathway inhibitors**

Compound **14** (Figure 4.3) was selected as the lead compound due to its superior clearance profile versus the first generation  $^{99m}\text{Tc}$ -tetrazines described in chapter 2, and its successful pretargeting with TCO-ALN. Initially the effect of alendronate on the distribution of compound **14** was investigated after a 75% reduction in gallbladder uptake was observed in pretargeting studies with compound **14** and TCO-ALN containing an excess of ALN. To investigate this reduced gallbladder uptake, biodistribution studies were performed, where alendronate was combined with **14** in PBS + 0.5% BSA + 0.01% polysorbate 80 at a concentration of 20.0 mg/kg (300  $\mu\text{g}$ /mouse). This concentration was selected based on half of the intravenous  $\text{LD}_{50}$  for alendronate (40 mg/kg for female mice), and discussions with the McMaster Central Animal Facility (CAF) regarding acceptable dosing levels.<sup>27</sup> At 6 hours post-injection, animals were sacrificed, organs and tissues were excised, and activity measured using a gamma counter. The percent injected dose was normalized by the weight of each organ or tissue to obtain a value of percent injected dose per gram (%ID/g).



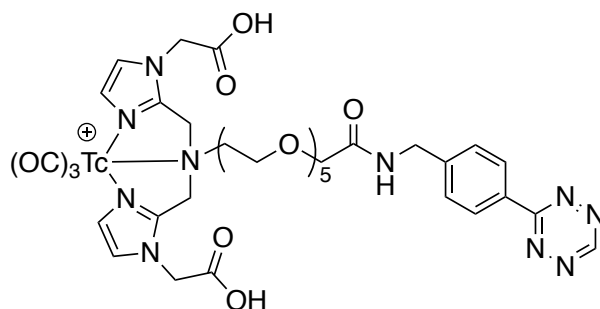


**Figure 4.3** Structure of compound **14**.

The uptake of **14** in the presence of alendronate was compared to previous studies of compound **14** alone (Figure 4.4). The data indicated there was no significant difference in the uptake in most organs when **14** was co-administered with ALN (liver:  $1.68 \pm 1.30$  and  $1.29 \pm 0.14$  %ID/g, large intestine:  $98.9 \pm 106$  and  $77.1 \pm 5.68$  %ID/g, small intestine:  $4.25 \pm 2.97$  and  $1.55 \pm 0.53$  %ID/g, blood:  $3.20 \pm 1.45$  and  $0.76 \pm 0.02$  %ID/g). There was however, a significant decrease in gall bladder uptake; with the %ID/g being reduced approximately six-fold ( $216 \pm 75.9$  to  $33.6 \pm 3.93$  %ID/g).

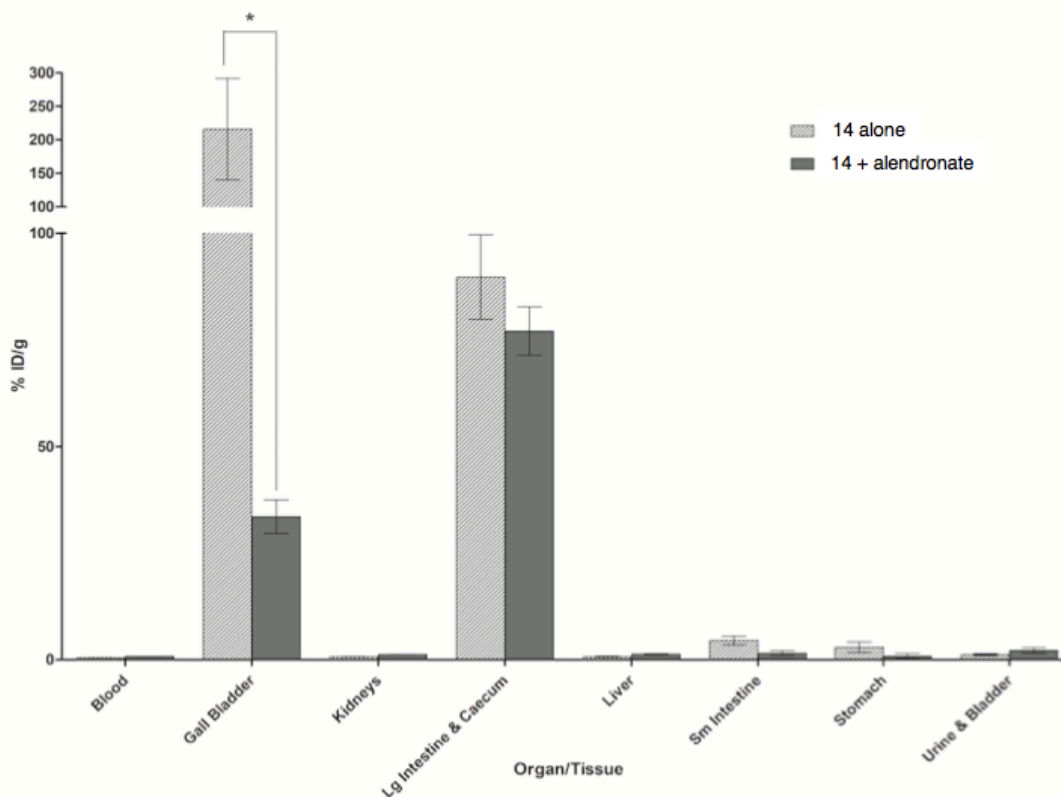


**Figure 4.4** Biodistribution of compound **14** alone (light grey) and **14** with alendronate (dark grey) (300  $\mu$ g). BALB/c mice (n=3 per compound) were injected with approximately 740 kBq of **14** and sacrificed 6 hours post injection. Data is expressed as the mean injected dose per gram (%ID/g)  $\pm$  SEM. Organs and tissues with uptake less than 1 %ID/g are not presented. \*p < 0.05.

An additional pretargeting study was performed with TCO-ALN plus ALN (226  $\mu$ g TCO-ALN, 74.0  $\mu$ g ALN/mouse). The purpose of this study was to determine if excess alendronate would have an effect on the targeting ability of TCO-ALN and to see if the observed reduction in the first study was associated

Ph.D. Thesis – H. Bilton; McMaster University – Chemistry and Chemical Biology

with biological variability. The study was performed by administering TCO-ALN (220  $\mu\text{g}/\text{mouse}$ ) with ALN (74  $\mu\text{g}/\text{mouse}$ ) in 0.9% saline via the tail vein. One hour following the TCO-ALN injection, compound **14** was administered. At 6 hours post injection of **14**, animals were sacrificed, organs and tissues were excised, and activity measured using a gamma counter.

Comparing the two pretargeting studies (Figure 4.5), using an unpaired students t-test, there was no significant change in radiotracer uptake in the knee with pure TCO-ALN or TCO-ALN with excess alendronate ( $20.1 \pm 4.91$  and  $14.9 \pm 2.43$  %ID/g respectively). Similarly, little difference was seen in other organs such as the blood, kidneys, liver, intestines, stomach and thyroid/trachea. The most notable difference in tracer uptake between these experiments was seen in the gall bladder. As seen in previous studies (Figure 4.5), a roughly six-fold decrease in gall bladder uptake was seen in the presence of excess alendronate experiment ( $91.5 \pm 17.1$  to  $28.8 \pm 2.63$  %ID/g).

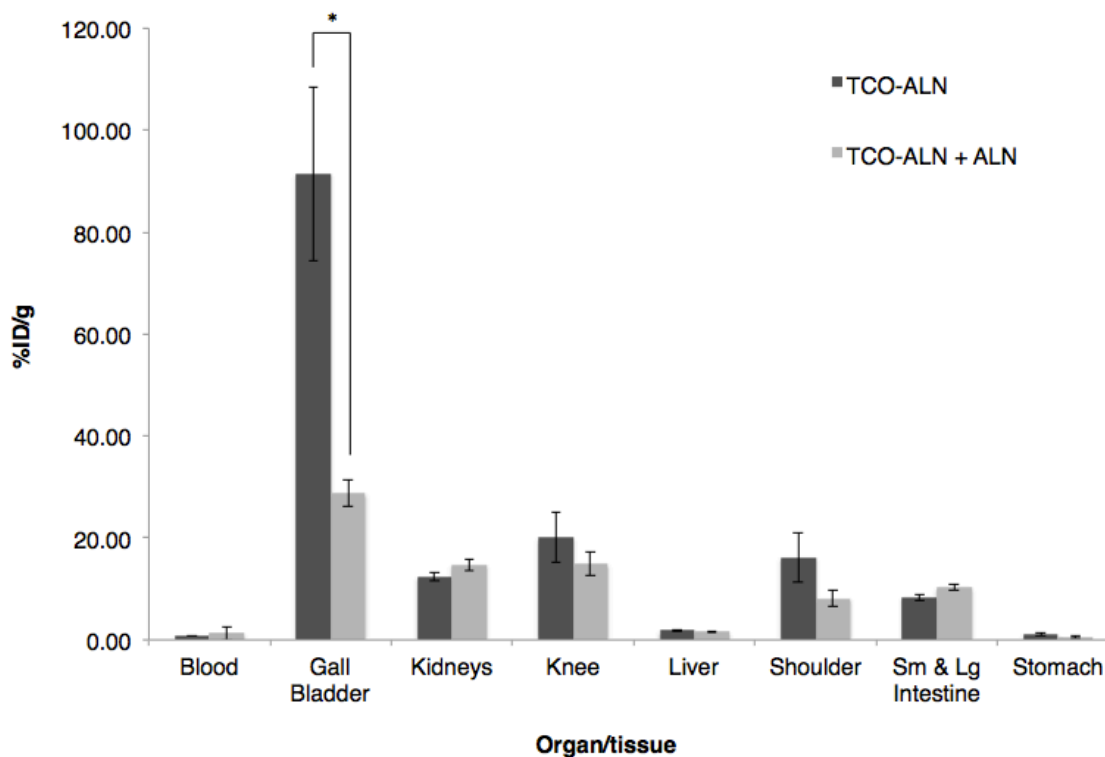


**Figure 4.5** Biodistribution data from pretargeting studies with compound **14** and TCO-ALN, or compound **14** and TCO-ALN + ALN. Compound **14** was administered (approximately 740 kBq) to BALB/c mice (n=3 per compound) 1 hour post injection of TCO-ALN. Mice were sacrificed 6 hours post injection of **14**. Data is expressed as the mean injected dose per gram (%ID/g)  $\pm$  SEM. Organs and tissues with uptake less than 1 %ID/g are not presented. \*p < 0.05.

As noted previously, alendronate and other nitrogen containing bisphosphonates inhibit the enzyme farnesylpyrophosphate synthase; an enzyme in the mevalonate pathway responsible for the synthesis of cholesterol and bile acids in the liver.<sup>20–22</sup> It was hypothesized that the inhibition of cholesterol and bile

acid formation could potentially be responsible for the reduced gall bladder activity. It is this reduction in gall bladder activity that may have caused a reduction in the uptake of compound **14**.

Since the results with alendronate were promising, it was hypothesized that a more potent nitrogen-containing bisphosphonate could further reduce gall bladder uptake. Zoledronate, an imidazole containing bisphosphonate (Figure 4.12C), is a known inhibitor of farnesyl pyrophosphate synthase in the mevalonate pathway similar to alendronate. However, zoledronate is a more potent inhibitor ( $IC_{50} = 4.1 \pm 0.22$  versus  $260 \pm 19.6$  nm).<sup>24</sup> The hypothesis is that by using a more potent inhibitor, a further reduction in gall bladder uptake of **14** could be achieved. This was tested by formulating **14** with zoledronate (135  $\mu$ g/mouse, 9 mg/kg) in PBS + 0.5% BSA + 0.01% polysorbate 80. Six hours following the injection of **14** with zoledronate, the animals were sacrificed and tissues collected and counted. Comparing the distribution of **14** with zoledronate and **14** alone, it appeared that there was no significant change in gall bladder uptake (Figure 4.6). Surprisingly, it appeared that alendronate had a much greater impact on reducing gall bladder uptake than zoledronate ( $33.6 \pm 3.93$  and  $241 \pm 15.7$  %ID/g, respectively). These results suggest that perhaps alendronate is acting through a different mechanism, or the bioavailability of zoledronate is significantly lower than alendronate.<sup>28,29</sup>

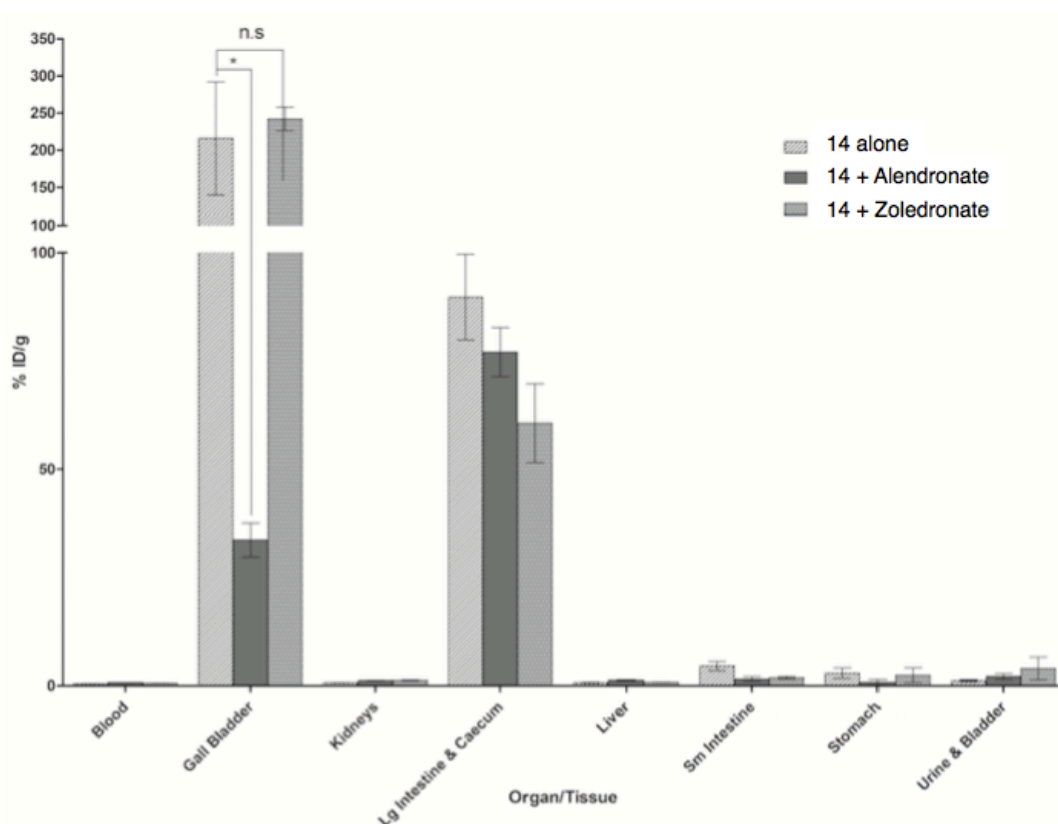


**Figure 4.6** Biodistribution of compound **14** alone, **14** with alendronate (300  $\mu$ g), and **14** with zoledronate (135  $\mu$ g). BALB/c mice were administered approximately 740 kBq of **14** and sacrificed 6 hours post injection. Data is expressed as the mean injected dose per gram (%ID/g)  $\pm$  SEM. Organs and tissues with uptake less than 1 %ID/g are not presented. \*p < 0.05.

#### 4.3.2 Biodistribution studies in the presence of taurine

Taurine (Figure 4.12B) is an amino acid derivative that can be found in tissues such as the heart, retina, liver and brain.<sup>30–32</sup> Taurine is a major component of bile, and plays a key role in many biological processes such as

conjugation of bile acids, osmoregulation, membrane stabilization, cardiovascular function, and function of skeletal muscle.<sup>31,32</sup>

The role of taurine in bile acid metabolism was of significant interest to this work, as it could potentially reduce radiotracer uptake. It is known that bile acids are conjugated with either taurine or glycine by Coenzyme A synthase and bile acid aminotransferase within the liver, for secretion of bile acids into bile.<sup>12,30,31,33</sup> With over 25 % of bile acids being conjugated to taurine within humans (95% in murine bile),<sup>12,33</sup> it was hypothesized that co-administration of taurine with **14** could reduce uptake in the gallbladder.

Similar to the biodistribution studies with alendronate, compound **14** was co-formulated with taurine (300  $\mu$ g/mouse, 20 mg/kg) in a solution of PBS + 0.5% BSA + 0.01% polysorbate 80. A biodistribution study of **14** + taurine at 6 hours post-injection was performed and compared to the previous studies of compound **14** with alendronate, and **14** alone (Figure 4.7). Comparing the biodistribution results at 6 hours post injection of **14** + taurine and **14** alone, it appears that taurine did not significantly decrease the amount of compound **14** within the gallbladder ( $100 \pm 53.0$  and  $216 \pm 75.9$  %ID/g, respectively). There was very little difference in the uptake in other organs such as the large intestine ( $73.7 \pm 4.89$  and  $98.9 \pm 106$  %ID/g), kidneys ( $0.73 \pm 0.03$  and  $1.38 \pm 1.32$  %ID/g), and stomach ( $17.2 \pm 7.89$  and  $21.0 \pm 13.7$  %ID/g, respectively).

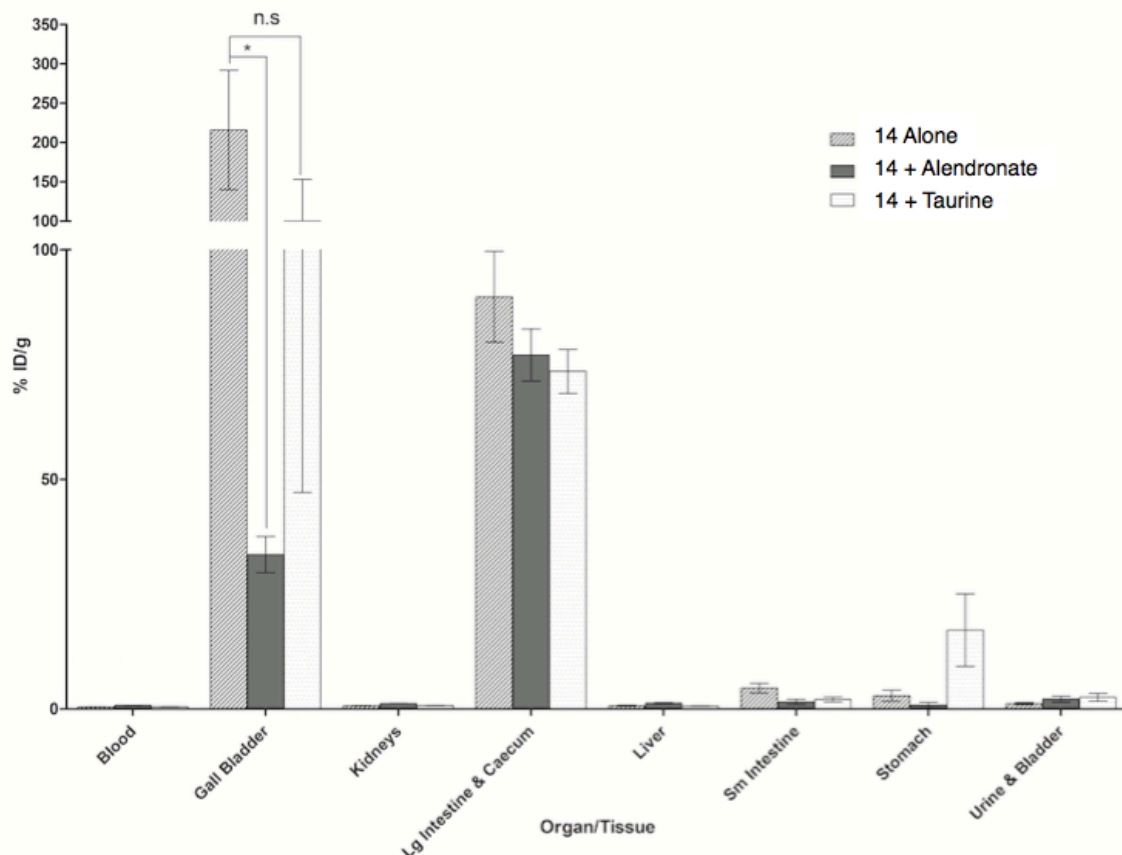


**Figure 4.7** Biodistribution of compound **14** alone, **14** with alendronate (300  $\mu$ g), and **14** with taurine (300  $\mu$ g). BALB/c mice were administered approximately 740 kBq of **14** and sacrificed 6 hours post injection. Data is expressed as the mean injected dose per gram (%ID/g)  $\pm$  SEM. Organs and tissues with uptake less than 1 %ID/g are not presented. \* $p < 0.05$ .



#### **4.3.3 *In vitro* and *in vivo* evaluation of P-glycoprotein/Multi-drug resistance protein inhibitors**

With success only being seen using alendronate thus far, the next step was to explore other key hepatic transporters and mechanisms of drug clearance. P-glycoprotein/Multi-drug resistance gene (P-gp/MDR) is a class of transporters that belongs to the ATP binding cassette family of transporters that is responsible for the export of compounds into the bile. P-gp/MDR is expressed in several organs such as the intestines, liver, kidneys, and the blood-brain barrier.<sup>34–36</sup> Specifically, P-gp/MDR is expressed on the apical membrane of hepatocytes. It is known that the inhibition or induction of P-gp/MDR can lead to changes in pharmacokinetic profile and efficacy of certain drugs. Unlike other transporters, P-gp/MDR has a wide variety of substrates such as organic cations, carbohydrates, amino acids and antibiotics.<sup>36</sup> Furthermore, P-gp/MDR is considered one of the most important transmembrane transporters in the human body, as it has an effect on the absorption and excretion of a wide-variety of drugs.<sup>36</sup>

The inhibition of P-gp/MDR has been studied as a method of reversing drug resistance in cancer cells. For this reason, many P-gp/MDR inhibitors are known as chemosensitizers, as they are able to increase the efficacy of chemotherapeutics when co-administered.<sup>35,37</sup> Similar to the wide range of substrates for P-gp/MDR, there are also hundreds of inhibitors of this transporter with varying potencies.<sup>35,36</sup> Many of these inhibitors have structural similarities,

such as aromatic rings, tertiary or secondary amino groups, and high lipophilicities.<sup>35</sup>

Several compounds were tested clinically for the inhibition of P-gp/MDR, such as the calcium channel blocker verapamil, antimalarial drugs quinine and quinidine, and the immunosuppressive agent Cyclosporin A. However, the high doses required to reach adequate inhibition *in vivo* resulted in toxicity.<sup>38</sup> Improving on previous results, a new generation of inhibitors are being tested. These include the antineoplastic drug Zosuquidar, the verapamil derivative Laniquidar, the chemotherapy drug mitotane, and the drug Biricodar which is being used to treat ovarian cancer.<sup>39</sup> These inhibitors have higher potencies than previous compounds, and greater specificity for the P-gp/MDR transporter.<sup>39</sup>

To evaluate if the <sup>99m</sup>Tc-tetrazine **14** is transported by P-gp/MDR, assays using human epithelial colorectal adenocarcinoma (Caco-2) cells, which are known to express P-gp, were conducted. Following an established procedure,<sup>25</sup> a cell inhibition assay was performed where P-gp positive cells (Caco-2) and P-gp negative cells (MCF7) were pre-incubated with several known P-gp inhibitors at a concentration of 10  $\mu$ M (Cyclosporin A, Pantoprazole, and Elacridar). As a negative control, wells containing P-gp positive or negative cells were incubated with only PBS. After a one hour of incubation, either <sup>99m</sup>Tc-Sestamibi (a known P-gp substrate) or compound **14** was added to the cells (15  $\mu$ L of a 15  $\mu$ Ci/mL solution in PBS). Activity uptake was terminated at 1 hour and the cells washed and then lysed. Cell media and lysates were collected and counted along with

standards of  $^{99m}\text{Tc}$ -Sestamibi and compound **14**. The counts were then normalized by protein concentration using a BCA assay.

Higher cellular binding/internalization was seen in both cell lines with  $^{99m}\text{Tc}$ -Sestamibi compared to studies with compound **14** (Figure 4.8). It also appeared that the presence of the P-gp inhibitors did not significantly increase cell permeability for the positive control as expected. Unfortunately, the same trend was observed with compound **14** in both cell lines (Figure 4.9). Comparing these results to that of an established flow cytometry assay, low P-gp expression in the Caco-2 cells are likely the source of the issue (data not shown). It has been reported that P-gp expression levels on Caco-2 cells can be highly variable depending on culturing times and conditions.<sup>40</sup>

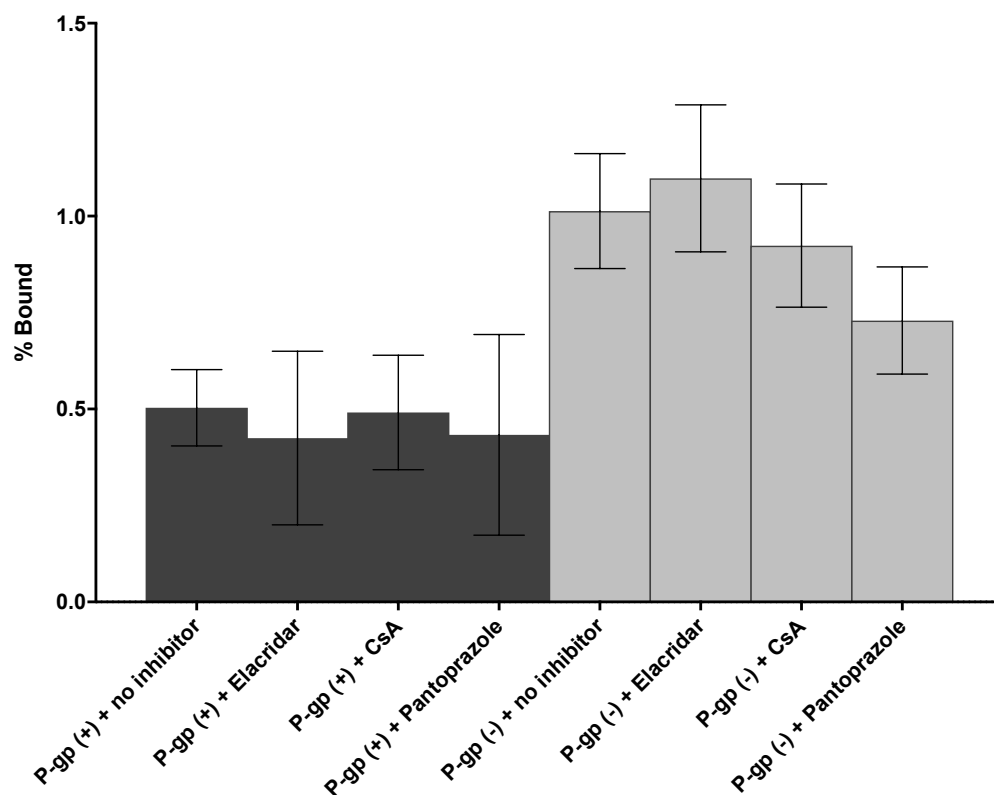


**Figure 4.8** Percent binding of  $^{99m}\text{Tc}$ -Sestamibi in Caco-2 (P-gp positive, dark bars) and MCF7 (P-gp negative, light bars) cell lines in the absence or presence of known P-gp inhibitors (10  $\mu\text{M}$ ).

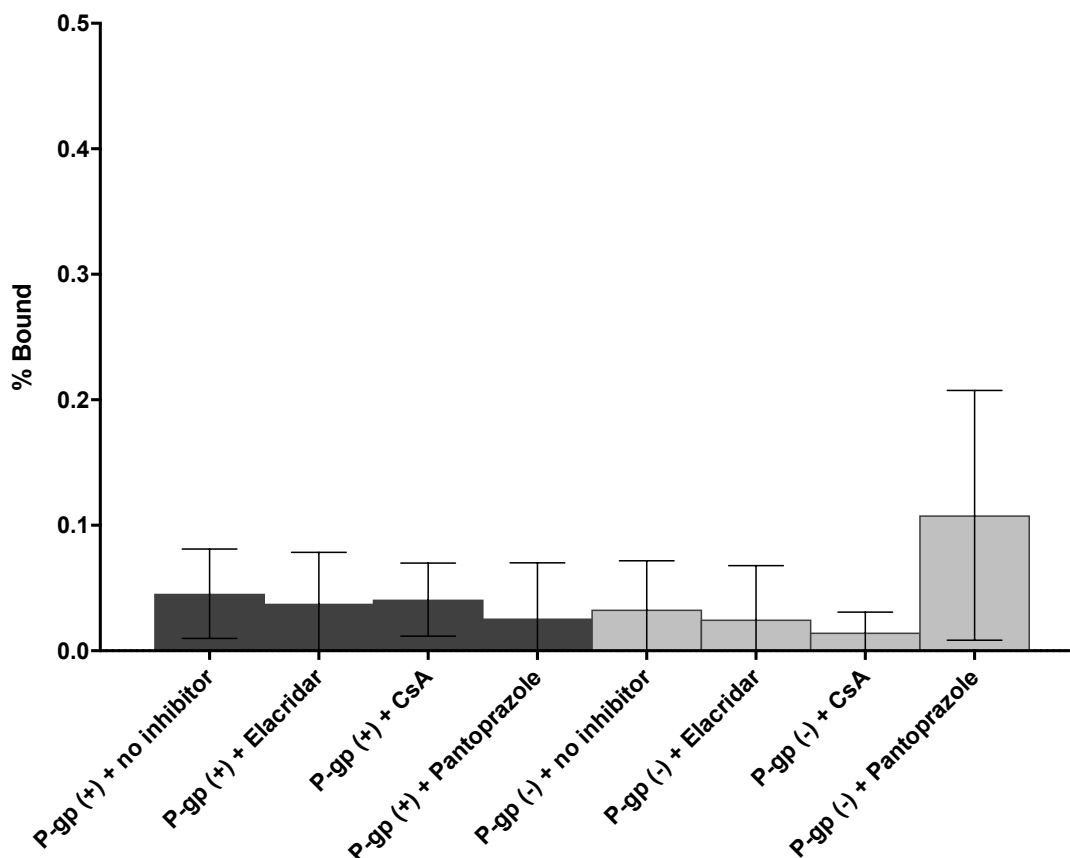


**Figure 4.9** Percent binding of compound **14** to Caco-2 (P-gp positive, dark bars) and MCF7 (P-gp negative, light bars) cells in the absence or presence of known P-gp inhibitors (10  $\mu$ M).

Given the issues with the cell assays, studies to evaluate the potential benefits of P-gp inhibition *in vivo* were performed. Similar studies had been performed to evaluate the effect of other inhibitors on compound **14** in sections 4.3.1 and 4.3.2. For these studies a positive control experiment was conducted, where the third generation P-gp inhibitor Elacridar was administered orally (62.4

mg/kg) 2 hours before administering  $^{99m}\text{Tc}$ -Sestamibi intravenously in a solution of PBS + 0.5% BSA + 0.01% polysorbate 80. In parallel, a second study was performed where  $^{99m}\text{Tc}$ -Sestamibi was administered intravenously without the pre-treatment of Elacridar. For both studies, animals were sacrificed at 6 hours post-injection and distribution studies were conducted. Comparing the results, it is clear that the uptake of  $^{99m}\text{Tc}$ -Sestamibi alone, and in the presence of Elacridar (Figure 4.10) showed that Elacridar successfully reduced gall bladder uptake ( $130 \pm 27.8$  to  $43.5 \pm 17.8$  %ID/g respectively), while increasing liver uptake ( $1.45 \pm 0.09$  to  $16.38 \pm 1.19$  %ID/g respectively).

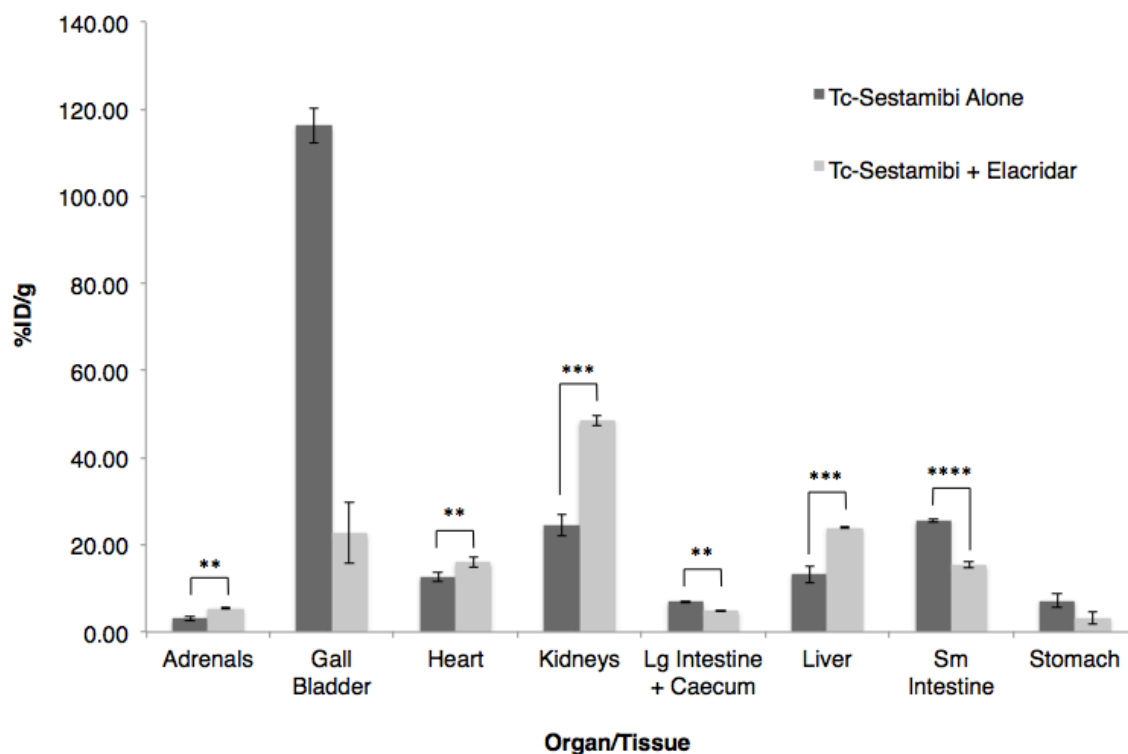


**Figure 4.10** Biodistribution data for  $^{99m}\text{Tc}$ -Sestamibi alone and  $^{99m}\text{Tc}$ -Sestamibi with Elacridar (62.4 mg/kg p.o.). BALB/c mice were administered approximately 740 kBq of  $^{99m}\text{Tc}$ -Sestamibi and sacrificed 1 hour post injection. Data is expressed as the mean injected dose per gram (%ID/g)  $\pm$  SEM. Organs and tissues with uptake less than 5 %ID/g are not presented. \* $p < 0.05$ , \*\* $p < 0.01$ , \*\*\* $p < 0.001$ , \*\*\*\* $p < 0.0001$ .

After performing the positive control studies, studies were performed with compound **14**, where Elacridar was administered orally (62.4 mg/kg) 2 hours before administering compound **14** intravenously in a solution of PBS + 0.5% BSA + 0.01% polysorbate 80. In parallel, a second study was performed where compound **14** was administered intravenously without pre-treatment with Elacridar. For both studies, animals were sacrificed and biodistribution studies were performed at 6 hours post-injection. Comparing the two studies (Figure 4.11), there was very little difference in the uptake of **14** in all organs. Specifically, there was no significant change in gallbladder uptake ( $284 \pm 118$  and  $460 \pm 330$ , respectively), suggesting that compound **14** is likely not a P-gp substrate.

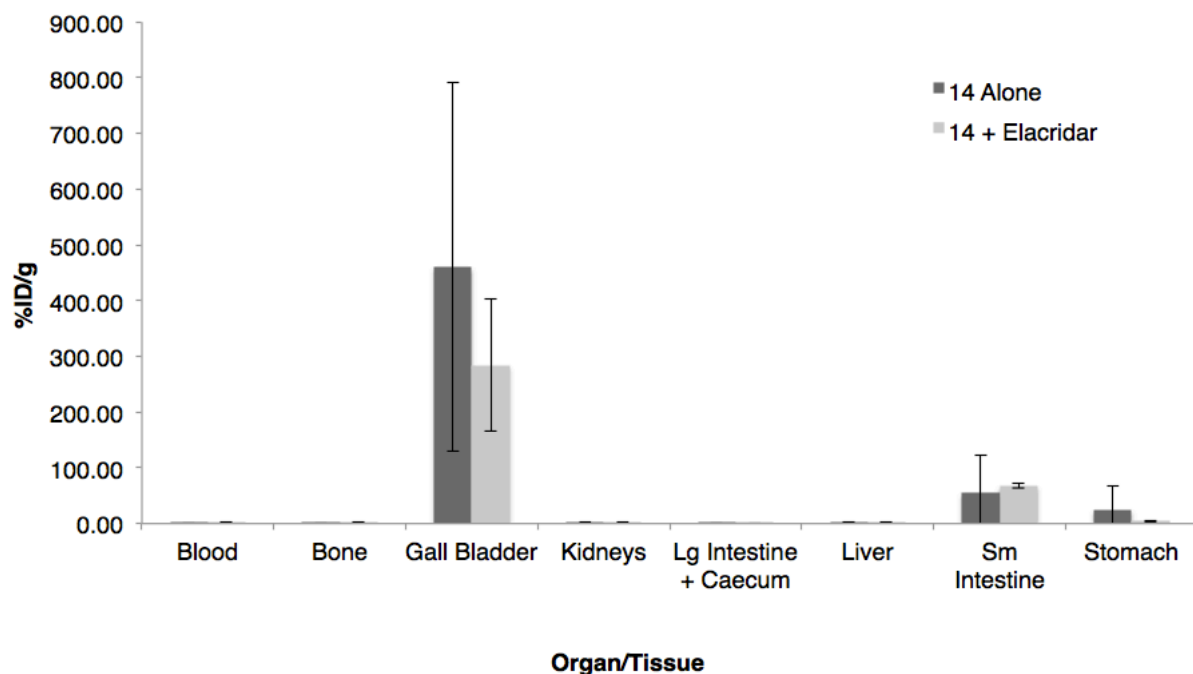


**Figure 4.11** Biodistribution data for compound **14** alone and **14** with Elacridar (62.4 mg/kg p.o.). BALB/c mice were administered approximately 740 kBq of **14** and sacrificed 1 hour post injection. Data is expressed as the mean injected dose per gram (%ID/g)  $\pm$  SEM. Organs and tissues with uptake less than 1 %ID/g are not presented.

#### 4.3.4 *In vivo* evaluation of OATP inhibitors

Furthering the study of the mechanism of gall bladder uptake, the organic anion transporting polypeptide (OATP) was explored. OATPs are a class of influx transporters located in the liver, brain, kidneys, intestine, and testes. These transporters regulate the cellular uptake of both endogenous compounds and xenobiotics. There are several subsets of OATPs,<sup>15</sup> with the OATP1B family of



transporters being the most relevant, as OATP1B1 is one of the most highly expressed transporters in the human liver, located on the basolateral membrane of hepatocytes.<sup>17</sup> Furthermore, mice possess a homologous analog of human OAT1B1 (OATP1B2) in the liver, making it a simple transporter to study, without the need for transgenic mouse models.<sup>41</sup>

The OATP1B1 inhibitor chosen was rifampicin, an approved antibiotic for the treatment of tuberculosis. Rifampicin inhibits OATP1B1 with an  $IC_{50}$  of 0.47-17  $\mu$ M, and OATP1B2 with an  $IC_{50}$  of 3.2  $\mu$ M.<sup>42–44</sup> Another OATP1B inhibitor that was used was indocyanine green (ICG). ICG is a less commonly used OATP inhibitor, but is a more clinically relevant compound compared to rifampicin, due to greater tolerance and fewer side effects.<sup>45,46</sup> ICG is approved for measuring cardiac output and hepatic function in patients. It has also proven to be an inhibitor of OATP1B1 with an  $IC_{50}$  of 3.16  $\mu$ M.<sup>47</sup>

To assess the effects of OATP1B1 inhibition on the clearance of **14**, biodistribution studies were performed, where **14** was co-formulated with either rifampicin (300  $\mu$ g/mouse, 20 mg/kg) or ICG (300  $\mu$ g/mouse, 20 mg/kg) in a solution of PBS + 0.5% BSA + 0.01% polysorbate 80 with 10% ethanol. At 6 hours post-injection, animals were sacrificed and organs were excised, washed, and counted. Results reported as %ID/g were compared to previous biodistribution studies of **14** alone (Figure 4.13).

Comparing the results of **14** co-formulated with rifampicin to that of **14** alone (Figure 4.13), it was apparent that there was no significant change in the

uptake in all major organs: gall bladder ( $182 \pm 60.2$  versus  $216 \pm 75.9$  %ID/g), liver ( $0.67 \pm 0.06$  versus  $1.68 \pm 1.30$  %ID/g), small intestines ( $3.40 \pm 0.93$  versus  $4.25 \pm 2.97$  %ID/g), large intestines ( $92.2 \pm 10.9$  versus  $98.9 \pm 106$  %ID/g), and kidneys ( $0.84 \pm 0.04$  versus  $1.38 \pm 1.32$  %ID/g). The data also showed that the uptake of **14** when co-formulated with indocyanine green did not result in a significant change in uptake when compared to studies with **14** alone (Figure 4.13): gall bladder ( $63.7 \pm 40.3$  versus  $216 \pm 75.9$  %ID/g), liver ( $0.53 \pm 0.21$  versus  $1.68 \pm 1.30$  %ID/g), large intestines ( $10.7 \pm 10.6$  versus  $98.9 \pm 106$  %ID/g), small intestines ( $20.73 \pm 8.30$  versus  $4.25 \pm 2.97$  %ID/g), and kidneys ( $0.45 \pm 0.18$  versus  $1.38 \pm 1.32$  %ID/g).

#### 4.3.5 *In vivo* evaluation of OAT inhibitors

Another transporter of interest is the organic anion transporter (OAT). OAT's are a family of solute carrier transport proteins located in liver hepatocytes. These transporters mediate cellular uptake of many xenobiotics and endogenous compounds. Similar to OATPs, OATs are a family of transporters, where OAT2 has comparable expression in both human and rodent livers and kidneys.<sup>48,49</sup> The OAT2 inhibitor of choice was indomethacin, which is a clinically approved nonsteroidal anti-inflammatory (NSAID) for the treatment of fever, pain, inflammation and many types of arthritis. Indomethacin inhibits OAT2 with an  $IC_{50}$  value of  $64.1 \mu M$ . Indomethacin can also inhibit others OATs (OAT1,  $IC_{50} = 3.83 \mu M$ , OAT3,  $IC_{50} = 0.61 \mu M$ ), and OAT4,  $IC_{50} = 10.1 \mu M$ ), however the low

expression of these OATs in the liver make them less significant in the context of our studies.<sup>50</sup>

To determine if OAT inhibition had an impact on the clearance of **14**, biodistribution studies were performed, where **14** was co-formulated with indomethacin (15  $\mu$ g/mouse, 1 mg/kg) in a solution of PBS + 0.5% BSA + 0.01% polysorbate 80 with 10% ethanol. At 6 hours post-injection, animals were sacrificed and organs were excised, washed and counted. Results of **14** co-formulated with indomethacin were compared to previous biodistribution studies of **14** alone (Figure 4.13). It was determined from these results that the presence of indomethacin in the formulation of **14** did not significantly change the radiotracers clearance, with most organs having no significant change in uptake: gall bladder ( $182 \pm 60.2$  versus  $216 \pm 75.9$  %ID/g), liver ( $0.67 \pm 0.06$  versus  $1.68 \pm 1.30$  %ID/g), small intestines ( $6.21 \pm 1.36$  versus  $4.25 \pm 2.97$  %ID/g), large intestines ( $130 \pm 12.2$  versus  $98.9 \pm 106$  %ID/g), and kidneys ( $0.96 \pm 0.09$  versus  $1.38 \pm 1.32$  %ID/g).

#### 4.3.6 *In vivo* evaluation of MRP inhibitors

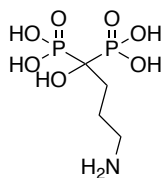
Another common liver transport system of interest for our studies was the multidrug resistance-associated protein (MRP). MRP is a family of efflux transporters that are expressed in the liver and intestines. These transporters are members of the ATP-binding cassette family that exports compounds from cells at the expense of ATP.<sup>14,51</sup> There are several subsets of MRP transporters within

the liver that often work together to transport similar compounds into the bile (such as hydrophobic anionic compounds and peptidomimetics).<sup>52,53</sup> Of the MRP subsets, MRP2, MRP3 and MRP6 are the most common for transporting xenobiotics into the bile, located on the apical membrane of hepatocytes.<sup>51,54</sup> The MRP inhibitor of choice for our studies was Montelukast. Montelukast, or better known as Singulair, is clinically approved leukotriene receptor antagonist that is used for the treatment of asthma. Montelukast has also been studied as an MRP inhibitor, with an  $IC_{50}$  of 26.9  $\mu$ M for MRP2 and 20.3  $\mu$ M for MRP3.<sup>55</sup>

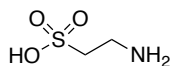
To evaluate the effect of MRP inhibitors on the clearance of **14**, Montelukast (375  $\mu$ g/mouse, 25 mg/kg) was co-formulated with **14** in a solution of PBS + 0.5% BSA + 0.01% polysorbate 80 with 10% ethanol. At 6 hours post-injection of the co-formulation, mice were sacrificed, organs excised and tissues counted. The results of the biodistribution study with Montelukast are shown in figure 4.13. Comparing the distribution of **14** in the presence of Montelukast to **14** alone, it appeared that there was no significant change in uptake in all major organs: gall bladder ( $225 \pm 77.8$  versus  $216 \pm 75.9$  %ID/g), liver ( $1.11 \pm 0.12$  versus  $1.68 \pm 1.30$  %ID/g), small intestine ( $5.88 \pm 2.04$  versus  $4.25 \pm 2.97$  %ID/g), large intestine ( $124 \pm 14.5$  versus  $98.9 \pm 106$  %ID/g), and kidneys ( $0.95 \pm 0.04$  versus  $1.38 \pm 1.32$  %ID/g).

**Table 4.1** Inhibitors of specific hepatobiliary transport pathways and their dose (i.v. = intravenous, p.o. = per os).

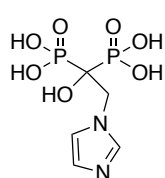
<b>Inhibitor</b>	<b>Target Pathway</b>	<b>Dose (mg/kg)</b>
Alendronate	Mevalonate	20 (i.v.)
Zoledronate	Mevalonate	9 (i.v.)
Rifampin	OATP	20 (i.v.)
Indocyanine green	OATP	20 (i.v.)
Indomethacin	OAT	1 (i.v.)
Montelukast	MRP/BCRP	25 (i.v.)
Taurine	Bile acid conjugation	20 (i.v.)
Elacridar	P-glycoprotein	62.4 (p.o.)



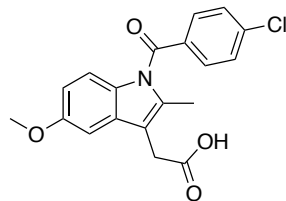
**A**



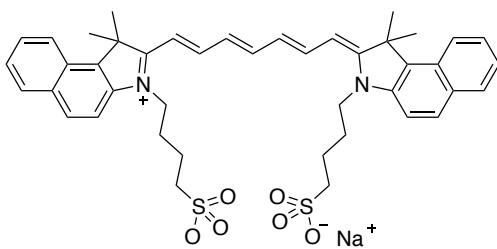
**B**



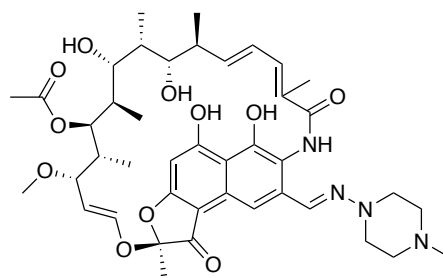
**C**



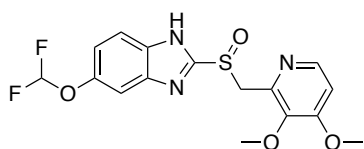
**D**



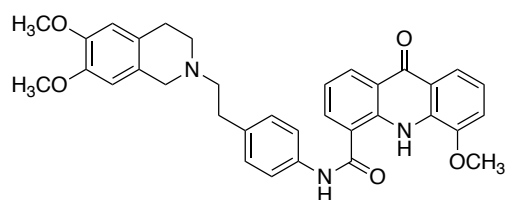
**E**



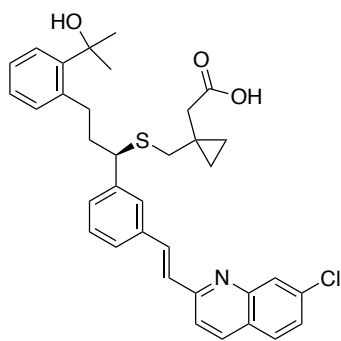
**F**



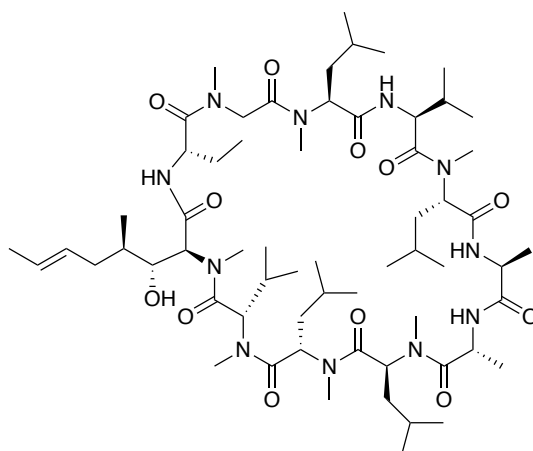
**G**



**H**



**I**



**J**

**Figure 4.12** Structures of key pathway inhibitors. A) Alendronate B) Taurine C) Zoledronate D) Indomethacin E) Indocyanine green F) Rifampicin G) Pantoprazole H) Elacridar I) Montelukast and J) Cyclosporin A.

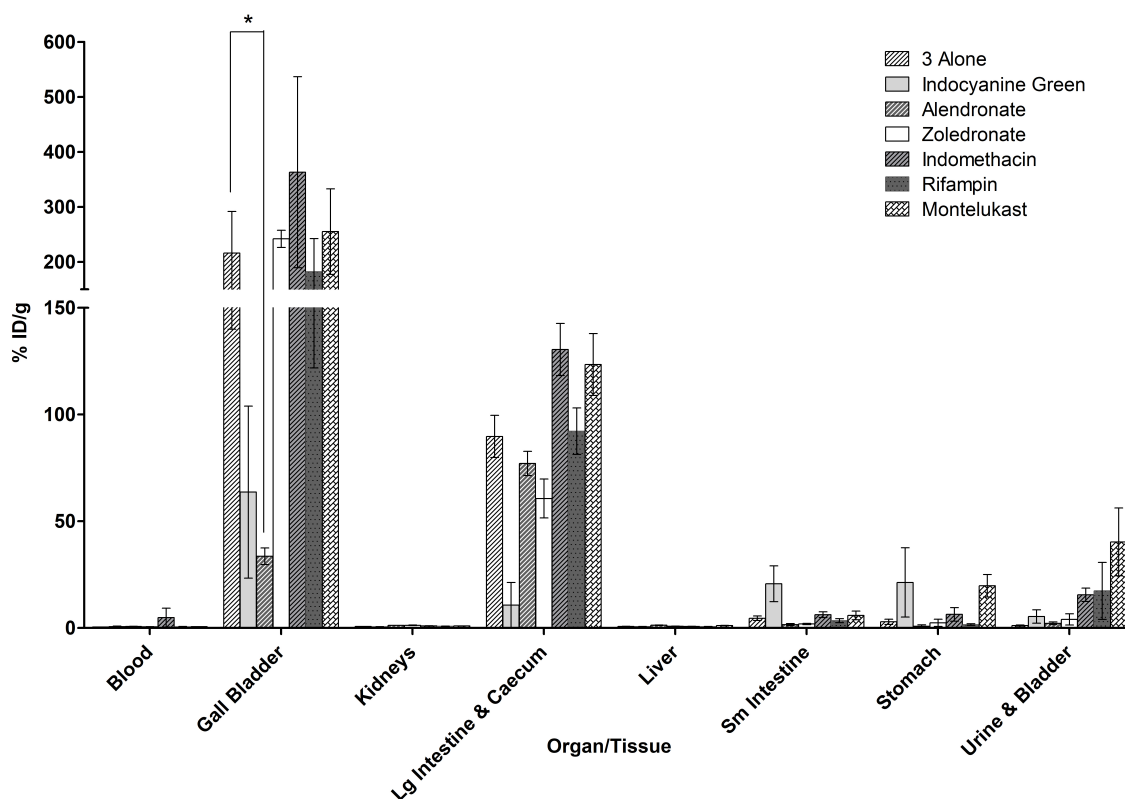


**Figure 4.13** Biodistribution data for compound **14** alone, and **14** with indocyanine green (300  $\mu$ g), alendronate (300  $\mu$ g), zoledronate (135  $\mu$ g), indomethacin (15  $\mu$ g), rifampicin (300  $\mu$ g), and Montelukast (375  $\mu$ g). Compound **14** (approximately 740 kBq) or **14** with each formulation additive were administered to healthy BALB/c mice (n=3 per compound). Biodistribution studies were conducted 6 hours post injection. Data is expressed as the mean injected dose per gram

(%ID/g)  $\pm$  SEM. Organs and tissues with uptake less than 1 %ID/g are not presented. \*p < 0.05.

After analyzing the data from all formulation studies, none of the new pathway inhibitors resulted in a significant change in distribution. More specifically, there was no significant change in gall bladder uptake of **14** in the presence of any inhibitor, with the exception of alendronate. There are several potential reasons as to why most inhibitors demonstrated negligible change in compound distribution. The first reason could be that **14** was not cleared through the specific pathway that was being studied. Second, there could potentially be a mismatch between the dosing of the inhibitor (amount administered) and the timing of the study.

#### **4.4 Conclusions and Future Work**

From this work, it was shown that the addition of alendronate to the formulation of compound **14** resulted in a six-fold decrease in gall bladder uptake. Known inhibitors of hepatobiliary pathways such as P-gp/MDR, OATP, OAT, MRP/BCRP, and bile acid conjugation were explored, and appeared to have little to no effect on the distribution of **14**. Although alendronate is a known inhibitor of the mevalonate pathway, the presence of other nitrogen-containing bisphosphonates did not elicit a change in the distribution of **14**. Further investigation is needed to determine the role of alendronate on the altered



distribution of **14**, and to elucidate the pharmacokinetic pathway in which **14** is being cleared. Unfortunately, these studies did not reveal additional information needed to optimize the structure of the tetrazines. Chapter 5 focuses on a parallel study that involved studying the impact of changing the donor groups on the chelate on the biodistribution of the associated  $^{99m}\text{Tc}$  complexes.

## 4.5 References

- (1) Maresca, K. P.; Hillier, S. M.; Femia, F. J.; Zimmerman, C. N.; Levadala, M. K.; Banerjee, S. R.; Hicks, J.; Sundararajan, C.; Valliant, J.; Zubietta, J.; Eckelman, W. C.; Joyal, J. L.; Babich, J. W. *Bioconjugate Chem.* **2009**, *20* (8), 1625–1633.
- (2) Maresca, K. P.; Marquis, J. C.; Hillier, S. M.; Lu, G.; Femia, F. J.; Zimmerman, C. N.; Eckelman, W. C.; Joyal, J. L.; Babich, J. W. *Bioconjugate Chem.* **2010**, *21*, 1032–1042.
- (3) Jiang, H.; Kasten, B. B.; Liu, H.; Qi, S.; Liu, Y.; Tian, M.; Barnes, C. L.; Zhang, H.; Cheng, Z.; Benny, P. D. *Bioconjugate Chem.* **2012**, *23* (11), 2300–2312.
- (4) Banerjee, S. R.; Pullambhatla, M.; Foss, C. A.; Falk, A.; Byun, Y.; Nimmagadda, S.; Mease, R. C.; Pomper, M. G. *J. Med. Chem.* **2013**, No. 3, 6108–6121.
- (5) García Garayoa, E.; Schweinsberg, C.; Maes, V.; Brans, L.; Bläuenstein, P.; Tourwe, D. A.; Schibli, R.; Schubiger, P. A. *Bioconjugate Chem.* **2008**, *19* (12), 2409–2416.
- (6) Cai, Z.; Ouyang, Q.; Zeng, D.; Nguyen, K. N.; Modi, J.; Wang, L.; White, A. G.; Rogers, B. E.; Xie, X.-Q.; Anderson, C. J. *J. Med. Chem.* **2014**, *57* (14), 6019–6029.
- (7) Ogawa, K.; Mukai, T.; Inoue, Y.; Ono, M.; Saji, H. *J. Nucl. Med.* **2006**, *47* (12), 2042–2047.

- (8) Taft, D. R. In *Pharmacology Principles and Practice*; Elsevier Inc., 2009; pp 175–199.
- (9) Aldred, E. In *Pharmacology*; 2009; pp 133–136.
- (10) Enhssen, A.; Kramer, W.; Wess, G. *Drug Discov. Today* **1998**, 3 (9), 409–418.
- (11) Hayes, K. C.; Livingston, A.; Trautwein, E. a. *Annu. Rev. Nutr.* **1992**, 12, 299–326.
- (12) Van Itallie, T. B.; Hashim, S. A. *Med. Clin. North Am.* **1963**, 47 (3), 629–648.
- (13) Coleman, R. *Biochem. J.* **1987**, 244 (2), 249–261.
- (14) Giacomini, K. M.; Huang, S.; Tweedie, D. J.; Benet, L. Z.; Brouwer, K. L. R.; Chu, X.; Dahlin, A.; Evers, R.; Fischer, V.; Hillgren, K. M.; Hoffmaster, K. A.; Ishikawa, T.; Keppler, D.; Kim, R. B.; Lee, C. A.; Niemi, M.; Polli, J. W.; Sugiyama, Y.; Swaan, P. W.; Ware, J. A.; Wright, S. H.; Yee, S. W.; Zamek-Gliszczynski, M. J.; Zhang, L. *Nat. Rev. Drug Discov.* **2010**, 9, 215–236.
- (15) Kalliokoski, A.; Niemi, M. *Br. J. Pharmacol.* **2009**, 158, 693–705.
- (16) Zhang, L. *Transporter-Mediated Drug-Drug Interactions (DDIs)*; 2010.
- (17) Karlgren, M.; Vildhede, A.; Norinder, U.; Wisniewski, J. R.; Kimoto, E.; Lai, Y.; Haglund, U.; Artursson, P. *J. Med. Chem.* **2012**, 55, 4740–4763.
- (18) Hermann, R.; Derendorf, H.; von Richter, O.; Rostami-Hodjegan, A. *J. Clin. Pharmacol.* **2018**, 58 (6), 704–716.
- (19) Scripture, C. D.; Figg, W. D. *Nat. Rev. Cancer* **2006**, 6 (7), 546–558.
- (20) Tricarico, P. M.; Girardelli, M.; Kleiner, G.; Knowles, A.; Valencic, E.; Crovella, S.; Marcuzzi, A. *Mol. Med. Rep.* **2015**, 12, 4238–4242.
- (21) Buhaescu, I.; Izzedine, H. *Clin. Biochem.* **2007**, 40 (9-10), 575–584.
- (22) Toyras, A.; Ollikainen, J.; Taskinen, M.; Monkkonen, J. *Eur. J. Pharm. Sci.* **2003**, 19, 223–230.

- (23) Thurnher, M.; Nussbaumer, O.; Gruenbacher, G. *Clin. Cancer Res.* **2012**, *18* (13), 3524–3531.
- (24) Dunford, J. E.; Kwaasi, A. A.; Rogers, M. J.; Barnett, B. L.; Ebetino, F. H.; Russell, R. G. G.; Oppermann, U.; Kavanagh, K. L. *J. Med. Chem.* **2008**, *51* (7), 2187–2195.
- (25) Jekerle, V.; Klinkhammer, W.; Scollard, D. A.; Breitbach, K.; Reilly, R. M.; Piquette-Miller, M.; Wiese, M. *Int. J. Cancer* **2006**, *119* (2), 414–422.
- (26) Zhou, Y. G.; Li, K. Y.; Li, H. De. *Eur. J. Clin. Pharmacol.* **2008**, *64* (7), 697–703.
- (27) European Medicines Agency. *Fosavance, INN-alendronate sodium/colecalciferol*; 2005.
- (28) Lin, J. H. *Bone* **1996**, *18* (2), 75–85.
- (29) Chen, T.; Berenson, J.; R, V.; Swift, R.; Gilchick, A.; Goodin, S.; LoRusso, P.; Ma, P.; Ravera, C.; Deckert, F.; Schran, H.; Seaman, J.; Skerjanec, A. *J. Clin. Pharmacol.* **2002**, *42*, 1228.
- (30) Chen, W.; Guo, J. X.; Chang, P. *Mol. Nutr. Food Res.* **2012**, *56* (5), 681–690.
- (31) Kendler, B. S. *Prev. Med. (Baltim)*. **1989**, *18*, 79–100.
- (32) Hayes, K. C.; Sturman, J. A. *Annu. Rev. Nutr.* **1981**, *1*, 401–425.
- (33) Danielsson, H.; Sjovall, J. *Annu. Rev. Biochem.* **1975**, *44* (1), 233–253.
- (34) Choudhuri, S.; Klaassen, C. *Int. J. Toxicol.* **2006**, *25*, 231–259.
- (35) Wang, R. B.; Kuo, C. L.; Lien, L. L.; Lien, E. J. *J. Clin. Pharm. Ther.* **2003**, *28*, 203–228.
- (36) Zhou, S. F. *Xenobiotica* **2008**, *38* (7-8), 802–832.
- (37) Shiraga, K.; Sakaguchi, K.; Senoh, T.; Ohta, T.; Ogawa, S.; Sawayama, T.; Mouri, H.; Fujiwara, A.; Tsuji, T. *J. Gastroenterol. Hepatol.* **2001**, *16*, 460–466.

- (38) Nobili, S.; Landini, I.; Giglioni, B.; Mini, E. *Curr. Drug Targets* **2006**, 7, 861–879.
- (39) Amin, M. L. *Drug Target Insights* **2013**, 2013 (7), 27–34.
- (40) Anderle, P.; Niederer, E.; Rubas, W.; Hilgendorf, C.; Spahn-Langguth, H.; Wunderli-Allenspach, H.; Merkle, H. P.; Langguth, P. *J. Pharm. Sci.* **1998**, 87 (6), 757–762.
- (41) Cheng, X.; Maher, J.; Chen, C.; Klaassen, C. D. *Drug Metab. Dispos.* **2005**, 33 (7), 1062–1073.
- (42) Zaher, H.; Zu Schwabedissen, H. E. M.; Tirona, R. G.; Cox, M. L.; Obert, L. A.; Agrawal, N.; Palandra, J.; Stock, J. L.; Kim, R. B.; Ware, J. A. *Mol. Pharmacol.* **2008**, 74 (2), 320–329.
- (43) Vavricka, S. R.; Van Montfoort, J.; Ha, H. R.; Meier, P. J.; Fattinger, K. *Hepatology* **2002**, 36 (1), 164–172.
- (44) Gui, C.; Miao, Y.; Thompson, L.; Wahlgren, B.; Mock, M.; Stieger, B.; Hagenbuch, B. *Eur. J. Pharmacol.* **2008**, 584 (1), 57–65.
- (45) Aldrich, S. *Indocyanine Green Safety Data Sheet*; 2018.
- (46) Aldrich, S. *Rifampicin Safety Data Sheet*; 2018.
- (47) De Graaf, W.; Häusler, S.; Heger, M.; Van Ginhoven, T. M.; Van Cappellen, G.; Bennink, R. J.; Kullak-Ublick, G. A.; Hesselmann, R.; Van Gulik, T. M.; Stieger, B. *J. Hepatol.* **2011**, 54, 738–745.
- (48) Buist, S. C. N.; Cherrington, N. J.; Choudhuri, S.; Hartley, D. P.; Klaassen, C. D. *J. Pharmacol. Exp. Ther.* **2002**, 301 (1), 145–151.
- (49) Kobayashi, Y.; Ohshiro, N.; Shibusawa, A. *Mol. Pharmacol.* **2002**, 62 (1), 7–14.
- (50) Khamdang, S.; Takeda, A.; Noshiro, R.; Narikawa, S.; Enomoto, A.; Naohiko, A.; Payachaturawat, P.; Endou, H. *J. Pharmacol. Exp. Ther.* **2002**, 303 (2), 534–539.
- (51) Sodani, K.; Patel, A.; Kathawala, R. J.; Chen, Z. S. *Chin. J. Cancer* **2012**, 31 (2), 58–73.

- (52) Slot, A. J.; Wise, D. D.; Deeley, R. G.; Monks, T. J.; Cole, S. P. C. *Drug Metab. Dispos.* **2008**, *36* (3), 552–560.
- (53) Williamson, G.; Aeberli, I.; Miguet, L.; Zhang, Z.; Sanchez, M. B.; Crespy, V.; Barron, D.; Needs, P.; Kroon, P. A.; Glavinas, H.; Krajcsi, P.; Grigorov, M. *Drug Metab. Dispos.* **2007**, *35* (8), 1262–1268.
- (54) Borst, P.; Evers, R.; Kool, M.; Wijnholds, J. *Biochim. Biophys. Acta - Biomembr.* **1999**, *1461* (2), 347–357.
- (55) Csandl, M. A.; Conseil, G.; Cole, S. P. C. *Drug Metab. Dispos.* **2016**, *44* (6), 857–866.

## 4.6 Supplemental Information

### Fluorescent Imaging of P-gp positive and negative cell lines

Caco-2 cells were plated at  $0.6 \times 10^5$  cells/well and incubated for 3 days at 37 °C with 5% CO<sub>2</sub>. MCF7 cells were plated at  $1.55 \times 10^5$  cells/well and incubated for 3 days at 37 °C with 5% CO<sub>2</sub>. Media was aspirated from wells, and cells were washed 3 times with ice cold 1 mL of PBS + 0.5% BSA. Wells 1-2 of each cell line were then incubated with 500  $\mu$ L of a solution of buffer and FITC-Ab (980  $\mu$ L of PBS + 0.5% BSA and 20  $\mu$ L of FITC-Ab – ice cold) for 40 minutes on ice in the dark (Note: plate was wrapped in tin foil). Well 3 was incubated with 500  $\mu$ L of PBS + 0.5% BSA with no FITC-Ab (to determine inherent cell fluorescence). Staining buffer was then aspirated from cells and washed 3 times with 1 mL of ice cold PBS + 0.5% BSA. Wells were filled with 300  $\mu$ L of ice cold PBS + 0.5% BSA. Bright field and fluorescent images were taken using the Olympus inverted bright field & fluorescent microscope (Model BX53F) equipped with a FITC filter.

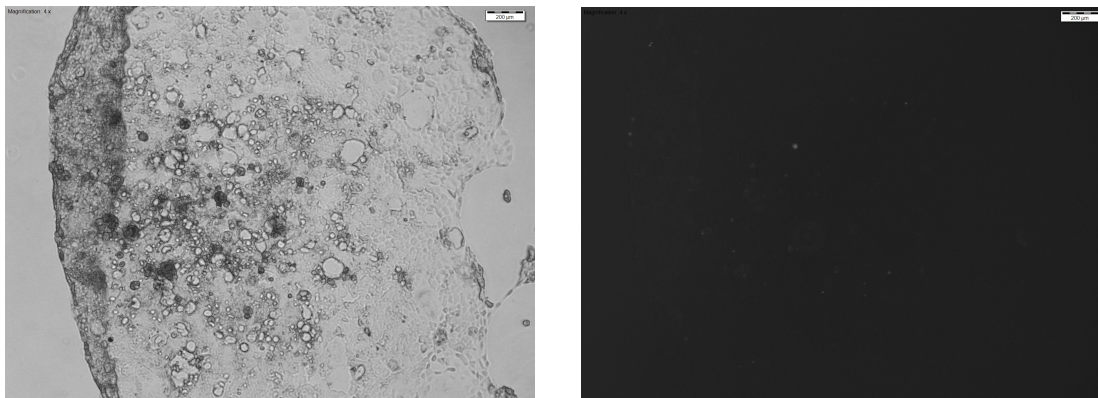


**Figure S 3.1** Bright field image (left) and fluorescent image (right) of P-gp (+) Caco-2 cells stained with FITC Mouse Anti-Human P-glycoprotein (CD243) Clone 17F9.

### **P-gp Expression Assay (Flow Cytometry)**

Caco-2 and MCF7 cells were plated in a T125 flask (approximately  $1 \times 10^6$  cells) and incubated for 3 days at 37 °C with 5% CO<sub>2</sub>. Cells were trypsinized, counted, and diluted to a concentration of  $1 \times 10^6$  cells/mL in media. Cells were then centrifuged to remove media, and suspended in PBS + 0.5% BSA at a concentration of  $1 \times 10^6$  cells/mL. Cells were washed 2 times with ice cold PBS + 0.5% BSA. Cells were re-suspended in ice cold PBS + 0.5% BSA and incubated with 7-aminoactinomycin D (7AAD) (10  $\mu$ L), FITC-Ab (20  $\mu$ L), both, or neither for 40 minutes on ice in the dark. After staining, cells were washed 3-5 times with ice cold PBS + 0.5 BSA. Cells were then re-suspended in flow buffer and loaded in to

flow cytometry tubes. Fluorescence was detected using a BD LSRFORTESSA cell analyzer equipped with an ultraviolet argon laser (excitation at 466 nm, emission at 535 nm band-pass filters).

## **Chapter 5: Towards a new $^{99m}\text{Tc}$ -labeled tetrazine-chelate derivative with improved pharmacokinetics**

### **5.1 Introduction**

An alternative strategy to studying clearance pathways using inhibitors is to change the nature of the chelate complexes to achieve the desired biodistribution. In chapter 2, attempts were made to alter the distribution of  $^{99m}\text{Tc}$ -tetrazines through the modification of linker groups, which had some success. Rather than modifying the linker groups alone, the nature of the donor groups on the chelate can also be changed.

A wide variety of chelate complexes of the  $^{99m}\text{Tc}[\text{Tc}(\text{CO})_3]^+$  core have been reported in the literature, where significant differences in clearance profiles were observed.<sup>1-4</sup> As one example, Banerjee and coworkers evaluated the impact of changing the nature of  $^{99m}\text{Tc}(\text{I})$  chelates on the biodistribution of small molecule inhibitors of prostate-specific membrane antigen (PSMA).<sup>1</sup> It was discovered that  $^{99m}\text{Tc}[\text{Tc}(\text{CO})_3]^+$  complexes containing pyridine and imidazole heteroatoms resulted in high gall bladder uptake, with predominately hepatobiliary clearance.<sup>1</sup> Furthermore, these compounds resulted in less than optimal target to non-target ratios. In contrast, a  $^{99m}\text{Tc}[\text{Tc}(\text{CO})_3]^+$  mixed chelate developed initially by Kluba and co-workers comprised of triazole, amine, and carboxylic acid donor ligands resulted in rapid renal clearance with exceptional target to non-target ratios.<sup>1,5</sup>



Based on this and other comparable studies,<sup>6</sup> the evaluation of different  $^{99m}\text{Tc}[\text{Tc}(\text{CO})_3]^+$  chelate complexes was investigated. Specifically, the effect of chelate composition on the distribution of  $^{99m}\text{Tc}$ -compounds was evaluated in an attempt to overcome high hepatobiliary clearance seen with previous compounds (Chapters 2, 3 and 4). Specifically, a triazole based chelate that showed promise as a PSMA-targeting agent<sup>3,6</sup> was further modified, and assessed *in vivo* to determine its potential to be used to create a  $^{99m}\text{Tc}$ -labeled tetrazine for pretargeting strategies.

## 5.2 Materials and Methods

### 5.2.1 General materials and instruments

All compounds were purchased from Sigma Aldrich, unless otherwise stated. Fmoc-Lysine( $\text{N}_3$ )-OH, Boc-propargylglycine·DCHA, and 3-azido-1-propanamine were purchased from Anaspec (Fremont, CA). 4-(1,2,4,5-Tetrazin-3-yl)phenyl) methanamine hydrochloride was purchased from Conju-Probe (San Diego, CA). NMR solvents were purchased from Caledon Laboratory Chemicals (Georgetown, ON). Sodium pertechnetate was provided by Mallinckrodt Pharmaceuticals from an Ultra-Technekow generator.

High performance liquid chromatography (HPLC) of radioactive compounds were performed on a Waters 1525 Binary (Midford, MA, USA) monitored simultaneously with 2998 photodiode array detector at 220/254 nm and

in line radioactivity Bioscan gamma detector with NaI (T1) scintillator using the Empower software package. Analytical HPLC of all other compounds were performed on a Varian Prostar 230 monitored simultaneously with a Prostar 335 PDA detector. HPLC method: Phenomenex C-18 analytical column (250 mm × 4.6 mm × 5 µm) operating at a flow rate of 1.0 mL/min (analytical) was used. The following solvent gradient was employed: Method 1 (solvent A = H<sub>2</sub>O + 0.1% TFA, solvent B = ACN + 0.1% TFA): 0-2 min 5% B, 2-21 min 5-15% B, 21-22 min 15-50% B, 22-24 min 50% B, 24-30 min 50-5% B, 30-32 min 5% B. Method 2 (solvent A = H<sub>2</sub>O + 0.1% TFA, solvent B = ACN + 0.1% TFA): 0-2 min 20% B, 2-19 min 20-80% B, 19-21 min 100% B, 21-27 min 20% B.

### **5.2.2 Synthesis of compounds 22-23b, 26-27, and 30-32**

The synthetic methods for compounds **22-23b**, **26-27**, and **30-32** are reported in Appendix II.

### **5.2.3 Animal models and biodistribution studies**

Animal studies were approved by the Animal Research Ethics Board at McMaster University in accordance with Canadian Council on Animal Care (CCAC) guidelines. Biodistribution studies were performed using female BALB/c mice (Charles River Laboratories, Kingston, NY) at the indicated time points. The mice were administered the agents via tail vein injection in a formulation of PBS + 0.5% BSA + 0.01% polysorbate 80 to a concentration of 7.4 MBq/mL.

## 5.3 Results and Discussion

### 5.3.1 Effect of chelates on distribution

In prior work (Chapter 2), it was determined that the addition of hydrophilic groups and linkers can aid in compound clearance. However, the addition of these groups could reduce, but not eliminate, undesired uptake in the gallbladder. To determine the extent to which the chelate was driving the undesired localization, compound **11b**, (the chelate found in **11a** without a tetrazine) was labeled with  $^{99m}\text{Tc}$  following the previously described procedure (Section 2.2.1). In brief, **11a** was heated in the presence of  $^{99m}\text{Tc}[\text{Tc}(\text{CO})_3(\text{OH}_2)_3]^+$  at 60 °C for 20 minutes at pH 3.5, followed by HPLC purification and TFA deprotection, resulting in **11b** which was obtained in 31% radiochemical yield.

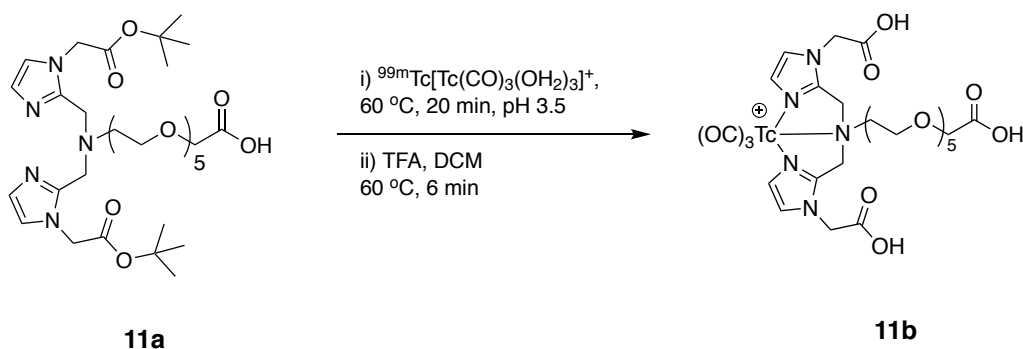


**Figure 5.1** Labeling of **11a** with  $^{99m}\text{Tc}$  to produce **11b**. Experimental details are provided in Appendix II.

Compound **11b** was administered to female BALB/c mice (~0.74 MBq) where at 1 hour post injection, animals were sacrificed and organs/tissues were excised. The %ID/g of each organ was plotted, and compared to the distribution of **14** (Figure 5.2). Comparing the clearance profile of **11b** and **14** (Figure 5.3), both compounds showed similar uptake in all organs. Specifically, the high uptake seen in the gallbladder ( $340 \pm 19.7$  for **11b**, and  $460 \pm 330$  % ID/g for **14**) and small intestine ( $90.0 \pm 7.25$  for **11b**, and  $54.9 \pm 67.0$  %ID/g for **14**) for both compounds suggests that the  $^{99m}\text{Tc}$ -complex, rather than the tetrazine moiety, was in fact driving off-target uptake. This conclusion is further supported by the fact that this high hepatobiliary uptake was not seen with other radiolabeled tetrazines derived from the same starting material (tetrazine amine).<sup>7,8</sup>

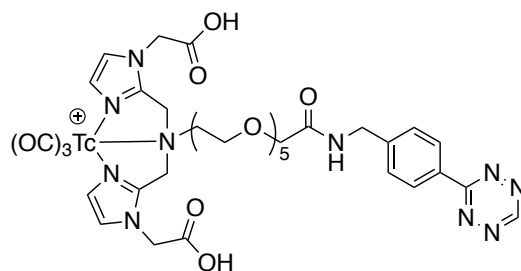


**Figure 5.2** Structure of compound **14**.

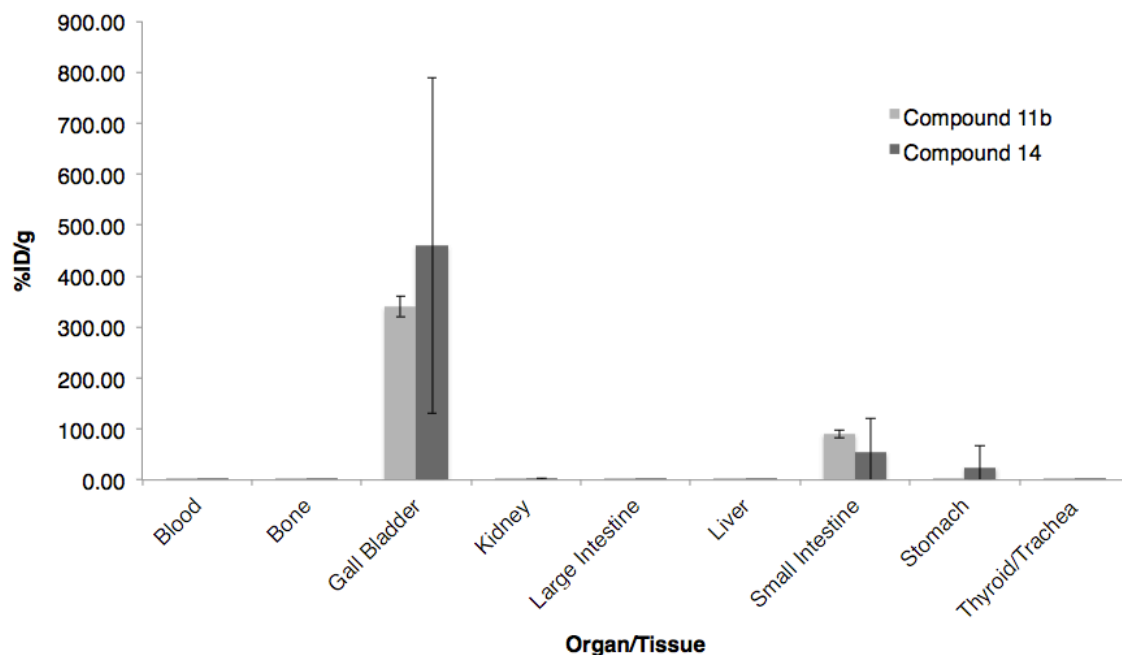


**Figure 5.3** Biodistribution data of **11b** (light bars) and **14** (dark bars). BALB/c mice (n=3 per compound) were injected with approximately 0.74 MBq of **11b** or **14** and sacrificed 1 hour post injection. Data is expressed as the mean injected dose per gram (%ID/g)  $\pm$  SEM. Note: large error bars are due to the variability associated with clearance organs.

These results suggest that it may be beneficial to investigate other  $^{99m}\text{Tc}$  chelates that have superior clearance from non-target tissues. As noted previously, a triazole-based chelate developed by Kluba and coworkers showed promise as a PSMA-targeting agent, with rapid clearance from non-target tissues and high target to non-target ratios.<sup>1,5</sup> At 2 hours post injection, the  $^{99m}\text{Tc}$ -triazole ligand had very little uptake in non-target tissues, with most tissues having  $<1$

%ID/g, with the exception of the liver ( $6.11 \pm 0.66$  %ID/g), spleen ( $4.42 \pm 1.68$  %ID/g), and kidneys ( $116.2 \pm 14.2$  %ID/g). Furthermore the  $^{99m}\text{Tc}$ -triazole ligand was able to effectively target PSMA expressing tumours when tagged with a Glu-Urea-Lys PSMA targeting moiety, with a tumour: blood ratio of  $109 \pm 28.8$  at 2 hours post injection.<sup>1</sup>

Compound **22** (Figure 5.4) was prepared following a literature procedure, where the synthetic methods are described in Appendix II.<sup>1</sup> To prepare **22**, **21** was first generated through a copper (I) catalyzed azide-alkyne cycloaddition (CuAAC) between Fmoc-azido-L-lysine (**19**), and Boc-propargylglycine (**20**), using copper acetate as the catalyst. The reaction was monitored by TLC and electrospray ionization mass spectrometry (ESI-MS), and allowed to continue until the starting material was fully consumed. Copper was removed using a Quadrapure IDA resin, and the product was purified by liquid-liquid extraction, followed by HPLC to give **22** in 45% yield. The Fmoc protecting group was then removed using a 1:1 v/v mixture of DMF and piperidine. This was followed by removal of the Boc protecting group using a 1:1 v/v mixture of DCM and TFA, which was done immediately prior to labeling with  $^{99m}\text{Tc}$ .

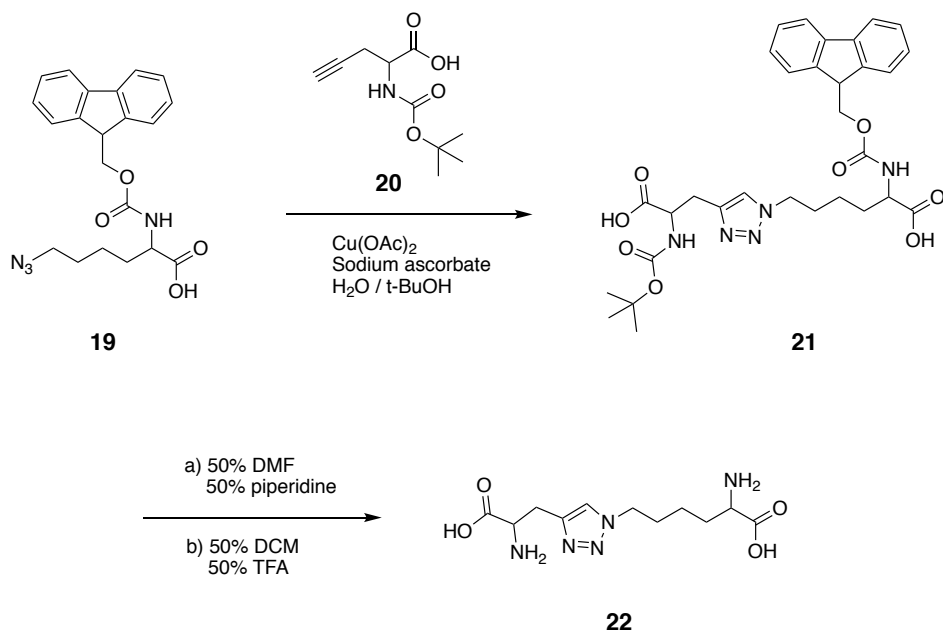


**Figure 5.4** Synthesis of **22** from **19**.<sup>1</sup>

The  $^{99\text{m}}\text{Tc}(\text{I})$  complex of the chelate, **23a** was prepared using a modified literature procedure that is reported in Appendix II.<sup>1</sup> Compound **22** was combined with  $^{99\text{m}}\text{Tc}[\text{Tc}(\text{CO})_3(\text{OH}_2)_3]^+$  at 60 °C for 10 minutes. The labeling was monitored by analytical HPLC, which showed nearly quantitative conversion (Figure 5.5 and 5.6) after 10 minutes. Compound **23a** was isolated by HPLC, and was stable for up to 6 hours at 37 °C in PBS (Figure S 5.5).

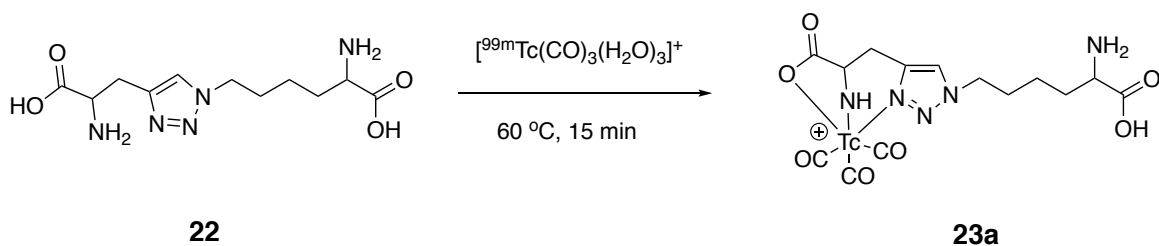


**Figure 5.5** Synthesis of **23a** from **22**.

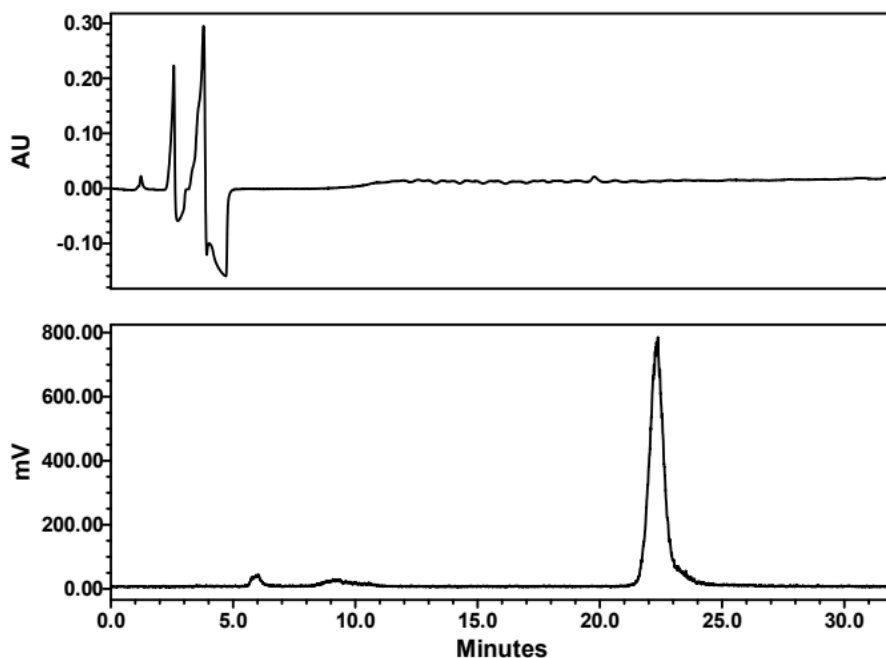


**Figure 5.6** HPLC traces of the reaction involving the treatment of **23a** with  $^{99m}\text{Tc}[\text{Tc}(\text{CO})_3(\text{OH}_2)_3]^+$  (UV – top, Gamma – bottom). (Method 1, 1 mL/min).

Biodistribution studies of **23a** were performed, and compared to that of **11b**. Compound **23a** was administered to female BALB/c mice ( $\sim 0.74$  MBq), and animals were sacrificed 1 hour post injection. Organs and tissues were excised, washed, and counted using a gamma counter. The %ID/g of each organ/tissue is presented in Figure 5.7 below. Comparing the results of **11b** and **23a**, it was clear that the triazole chelate of compound **23a** had a more desirable clearance profile than **11b**, with maximum compound uptake in the kidneys being 5 times lower than any organs seen with **11b** at 1 hour post injection. This clearance profile is



greatly improved for most tissues where **11b** had uptake in some organs such as the gall bladder that reached values as high as 340 %ID/g (Figure 5.7).

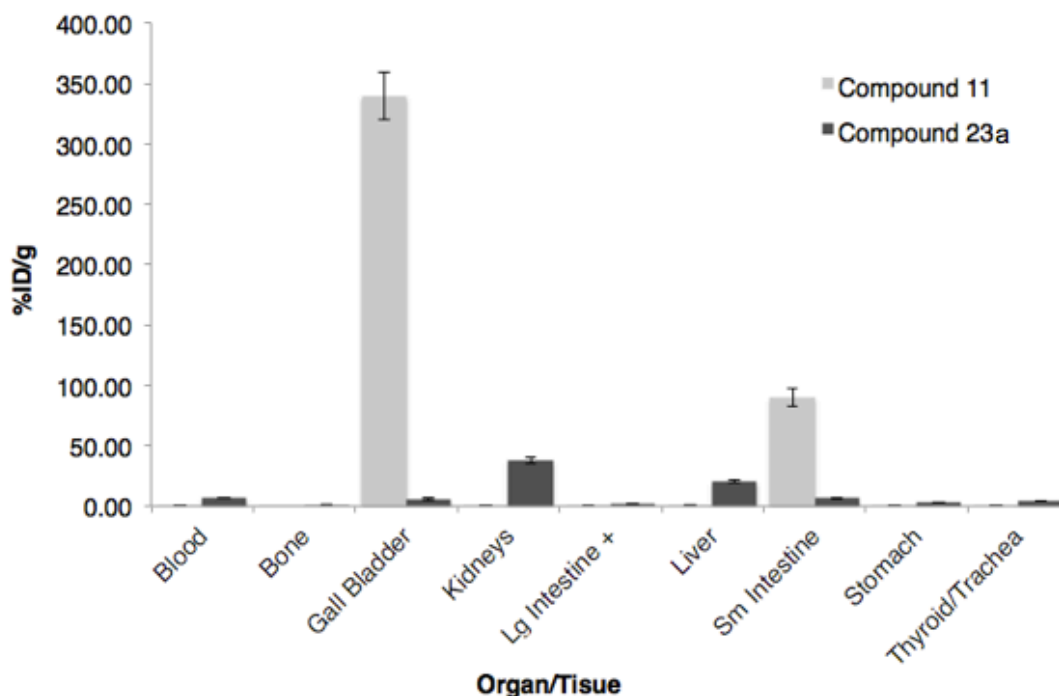


**Figure 5.7** Biodistribution of **11b** (light bars) and **23a** (dark bars). BALB/c mice (n=3 per compound) were injected with approximately 0.74 MBq of **11** or **23a** and sacrificed 1 hour post injection. Data are expressed as the mean injected dose per gram (%ID/g)  $\pm$  SEM. Organs and tissues containing <1% ID/g were excluded from the graph.

Moving forward with these promising results, the next step was to develop a synthetic method to couple the chelate to a tetrazine (Figure 5.9). This addition was performed using a modified procedure, where a tetrazine-acid derivative was

synthesized (compound **26**) through an amide forming reaction between a commercially available tetrazine amine and glutaric anhydride in dichloromethane and triethylamine. The reaction was monitored by TLC and purified by column chromatography, resulting in **26** in an 89% yield. Next, **26** was activated via an NHS ester (compound **27**) using NHS and 1-ethyl-3-(3-dimethylaminopropyl)carbodiimide (EDC) in DMF, and purified by column chromatography, resulting in an 85% yield (Figure 5.8).

Next, attempts were made to link the two components in the presence of diisopropylethylamine. Unfortunately, this reaction was unsuccessful when performed under several reaction conditions in different solvents (Table 5.1). Furthermore, additional coupling agents were explored including 2,3,5,6-tetrafluorophenyl trifluoroacetate (TFP), benzotriazol-1-yl-oxytripyrrolidinophosphonium hexafluorophosphate (PyBOP), and 2-(1*H*-benzotriazol-1-yl)-1,1,3,3-tetramethyluronium hexafluorophosphate (HBTU); all failing to produce the desired tetrazine-functionalized triazole (Figure 5.9).

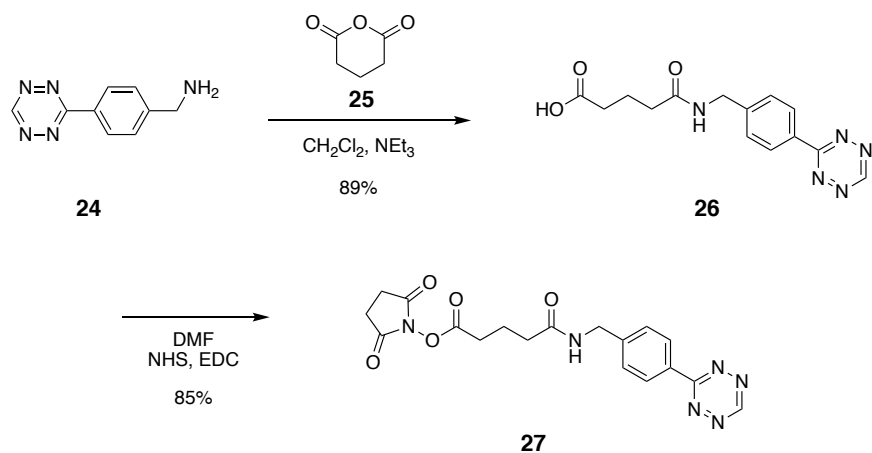


**Figure 5.8** Synthesis of compound **27**.

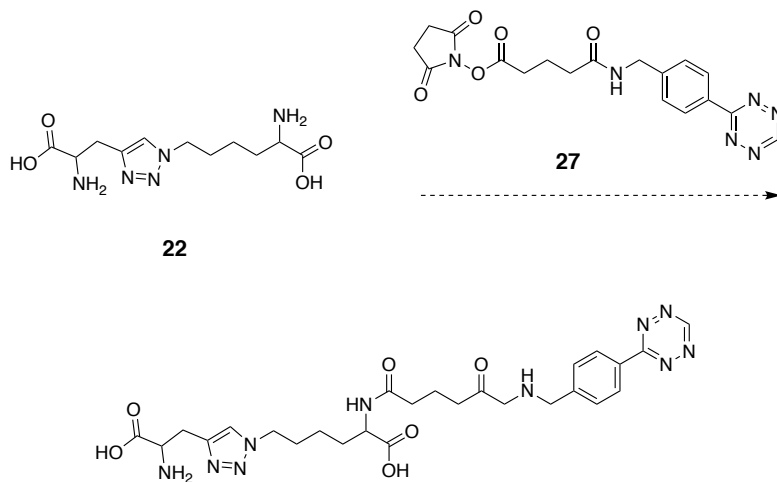


**Figure 5.9** Proposed amide coupling of **22** and **27**.

**Table 5.1** List of reaction conditions of **22** with **27**.

Coupling Agent	Temp (°C)	Time (h)	Result
N-Hydroxysuccinimide (NHS)	rt	24	N.R.
	30		
	60		
2,3,5,6-Tetrafluorophenyl trifluoroacetate (TFP)	rt	48	
Benzotriazol-1-yl-oxytripyrrolidinophosphonium hexafluorophosphate (PyBOP)	rt	48	
	30		
2-(1 <i>H</i> -Benzotriazol-1-yl)-1,1,3,3-tetramethyluronium hexafluorophosphate (HBTU)	rt	48	

In an attempt to test the reactivity of the  $\alpha$ -amine of the lysine derivative, a commercially available active ester, Boc-HYNIC-NHS, was combined with **23b** and diisopropylethylamine (Figure 5.10). Following the reaction by TLC and ESI-MS, it was determined that the desired product formed after 18 hours, however the yield was low (<13%). This suggests that the lysine can in fact couple to active esters however the combination of the  $\alpha$ -amine being a poor nucleophile, and the poor reactivity of the tetrazine-NHS ester may be responsible for the desired reaction between **22** and **27** failing to proceed.

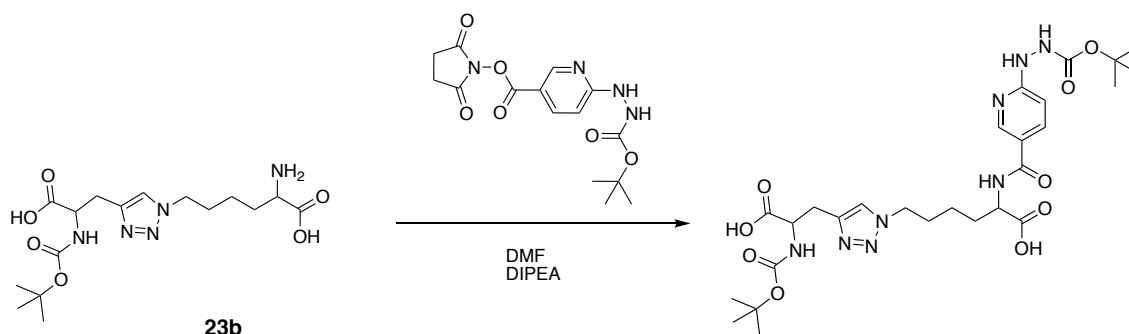


**Figure 5.10** Attempted coupling of **23b** with a commercially available active ester, Boc-HYNIC-NHS.

### 5.3.3 Alternative synthesis of a triazole based chelate

To overcome the reactivity issues that prevented the reaction between **23b** and **27**, attempts were made to prepare the modified triazole ligand, **30** (Figure 5.11). Here, the Fmoc-azidolysine was replaced with 3-azido-1-propanamine to simplify the coupling reaction by removing the carboxylic acid adjacent to the amino group. The CuAAC reaction and purification was performed under the same conditions used to generate **22**, producing **30** in 70% yield.<sup>1</sup> The reaction between **27** and **30**, to generate **31** was monitored by TLC and ESI-MS over 18 hours, where the desired product (**31**) was isolated by HPLC in 9% yield.

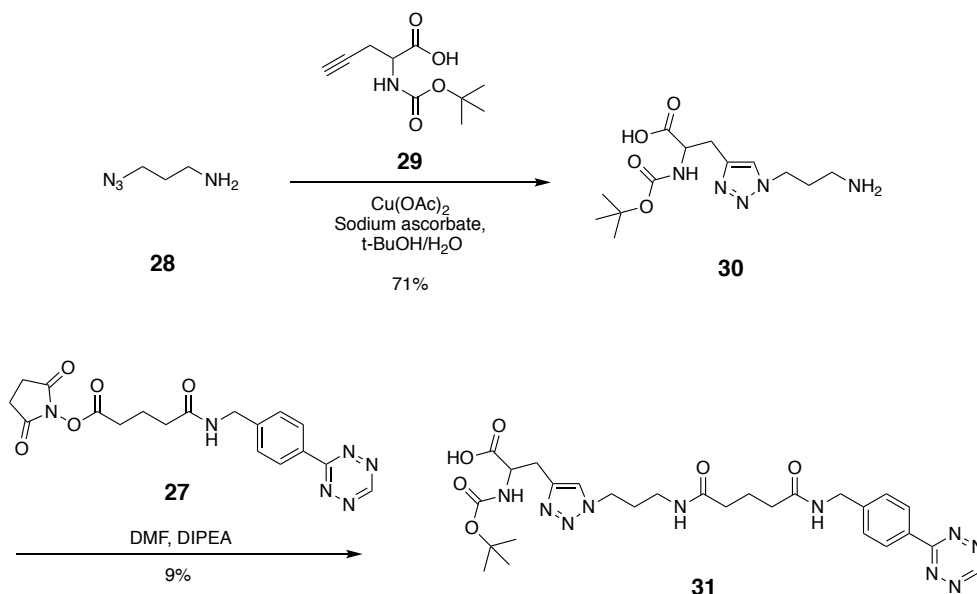


**Figure 5.11** Synthesis of **31**.

Following purification, the Boc group in **31** was removed using a 1:1 v/v solution of DCM and TFA at 60 °C for 10 minutes. Next, the deprotected ligand was heated with  $^{99\text{m}}\text{Tc}[\text{Tc}(\text{CO})_3(\text{OH}_2)_3]^+$  at 60 °C for 15 minutes, resulting in **32**, which was isolated by HPLC in 15% radiochemical yield (Figure 5.12). The decrease in labeling yields between **23a** and **31** was somewhat surprising but is likely due to the presence of the tetrazine moiety. The literature conditions used for labeling the triazole chelate is performed at pH 7.<sup>1</sup> However, at neutral pH with heating, the tetrazine showed significant degradation. To minimize this, the synthesis of **31** had to be performed at pH 5.5, which was suboptimal with respect to the triazole. Notwithstanding, sufficient material could be produced for biodistribution studies.

Following the preparation of **32**, biodistribution studies were conducted and compared to **23a**. The same procedure was followed, where female BALB/c mice were administered **32** (0.74 MBq) and the animals sacrificed at 1 and 6 hours post injection. The data for **23a** and **32** is displayed as the %ID/g in Figure 5.13.

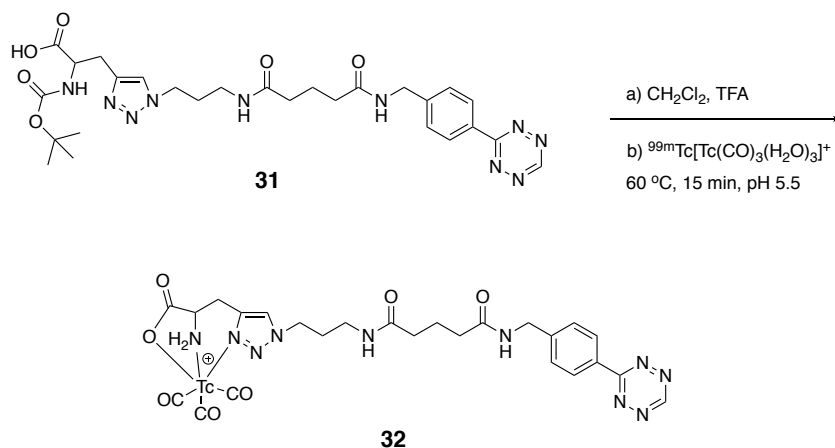


**Figure 5.12**  $^{99\text{m}}\text{Tc}$  labeling of **31** to produce **32**.

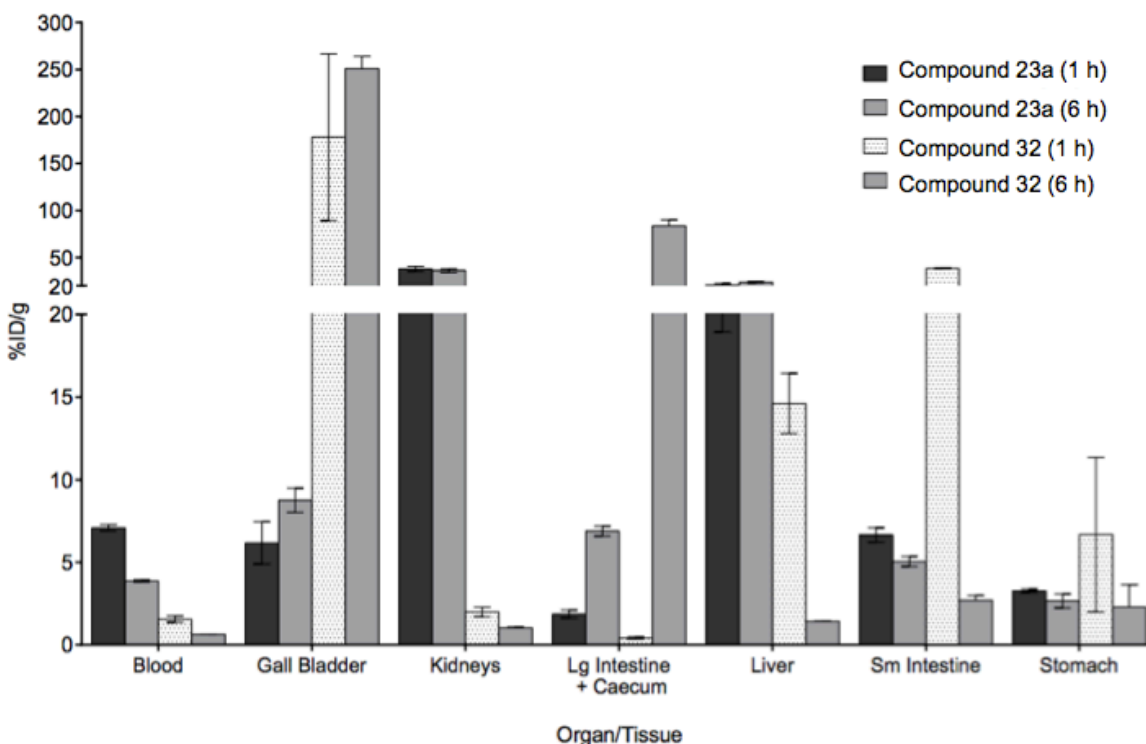


**Figure 5.13** Biodistribution of **23a** (solid bars) and **32** (patterned bars). BALB/c mice (n=3 per compound) were injected with approximately 0.74 MBq of **23a** or **32** and sacrificed 1 and 6 hours post injection. Data is expressed as the mean injected dose per gram (%ID/g)  $\pm$  SEM. Organs with less than 5 %ID/g were excluded from the graph.

Comparing the biodistribution data for compounds **23a** to **32**, revealed that the addition of the lipophilic tetrazine and linker altered the distribution of the  $^{99m}\text{Tc}$ -triazole complex. Unfortunately, there was a significant increase in hepatobiliary uptake, specifically in the gall bladder ( $8.25 \pm 1.28$  %ID/g versus  $251 \pm 13.2$  %ID/g at 6 hours). This is not entirely surprising, as compound **23a**



had a free amine and carboxylic acid, adding significant hydrophilicity to the compound. Based on this data, work was initiated on the synthesis of a polar analog of **32** bearing the amino and carboxylic acid functional groups found in **23a**, which is discussed in Chapter 7.

## 5.4 Conclusion

Biodistribution studies comparing a bifunctional triazole based chelate versus the chelates used for the previously synthesized  $^{99m}\text{Tc(I)}$ -tetrazines led to the discovery that the  $^{99m}\text{Tc(I)}$ -complex rather than the tetrazine was the main driving force behind persistent off-target uptake. An alternate  $^{99m}\text{Tc(I)}$ -chelate was identified and shows promise by having an improved clearance profile compared to the imidazole based tridentate chelate used previously. Unfortunately, the addition of a tetrazine moiety for the purposes of pretargeting proved to be a synthetic challenge. A simpler triazole ligand functionalized with a tetrazine was prepared and evaluated *in vivo*, however without the additional polar functional groups, which made the synthesis of the desired chelate complicated, the ligand showed high hepatobiliary uptake similar to the previous generations of  $^{99m}\text{Tc}$ -tetrazines.

## 5.5 References

- (1) Banerjee, S. R.; Pullambhatla, M.; Foss, C. A.; Falk, A.; Byun, Y.; Nimmagadda, S.; Mease, R. C.; Pomper, M. G. *J. Med. Chem.* **2013**, No. 3, 6108–6121.
- (2) García Garayoa, E.; Schweinsberg, C.; Maes, V.; Brans, L.; Bläuenstein, P.; Tourwe, D. A.; Schibli, R.; Schubiger, P. A. *Bioconjugate Chem.* **2008**, *19* (12), 2409–2416.
- (3) Vallabhajosula, S.; Nikolopoulou, A.; Babich, J. W.; Osborne, J. R.; Tagawa, S. T.; Lipai, I.; Solnes, L.; Maresca, K. P.; Armor, T.; Joyal, J. L.; Crummet, R.; Stubbs, J. B.; Goldsmith, S. J. *J. Nucl. Med.* **2014**, *55* (11), 1791–1798.
- (4) Jiang, H.; Kasten, B. B.; Liu, H.; Qi, S.; Liu, Y.; Tian, M.; Barnes, C. L.; Zhang, H.; Cheng, Z.; Benny, P. D. *Bioconjugate Chem.* **2012**, *23* (11), 2300–2312.
- (5) Kluba, C. A.; Mindt, T. L. *Molecules* **2013**, *18*, 3206–3226.
- (6) Maresca, K. P.; Marquis, J. C.; Hillier, S. M.; Lu, G.; Femia, F. J.; Zimmerman, C. N.; Eckelman, W. C.; Joyal, J. L.; Babich, J. W. *Bioconjugate Chem.* **2010**, *21*, 1032–1042.
- (7) Zeglis, B. M.; Brand, C.; Abdel-Atti, D.; Carnazza, K. E.; Cook, B. E.; Carlin, S.; Reiner, T.; Lewis, J. S. *Mol. Pharm.* **2015**, *12* (10), 3575–3587.
- (8) Vito, A.; Alarabi, H.; Czorny, S.; Beiraghi, O.; Kent, J.; Janzen, N.; Genady, A. R.; Alkarmi, S. a.; Rathmann, S.; Naperstkow, Z.; Blacker, M.; Llano, L.; Berti, P. J.; Valliant, J. F. *PLoS One* **2016**, *11* (12), 1–15.

## **Chapter 6: $^{99m}\text{Tc}$ -labeled tetrazines for the development of multimodal imaging probes**

### **6.1 *In vivo* biodistribution of radiolabeled acoustic protein nanostructures<sup>‡</sup>**

Prior work to create  $^{99m}\text{Tc}$ -labeled tetrazines resulted in a lead compound that was used to successfully label a TCO-derived small molecule *in vivo*. Unfortunately, the same approach was not effective for labeling TCO-derived antibodies *in vivo*, but was effective in promoting efficient bioconjugation reactions in solution. To this end, the chemistry reported in chapters 2 and 3 represent a mild and high yielding approach to labeling molecules with  $^{99m}\text{Tc}$ . To demonstrate the broader utility of these  $^{99m}\text{Tc}$  labeled tetrazines as a radiolabeling platform, work was done to create multi-modal ultrasound (US)-SPECT probes. US contrast agents have short half-lives *in vivo* and are susceptible to degradation under normal labeling conditions, thus requiring rapid and highly selective radiochemical methods. The successful development of an US-SPECT probe was achieved, where the approach was described in section 6.1. This work received the MILabs image of the year award and was presented at the Society of Nuclear Medicine and Molecular Imaging (SNMMI) conference in 2018. Furthermore, this work was published in the Journal of Molecular Imaging and Biology, under the citation:

J. Le Floch, A. Zlitni, H. A. Bilton, M. Yin, A. Farhadi, N. R. Janzen, M.G. Shapiro, J. F. Valliant, F. S. Foster, *Mol Imaging Biol.* **2018**, 20(2);230-239

Reprinted with permission from Springer Link.

With respect to this particular citation, I was responsible for the development and characterization of the tetrazine-chelate precursor, the Re-standard, and the  $^{99m}\text{Tc}$ -labeled tetrazine derivative. Aimen Zlitni was responsible for the development of the TCO-functionalized GVs, and the preparation of the  $^{99m}\text{Tc}$ -labeled GVs. Melissa Yin was responsible for the preparation of the GVs, and Johann Le'Floch was responsible for conducting all SPECT-CT imaging.

### 6.1.1 Introduction

Ultrasound (US) is one of the most widely available forms of imaging in biomedicine.<sup>1,2</sup> Its low cost, real-time imaging, high spatial resolution, and portability makes US a staple in hospitals around the world.<sup>3,4</sup> An US image is acquired by placing a transducer to the surface of the patient's skin, which transmits high frequency sound waves. These waves are then scattered or reflected back to the probe when they encounter an interface between structures with different densities (e.g. soft tissue and bone). These reflected waves are then processed by the computer to determine the depth of the density interface, determined by the time that the wave was returned to the probe, and the speed of sound in tissue. Once calculated, the computer can display the image on the

screen as a two-dimensional image. This image can be used to obtain anatomical information, and aid in tracking needle biopsies.<sup>5</sup>

Although US has traditionally been used to obtain anatomical information, the need for US to image biochemical processes within the body has led to the development of US agents for contrast enhanced ultrasound (CEUS) imaging. CEUS, with lipid- or protein-stabilized gas microbubbles, plays an important role in patient care and is evolving as a fundamental screening tool in cardiology, oncology and gynecology.<sup>4</sup> CEUS is used in a variety of clinical applications such as detecting and characterizing focal liver lesions,<sup>6</sup> evaluating cerebral circulation for stroke<sup>7</sup>, brain death diagnosis,<sup>8</sup> kidney,<sup>9</sup> liver and pancreas cancer prognosis, and contrast echocardiography.<sup>10–13</sup> The majority of these clinical applications are based on perfusion imaging and utilize conventional “untargeted” microbubbles.

Considerable efforts have been directed toward the development of targeted microbubbles to allow visualization of specific biomarkers of disease using CEUS (i.e., molecular imaging). Unfortunately, after two decades of investigation, there is only one example of molecular US imaging in the clinic, i.e., targeted US imaging of kinase insert domain receptor in prostate,<sup>3,14</sup> ovarian, and breast cancer patients.<sup>15</sup> The limited number of agents undergoing advanced testing is due to both regulatory issues and limitations of existing microbubbles, which are restricted to the vascular space due to their large size and limited *in vivo* stability (seconds to minutes). Furthermore, other candidates including

solid,<sup>16</sup> liquid,<sup>17</sup> hollow, or phase-change contrast agents have been investigated and demonstrate weak echogenicity,<sup>18,19</sup> and poor stability and require cumbersome synthesis. To maximize the utility of targeted molecular US imaging, there is a need to discover and fully characterize novel nanosized US imaging agents with strong echogenicity, longer *in vivo* stability, and modifiable surfaces to allow the agents to bind to a wide array of disease biomarkers.

A promising US contrast agent based on naturally occurring nanostructures, called gas vesicles (GVs), has been reported.<sup>2</sup> The biological function of the GV is to provide buoyancy to a wide range of aqueous haloarchaea and cyanobacteria. GV has been studied for over 100 years,<sup>20</sup> resulting in considerable knowledge of their biochemical and genetic structure.<sup>21</sup> GV is gas-filled, protein-shelled nanostructures with typical widths of 45–250 nm and lengths of 100–600 nm that exclude water and are permeable to gas.<sup>22</sup>

Because of these properties, Shapiro *et al.* recently explored the potential of GV for contrast enhanced ultrasound imaging.<sup>2</sup> They showed that GV exhibits non-linear ultrasonic properties, which could be due to buckling,<sup>23</sup> substantially improve contrast in ultrasound images and have no adverse side effects in mice. Due to their small volume, they have the potential to access extravascular targets via the enhanced and permeable retention effect,<sup>24</sup> a feature that can be further enhanced through the ability to genetically engineer their protein shell.<sup>25</sup> While the *in vitro* and *in vivo* US properties of GV have been characterized, it is crucial to understand their pharmacokinetic properties and excretion route as the basis from

which to create targeted constructs and fully exploit their potential as molecular ultrasound contrast agents. Here, we report a mild and convenient methodology to functionalize and radiolabel GVs and the first quantitative spatio-temporal distribution study of radiolabeled GVs in mice using single photon emission computed tomography (SPECT) and quantitative tissue counting.

## 6.1.2 Results

### 6.1.2.1 *Radiolabeling*

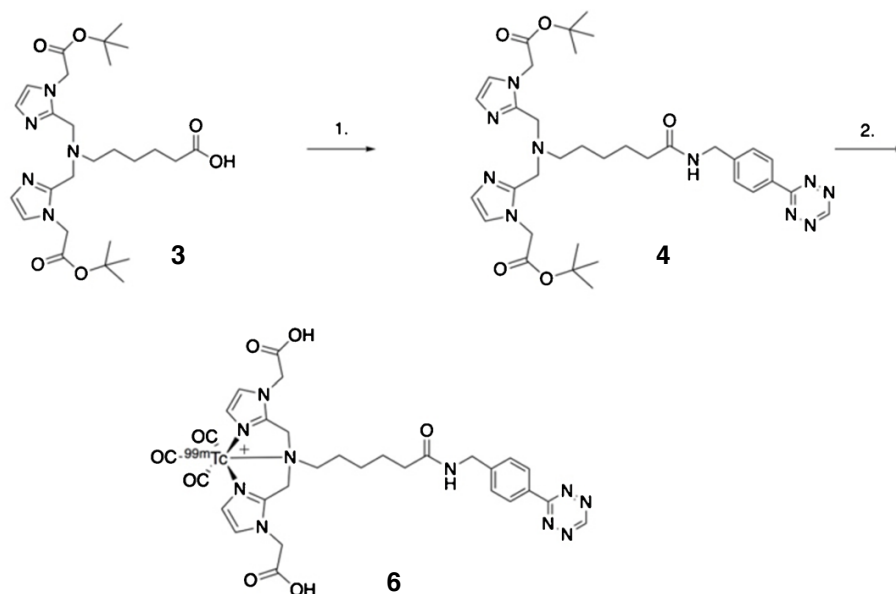
Most  $^{99m}\text{Tc}$  labeling procedures require the use of reducing agents or harsh conditions;<sup>26,27</sup> consequently, an indirect approach to radiolabel GVs was developed. The approach took advantage of the highly efficient and rapid bioorthogonal reaction between trans-cyclooctene and tetrazine.<sup>28</sup> First, excess of (E)-cyclooct-4-enyl-2,5-dioxopyrrolidin-1-yl carbonate (TCO-NHS) was added to GVs to react with the amine groups present on the GV shell. Any residual TCO-NHS was removed by dialysis and TCO-GVs solution concentrated by centrifugal flotation. This was then followed by the addition of a novel [ $^{99m}\text{Tc}$ ]Tz (compound 6 from chapter 2) which was recently reported.<sup>29</sup> The [ $^{99m}\text{Tc}$ ]Tz was first synthesized and isolated in a 45% radiochemical yield and 99% radiochemical purity. The [ $^{99m}\text{Tc}$ ]Tz (140 MBq, 0.5 mL) was then added to a solution of TCO-GVs ( $\text{OD}_{500\text{nm}} = 40$ , 1 mL) and incubated for 30 min at room temperature (Figure 6.1). The  $^{99m}\text{Tc}$  labeled GVs ([ $^{99m}\text{Tc}$ ]GVs) were then purified from any residual

[<sup>99m</sup>Tc]Tz via a simple centrifugation and washing step. With mild centrifugation (300 rcf, 5 min), the labeled GVs were easily isolated from residual [<sup>99m</sup>Tc]Tz and formulated for injection. For quality control, a sample of the labeling mixture before and after purification was taken, sonicated, and injected into an HPLC system equipped with a size exclusion column and a gamma detector. The HPLC gamma trace of the crude mixture showed two broad peaks. The first one represents [<sup>99m</sup>Tc]GVs (retention time = 2 min) while the second represents free [<sup>99m</sup>Tc]Tz (**6**, retention time = 6 min) (Figure S 6.1a). Following purification, the gamma trace only exhibited one peak representing [<sup>99m</sup>Tc]GVs. The desired product was isolated in 59% radiochemical yield with >99% radiochemical purity (Figure S 6.1b).

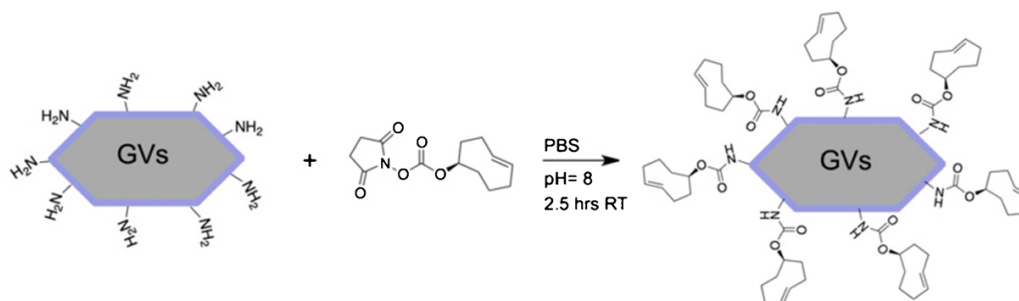
The stability study revealed that, after incubation of the [<sup>99m</sup>Tc]GVs in plasma at 37 °C for 120 min, there was little to no loss of the [<sup>99m</sup>Tc]Tz from the surface of the GVs (Table S 6.1). In addition, 31% of GVs after 60 min are still intact, while the rest had either collapsed or had non-specific binding to plasma components (Table S 6.2). The activity seen in the plasma layer is likely collapsed GVs rather than the release of the [<sup>99m</sup>Tc]Tz based on the radioTLC data (Figure S 6.2). This is consistent with the covalent nature of the bond between the components, which is known to be stable *in vivo*.



**a**



**b**



**c**

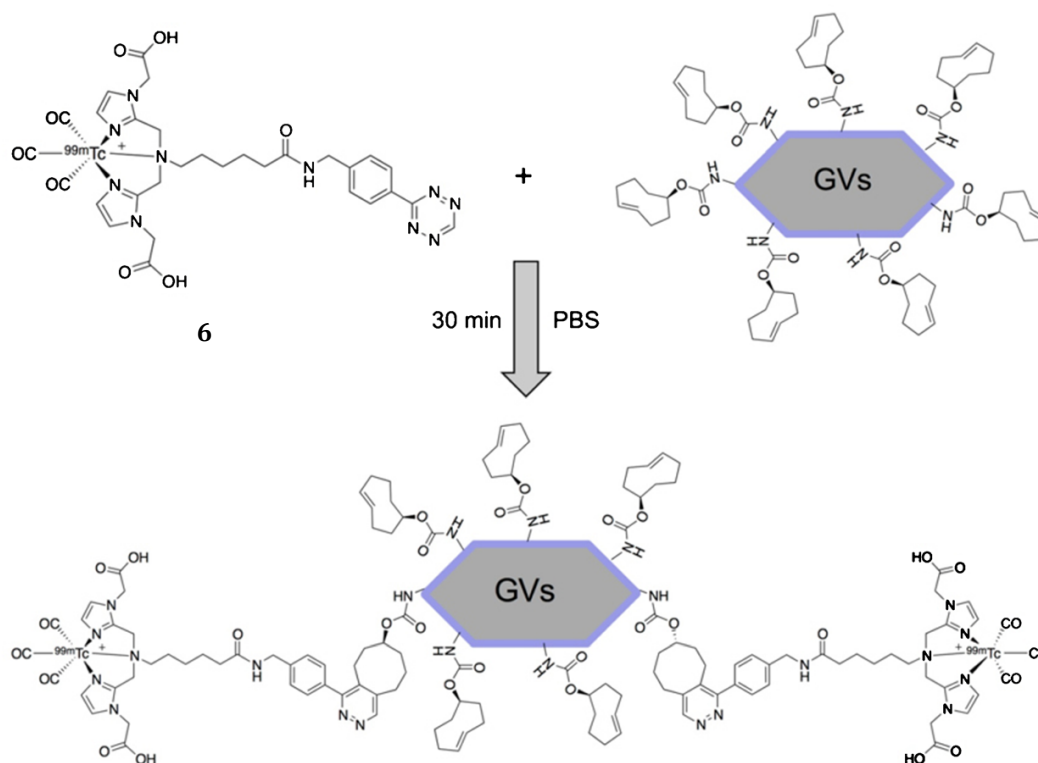


**Figure 6.1** Radiolabeling methodology and processes. A) Synthesis of [ $^{99m}\text{Tc}$ ]Tz complex **6**. (1) PyBOP, DIPEA, DMF, ((4- tetrazine-3-yl)phenyl)methanamine hydrochloride, rt., 12 h (2) (i)  $^{99m}\text{Tc}[\text{Tc}(\text{CO})_3(\text{OH}_2)_3]^+$ , MeOH, saline, 60 °C (MW), 20 min. (ii) TFA, DCM, 60 °C (MW), 6 min. B) Representation of the chemistry used to prepare TCO conjugated GVs. TCO-GVs were purified by dialysis and concentrated to an optical density ( $\text{OD}_{500\text{nm}}$ ) of 40. C) Chemistry used to label TCO-GVs with compound **6**. [ $^{99m}\text{Tc}$ ]Tz (**6**) was added to TCO-GVs in PBS for 30 min and the [ $^{99m}\text{Tc}$ ]GVs purified by centrifugal flotation.

#### **6.1.2.2 Biodistribution: Ex Vivo Tissue Counting and SPECT**

The distribution of [ $^{99m}\text{Tc}$ ]GVs was evaluated by *ex vivo* tissue counting following necropsy and dynamic SPECT/CT imaging. The tissue counting studies revealed, 5 min post [ $^{99m}\text{Tc}$ ]GV injection, more than 5 % ID/g uptake in the gall bladder, liver, lungs, spleen, and bladder/urine while all other mouse organs or fluids typically exhibited less than 2% ID/g uptake (Figure 6.2a). A small amount of [ $^{99m}\text{Tc}$ ]GVs was detected in the blood 5 min following injection which eventually decreased to 0.5 % ID/ g after 2 h. Uptake at sites that showed early and high localization remained high throughout the duration of the study. The biodistribution of [ $^{99m}\text{Tc}$ ]Tz alone also showed high gall bladder and small intestine concentrations, but there was significantly less activity in the liver, spleen, and lungs (particularly at later time points). It also showed faster blood

clearance compared to [ $^{99\text{m}}\text{Tc}$ ]GVs (Figure 6.2b).

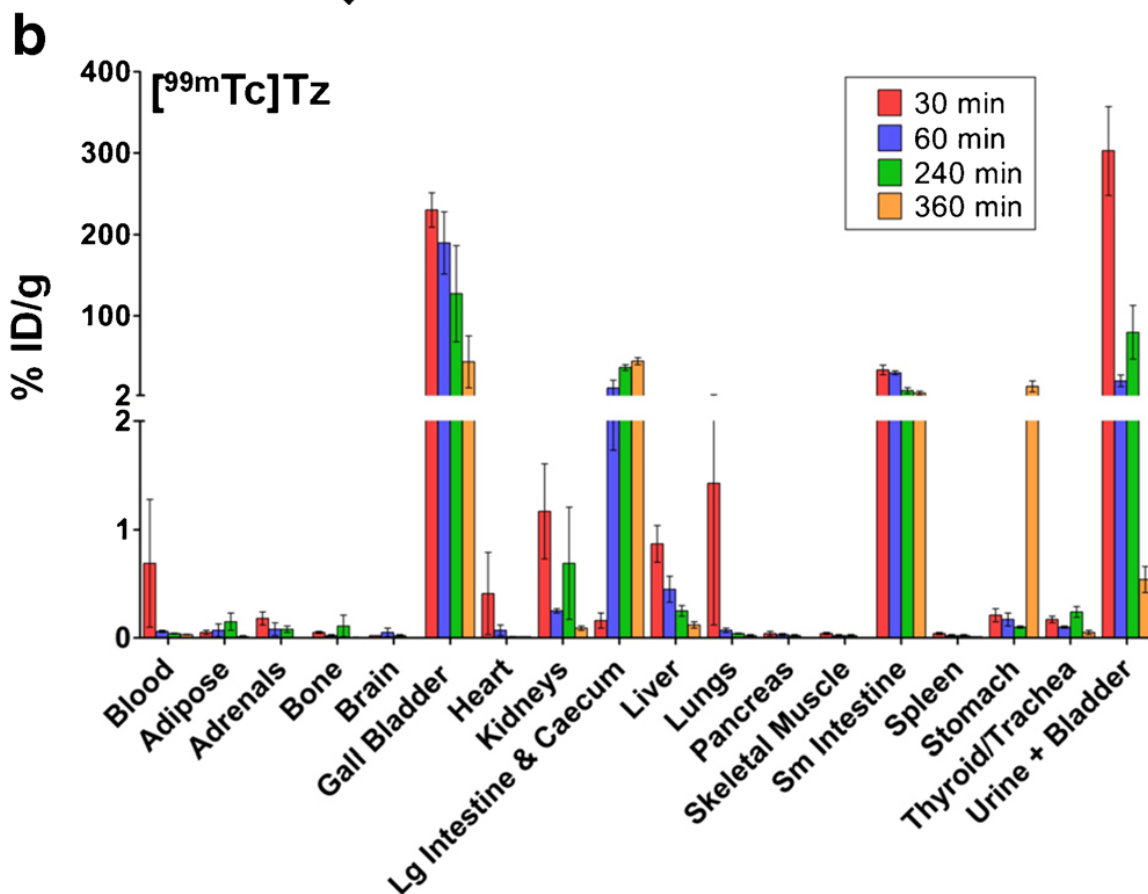
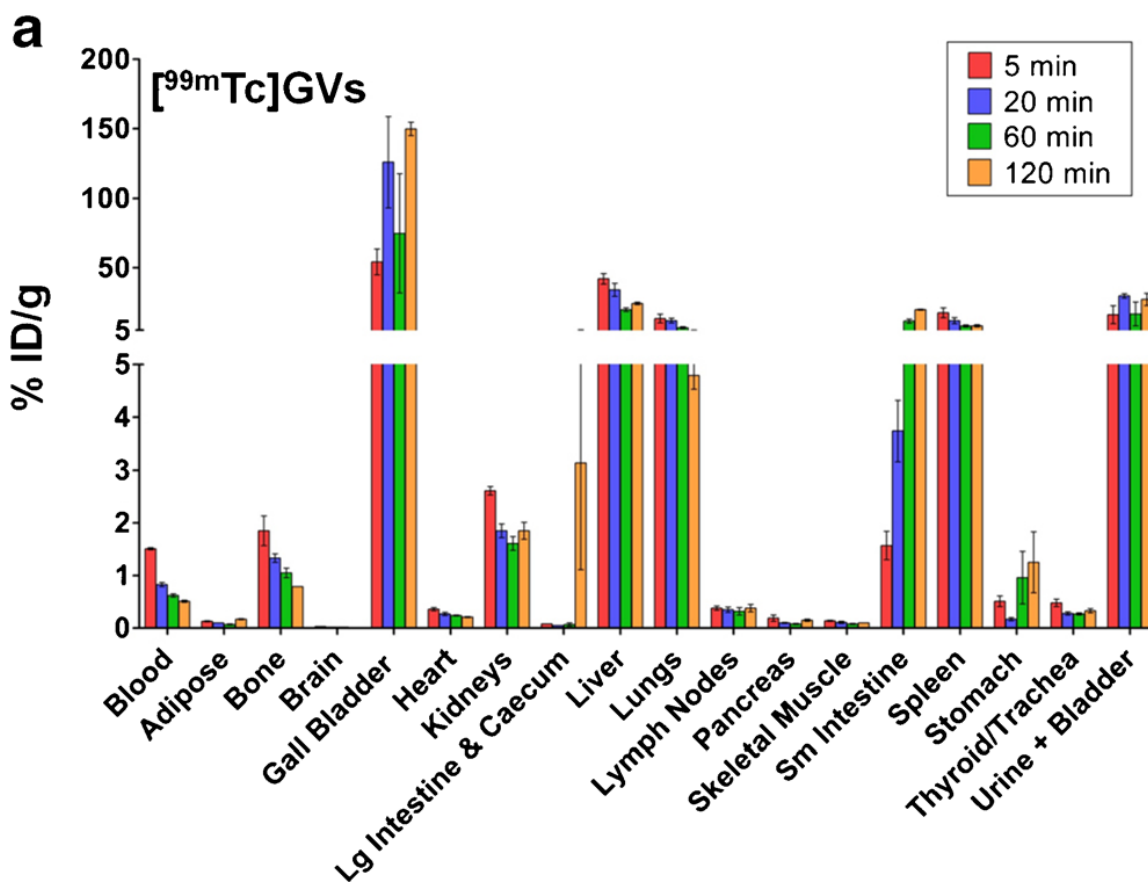


**Figure 6.2** Quantitative *ex vivo* tissue counting biodistribution data for [ $^{99m}\text{Tc}$ ]GVs and [ $^{99m}\text{Tc}$ ]Tz (**6**). Groups of mice ( $n = 3$ / time point) were euthanized at 5, 20, 60, and 120 min ([ $^{99m}\text{Tc}$ ]GVs) or at 30, 60, 240, and 360 min ([ $^{99m}\text{Tc}$ ]Tz). Tissues and fluids were then collected and activity counted. A) The uptake of [ $^{99m}\text{Tc}$ ]GVs was mainly found in the gall bladder, liver, lungs, small intestine, spleen, and bladder. B) In contrast, [ $^{99m}\text{Tc}$ ]Tz was mainly found in the gall bladder, small intestine, large intestine and cecum, and bladder. Data are reported in % injected dose (ID)/g  $\pm$  SEM.

In Figure 6.3, the 3D maximum intensity projections (MIP) of the *in vivo* dynamic SPECT data showed the spatial extent and signal intensity variations in the volume occupied by [ $^{99m}\text{Tc}$ ]GVs in mouse organs at time points corresponding to those of the tissue counting studies. There was no large spatial variation in signal intensities observed 2 h following [ $^{99m}\text{Tc}$ ]GVs injection; therefore, the spatial uptake of [ $^{99m}\text{Tc}$ ]GVs in a given organ was relatively uniform. Overall, 3D MIP findings correlated with the *ex vivo* tissue counting biodistribution findings.

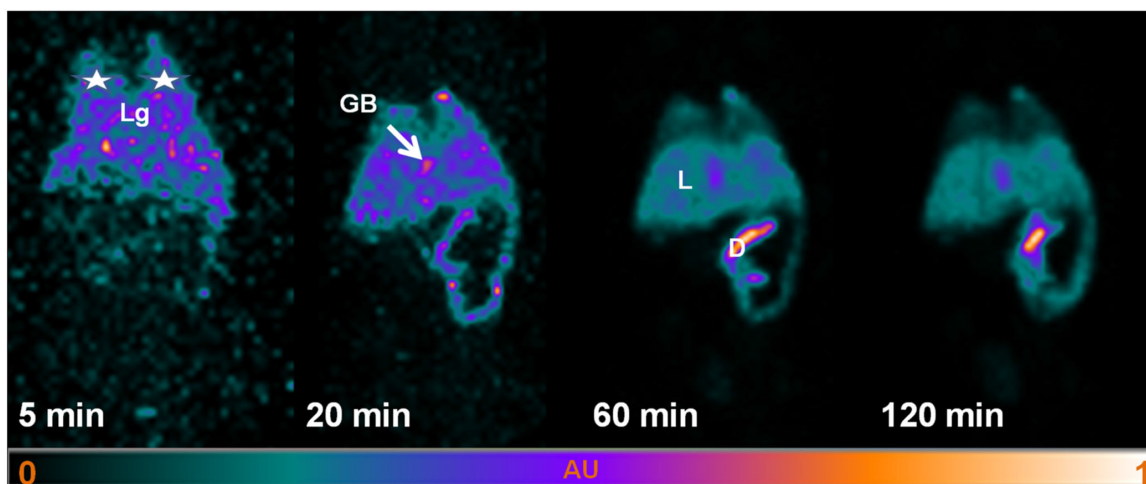


**Figure 6.3** Maximum intensity projection (MIP) of SPECT images following  $[^{99m}\text{Tc}]$ GVs injection. Rapid uptake of  $[^{99m}\text{Tc}]$ GVs is shown in the lungs (white stars, Lg), gall bladder (GB) and liver (L), followed by duodenum (D) and small intestines over time.

Likewise, *ex vivo* tissue counting and *in vivo* SPECT quantitative biodistributions were also in good overall agreement at the studied time points (Figure 6.4), notably the reticuloendothelial system (RES) uptake (lungs, liver, spleen), the increase localization over time in the duodenum/small intestine, and the relatively short lived presence of GV in the blood.

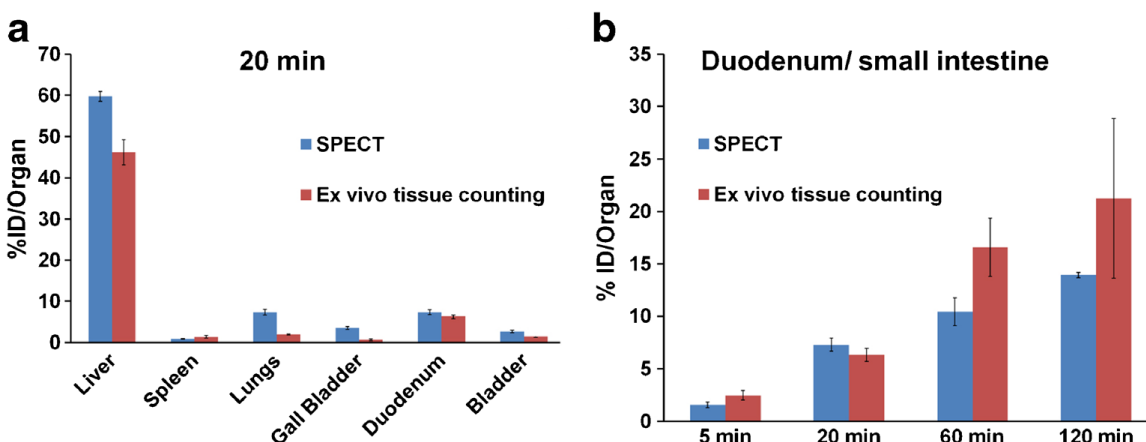


**Figure 6.4** *Ex vivo* tissue counting and SPECT biodistribution. A) Comparison of both biodistribution data reporting the uptake of [ $^{99m}\text{Tc}$ ]GVs in major organ/tissues 20 min following injection. B) [ $^{99m}\text{Tc}$ ]GVs uptake in the duodenum (SPECT) and small intestine (*ex vivo* tissue counting) showing a similar increase at corresponding time points (4 time points,  $n = 3$  per time point). Each SPECT reported values were calculated using the segmentation results multiplied by the volume of the corresponding segmented organ. Data are reported in %ID/organ  $\pm$  SEM (*Ex vivo* counting data is not normalized for weight, 4 time points,  $n = 3$  per time point, SPECT  $n = 23, 55, 31$ , and  $8$  at  $5, 20, 60$ , and  $120$  min, respectively).

In Fig. 6.5, 3D segmentation rendering of the mouse organs allowed the calculation of the volume occupied by [ $^{99m}\text{Tc}$ ]GVs in each organ (Table S 6.3). The volumes of these organs derived from the segmentation are similar to these found in healthy mice in the literature, e.g., the liver and the gall bladder volumes.<sup>30,31</sup> The *in vivo* dynamic uptake of [ $^{99m}\text{Tc}$ ]GVs in segmented organs is

Ph.D. Thesis – H. Bilton; McMaster University – Chemistry and Chemical Biology

reported in Figure 6.5b. The overall uptake of native versus collapsed [ $^{99m}\text{Tc}$ ]GVs by organs was similar. In addition, the change in the amount of activity and volume injected in mice did not alter the overall biodistribution of [ $^{99m}\text{Tc}$ ]GVs in mouse organs and all SPECT data was therefore pooled together. Based on this data, [ $^{99m}\text{Tc}$ ]GVs were rapidly taken up by the liver, spleen, and lungs, reaching a plateau within 10 min. In contrast, the uptake of [ $^{99m}\text{Tc}$ ]GVs in the gall bladder peaked 20 min following injection and then significantly decreased for 30 min ( $p = 0.001748$ ). The liver showed a peak value of  $32 \pm 3$  % ID/cm<sup>3</sup> at  $8 \pm 2$  min (Figure 6.5b). In contrast, [ $^{99m}\text{Tc}$ ]GVs had a slow uptake in the duodenum for the first 20 min, but the uptake increased over time (Figure 6.5b). [ $^{99m}\text{Tc}$ ]GV uptake, reported as an average between 10 and 120 min in % ID/cm<sup>3</sup>  $\pm$  SD, was consistently observed in the liver ( $30 \pm 2$ ), spleen ( $4 \pm 1$ ), lungs ( $11 \pm 1$ ), gall bladder ( $76 \pm 24$ ), as well as in the duodenum and small intestine ( $21 \pm 7$ ), and bladder ( $8 \pm 4$ ). The averaged uptake rate constant of the gall bladder was 2-, 4-, and 9-fold faster than the uptake rate constants of the liver, the lungs, and the spleen, respectively (Table S 6.4).



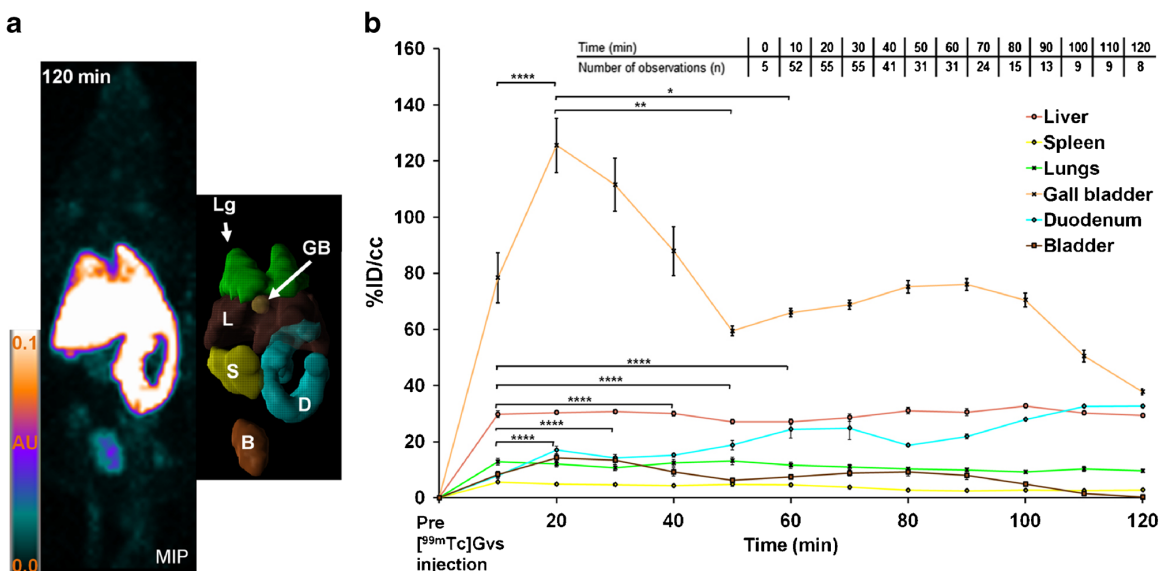


**Figure 6.5** MIP, 3D segmentation, and time activity curves (TACs) of segmented organs. A) MIP of SPECT data and associated 3D segmentation of individual organs at 120 min (lungs in green (Lg), liver in brown (L), gall bladder (GB) in light orange, spleen (S) in yellow, duodenum in light blue (D), and bladder in light brown (B)). B) TACs showed the uptake of  $[^{99m}\text{Tc}]\text{GVs}$  in segmented organs. TACs are reported in percent injected dose per volume of tissue ( $\% \text{ID}/\text{cm}^3$ ) by averaging together data acquired within a time periods of 10 min to yield the mean and associated standard error of the mean (SEM). The inset shows the number of observations (n) for each time point. Significant statistical differences are only shown for the gall bladder and duodenum for each data point between 10 and 60 min (\* $p \leq 0.05$ , \*\* $p \leq 0.01$ , \*\*\*\* $p \leq 0.0001$ ).

### 6.1.2.3 *Fluorescence Imaging*

To confirm and better understand the spatial distribution of GVs at the microscopic level in liver and spleen tissues, fluorescence imaging on histology was performed. GVs were successfully tagged with Alexa-488 fluorophore (Alexa488-GVs) and were allowed to circulate long enough to distribute in all mouse organs including in the small intestines. Native GVs did not exhibit any fluorescent signals in the liver or in spleen tissues. In contrast, there was a marked and consistent fluorescent signal from Alexa488-GVs in the liver and spleen tissues (Figure 6.6).

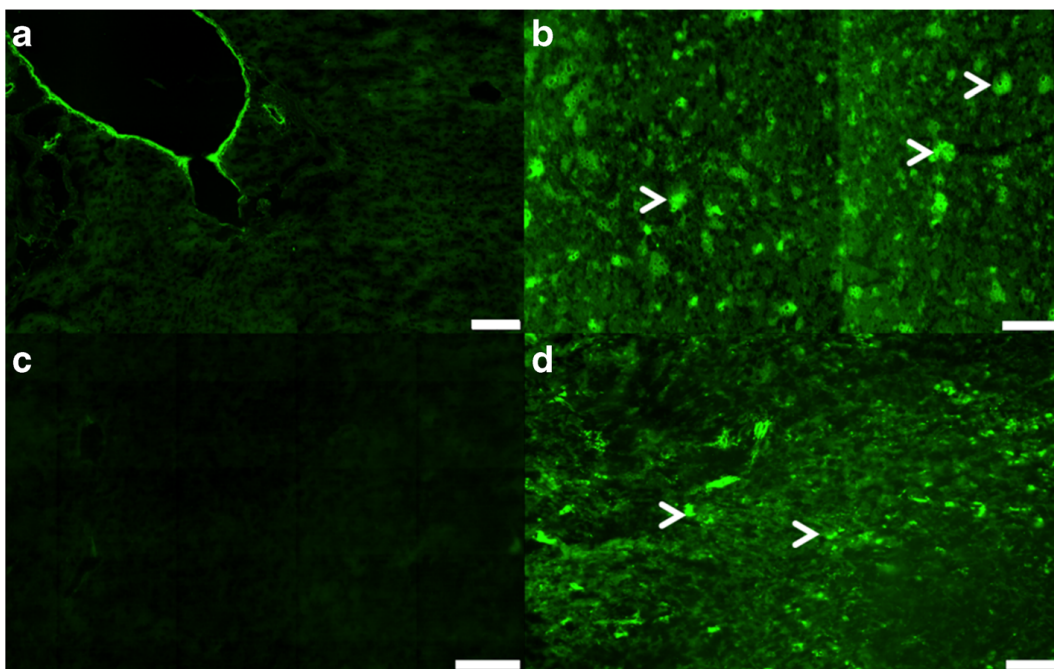


**Figure 6.6** Fluorescence imaging of the liver and spleen tissues. Native GVs in A) the liver and in C) the spleen tissues showing only autofluorescence. Alexa 488 fluorophore tagged GVs in B) the liver and D) spleen tissues showing an increase

green signal intensity. White arrows show clustering of Alexa488-GVs in both tissues. Scale bar is 100  $\mu\text{m}$  (a–c) and 50  $\mu\text{m}$  (d). Magnification:  $\times 20$  (a, c) and  $\times 10$  (b, d).

### 6.1.3 Discussion

This study is the first to report the radiolabeling and biodistribution of GVs using both *ex vivo* tissue counting and SPECT imaging in mice. The labeling was performed using bioorthogonal chemistry between TCO-functionalized GVs and a  $^{99\text{m}}\text{Tc}$  labeled tetrazine. The indirect approach avoided degradation of the GVs and non-specific labeling that could occur when using conditions typically employed during direct technetium labeling procedures. With this method, [ $^{99\text{m}}\text{Tc}$ ]GVs were produced in a good radiochemical yield and high purity where the radiolabel-GV conjugate demonstrated high stability in plasma.

Twenty minutes following administration, the biodistribution and imaging studies of the labeled GVs in organs revealed that the reticuloendothelial system (RES) absorbed 84% of native and collapsed [ $^{99\text{m}}\text{Tc}$ ]GVs with the biliary system and small intestine assimilating the majority of the remaining material (13%). Almost no [ $^{99\text{m}}\text{Tc}$ ]GVs remained in the blood 2 min after their injection, and they were more rapidly taken up by the gall bladder than the liver. Fluorescence imaging of the liver and spleen tissues further confirmed these findings.

#### **6.1.3.1 RES Uptake**

The uptake of radiolabeled GVs in non-target tissues is not surprisingly due to resident mature macrophages located close to the vessel walls,<sup>32</sup> removing [<sup>99m</sup>Tc]GVs from blood circulation rapidly. Furthermore, uptake and retention in the liver, spleen, and lungs is likely from Kupffer, red pulp macrophages, and reticular cells, respectively, present in these tissues. Given the nanometer size, lemon shape, negatively charged surface (– 49 mV) of the *Halobacterium salinarum* GVs, and their low dispersibility/hydrophobicity,<sup>22</sup> their rapid uptake by the RES was similar to other types of nanoparticles.<sup>33,34</sup> Indeed, intact and degraded [<sup>99m</sup>Tc]GV accumulation and saturation in the liver are likely due to their size since the liver sieve, i.e., the existence of vascular fenestrations measuring 50–100 nm along the liver margin,<sup>35</sup> would potentially facilitate non-specific uptake of individual radiolabeled GVs and degraded products. Likewise, [<sup>99m</sup>Tc]GVs and degraded products were hardly taken up by the kidneys since only smaller-sized nanoparticles with diameters below 5 nm are filtered by the renal system when delivered intravenously.<sup>36</sup> Furthermore, the lemon shape and ability to change shape of the [<sup>99m</sup>Tc]GVs, during gas exchange, could also be factors playing a role in biodistribution and, especially, in their spatial distribution in a given organ since Black *et al.* showed that differences in shape of radiolabeled gold nanoparticles clearly influenced their uptake and spatial distribution not only in tumors but also in the liver.<sup>37</sup>

#### **6.1.3.2      *Gall Bladder and Intestine Uptake***

Interestingly, uptake within the biliary system and intestines accounted for 13% of [ $^{99m}\text{Tc}$ ]GVs 20 min following administration. Of these organs, uptake in the gall bladder and duodenum was seen immediately, with an increase in uptake in these organs up to 20 min post injection. Thereafter, uptake was observed in the rest of the small intestine. Since no [ $^{99m}\text{Tc}$ ]GVs were observed in the stomach, these results suggest that radiolabeled GV s were captured by the hepatocytes in the liver, then secreted through the hepatic ducts and stored into the gall bladder. Assuming the endocytosis of [ $^{99m}\text{Tc}$ ]GVs or [ $^{99m}\text{Tc}$ ]GV fragments by hepatocytes, it is likely that radiolabeled GV s start degrading due to protease digestion in the liver. Likewise, the two times faster rate of uptake of [ $^{99m}\text{Tc}$ ]GVs in the gall bladder would suggest some intact GV s reaching the gall bladder, followed by a similar degradation pathway of [ $^{99m}\text{Tc}$ ]GV population to that in the liver.

When the bile is secreted, further degraded radiolabeled GV s were likely subsequently released from the gall bladder to the duodenum through the common bile duct that joins the common hepatic duct and connects to the duodenum. Hence, the distribution in the gall bladder and small intestine is therefore likely explained by the size of individual radiolabeled GV s and/or cluster of radiolabeled GV s and of the presence of fragmented [ $^{99m}\text{Tc}$ ]GVs that are all compounds too large to be cleared by the kidneys.<sup>36</sup>

#### **6.1.3.3        *GVs as Potential Ultrasound Contrast Agent***

The biodistribution studies showed a relatively short-lived presence of GVs in the blood. This limits the utility of native GVs for tumor imaging, as GVs will likely not circulate long enough to extravasate into target tissues. Ongoing research efforts are focused on investigating the impact of shell alterations of native GVs on their biodistribution as well as the effect of PEGylation of native and modified GVs on their pharmacokinetic properties. In addition, a better understanding of the integrity and degradation of radiolabeled GVs, in particular those with surface modifications to prolong circulation, will also need to be further investigated. Notably, no acute toxicity or adverse effects in mice were observed in our study where up to five times higher concentrations were used than in previous studies.<sup>2</sup> However, more extensive toxicity studies on the optimal construct once developed will be needed prior to translation.

#### **6.1.4 Conclusion**

A convenient method for radiolabeling GVs with  $^{99m}\text{Tc}$  along with the first quantitative biodistribution study of [ $^{99m}\text{Tc}$ ]GVs was reported. Results in healthy mice showed, not unexpectedly, a rapid uptake of radiolabeled GVs by the RES, providing a baseline for enhancing the *in vivo* properties of this novel class of ultrasound contrast agents. The reported labeling strategy conveniently offers the means to assess the impact of ongoing efforts associated with adding different pharmacokinetic modifiers and targeting molecules.

## 6.1.5 Experimental

### 6.1.5.1 *Gas Vesicle Preparation*

GV culturing, isolation and purification were carried out as previously described.<sup>2,38</sup> In brief, *Halobacteria* sp. NCR-1 (Carolina Biological Supply, Burlington, NC) were cultured in high salt Carolina media, at 42 °C, in an incubation shaker at 100 revolution per minutes (rpm) (Ecotron, Infors AG, Switzerland). GVs were then isolated using TMC lysis buffer and purified through multiple rounds (5 to 6) of centrifugation at 300 rcf with the centrifuge maintained at 4°C.

### 6.1.5.2 *Radiolabeling of GVs with Technetium-99m*

The <sup>99m</sup>Tc labeled tetrazine ([<sup>99m</sup>Tc]Tz), compound **6** (Figure 6.1a), was prepared following literature methods in good radiochemical yield and high purity (Figure S 6.1a, b).<sup>26,29</sup> Trans-cyclooctene (TCO)-conjugated GVs (TCO-GVs) were prepared by adding (E)-cyclooct-4-enyl-2,5-dioxopyrrolidin-1-yl carbonate (TCO-NHS) (855.1 µg, 3.2 µmol; Click Chemistry Tools, 1016-100) in dimethyl sulfoxide (DMSO, 197.3 µL) to a solution of GVs (OD<sub>500nm</sub> = 55.2, 1.8 mL) in PBS at pH 8. The solution was left to mix on a shaker for 2.5 h and the desired TCO-GVs purified by dialysis using 6–8 kD dialysis membrane submerged in PBS overnight (Spectra/Por 1 Dialysis Membrane, Spectrum Labs, USA). The TCO-GVs were then concentrated using centrifugal flotation at 300 rcf for 15 min (Figure 6.1b). Compound **6** (29 MBq, 100 µL) was then added to a solution of

TCO-GVs ( $OD_{500nm} = 50$ , 400  $\mu$ L) at room temperature and left shaking for 30 min.  $^{99m}\text{Tc}$  labeled GVs ( $[^{99m}\text{Tc}]\text{GVs}$ ) were then washed with PBS and purified from any residual **6** using a single round of centrifugal flotation (Figure 6.1c). To assess the purity, a sample of the mixture was taken before and after purification, sonicated and injected into a HiTrap size-exclusion cartridge attached to a high-performance liquid chromatography (HPLC) fitted with a gamma detector. The column was eluted with 100 mM ammonium bicarbonate in water at 1 mL/min flow rate (isocratic elution 0–8 min 100 %).

#### **6.1.5.3.      *Stability Study in Plasma***

To determine the stability of  $[^{99m}\text{Tc}]\text{GVs}$  in plasma, samples were prepared following the procedures described above. To assess the purity, a sample of the mixture was taken and spotted on an iTLC-SG glass microfiber chromatography paper (Agilent Technologies, SGI0001) plate and run with a mobile phase of 75 % MeOH, 25 %  $\text{H}_2\text{O}$ , and visualized on a Bioscan AR-2000 Imaging Scanner. The purified  $[^{99m}\text{Tc}]\text{GVs}$  (3.4 MBq, 100  $\mu$ L) was then added to mouse plasma (900  $\mu$ L) and incubated on a shaker for 120 min at 37 °C. Samples were taken at 2, 5, 10, 20, 60, and 120 min and analyzed for purity by RadioTLC (Figure S 6.2). At 60 and 120 min, 450  $\mu$ L samples were taken, and the GV layer was separated from the plasma by centrifugal flotation (400 rcf, 10 min). The activity in the plasma and GV layers was measured using a dose calibrator.



#### **6.1.5.4 Biodistribution Studies**

All experimental procedures were approved by the Animal Care Committees at Sunnybrook Research Institute and McMaster University.

#### **6.1.5.5 Quantitative Tissue Counting**

Studies were performed on healthy female, 5–6-week-old CD1 mice (Charles River Laboratory, Kingston, NY). Mice were injected intravenously (i.v.) with 0.7 MBq of [ $^{99m}\text{Tc}$ ]Tz as a control or with 0.4 MBq of [ $^{99m}\text{Tc}$ ]GVs via the tail vein. Mice were anesthetized with 3 % isoflurane and euthanized by cervical dislocation at 30, 60, 240, and 360 min for the control, while the [ $^{99m}\text{Tc}$ ]GVs studies were performed at 5, 20, 60, and 120 min post-injection (n = 3 per time point). Blood, adipose, bone, brain, gall bladder, heart, kidneys, large intestine and cecum (with contents), liver, lungs, lymph nodes (axillary and brachial), pancreas, skeletal muscle, small intestine (with contents), spleen, stomach (with contents), thyroid/trachea, and bladder with urine and tail were collected, weighed, and counted in an automated gamma counter (PerkinElmer Wallac Wizard 1470 gamma counter, PerkinElmer, Waltham, USA). Decay correction was used to normalize organ activity measurements to time of dose preparation for data calculations with respect to the injected dose (reported as % injected dose (ID) per gram and % ID per organ).

#### **6.1.5.6        *SPECT/CT Imaging***

Studies were performed following i.v. injection of intact or collapsed [<sup>99m</sup>Tc]GVs at a constant flow rate of 500 µL/min (New Era Pump Systems, NE-1000, NY, USA) via the tail vein of healthy CD1 or SHO mice (Charles River Laboratory, 4–6 weeks of age, n = 6). Mice were anesthetized with isoflurane (2–2.5 % maintenance, Univentor 410, Univentor Ltd., Malta) and prepared for the GV injection. Collapsed GVs were obtained by reaching the collapse pressure inside a syringe (by capping the nozzle and pushing the piston). Once collapsed, GVs lose their ultrasonic contrast properties and cannot be investigated with ultrasound. Following catheterization, mice were placed in prone position on the mouse bed, which maintained its body temperature at 37 °C. The amount of activity injected ranged from 2.2 to 20.5 MBq. The volume injected ranged from 80 to 330 µL, and the concentration ranged from 18 to 33 OD<sub>500nm</sub>. SPECT imaging was performed during and immediately after GV injection.

Fast dynamic whole body scans were performed on a SPECT imaging system (VECTor+, MILabs, Utrecht, The Netherlands) using a high-energy collimator (HE-UHR-RM, MILabs) with 156 clustered multi-pinholes collimator of 1.8 mm. An image was acquired prior to [<sup>99m</sup>Tc]GVs injection. Following activity measurement in the syringe with a dose calibrator (Capintec Inc., NJ, USA), subsequent images were then collected by running the same acquisition with a scan time ranging from 33 to 84 s and for up to 120 min during and after injection of [<sup>99m</sup>Tc]GVs. For calibration of SPECT images, a 1-mL syringe filled with a

solution of known activity of [ $^{99m}\text{Tc}$ ]GVs in PBS (measured by the dose calibrator for each experiment) was scanned using the same collimator after the animal experiment. To obtain anatomical details, anesthetized mice were then scanned using an *in vivo* X-ray microtomography system (SkyScan 1176, Bruker Corp., Kontich, Belgium) at 35  $\mu\text{m}$  pixel resolution and 360° scanning with a rotation step of 1.4° per image, 66 ms exposition time, 1 mm aluminum filter, 65 kV, and 385  $\mu\text{A}$ .

#### **6.1.5.7 SPECT/CT Data Processing and Statistical Analysis**

All SPECT images were reconstructed using the pixel-based maximum likelihood expectation maximization (POSEM, VECTor+ software, MILabs, The Netherlands) algorithm using 16 subsets, 15 iterations, and a small voxel size of 0.512 mm<sup>3</sup>.<sup>39,40</sup> During reconstruction, correction for scattering is performed using a triple-energy window method<sup>41</sup>, i.e.,  $^{99m}\text{Tc}$  energy window with the photopeak window centered at the peak of the data set (142 keV), with a width set to 20 %, together with the left and right background windows centered at 125 and 159 keV, with a width set to 4.5 and 3.6 %, respectively. After reconstruction, the images were corrected for decay using the half-life of  $^{99m}\text{Tc}$  (6.02 h), attenuation correction was applied, and quantified SPECT images were obtained by using a calibration factor.<sup>42,43</sup> Images were then processed using a semi-automatic segmentation based on the local mean analysis and 3D rendering tools in PMOD (PMOD Technologies LLC, v3.7, Zurich, Switzerland). Briefly, the segmentation

method first separates the mouse body from the background noise using a histogram-based algorithm. Secondly, the local mean time activity curve (TAC) and background noise are computed in the vicinities of selected points within mouse organs. Finally, the image is segmented into regions, which are merged according to their TACs in a hierarchical manner.<sup>44</sup> The resulting segmentation was checked slice by slice for imperfections, and any corrections including erosion, dilation, and/or deletion of voxels were made using PMOD morphological operations. TACs were generated according to individual segmented organs and are reported by averaging together data acquired within a time period of 10 min to yield the mean and associated standard error of the mean.

CT images were reconstructed using an implementation of the Feldkamp cone-beam algorithm and beam hardening, and ring artifacts were corrected in Nrecon (Bruker Corp.).<sup>45</sup> The registration of CT and SPECT images and the movies were generated using PMOD Fusion tools (PMOD Technologies LLC).

Statistical analyses were performed using NCSS 11 (NCSS, LLC. Kaysville, UT, USA). All data are expressed as mean  $\pm$  SEM where n is the number of observations in the dynamic *in vivo* SPECT biodistribution study. The reported standardized uptake values (%ID/cm<sup>3</sup>) for each tissue were analyzed over the time period studied using two-sample test followed by a Mann-Whitney U test and a Kolmogorov-Smirnov test. An alpha error level of 5 % was used for the tests.

#### **6.1.5.8      *Fluorescence Imaging from Histology***

GVs were labeled with a fluorophore (Alexa- 488, Sigma, USA) using standard amino-N-hydroxysuccinimide crosslinking.<sup>25</sup> Two healthy mice were injected i.v. with either Alexa-488 tagged GV's or native GV's (control) ( $OD_{500nm} = 20, 130 \mu L$ ) and euthanized 20 min following injection. The liver and spleen were collected, embedded in optimal cutting temperature compound, and snap frozen in nitrogen, then stored in a  $-80^{\circ}C$  freezer. Subsequently, the liver and spleen tissues were sectioned ( $4-5 \mu m$ , Cryostat, LEICA CM 3050 S, USA). Slides were then observed using an Olympus microscope (Olympus VS120 Virtual Slide Microscope, VS120-L100-W, ON, Canada) with identical acquisition parameters. Images were stored in the proprietary format and, later, visualized on a personal computer using OlyVIA (OLYMPUS OlyVIA 2.9). For each liver and spleen, up to three sections were observed.

### **6.2    The development of a nanoscale multimodal ultrasound-photoacoustic dual imaging agent <sup>§</sup>**

<sup>§</sup> This work was done in collaboration with Samantha Slikboer. I was responsible for the synthesis of the TCO-GVs, preparation, optimization and purification of the IR-GVs. Samantha Slikboer was responsible for the synthesis and characterization of the nearIR-tetrazine dye precursor, and conducting the US/PA

imaging experiments. Yohannes Soenjaya was responsible for the isolation and purification of the GVs, and preliminary PA/US imaging.

### 6.2.1 Introduction

The benefits of using CEUS imaging agents for non-invasive detection of cancer and other diseases has previously been discussed.<sup>46</sup> Although US contrast agents can be used to better differentiate disease from surrounding tissue,<sup>47</sup> dual-modality imaging agents can be used to provide complementary information such as the ability to obtain structural and functional images simultaneously.

Photoacoustic (PA) imaging is a method that takes advantage of both the high contrast of optical imaging, and the high resolution and depth of penetration of ultrasound through the application of the photoacoustic effect.<sup>48</sup> PA imaging works by sending high intensity, short-pulsed lasers with pulse widths of several nanoseconds to the area of interest. These lasers cause local heat deposition resulting in thermoelastic expansion. This thermoelastic expansion causes the emission of acoustic waves that are then detected by the transducer (Figure 6.7). PA imaging provides high-resolution ( $\sim 100 \mu\text{m}$ )<sup>49</sup> images and greater penetration depth than other optical imaging modalities and therefore has the potential to be used in a clinical setting.

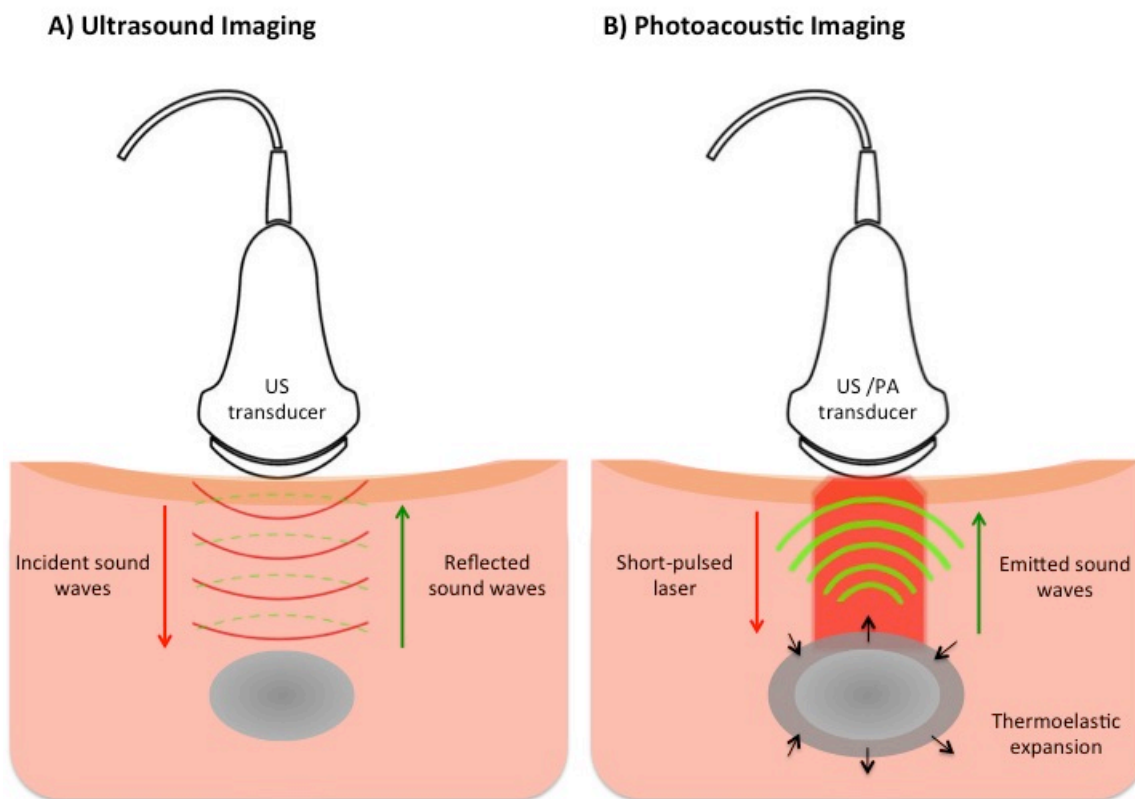


**Figure 6.7** Schematic of ultrasound and photoacoustic imaging systems.

PA and US are complementary imaging modalities, as they both utilize sound waves for detection. This means that PA probes can easily be integrated into existing US machines. PA imaging can further complement US contrast agents, as healthy tissues have very low acoustic scattering with PA. Furthermore, the PA signal from certain classes of contrast agents can easily be differentiated from the innate PA signal from oxy and deoxy-hemoglobin, resulting in very low background. The use of a multimodal-imaging agent can provide a

more comprehensive characterization of tissues than US alone, and can aid in anatomical referencing during PA image reconstruction.<sup>48,50</sup>

Despite the potential advantages, few dual modality US-PA contrast agents have been developed. For the few that have been reported, most involve simple encapsulation of a PA agent, or require integration of the PA contrast agent into the shell of the US agent.<sup>48,51–53</sup> Furthermore, majority of these agents are micron sized particles, limiting them to the vasculature. Herein we describe a simple synthesis of a US-PA contrast-imaging agent through the surface functionalization of nanoscale gas vesicles (GVs) with a tetrazine-functionalized IR-783 PA dye (IR-Tz).

## 6.2.2 Results and Discussion

### 6.2.2.1 *Functionalization of TCO-GVs with a tetrazine-nearIR dye derivative*

Building off of the TCO-GV platform developed in section 6.1.2.1,<sup>46,54</sup> TCO-GVs were functionalized with an IR-783-tetrazine PA dye (IR-Tz) to prepare a multimodal US/PA imaging agent. The TCO-GVs ( $OD_{500nm} = 40$ , 300  $\mu$ L) were combined with the IR-Tz (1.5 mg, 1.4  $\mu$ mol) and gently shaken for 30 min to produce an IR-GV conjugate that was purified through two rounds of centrifugal floatation (300 rcf, 1 hour).



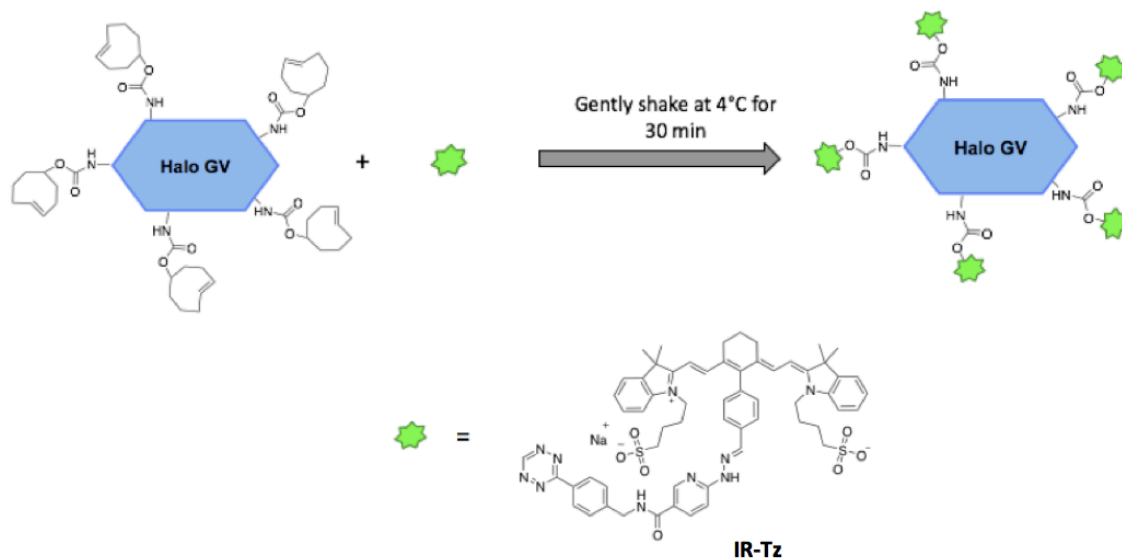


**Figure 6.8** Synthesis of IR-GVs.

To confirm the conjugation of the IR-Tz to the TCO-GV surface, the absorption spectra of TCO-GVs, IR-Tz, and IR-GVs were measured from 260-1060 nm on a Tecan-96 well plate reader (Figure 6.9). The spectrum of IR-Tz shows two maxima centered at 670 and 780 nm. These same maxima were seen in the spectrum of the IR-GV derivative, which is consistent with coupling of the dye-tetrazine to the TCO-GV surface. Note that the absorbance values for the IR-GVs are lower than those of IR-Tz due to a concentration difference of IR-Tz in solution vs. on the GV surface. To further explain, TCO-GVs were incubated in a 450  $\mu$ M solution of IR-Tz, however upon purification, the unbound IR-Tz was removed, thus lowering the concentration of IR-Tz in the sample considerably.

The visible color change between TCO-GVs and IR-GVs is a further indication that the reaction between the dye-tetrazine and the TCO-GV was successful.

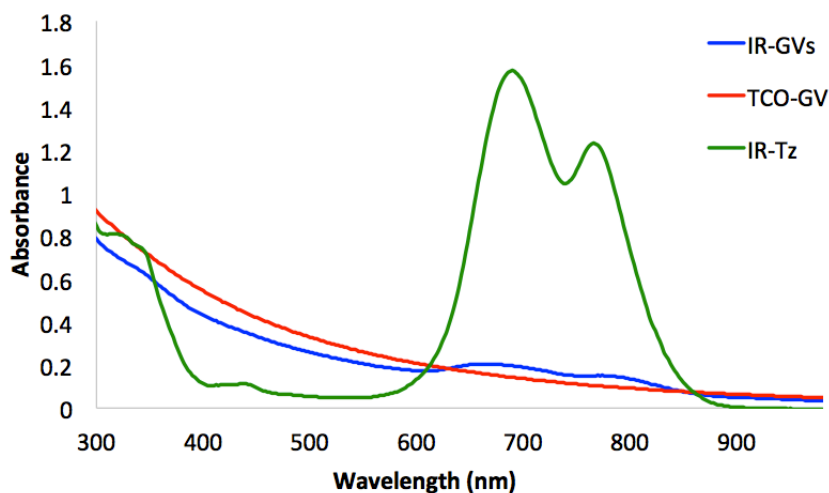


**Figure 6.9** Absorbance spectra of IR-Tz (green), TCO-GV (red), and IR-GV (blue) in PBS.

#### **6.2.2.2 Loading and stability studies of IR-GVs**

The PA spectra of TCO-GVs and IR-GVs were compared in a gel phantom before and after setting the US B-mode 2-D power to 100% at 100 dB to “pop” the GVs (Figure 6.10). A large drop in PA signal was observed for both GV constructs, indicative of the dye-GVs being “popped”. One explanation for this drop in PA signal is due to self-quenching of the IR dye. It has been shown in literature that cyanine dyes have the ability to self-quench when in close proximity to one another.<sup>55,56</sup> Thus, when the IR-GVs are popped, the IR-dye on the GV

surface can more easily interact resulting in a drop in PA signal. However, confirmation of the exact mechanism of this PA signal decrease will require additional work. Notwithstanding, the change in PA signal offers a convenient way to determine the lifetime of dye-conjugated GVs.

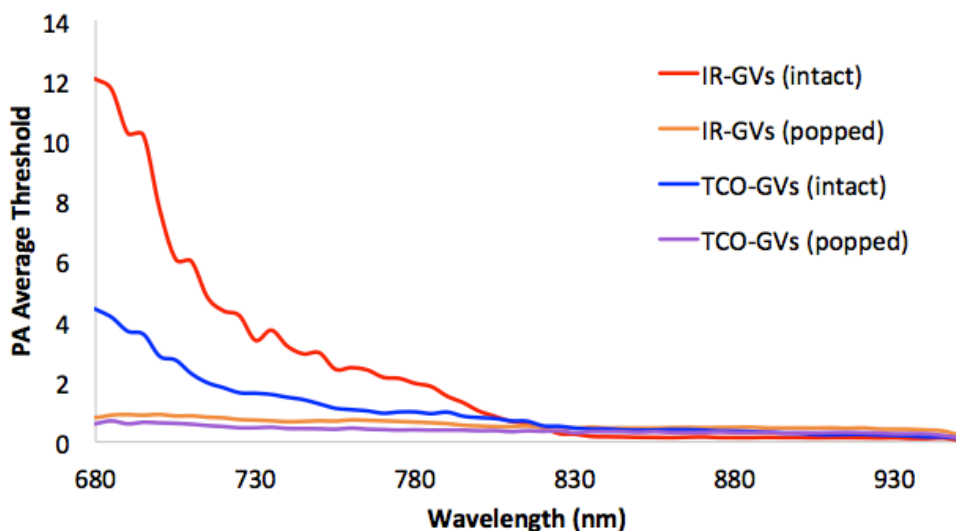


**Figure 6.10** Photoacoustic average threshold. Intact TCO-GVs (blue), popped TCO-GVs (purple), intact IR-GVs (red), and popped IR-GVs (orange).

To determine the maximum loading capacity of the IR-Tz on the TCO-GVs, increasing amounts of IR-Tz were added to TCO-GVs, the suspensions allowed to shake for 30 min at 4°C, followed by centrifugation for 1 hour at 300 rpm. The supernatant was collected and both the absorbance and PA signal was measured to determine if excess dye was present. Comparing the absorbance and PA signal of each series of IR-GV reactions, it was clear that the dye is still present in

all samples containing  $>0.125$  mg of IR-Tz (Figure 6.11 and 6.12). With a loading capacity of  $0.125$  mg, this equates to approximately  $114$  nmol of dye functionalized to the GV surface ( $300\ \mu\text{L}$ ,  $30$  OD).

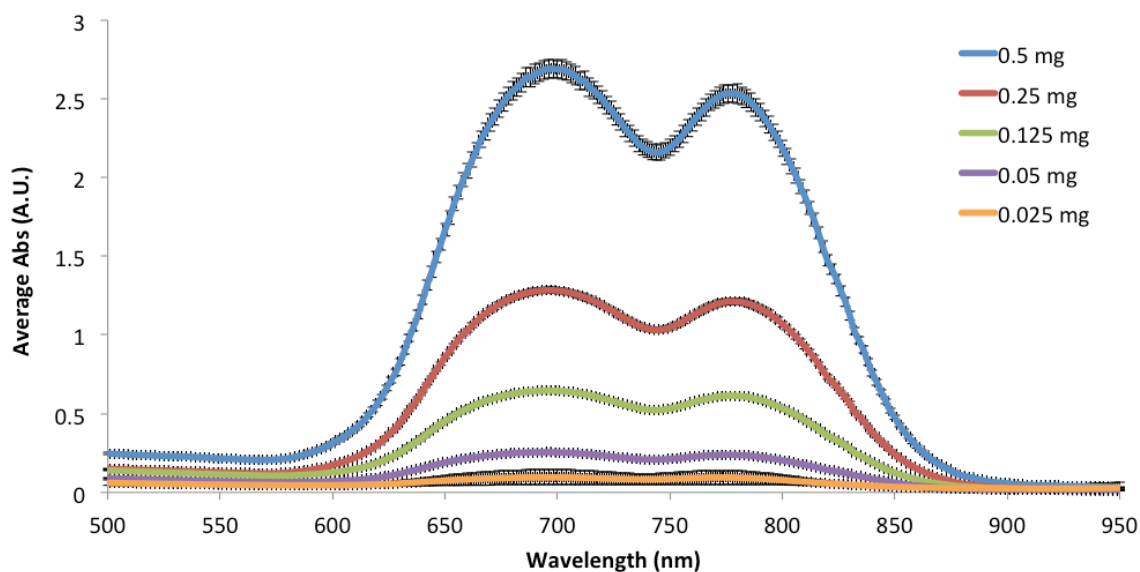


**Figure 6.11** Average absorbance ( $n=3$ ) vs. wavelength for the loading study, with increasing amounts of IR-Tz added to  $30$  OD of TCO-GVs.

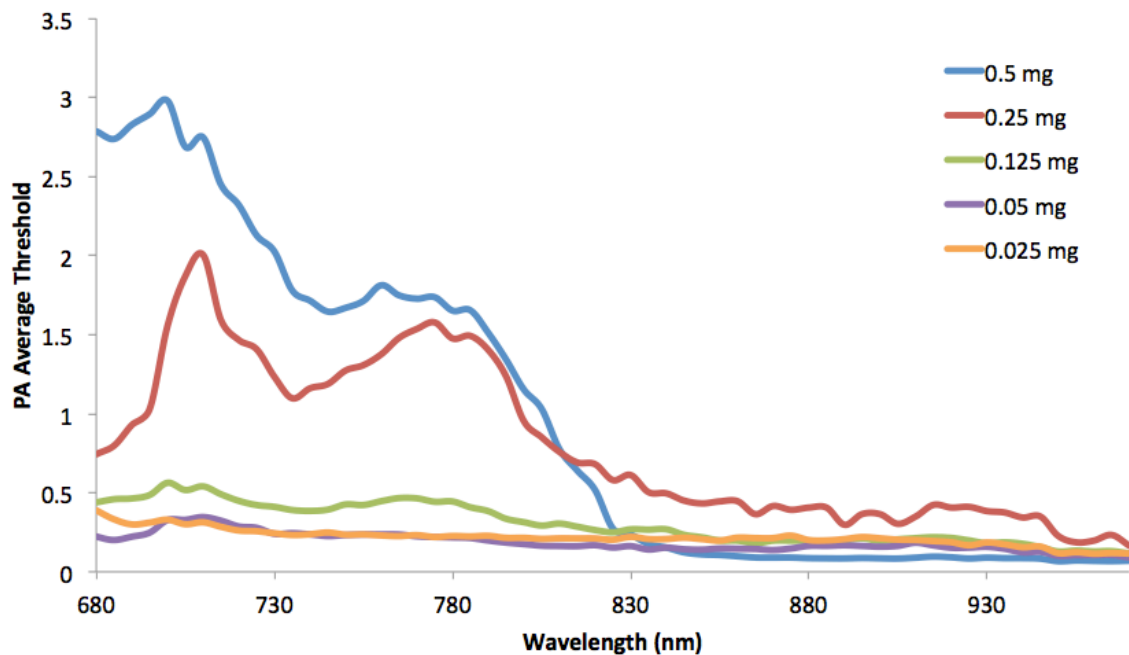


**Figure 6.12** PA average signal of loading study samples, with increasing amounts of IR-Tz added to 30 OD of TCO-GVs.

#### 6.2.2.3 *Imaging of IR-GVs in mouse blood*

To assess the feasibility of the IR-GV construct as a multi-modal imaging agent *in vivo*, un-mixing of the PA signal from whole blood was performed (Figure 6.13). It is well known that both oxy and deoxy-hemoglobin give a strong endogenous PA signal that can interfere with contrast agents.<sup>57</sup> In Figure 6.13, the signal of IR-GVs is shown in green, which could be unmixed from blood (shown in red) at both 15 and 30 OD, confirming the feasibility of the IR-GVs to be used as a multimodal-imaging agent *in vivo*.

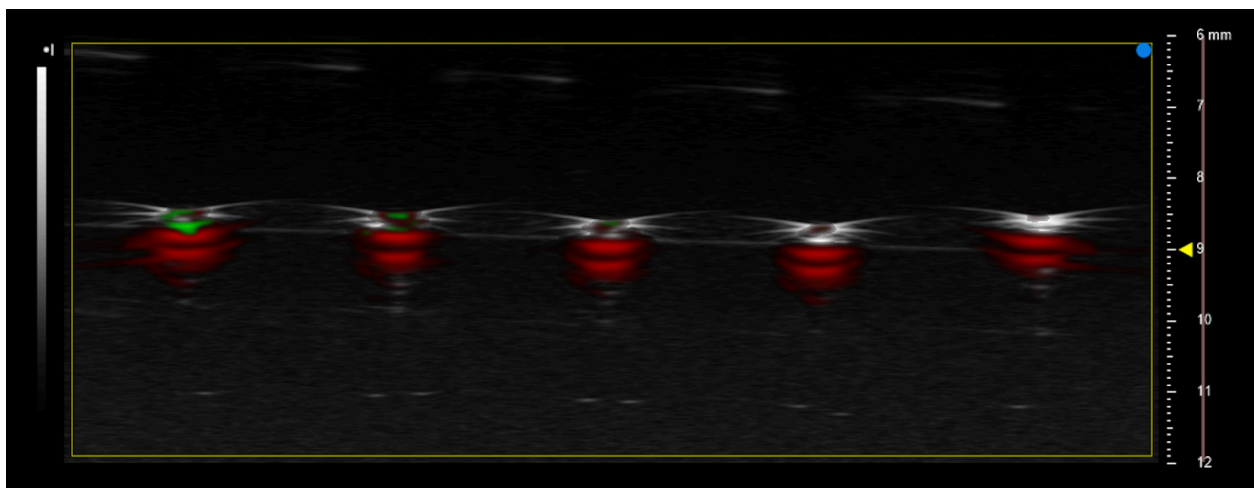


**Figure 6.13** Unmixing of IR-GVs at various concentrations from whole blood. (green = IR-GVs, red = oxy hemoglobin, blue = deoxy hemoglobin). From left to right: 30 OD, 15 OD, blood alone, 3 OD, 0.3 OD.

### 6.2.3 Conclusion and Future Work

In conclusion, a dual modality US-PA imaging agent was prepared using TCO-functionalized GVs and a novel IR-dye-tetrazine. The imaging agent was prepared using robust synthesis and purification methods where loading experiments indicated 114 nmol of dye-tetrazine was present on the surface of 30 OD TCO-GVs. At this concentration, the PA signal from the IR-GVs can easily be detected in both gel phantoms and blood. Furthermore, the IR-GV signal can be unmixed from oxy and deoxy-hemoglobin in the blood. Further work is required to demonstrate the ability of the IR-GVs to be implemented as a US/PA imaging agent in tumour bearing mice.

#### **6.2.4 General Methods**

All starting materials were purchased from Sigma Aldrich, unless otherwise stated. (E)-Cyclooct-4-enyl-2,5-diocopyrrolidin-1-yl carbonate (TCO-NHS) and 4-(1,2,4,5-tetrazin-3-yl)phenyl)methanamine hydrochloride (Tz) were purchased from Conju-Probe (San Diego, CA). Blood studies were performed using healthy female, BALB/c mice (Charles River Laboratory, Kingston, NY). Photoacoustic imaging was performed using Vevo LAZR-X (FUJIFILM VisualSonics Inc., Toronto, ON, Canada) imaging system equipped with a 680-970 nm laser. A 30-MHz, linear array ultrasound transducer with integrated fiber optic light delivery (LZ-400 and MX-400, FUJIFILM VisualSonics, Inc.) was used. The integrated fiber bundle delivered 15 to 20 mJ/cm<sup>2</sup> of light.

#### **6.2.5 Experimental**

##### ***6.2.5.1 Synthesis of IR-GVs***

Gas vesicle culturing, isolation and purification methods were repeated in the same manner described previously.<sup>2</sup> Halobacteria sp. NCR-1 (Carolina Biological Supply, Burlington, NC) were cultured in high salt Carolina media at 42 °C in a shaking incubator at 100 rpm (Ecotron, Infors AG, Switzerland). GVs were isolated by TMC lysis buffer and purified by centrifugal floatation (5 to 6 rounds) at 300 rcf in a centrifuge maintained at 4 °C.

Trans-cyclooctene (TCO)-conjugated GVs (TCO-GVs) were prepared as previously described.<sup>46</sup> (E)-cyclooct-4-enyl-2,5-diocopyrrolidin-1-yl carbonate (TCO-NHS) (750  $\mu$ g, 2.8  $\mu$ mol) in dimethyl sulfoxide (DMSO, 100  $\mu$ L) was added to a solution of GVs ( $OD_{500nm} = 77.2$ , 300  $\mu$ L) in PBS and diluted with 477  $\mu$ L of DI water. The solution was left on a shaker for 2.5 h in a cold room. The final TCO-GVs were purified by dialysis using a 6-8 kD dialysis membrane submerged in DI water overnight in a cold room (Spectra/Por 1 Dialysis Membrane, Spectrum Labs, USA). The TCO-GVs were then concentrated by centrifugal floatation at 300 rcf for 45 minutes. TCO-GVs<sup>58</sup> ( $OD_{500nm} = 40$ , 300  $\mu$ L) were added to a solution of IR-Tz in 100  $\mu$ L DMSO (1.5 mg, 1.4  $\mu$ mol) and left shaking in a cold room for 30 min (Figure 5.8). The IR-GVs were then washed with cold PBS and purified from any residual TCO-GVs using two rounds of centrifugal floatation at 300 rcf for 1 h, until the bottom PBS layer was colourless.

#### **6.2.5.2 Photoacoustic Imaging Studies**

Phantom imaging studies were performed in a Vevo PHANTOM (FUJIFILM VisualSonics Inc., Toronto, ON, Canada). Samples were loaded using a 27 gauge needle into the provided tubing. B-mode 2-D power was set to 1% to prevent popping GVs while imaging. To intentionally “pop” GVs, the 2-D power was set to 100% and the dynamic range was increased to 100 dB.



Gel phantoms were prepared using agarose (3 g) dissolved in 1x PBS (100 mL) then heated to boiling and set in a gel mould with tubing to create voids to load the sample. Using a syringe, samples were injected into voids made in the gel and imaged in the presence of ultrasound gel.

#### **6.2.5.3 Blood Studies**

Studies were performed in whole mouse blood treated with 10% EDTA to prevent clotting. To the blood (50  $\mu$ L), IR-GVs (50  $\mu$ L) at varying optical densities (30, 15, 3, and 0.3 OD) were added and mixed. Samples were loaded into the Vevo PHANTOM, and PA images were obtained of the IR-GV samples in blood, and blood alone. Unmixing of PA signal from the IR-Tz and blood was performed by the Vevo LAZR-X at a predetermined wavelength.

### **6.3 References**

- (1) Smith-Bindman, R.; Miglioretti, D. L.; Johnson, E.; Lee, C.; Feigelson, H. S.; Flynn, M.; Greenlee, R. T.; Kruger, R. L.; Hornbrook, M. C.; Roblin, D.; Solberg, L. I.; Vanneman, N.; Weinmann, S.; Williams, A. E. *JAMA* **2012**, *307* (22), 2400–2409.
- (2) Shapiro, M. G.; Goodwill, P. W.; Neogy, A.; Yin, M.; Foster, F. S.; Schaffer, D. V.; Conolly, S. M. *Nat. Nanotechnol.* **2014**, *9* (4), 311–316.
- (3) Tranquart, F.; Arditi, M.; Bettinger, T.; Frinking, P.; Hyvelin, J.; Nunn, A.; Pochon, S.; Tardy, I. *Z Gastroenterol* **2014**, *52* (11), 1268–1276.

- (4) Abou-Elkacem, L.; Bachawal, S. V.; Willmann, J. K. *Eur. J. Radiol.* **2015**, *84* (9), 1685–1693.
- (5) Halpern, E. J. *Rev. Urol.* **2006**, *8* (1), S29–S37.
- (6) Strobel, D.; Seitz, K.; Blank, W.; Schuler, A.; Dietrich, C.; Von Herbay, A.; Friedrich-Rust, M.; Kunze, G.; Becker, D.; Will, U.; Kratzer, W.; Albert, F. W.; Pachmann, C.; Dirks, K.; Strunk, H.; Greis, C.; Bernatik, T. *Ultraschall der Medizin* **2008**, *29* (5), 499–505.
- (7) Allendoerfer, J.; Tanislav, C. *Ultraschall der Medizin* **2008**, *29*, 210–214.
- (8) Welschehold, S.; Geisel, F.; Beyer, C.; Reuland, A.; Kerz, T. *J. Neurol. Neurosurg. Psychiatry* **2013**, *84* (8), 939–940.
- (9) Siracusano, S.; Bertolotto, M.; Ciciliato, S.; Valentino, M.; Liguori, G.; Visalli, F. *World J. Urol.* **2011**, *29* (5), 633–638.
- (10) Wilson, S.; Burns, P. *AM J Cardiol* **2000**, *86* (6), 669–674.
- (11) D’Onofrio, M.; Canestrini, S.; De Robertis, R.; Crosara, S.; Demozzi, E.; Ciaravino, V.; Pozzi Mucelli, R. *Eur. J. Radiol.* **2015**, *84* (9), 1644–1649.
- (12) Lindner, J. R. *Nat. Rev. Cardiol.* **2009**, *6* (7), 475–481.
- (13) Mulvagh, S. L.; Rakowski, H.; Vannan, M. A.; Abdelmoneim, S. S.; Becher, H.; Bierig, S. M.; Burns, P. N.; Castello, R.; Coon, P. D.; Hagen, M. E.; Jollis, J. G.; Kimball, T. R.; Kitzman, D. W.; Kronzon, I.; Labovitz, A. J.; Lang, R. M.; Mathew, J.; Moir, W. S.; Nagueh, S. F.; Pearlman, A. S.; Perez, J. E.; Porter, T. R.; Rosenbloom, J.; Strachan, G. M.; Thanigaraj, S.; Wei, K.; Woo, A.; Yu, E. H. C.; Zoghbi, W. A. *J. Am. Soc. Echocardiogr.* **2008**, *21* (11), 1179–1201.
- (14) Smeenge, M.; Tranquart, F.; Mannaerts, C. K.; De Reijke, T. M.; Van De Vijver, M. J.; Laguna, M. P.; Pochon, S.; De La Rosette, J. J. M. C. H.; Wijkstra, H. *Invest. Radiol.* **2017**, *52* (7), 419–427.
- (15) Willmann, J. K.; Bonomo, L.; Testa, A. C.; Rinaldi, P.; Rindi, G.; Valluru, K. S.; Petrone, G.; Martini, M.; Lutz, A. M.; Gambhir, S. S. *J. Clin. Oncol.* **2017**, *35* (19), 2133–2140.
- (16) Liu, J.; Levine, A. L.; Mattoon, J. S.; Yamaguchi, M.; Lee, R. J.; Pan, X.; Rosol, T. J. *Phys. Med. Biol.* **2006**, *51*, 2179–2189.

- (17) Lanza, G.; Wallace, K.; Scott, M.; Cacheris, W.; Abendschein, D.; Christy, D.; Sharkey, A.; Miller, J.; Gaffney, P.; Wickline, S. *Circulation* **1997**, *20* (95), 2458.
- (18) Kripfgans, O. D.; Fowlkes, J. B.; Miller, D. L.; Eldevik, O. P.; Carson, P. L. *Ultrasound Med. Biol.* **2000**, *26* (7), 1177–1189.
- (19) Martinez, H. P.; Kono, Y.; Blair, S. L.; Sandoval, S.; Wang-Rodriguez, J.; Mattrey, R. F.; Kummel, A. C.; Trogler, W. C. *Medchemcomm* **2010**, *1* (4), 266–270.
- (20) Walsby, A.; Hayes, P. *Biochem J* **1989**, *264*, 313–322.
- (21) Pfeifer, F. *Nat. Rev. Microbiol.* **2012**, *10* (10), 705–715.
- (22) Walsby, A. E. *Microbiol. Rev.* **1994**, *58* (1), 94–144.
- (23) Cherin, E.; Melis, J. M.; Bourdeau, R. W.; Yin, M.; Kochmann, D. M.; Foster, F. S.; Shapiro, M. G. *Ultrasound Med. Biol.* **2017**, *43* (5), 1016–1030.
- (24) Maeda, H.; Nakamura, H.; Fang, J. *Adv. Drug Deliv. Rev.* **2013**, *65* (1), 71–79.
- (25) Lakshmanan, A.; Farhadi, A.; Nety, S. P.; Lee-Gosselin, A.; Bourdeau, R. W.; Maresca, D.; Shapiro, M. G. *ACS Nano* **2016**, *10* (8), 7314–7322.
- (26) Maresca, K. P.; Marquis, J. C.; Hillier, S. M.; Lu, G.; Femia, F. J.; Zimmerman, C. N.; Eckelman, W. C.; Joyal, J. L.; Babich, J. W. *Bioconjugate Chem.* **2010**, *21*, 1032–1042.
- (27) James, S.; Maresca, K. P.; Allis, D. G.; Valliant, J. F.; Eckelman, W.; Babich, J. W.; Zubieta, J. *Bioconjugate Chem.* **2006**, *17*, 579–589.
- (28) Blackman, M. L.; Royzen, M.; Fox, J. M. *J. Am. Chem. Soc.* **2008**, *130* (41), 13518–13519.
- (29) Bilton, H.; Ahmad, Z.; Valliant, J. *J. Label. Compd. Radiopharm.* **2015**, *58*, S61.
- (30) Al-Azzawi, H. H.; Mathur, A.; Lu, D.; Swartz-Basile, D. A.; Nakeeb, A.; Pitt, H. A. *J. Surg. Res.* **2006**, *136* (2), 192–197.

- (31) Melloul, E.; Raptis, D. A.; Boss, A.; Pfammater, T.; Tschuor, C.; Tian, Y.; Graf, R.; Clavien, P. A.; Lesurtel, M. *J. Surg. Res.* **2014**, *187* (2), 458–465.
- (32) Kaminskis, L.; Boyd, B. In *Intracellular Delivery*; 2011; pp 155–178.
- (33) McNeil, S. E. *Wiley Interdiscip. Rev. Nanomedicine Nanobiotechnology* **2009**, *1* (3), 264–271.
- (34) Nel, A. E.; Mädler, L.; Velegol, D.; Xia, T.; Hoek, E. M. V.; Somasundaran, P.; Klaessig, F.; Castranova, V.; Thompson, M. *Nat. Mater.* **2009**, *8* (7), 543–557.
- (35) Braet, F.; Wisse, E.; Bomans, P. *Microsc. Res. Tech.* **2007**, *70*, 230–242.
- (36) Soo Choi, H.; Liu, W.; Misra, P.; Tanaka, E.; Zimmer, J. P.; Itty Ipe, B.; Bawendi, M. G.; Frangioni, J. V. *Nat. Biotechnol.* **2007**, *25* (10), 1165–1170.
- (37) Black, K. C. L.; Wang, Y.; Luehmann, H. P.; Cai, X.; Xing, W.; Pang, B.; Zhao, Y.; Cutler, C. S.; Wang, L. V.; Liu, Y.; Xia, Y. *ACS Nano* **2014**, *8* (5), 4385–4394.
- (38) Lakshmanan, A.; Lu, G. J.; Farhadi, A.; Nety, S. P.; Kunth, M.; Lee-Gosselin, A.; Maresca, D.; Bourdeau, R. W.; Yin, M.; Yan, J.; Witte, C.; Malounda, D.; Foster, F. S.; Schröder, L.; Shapiro, M. G. *Nat. Protoc.* **2017**, *12* (10), 2050–2080.
- (39) Van der Have, F.; Vastenhouw, B.; Rentmeester, M.; Beekman, F. J. *IEEE Trans. Med. Imaging* **2008**, *27* (7), 960–971.
- (40) Branderhorst, W.; Vastenhouw, B.; Beekman, F. J. *Phys. Med. Biol.* **2010**, *55* (7), 2023–2034.
- (41) Ogawa, K.; Harata, Y.; Ichihara, T.; Kubo, A.; Hashimoto, S. *IEEE Trans. Med. Imaging* **1991**, *10* (3), 408–412.
- (42) Wu, C.; Van Der Have, F.; Vastenhouw, B.; Dierckx, R. A. J. O.; Paans, A. M. J.; Beekman, F. J. *Eur. J. Nucl. Med. Mol. Imaging* **2010**, *37* (11), 2127–2135.
- (43) Wu, C.; De Jong, J. R.; Gratama Van Andel, H. A.; Van Der Have, F.; Vastenhouw, B.; Laverman, P.; Boerman, O. C.; Dierckx, R. A. J. O.; Beekman, F. J. *Phys. Med. Biol.* **2011**, *56* (18).

- (44) Maroy, R.; Boisgard, R.; Comtat, C.; Frouin, V.; Cathier, P.; Duchesnay, E.; Dolle, F.; Nielsen, P.; Trebossen, R.; Tavitian, B. *IEEE Trans. Med. Imaging* **2008**, *27* (3), 342–354.
- (45) Feldkamp, L. A. *Opt. Soc. Am. A* **1984**, *1* (6), 612–619.
- (46) Le Floch'h, J.; Zlitni, A.; Bilton, H. A.; Yin, M.; Farhadi, A.; Janzen, N. R.; Shapiro, M. G.; Valliant, J. F.; Foster, F. S. *Mol. Imaging Biol.* **2018**, *20* (2), 230–239.
- (47) Garcia-Urbe, A.; Erpelding, T. N.; Krumholz, A.; Ke, H.; Maslov, K.; Appleton, C.; Margenthaler, J. A.; Wang, L. V. *Sci. Rep.* **2015**, *5*, 1–8.
- (48) Huynh, E.; Leung, B. Y. C.; Helfield, B. L.; Shakiba, M.; Gandier, J.-A.; Jin, C. S.; Master, E. R.; Wilson, B. C.; Goertz, D. E.; Zheng, G. *Nat. Nanotechnol.* **2015**, *10* (4), 325–332.
- (49) Weber, J.; Beard, P. C.; Bohndiek, S. E. *Nat. Methods* **2016**, *13* (8), 639–650.
- (50) Wang, L. V. *Nat. Photonics* **2009**, *3* (9), 503–509.
- (51) Kim, C.; Qui, R.; Xu, J. S.; Wang, L. V.; Xu, R. *J. Biomed. Opt.* **2010**, *15* (1), 010510.
- (52) Wilson, K.; Homan, K.; Emelianov, S. *Nat. Commun.* **2012**, *3*, 610–618.
- (53) Jeon, M.; Song, W.; Huynh, E.; Kim, J.; Kim, J.; Helfield, B. L.; Leung, B. Y. C.; Goertz, D. E.; Zheng, G.; Oh, J.; Lovell, J. F.; Kim, C. *J. Biomed. Opt.* **2014**, *19* (1), 016005.
- (54) Shapiro, M. G.; Goodwill, P. W.; Neogy, A.; Yin, M.; Foster, F. S.; Schaffer, D. V.; Conolly, S. M. *Nat. Nanotechnol.* **2014**, *9* (4), 311–316.
- (55) Cohen, S.; Margel, S. *J. Nanobiotechnology* **2012**, *10*, 2–9.
- (56) Li, C.; Greenwood, T. R.; Bhujwalla, Z. M.; Glunde, K. *Org. Lett.* **2006**, *8* (17), 3623–3626.
- (57) Valluru, K. S.; Wilson, K. E.; Willmann, J. K. *Radiology* **2016**, *280* (2), 332–349.

- (58) Naperstkow, Z. Synthesis and Evaluation of Nuclear and Optical Tetrazine-6-Hydrazinopyridine-3-Carboxylic Acid Probes for Molecular Imaging using Pretargeting and Bioorthogonal Chemistry, McMaster University, 2017.

## 6.4 Supplemental Information

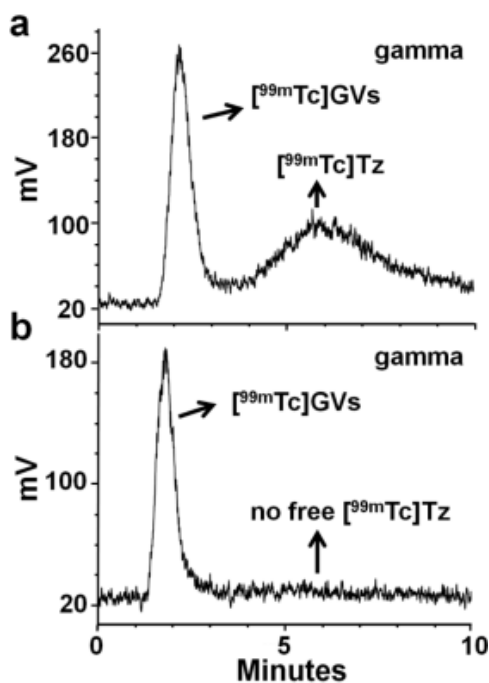


**Figure S6.1** Size exclusion HPLC chromatograms (gamma detection). **A)** Chromatogram of the reaction mixture containing both  $[^{99m}\text{Tc}]\text{GVs}$  and free  $[^{99m}\text{Tc}]\text{Tz}$  (6). **B)** Purified  $[^{99m}\text{Tc}]\text{GVs}$  showing no residual  $[^{99m}\text{Tc}]\text{Tz}$ .

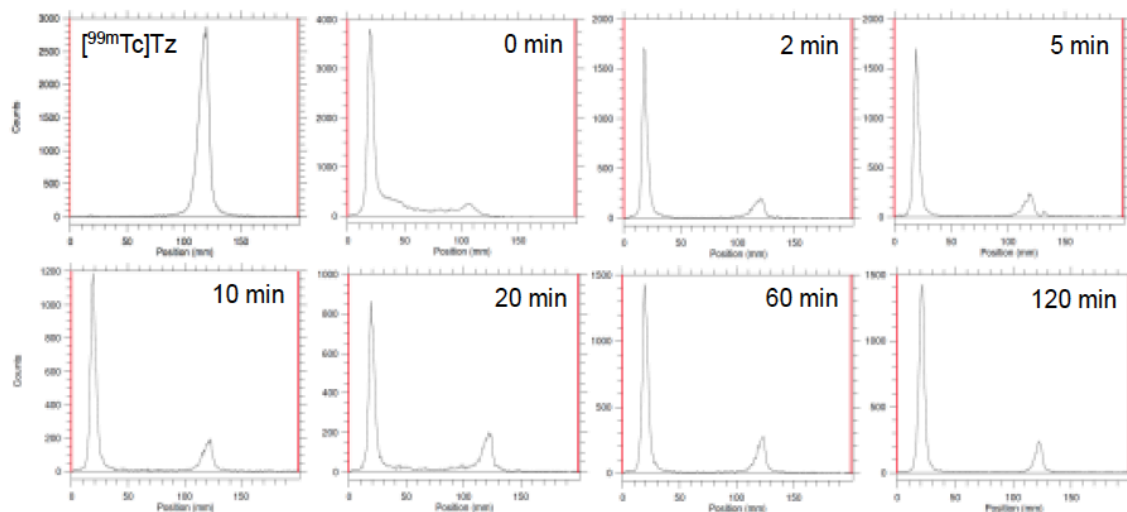


**Figure S6.2** Radio-TLC analysis of  $[^{99m}\text{Tc}]\text{Tz}$  (Top-left). Radio-TLC analysis of  $[^{99m}\text{Tc}]\text{GVs}$  incubated at 37 °C in plasma at the indicated time points. Radio-TLC was eluted with 75% methanol and 25% water.

**Table S6.1 Stability in plasma.** Table reports the stability of  $[^{99m}\text{Tc}]\text{GVs}$  in plasma at 37 °C for up to 120 minutes.

Sample	% $[^{99m}\text{Tc}]\text{GVs}$	% Compound 3
$[^{99m}\text{Tc}]\text{Tz}$	0	100
Plasma $[^{99m}\text{Tc}]\text{GVs}$ 0 min	87	13
Plasma $[^{99m}\text{Tc}]\text{GVs}$ 2 min	80	20
Plasma $[^{99m}\text{Tc}]\text{GVs}$ 5 min	78	22
Plasma $[^{99m}\text{Tc}]\text{GVs}$ 10 min	78	22
Plasma $[^{99m}\text{Tc}]\text{GVs}$ 20 min	71	29
Plasma $[^{99m}\text{Tc}]\text{GVs}$ 60 min	76	24
Plasma $[^{99m}\text{Tc}]\text{GVs}$ 120 min	81	19

**Table S6.2 Activity in plasma layers.** Table reports the % Activity in the GV and plasma layers after centrifugal flotation at 60 and 120 minutes.

Time	% Activity in GV layer	% Activity in plasma layer
60 min	31	69
120 min	44	56

**Table S6.3 3D Segmentation quantification.** Table reports the mean and SEM of the volume of segmented organs.

Organs	Liver	Spleen	Lungs	Gall Bladder	Duodenum	Bladder
Volume (cm <sup>3</sup> )	1.964	0.166	0.609	0.028	0.427	0.183
SEM (n=6)	0.176	0.017	0.032	0.005	0.082	0.020

**Table S6.4 Dynamic Uptake quantification.** Table reports the mean and SEM of the uptake rate constants. Rate constants were calculated using a linear regression for all organs using the 0-10 min range except for the duodenum for which the 30-60 min range was used.

Organs	Liver	Spleen	Lungs	Gall Bladder	Duodenum	Bladder
Uptake Rate Constants (%ID/cc/min)	2.760	0.584	1.433	5.254	0.935	0.422
SEM (n=6)	0.270	0.181	0.467	1.762	0.266	0.174



## 7 Summary and Future Work

### 7.1 Summary

The overall goal of this thesis was to create and advance the knowledge needed to effectively develop a  $^{99m}\text{Tc}$ -labeled tetrazine for the creation of new radiopharmaceuticals via pretargeting and bioorthogonal chemistry. The first step was to synthesize a chelate-tetrazine derivative capable of being labeled with  $^{99m}\text{Tc}$ . The approach taken was to use a well known tridentate chelate that can bind the  $^{99m}\text{Tc}[\text{Tc}(\text{CO})_3]^+$  core.<sup>1</sup> Once the synthesis, characterization, and  $^{99m}\text{Tc}$  labeling was completed, preliminary distribution studies were performed in mice (Chapter 2). Rapid blood clearance, high off-target uptake, and slow clearance through the hepatobiliary system resulted in exploring several different avenues to improve the pharmacokinetic profile of the 1<sup>st</sup> generation ligands.

The first avenue involved evaluating the effect of hydrophilic linkers on distribution. Two derivatives of the initial  $^{99m}\text{Tc}$ -tetrazine were synthesized, one with a PEG<sub>5</sub> linker and another with a PEG<sub>10</sub>. It appeared that the addition of the PEG linkers somewhat improved compound distribution, but did not completely mitigate the slow clearance through the gallbladder and intestines.<sup>2</sup> However, when these  $^{99m}\text{Tc}$ -tetrazines were used in pretargeting studies with a TCO-bisphosphonate for bone imaging, it appeared that the addition of the PEG<sub>5</sub> linker greatly improved pharmacokinetics, making it the lead compound (Chapter 2).<sup>3</sup>

Moving forward, the ability of the  $^{99m}\text{Tc}$ -tetrazines to couple with an established TCO-antibody conjugate was evaluated *in vitro* and *in vivo* (Chapter 3). *In vitro* studies mimicking the dynamic flow conditions found in tumour capillaries demonstrated successful reaction of the  $^{99m}\text{Tc}$ -tetrazine with a TCO-functionalized antibody localized on the surface of cancer cells. However, pretargeted imaging studies *in vivo* yielded poor tumour uptake, with tumour: blood ratios  $<1$  for all of the  $^{99m}\text{Tc}$ -tetrazines tested. It was hypothesized that the rapid blood clearance of the  $^{99m}\text{Tc}$ -tetrazines, combined with the low quantity of TCO-antibody administered resulted in insufficient reaction rates to achieve a suitable concentration of the  $^{99m}\text{Tc}$ -tetrazine at the tumour site.

In an attempt to understand the mechanism of compound clearance, distribution studies were performed, where the lead  $^{99m}\text{Tc}$ -tetrazine was co-formulated with several clinically approved hepatic transport inhibitors (Chapter 4).<sup>4,5</sup> It was found that when the  $^{99m}\text{Tc}$ -tetrazine was co-formulated with alendronate, gallbladder uptake was reduced 3-fold. It was hypothesized that since nitrogen containing-bisphosphonates are known inhibitors of the mevalonate pathway,<sup>6–8</sup> the presence of alendronate could potentially reduce bile production and thus slow gall bladder activity. However, further investigation is needed to confirm the role of alendronate on the altered distribution of the  $^{99m}\text{Tc}$ -tetrazine.

In an attempt to further improve the tetrazine ligands, distribution studies were performed on the lead  $^{99m}\text{Tc}$  compound with and without a tetrazine group

appended to the chelate. Distribution studies suggested that the  $^{99m}\text{Tc}$ -chelate complex was playing a greater role in driving compound clearance compared to the tetrazine. With this information, the effect of different  $^{99m}\text{Tc}$  chelates was evaluated. With a triazole-glycine containing  $^{99m}\text{Tc}$ -chelate showing promising clearance in literature,<sup>9,10</sup> a derivative of this triazole-chelate was synthesized and characterized. This ligand was successfully labeled with  $^{99m}\text{Tc}$ , and showed a greatly improved clearance profile from the previous  $^{99m}\text{Tc}$  imidazole-based chelates (Chapter 5). However, the synthetic challenges faced when functionalizing this ligand with a tetrazine led to the synthesis of a modified triazole-tetrazine ligand. Unfortunately, the addition of a lipophilic linker combined with a lipophilic tetrazine caused this new  $^{99m}\text{Tc}$ -triazole-tetrazine to have predominately hepatobiliary clearance, similar to the issues seen with the imidazole-based chelates.

Additional work focused on utilizing the bioorthogonal chemical reaction between a  $^{99m}\text{Tc}$ -tetrazine (Chapter 2) and trans-cyclooctene for the development of multi-modal imaging probes (Chapter 6). By exploiting the mild conditions required for the bioorthogonal reaction between tetrazine and trans-cyclooctene, temperature and pH sensitive nanoscale gas vesicles were successfully functionalized with a  $^{99m}\text{Tc}$ -tetrazine, creating a dual SPECT/US imaging probe. The stability and distribution of this dual-imaging probe was demonstrated *in vitro* and *in vivo*. Additionally, an near-infrared dye functionalized-tetrazine was also attached to the surface of the gas vesicles using the same tetrazine-TCO platform

Ph.D. Thesis – H. Bilton; McMaster University – Chemistry and Chemical Biology

developed previously, resulting in a dual-modality PA/US imaging probe. The compound stability was demonstrated *in vitro*, and the PA signal was easily detectable when mixed with blood.

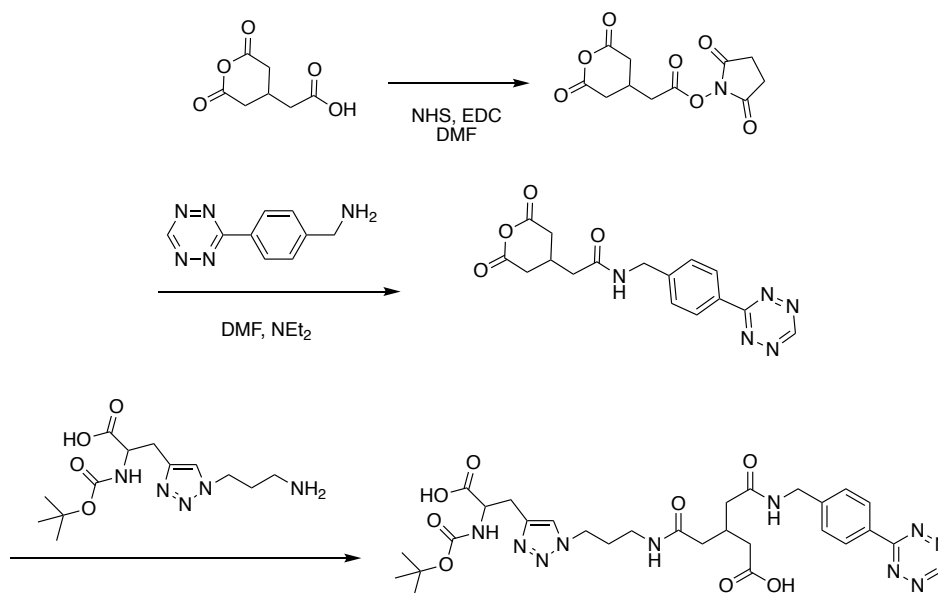
## 7.2 Future Work

### 7.2.1 Development of a more hydrophilic triazole ligand

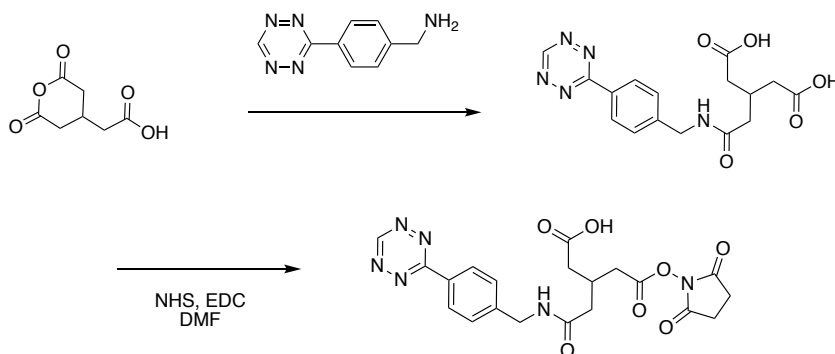
Work towards the synthesis of a more hydrophilic triazole-tetrazine should be conducted. In a similar manner to the previous synthesis (Section 5.3.2, Figure 5.7), a tetrazine acid can be synthesized using a reactive cyclic anhydride. Differing from the previous synthesis, a carboxylic acid functionalized anhydride can be used to add additional hydrophilicity to the ligand. This synthesis can be carried out in several ways. The first method could be where the carboxylic acid on the 2-(2,6-dioxooxan-4-yl)acetic acid is functionalized with an NHS ester. Next, the commercially available tetrazine can react with the NHS ester, producing a tetrazine-functionalized cyclic anhydride (Figure 7.1). This cyclic anhydride could then be combined with the previously synthesized (Section 5.3.3) triazole-propanamine ligand **30** to afford a more polar triazole-tetrazine ligand.

An alternative synthesis would be combining the commercially available tetrazine with the acid-functionalized cyclic anhydride, resulting in a diacid-functionalized tetrazine (Figure 7.2). This intermediate could then be combined with one equivalent of N-hydroxysuccinimide, to create an NHS ester. This ester

could then be treated with the previously synthesized triazole-propanamine ligand (**30**) to afford a new triazole-tetrazine ligand. A third alternative would be to switch the order of addition of the amines, reacting the triazole-propanamine ligand with NHS-ester of the cyclic anhydride before adding the tetrazine ligand. This may overcome any issues with tetrazine stability during synthesis or purification.



**Figure 7.1** Proposed synthesis of a polar triazole-tetrazine chelate derivative.



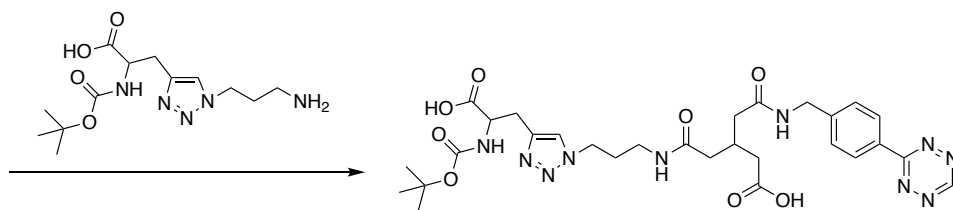


**Figure 7.2** Alternate synthesis of a more hydrophilic triazole-tetrazine ligand.

Once a new triazole-tetrazine ligand has been synthesized, labeling with  $^{99m}\text{Tc}$  should be conducted starting with the conditions described in Section 5.3.3. Once optimized, biodistribution studies should be conducted of the  $^{99m}\text{Tc}$ -tetrazine alone, and compared to previous compounds such as **32**. If the clearance has improved, which would be defined by reduced gall bladder uptake and reasonable blood half-life, pretargeting studies should be conducted with TCO-ALN and compared to the lead imidazole-based  $^{99m}\text{Tc}$ -tetrazine **14**. The presence of the triazole-based chelate combined with a more hydrophilic linker should result in a new lead compound that has high target to non-target ratios with very low hepatobiliary uptake. If this is the case, this new  $^{99m}\text{Tc}$ -tetrazine should be tested with a validated TCO-functionalized antibody for targeting. The ability to produce a  $^{99m}\text{Tc}$ -labeled antibody with high contrast images is something that has been highly sought after in literature, but has yet to be successfully demonstrated.

Chemical structures of two macrocyclic complexes. The left structure is a Tc(III) complex with a tris(oxo)antenna and a 4-phenyl-1H-1,2,4-triazole-3-ylmethyl group. The right structure is a Re(III) complex with a tris(oxo)antenna and a 4-phenyl-1H-1,2,4-triazole-3-ylmethyl group. Both complexes feature a macrocyclic ligand with two carboxylic acid groups and a pentamethylene spacer.

Once the labeling has been optimized, *in vitro* studies should be performed to evaluate the stability of the  $^{188}\text{Re}$ -complex over time. Next, *in vivo* distribution

studies can be performed to determine the effect of changing the nature of the metal and radiolysis on the observed distribution. Following distribution studies, pretargeted imaging and therapy studies can be performed using an appropriate TCO-antibody. The ability to develop an isostructural compound that can be used with  $^{99m}\text{Tc}$  for imaging and  $^{188}\text{Re}$  for therapy using antibodies and pre-targeting would be an unprecedented achievement.

#### **7.2.4 The development of a targeted PA/US contrast agent for tumour imaging**

Moving forward with the previously synthesized GV-based PA/US multimodal imaging agent, *in vivo* studies should be performed to evaluate the stability of the IR-GV complex. Furthermore, tumour studies should be performed and the passive targeting ability of this compound, which would exploit the EPR effect, should be evaluated with PA and US. Ideally, the compound should be able to visualize the tumour without the need for an additional targeting vector, due to the nanoscale size of the agent, and thus the ability to penetrate the vasculature.<sup>12</sup>

In addition to the development of multimodal imaging probes using GVs, it is also of interest to develop targeted CEUS agents for imaging specific disease biomarkers. By developing a nanoscale CEUS agent, one would be able to target disease biomarkers beyond the tumour vasculature, providing a more



comprehensive image of the disease states. Furthermore, targeted CEUS agents would highlight areas of disease and aid medical professionals in obtaining accurate needle biopsies without the need for repeated biopsy sampling.

To develop a nanoscale CEUS agent, the same TCO-GV platform developed previously (Chapter 6) could be used, and paired with a tetrazine functionalized targeting vector. With most US guided needle biopsies being performed on breast and prostate cancer patients, it is of interest to develop targeted CEUS agents for biomarkers overexpressed in these cancers.

Due to the prevalence of prostate cancer, there have been many small molecule targeting vectors that have been developed to target overexpressed biomarkers within prostate tumours.<sup>13,14</sup> Of these targeting vectors, a glutamate-urea-lysine compound has been developed, that successfully targets the prostate specific membrane antigen (PSMA), which is overexpressed one thousand fold in prostate cancers compared to healthy tissues.<sup>13,15</sup> This glutamate-urea-lysine core has had much success in targeting PSMA, and is currently being utilized in several clinical trials for imaging and therapeutic applications.<sup>16–20</sup> Several acid-containing compounds have been coupled to the terminal amine of the lysine in the glutamate-urea-lysine core, suggesting that the functionalization of this small molecule with a previously synthesized tetrazine-acid (chapter 5) should be feasible (Figure 7.4).<sup>10,21–26</sup>

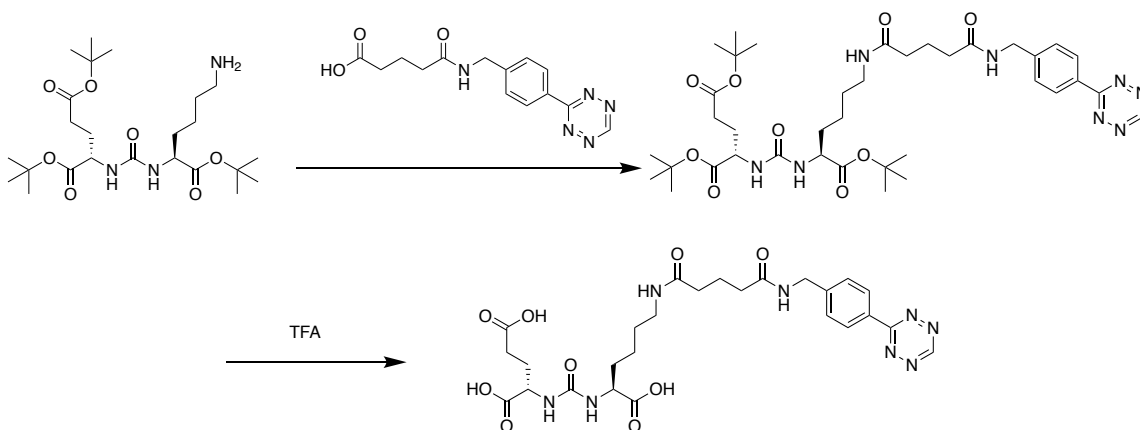


**Figure 7.4** Amide coupling of a tetrazine-acid to glutamate-urea-lysine.

Once a tetrazine-functionalized PSMA targeting vector has been developed, it can be added to the TCO-GV surface to create PSMA-targeted gas vesicles (PSMA-GVs) (Figure 7.5). Once prepared, PSMA-GVs can then be evaluated *in vivo*, where two subcutaneous tumours consisting of PSMA+ (e.g. LNCaP) and PSMA- (e.g. PC3) cells can be used to determine the targeting ability of PSMA-GVs, monitored by US.

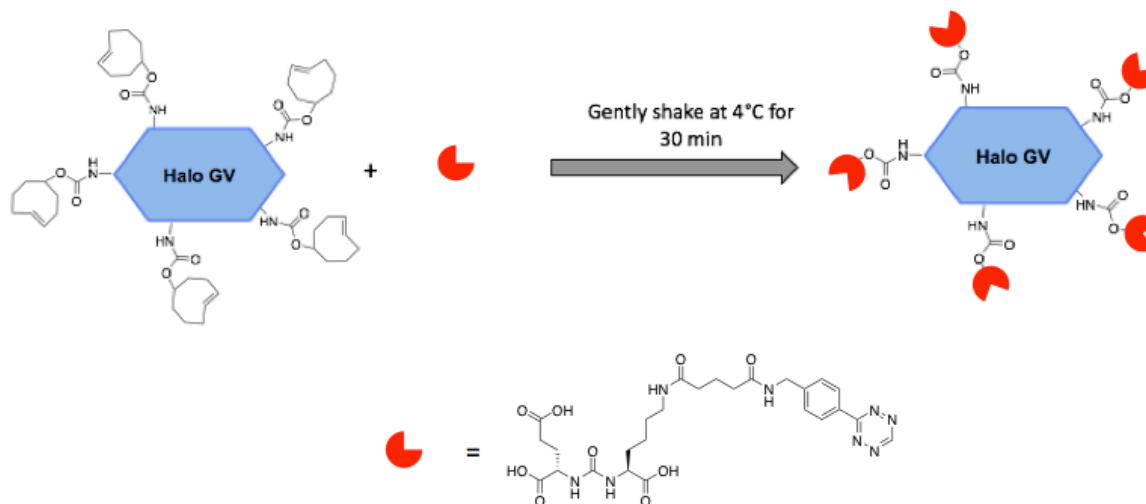


**Figure 7.5** Functionalization of TCO-GVs with a PSMA-tetrazine for prostate cancer imaging.

Along with the development of targeted GVs for prostate cancer, this platform can also be translated to breast cancer imaging. Several small molecules and peptides have been reported in literature for targeting the urokinase-type plasminogen activator receptor (uPAR), which is an established biomarker indicating invasiveness and metastatic potential of many cancers, including breast.<sup>27–29</sup> Of these targeting vectors, a small peptide named AE105 has proven to be an exceptional targeting vector for uPAR, and is currently the core of a <sup>68</sup>Ga PET tracer in clinical trials.<sup>14</sup> The structure of the uPAR targeting peptide AE105 is displayed in figure 7.6 below, where the location of potential tetrazine functionalization is highlighted in red.



- (8) Tricarico, P. M.; Girardelli, M.; Kleiner, G.; Knowles, A.; Valencic, E.; Crovella, S.; Marcuzzi, A. *Mol. Med. Rep.* **2015**, *12*, 4238–4242.
- (9) Kluba, C. A.; Mindt, T. L. *Molecules* **2013**, *18*, 3206–3226.
- (10) Banerjee, S. R.; Pullambhatla, M.; Foss, C. A.; Falk, A.; Byun, Y.; Nimmagadda, S.; Mease, R. C.; Pomper, M. G. *J. Med. Chem.* **2013**, No. 3, 6108–6121.
- (11) Rathmann, S. M.; Ahmad, Z.; Slikboer, S.; Bilton, H. A.; Snider, D. P.; Valliant, J. F. In *Radiopharmaceutical Chemistry*; Lewis, J. S., Windhorst, A. D., Zeglis, B. M., Eds.; SpringerLink, 2019; pp 311–333.
- (12) Maeda, H.; Nakamura, H.; Fang, J. *Adv. Drug Deliv. Rev.* **2013**, *65* (1), 71–79.
- (13) Kozikowski, A. P.; Nan, F.; Conti, P.; Zhang, J.; Ramadan, E.; Bzdega, T.; Wroblewska, B.; Neale, J. H.; Pshenichkin, S.; Wroblewski, J. T. *J. Med. Chem.* **2001**, *44* (3), 298–301.
- (14) Skovgaard, D.; Persson, M.; Brandt-Larsen, M.; Christensen, C.; Madsen, J.; Klausen, T. L.; Holm, S.; Andersen, F. L.; Loft, A.; Berthelsen, A. K.; Pappot, H.; Brasso, K.; Kroman, N.; Højgaard, L.; Kjaer, A. *J. Nucl. Med.* **2017**, *58* (3), 379–386.
- (15) Ghosh, A.; Heston, W. D. W. *J. Cell. Biochem.* **2004**, *91* (3), 528–539.
- (16) Schmidkonz, C.; Hollweg, C.; Beck, M.; Reinfelder, J.; Goetz, T. I.; Sanders, J. C.; Schmidt, D.; Prante, O.; Bäuerle, T.; Cavallaro, A.; Uder, M.; Wullich, B.; Goebell, P.; Kuwert, T.; Ritt, P. *Prostate* **2018**, *78* (1), 54–63.
- (17) Kratochwil, C.; Bruchertseifer, F.; Giesel, F. L.; Weis, M.; Verburg, F. A.; Mottaghy, F.; Kopka, K.; Apostolidis, C.; Haberkorn, U.; Morgenstern, A. *J. Nucl. Med.* **2016**, *57* (12), 1941–1944.
- (18) Kratochwil, C.; Giesel, F. L.; Stefanova, M.; Beneova, M.; Bronzel, M.; Afshar-Oromieh, A.; Mier, W.; Eder, M.; Kopka, K.; Haberkorn, U. *J. Nucl. Med.* **2016**, *57* (8), 1170–1176.
- (19) Gorin, M. A.; Rowe, S. P.; Patel, H. D.; Vidal, I.; Mana-ay, M.; Javadi, M. S.; Solnes, L. B.; Ross, A. E.; Schaeffer, E. M.; Bivalacqua, T. J.; Partin, A. W.; Pienta, K. J.; Szabo, Z.; De Marzo, A. M.; Pomper, M. G.; Allaf, M. E. *J. Urol.* **2018**, *199* (1), 126–132.

- (20) Haberkorn, U.; Eder, M.; Kopka, K.; Babich, J. W.; Eisenhut, M. *Clin. Cancer Res.* **2016**, *22* (1), 9–15.
- (21) Lee, J. B.; Zhang, K.; Tam, Y. Y. C.; Quick, J.; Tam, Y. K.; Lin, P. J.; Chen, S.; Liu, Y.; Nair, J. K.; Zlatev, I.; Rajeev, K. G.; Manoharan, M.; Rennie, P. S.; Cullis, P. R. *Mol. Ther. - Nucleic Acids* **2016**, *5*.
- (22) Maresca, K. P.; Hillier, S. M.; Femia, F. J.; Keith, D.; Barone, C.; Joyal, J. L.; Zimmerman, C. N.; Kozikowski, A. P.; Barrett, J. A.; Eckelman, W. C.; Babich, J. W. *J. Med. Chem.* **2009**, *52* (2), 347–357.
- (23) Banerjee, S. R.; Pullambhatla, M.; Byun, Y.; Nimmagadda, S.; Foss, C. A.; Green, G.; Fox, J. J.; Lupold, S. E.; Mease, R. C.; Pomper, M. G. *Angew. Chemie Int. Ed.* **2011**, *50*, 9167–9170.
- (24) Donovan, A. C.; Valliant, J. F. *J. Org. Chem.* **2009**, *74* (21), 8133–8138.
- (25) Darwish, A.; Blacker, M.; Janzen, N.; Rathmann, S. M.; Czorny, S.; Hillier, S. M.; Joyal, J. L.; Babich, J. W.; Valliant, J. F. *ACS Med. Chem. Lett.* **2012**, *3* (4), 313–316.
- (26) Li, M.; Banerjee, S. R.; Zheng, C.; Pomper, M. G.; Barman, I. *Chem. Sci.* **2016**, *7* (11), 6779–6785.
- (27) Ding, J.; Song, N.; Li, Z. *Chem. Commun.* **2010**, *46* (45), 8668–8670.
- (28) Persson, M.; Madsen, J.; Ostergaard, S.; Jensen, M. M.; Jorgensen, J. T.; Juhl, K.; Lehmann, C.; Ploug, M.; Kjaer, A. *J. Nucl. Med.* **2012**, *53* (1), 138–145.
- (29) Montuori, N.; Pesapane, A.; Rossi, F. W.; Giudice, V.; De Paulis, A.; Selleri, C.; Ragno, P. *Transl. Med.* **2016**, *15* (3), 15–21.
- (30) Jalilian, A. R.; Osso, J. *Iran. J. Nucl. Med.* **2017**, *25* (1), 1–10.

## APPENDIX I

### Supporting Information for Chapter 2

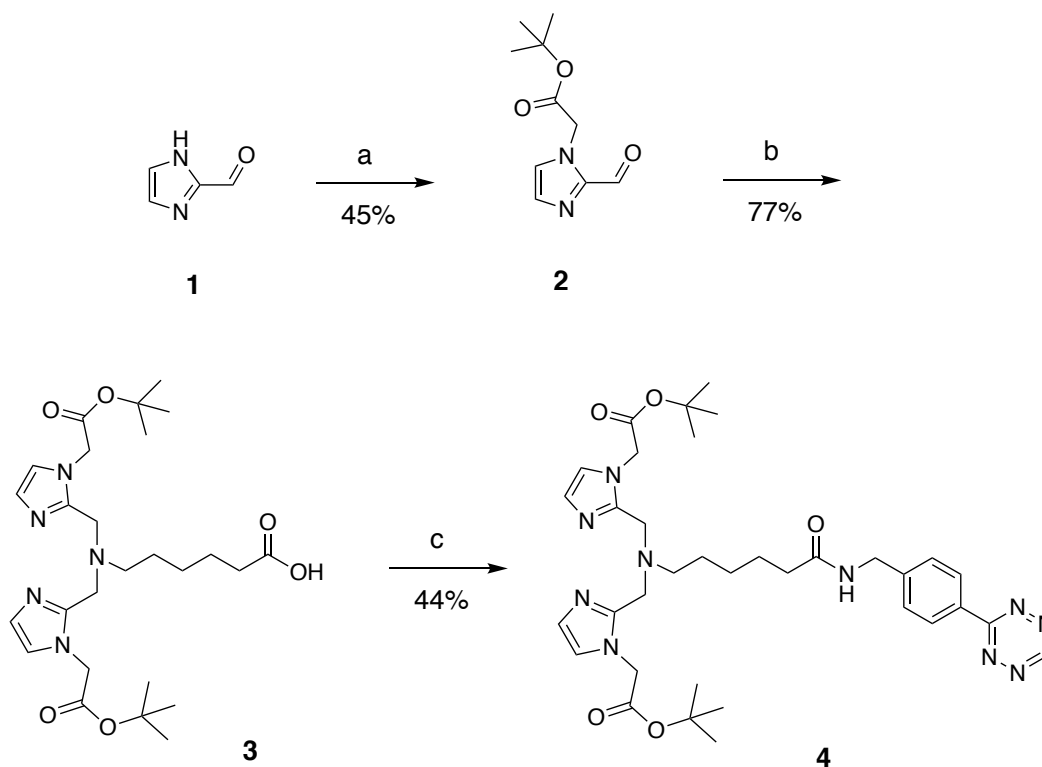


**Figure S2.1** Synthesis of **4** from **1**. a) DMF, DIPEA, *t*-butylbromoacetate, 80 °C, 4 h. b) DCE, NaBH(OAc)<sub>3</sub>, 6-aminocaproic acid, 50 °C, 12 h. c) PyBOP, DIPEA, DMF, ((4-tetrazine-3-yl)phenyl)methanamine hydrochloride, rt, 12 h.

***tert*-Butyl 2-(2-formyl-1*H*-imidazol-1-yl)acetate (**2**).** Compound **2** was prepared using a literature procedure.<sup>1</sup> To a solution of imidazole-2-carboxaldehyde (2.02 g, 21.0 mmol) in anhydrous DMF (10 mL), *tert*-butyl bromoacetate (4.12g, 21.1 mmol), potassium iodide (120 mg, 0.73 mmol) and DIPEA (5.50 mL, 31.6 mmol)

were added. The reaction was allowed to stir for 4 hours at 80 °C under Argon whereupon the solvent was removed under reduced pressure. The resulting thick brown oil was extracted with DCM (3 × 30 mL), the organic layers combined, extracted with H<sub>2</sub>O (3 × 30 mL) and then dried over sodium sulfate. The organic layer was evaporated to dryness under reduced pressure to yield a dark brown oil. The desired product was isolated by column chromatography, using an SP1 Biotage SNAP 100 g column (1% MeOH/DCM), yielding a yellow oil (2.00 g, 9.47 mmol, 45%). TLC R<sub>f</sub> = 0.26 (1% MeOH/DCM); <sup>1</sup>H NMR (600 MHz, CDCl<sub>3</sub>): δ 9.66 (s, 1H), 7.19 (s, 1H), 7.07 (s, 1H), 4.92 (s, 2H), 1.36 (s, 9H). <sup>13</sup>C NMR (150 MHz, CDCl<sub>3</sub>): δ 181.9, 166.0, 143.4, 131.3, 127.1, 83.1, 49.4, 27.8. HRMS (ES<sup>+</sup>) m/z calculated for C<sub>10</sub>H<sub>15</sub>N<sub>2</sub>O<sub>3</sub> [M+H<sup>+</sup>] 211.1083, found 211.1077.



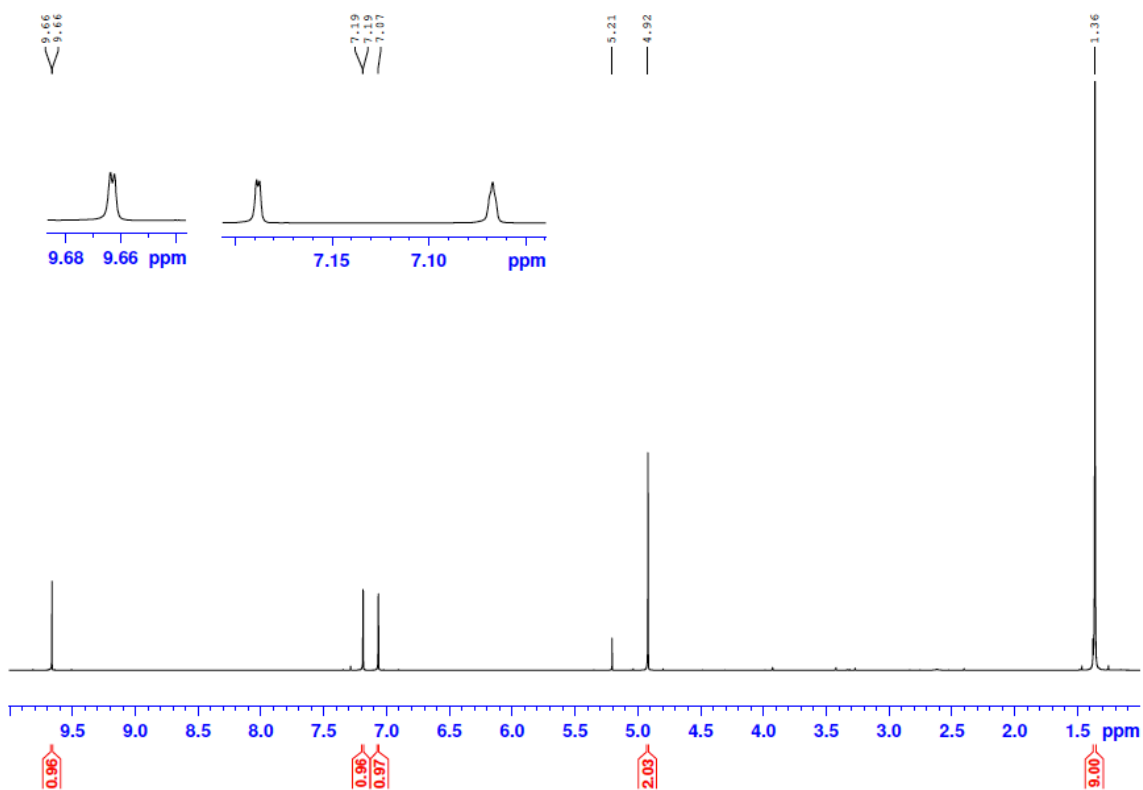


**Figure S2.2**  $^1\text{H}$  NMR (600 MHz,  $\text{CDCl}_3$ ) of **2**.

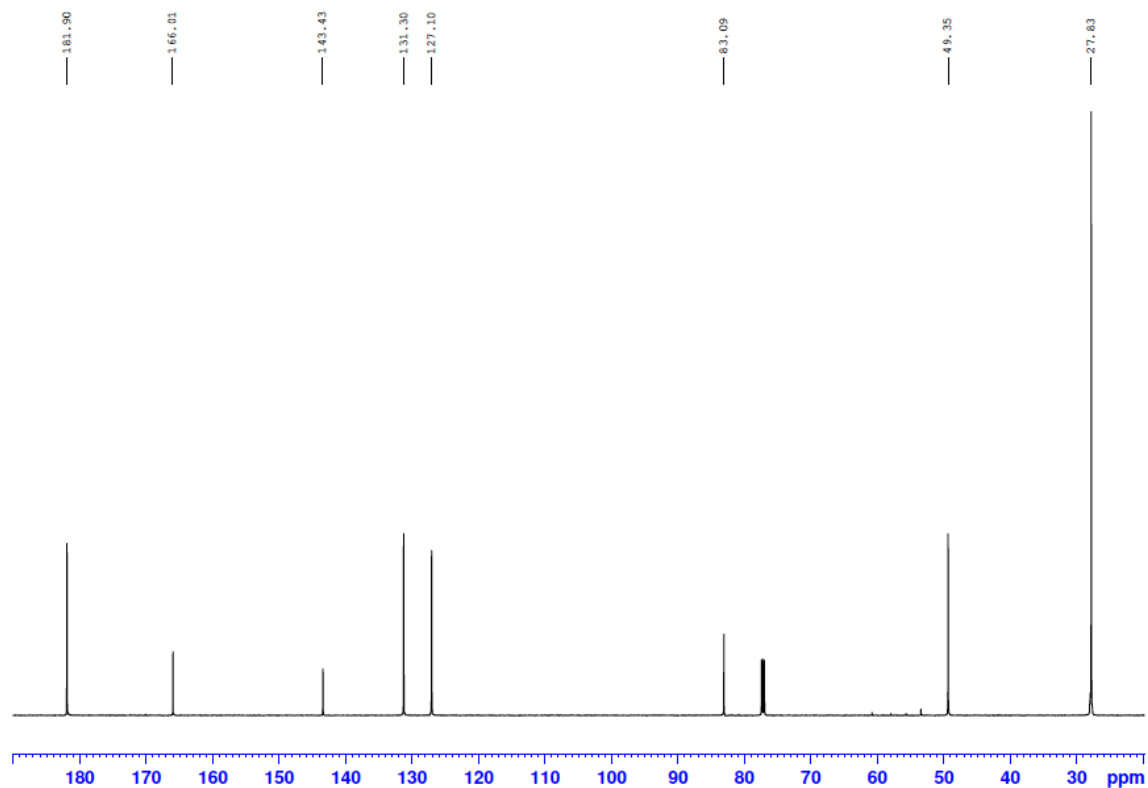
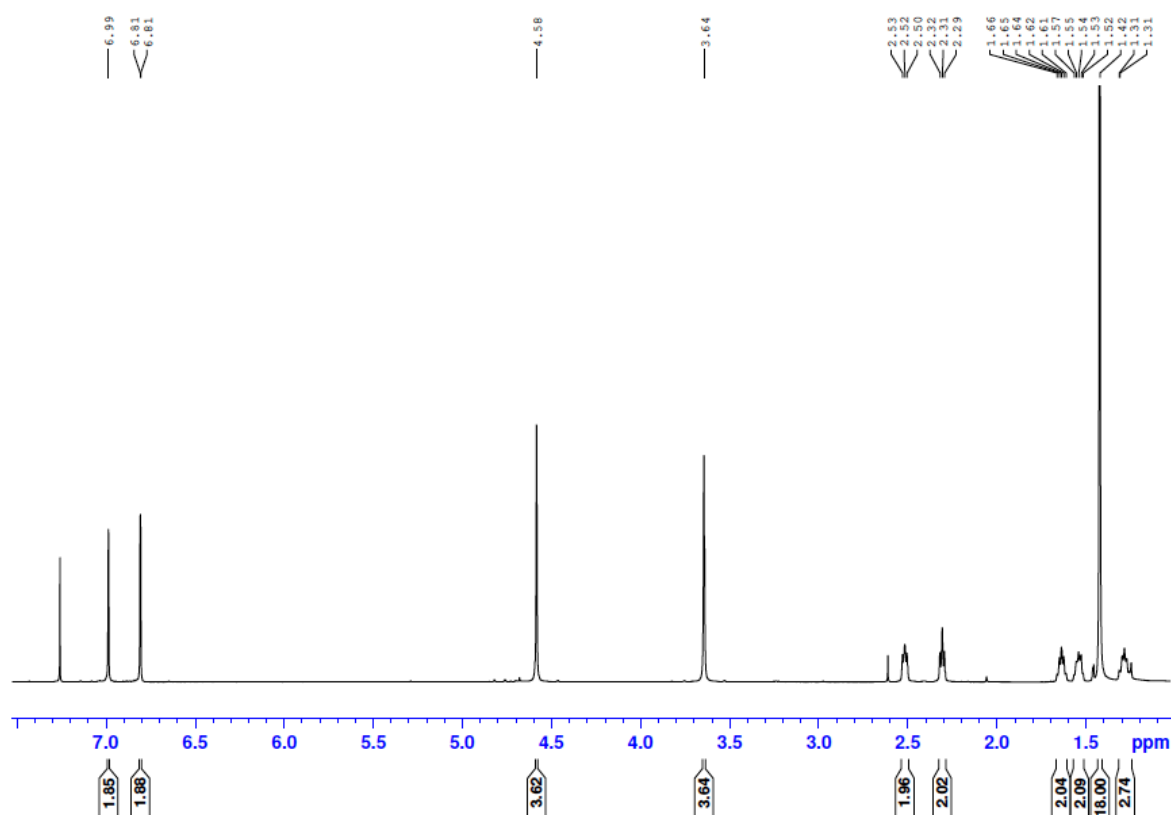


**Figure S2.3**  $^{13}\text{C}$  NMR (150 MHz,  $\text{CDCl}_3$ ) of **2**.

**6-(Bis((1-(2-(*tert*-butoxy)-2-oxoethyl)-1*H*-imidazol-2-yl)methyl)amino)**

**hexanoic acid (3).** To a solution of compound **2** (1.81 g, 8.63 mmol) in anhydrous DCE (15.5 mL), 6-aminocaproic acid (561 mg, 4.28 mmol) was added. The reaction mixture was stirred for 1.5 hours at room temperature under argon. Sodium triacetoxyborohydride (2.75 g, 13.0 mmol) was then added and the mixture stirred for an additional 12 hours. The solvent was evaporated under reduced pressure yielding an off-white oil. The desired product was isolated by column chromatography (10% MeOH/EtOAc), which, following evaporation and lyophilization yielded a **3** as a white powder (1.72 g, 77%). TLC  $R_f$  = 0.16 (10%



196

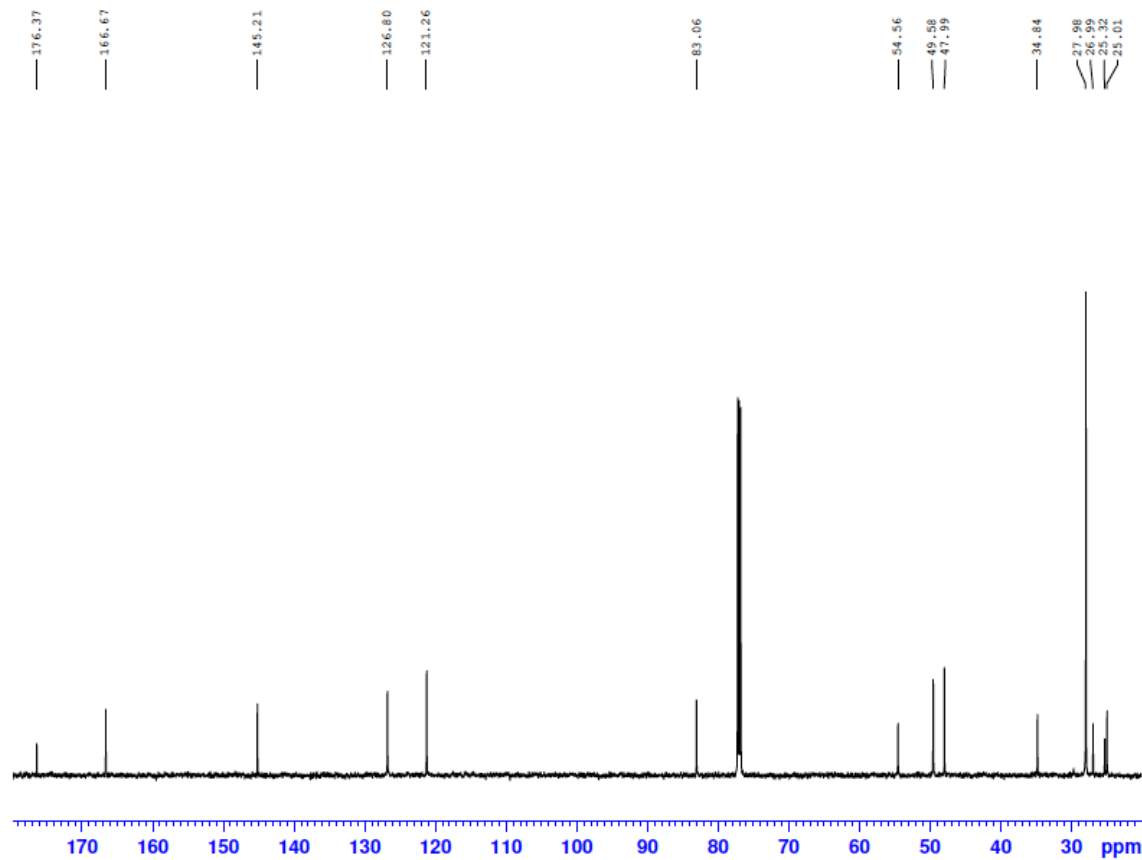


**Figure S2.5**  $^{13}\text{C}$  NMR (150 MHz,  $\text{CDCl}_3$ ) of 6-(Bis((1-(2-(*tert*-butoxy)-2-oxoethyl)-1*H*-imidazol-2-yl)methyl)amino)hexanoic acid (**3**).

***tert*-Butyl** {2-[[[1-(*tert*-butoxycarbonylmethyl)-1*H*-imidazol-2-yl]methyl][6-oxo-6-([*p*-(1,2,4,5-tetrazin-3-yl)phenyl]methyl)amino)hexyl]amino)methyl]-1*H*-imidazol-1-yl}acetate (**4**). In one vial, compound **3** (123 mg, 0.13 mmol), benzotriazol-1-yl-oxytripyrrolidinophosphonium hexafluorophosphate (PyBOP) (213.9 mg, 0.41 mmol) and *N,N*-dimethylformamide (DMF) (15 mL) were combined and stirred at room temperature under argon for 15 minutes. In a separate vial, ((4-tetrazine-3-yl)phenyl)methanamine hydrochloride (34.2 mg,

0.15 mmol), N,N-diisopropylethylamine (DIPEA) (0.62 mL, 3.56 mmol) and DMF (15 mL) were combined and stirred at room temperature under argon for 15 minutes. The two vials were then combined, and allowed to stir at room temperature under argon gas for 12 hours, where the solvent was then removed under reduced pressure. The desired product was isolated by semi-preparative HPLC (Method 1, 4 mL/min), yielding **4** a bright pink oil (64.9 mg, 44%). TLC  $R_f$  = 0.16 (10% MeOH/DCM);  $^1\text{H}$  NMR (600 MHz,  $\text{CDCl}_3$ ):  $\delta$  10.19 (s, 1H), 8.56 (d,  $J$  = 12 Hz, 2H), 7.51 (d,  $J$  = 6 Hz, 2H), 6.89 (s, 2H), 6.82 (d,  $J$  = 6 Hz, 2H), 4.57 (s, 4H), 4.56 (s, 1H), 4.55 (s, 1H), 3.59 (s, 4H), 2.49-2.52 (t,  $J$  = 12 Hz, 2H), 2.23 (t,  $J$  = 6 Hz, 2H), 1.63 (m, 2H), 1.50 (m, 2H), 1.42 (s, 18H), 1.29 (m, 2H).  $^{13}\text{C}$  NMR (150 MHz,  $\text{CDCl}_3$ ):  $\delta$  173.5, 167.0, 166.5, 158.0, 145.5, 144.7, 130.7, 128.8, 128.7, 127.7, 121.5, 83.3, 54.2, 50.3, 48.1, 43.3, 36.3, 28.2, 26.5, 25.2. HRMS ( $\text{ES}^+$ )  $m/z$  calculated for  $\text{C}_{35}\text{H}_{49}\text{N}_{10}\text{O}_5$  [ $\text{M}+\text{H}^+$ ] 689.3887, found 689.3884.

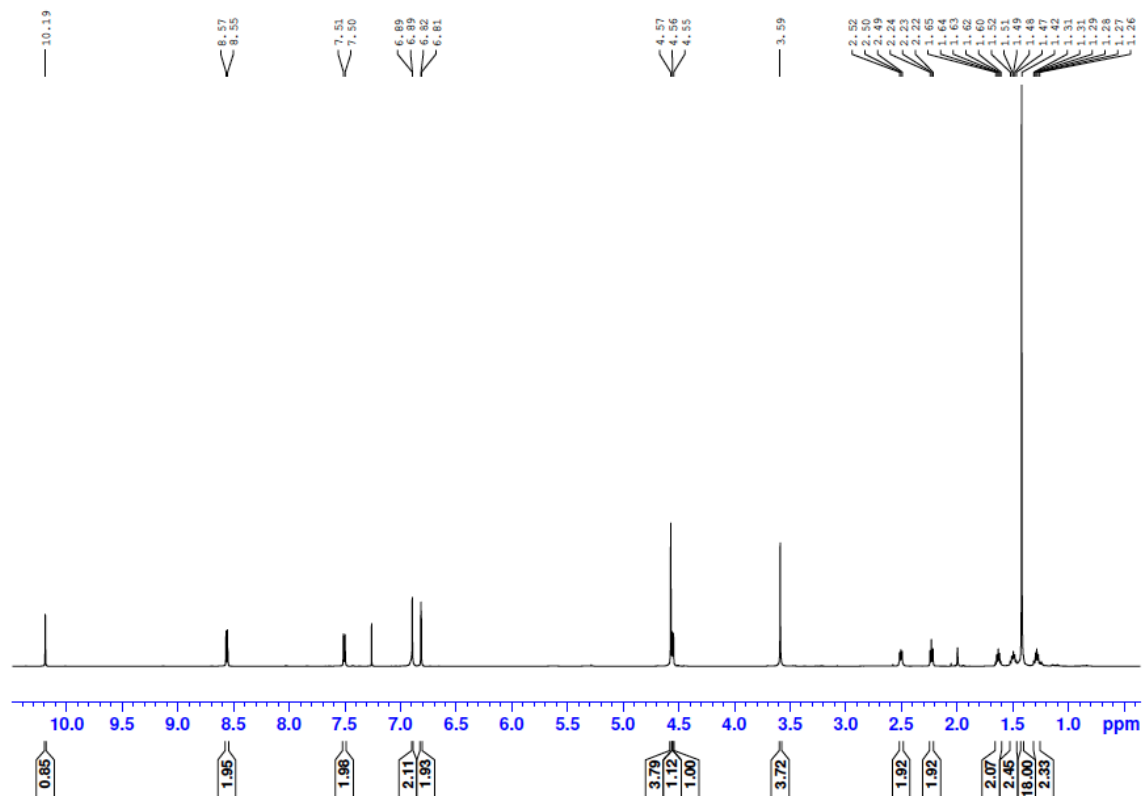


**Figure S2.6**  $^1\text{H}$  NMR (600 MHz,  $\text{CDCl}_3$ ) of *tert*-Butyl {2-([1-(*tert*-butoxycarbonylmethyl)-1*H*-imidazol-2-yl]methyl)[6-oxo-6-([*p*-(1,2,4,5-tetrazin-3-yl)phenyl]methyl)amino)hexyl]amino)methyl]-1*H*-imidazol-1-yl}acetate (4).

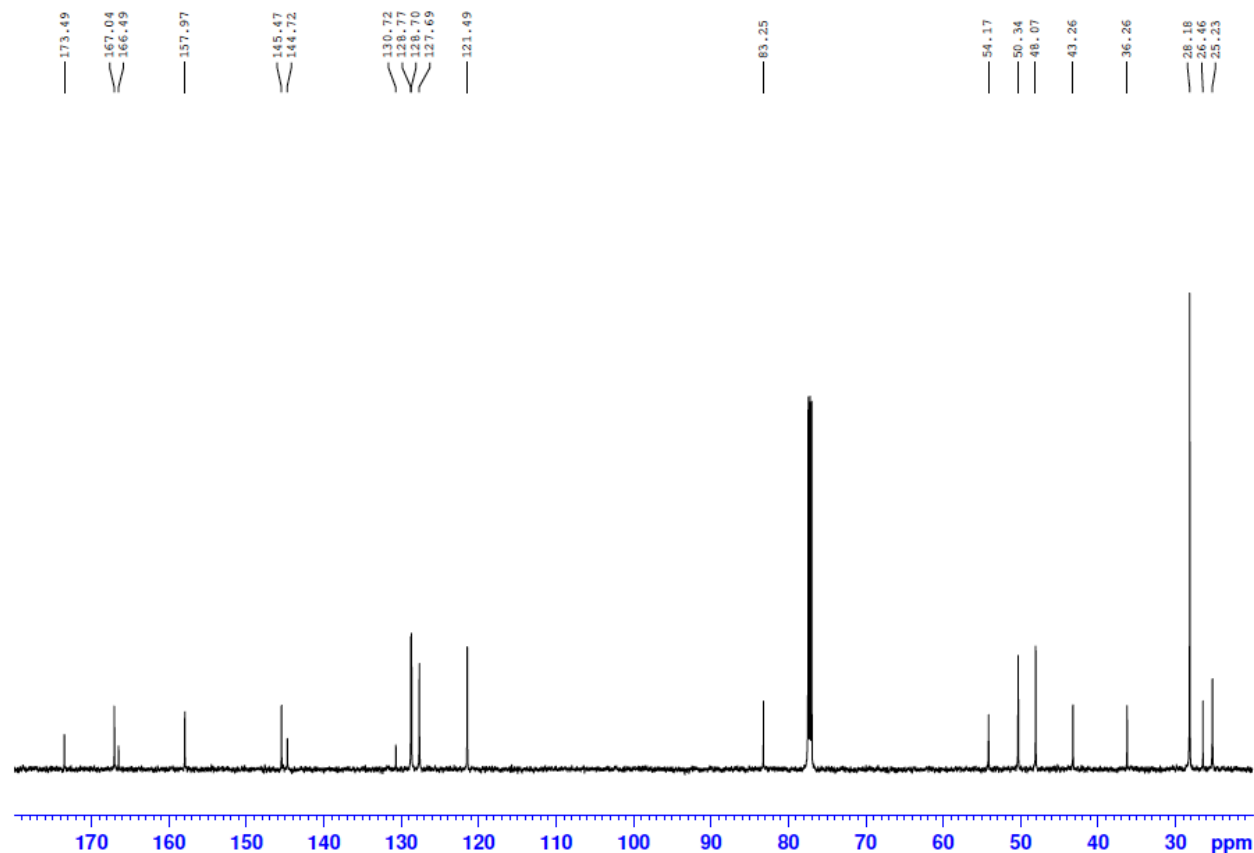


**Figure S2.7**  $^{13}\text{C}$  NMR (150 MHz,  $\text{CDCl}_3$ ) of *tert*-Butyl {2-[(1-(*tert*-butoxycarbonylmethyl)-1*H*-imidazol-2-yl)methyl][6-oxo-6-([*p*-(1,2,4,5-tetrazin-3-yl)phenyl)methyl]amino)hexyl]amino)methyl]-1*H*-imidazol-1-yl}acetate (**4**).

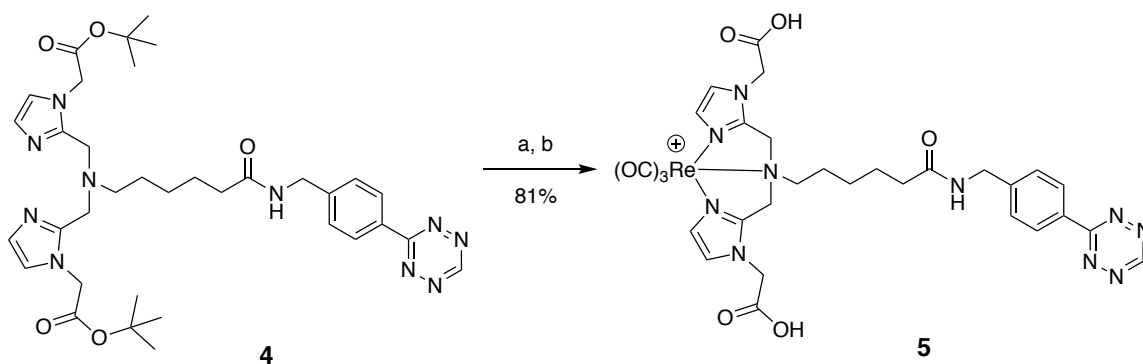


**Figure S2.8** Synthesis of **5** from **4**. a)  $\text{Re}(\text{CO})_3(\text{H}_2\text{O})_3\text{Br}$ , ACN, MW, 60 °C, 20 min. b) DCM, TFA, MW, 60 °C, 6 min.

***tert*-Butyl {2-[[[1-(*tert*-butoxycarbonylmethyl)-1*H*-imidazol-2-yl]methyl][6-oxo-6-([*p*-(1,2,4,5-tetrazin-3-yl)phenyl]methyl)amino)hexyl]amino)methyl]-1*H*-imidazol-1-yl]acetate rhenium tricarbonyl complex (**5**)**. To a microwave vial, compound **4** (21.6 mg, 0.03 mmol),  $\text{Re}(\text{CO})_3(\text{H}_2\text{O})_3\text{Br}$  (16.2 mg, 0.04 mmol) and acetonitrile (ACN) (3 mL) were combined. The vial was sealed and heated in a microwave for 20 minutes at 60 °C. Solvent was removed under reduced pressure. Next, the crude product was dissolved in a 1:1 solution of DCM:TFA (1 mL) and added to a microwave vial. The vial was sealed and heated in a microwave for 6 minutes at 60 °C. Solvent was removed under reduced pressure. The desired product was isolated by semi-preparative HPLC (Method 1), yielding **5** as a bright pink oil (17.4 mg, 81%). TLC  $R_f$  = 0.21 (10% MeOH/DCM)  $^1\text{H}$  NMR (600 MHz, MeOD):  $\delta$ 10.24 (s, 1H), 8.48 (d,  $J$  = 12 Hz, 2H), 8.14 (s, 1H), 7.50 (d,  $J$  = 6 Hz, 2H), 6.94 (s, 2H), 6.92 (s, 2H), 4.53 (q,  $J$  = 12 Hz, 4H), 4.44 (d, 4H), 4.31 (d,  $J$  = 18 Hz, 2H), 3.56 (t,  $J$  = 12 Hz, 2H), 3.27 (s, 2H), 2.28 (t,  $J$  = 6 Hz, 2H), 1.85 (m, 2H), 1.71 (m, 2H), 1.37 (m, 2H).  $^{13}\text{C}$  NMR (150 MHz, MeOD):  $\delta$ 197.5, 195.8, 167.9, 152.8, 133.7, 130.7, 129.4, 128.9, 124.9, 85.1, 71.1, 60.5, 60.0, 59.7, 50.3, 49.9, 35.1, 28.3, 27.3, 26.4, 25.9. HRMS ( $\text{ES}^+$ )  $m/z$  calculated for  $\text{C}_{30}\text{H}_{32}\text{N}_{10}\text{O}_8\text{Re}^+$  [ $\text{M}+\text{H}^+$ ] 847.1962, found 847.1953.



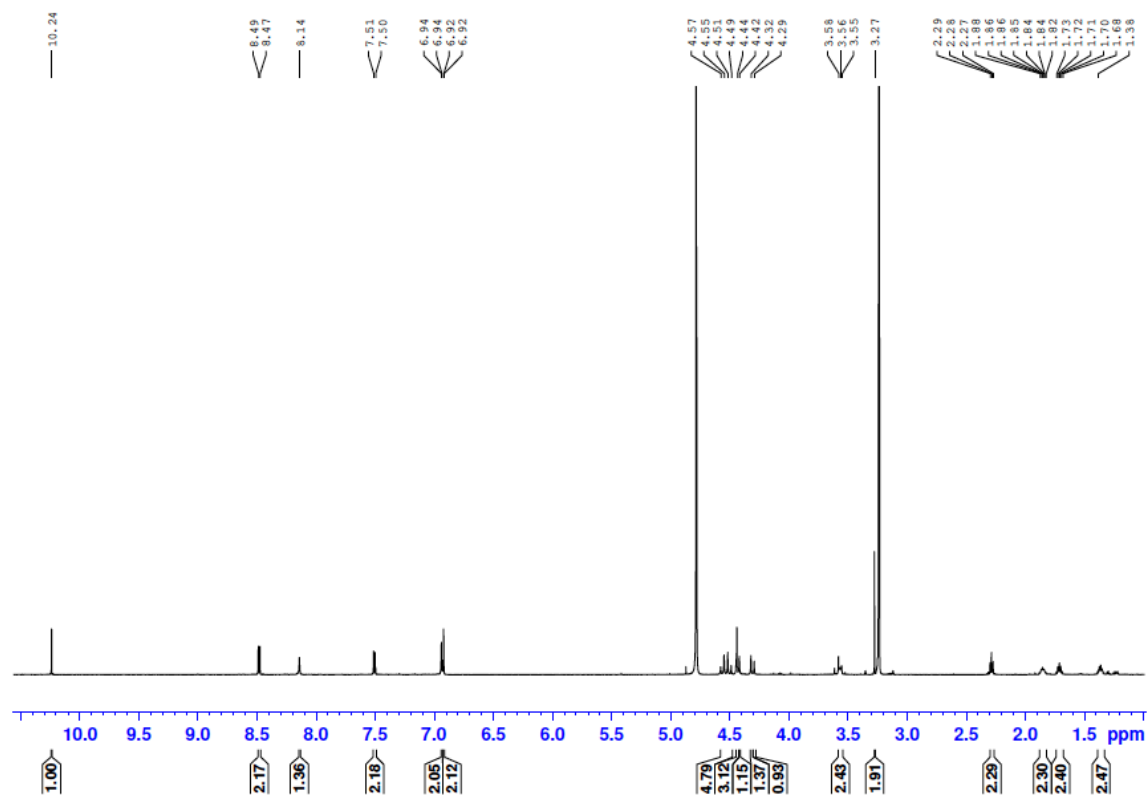


**Figure S2.9**  $^1\text{H}$  NMR (600 MHz, MeOD) of *tert*-Butyl {2-[(1-(*tert*-butoxycarbonylmethyl)-1*H*-imidazol-2-yl)methyl][6-oxo-6-({[*p*-(1,2,4,5-tetrazin-3-yl)phenyl]methyl}amino)hexyl]amino)methyl]-1*H*-imidazol-1-yl}acetate rhenium tricarbonyl complex (**5**).

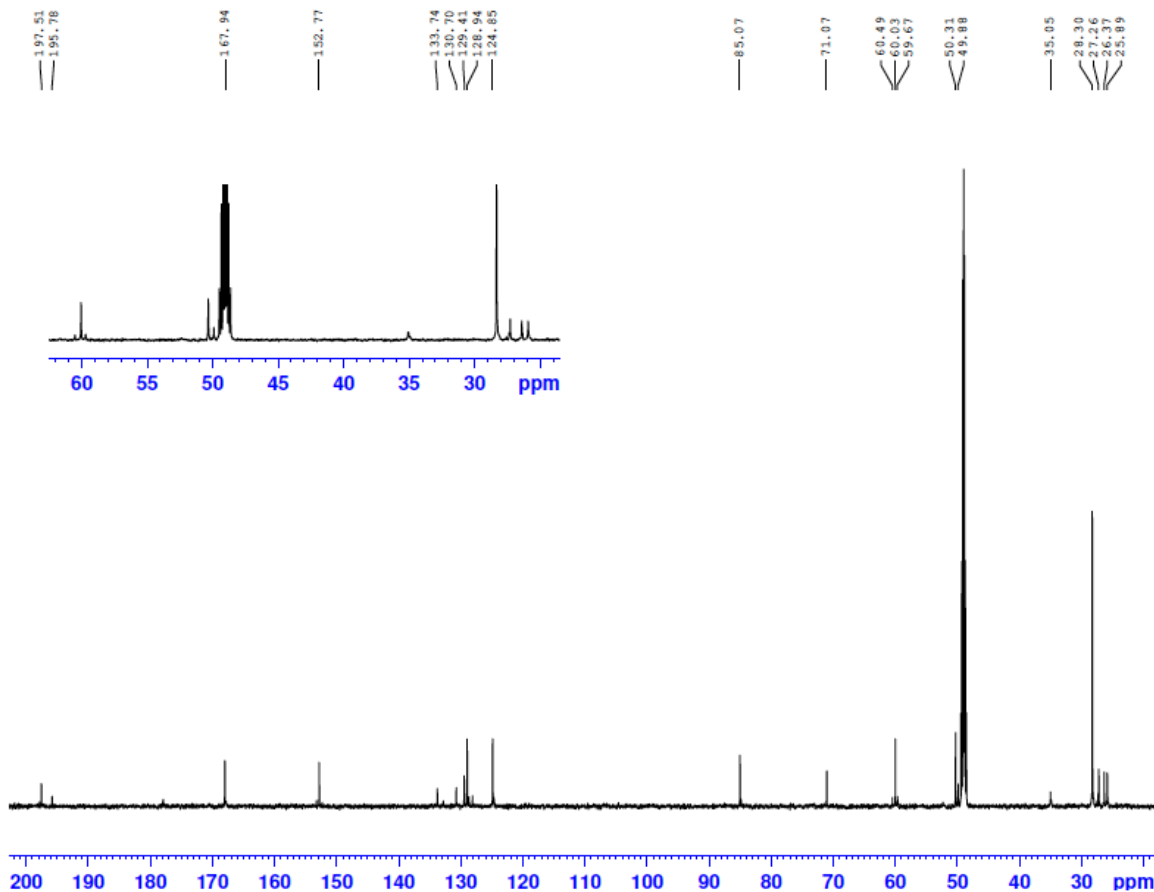


**Figure S2.10**  $^{13}\text{C}$  NMR (150 MHz, MeOD) of *tert*-Butyl {2-([1-(*tert*-butoxycarbonylmethyl)-1*H*-imidazol-2-yl]methyl)[6-oxo-6-([*p*-(1,2,4,5-tetrazin-3-yl)phenyl]methyl)amino)hexyl]amino)methyl]-1*H*-imidazol-1-yl}acetate rhenium tricarbonyl complex (**5**).

**Preparation of  $^{99\text{m}}\text{Tc}[\text{Tc}(\text{CO})_3(\text{H}_2\text{O})_3]^+$ .** A sealed 0.5-2 mL microwave vial containing  $\text{K}_2[\text{BH}_3\text{CO}_2]$  (10.0 mg, 73.5  $\mu\text{mol}$ ),  $\text{Na}_2\text{CO}_3$  (15.0 mg, 141  $\mu\text{mol}$ ),  $\text{Na}_2\text{B}_4\text{O}_7 \cdot 10\text{H}_2\text{O}$  (20.0 mg, 52.4  $\mu\text{mol}$ ), and Na/K-tartrate (25.0 mg, 88.6  $\mu\text{mol}$ ) was flushed with Argon gas for 10 minutes.  $^{99\text{m}}\text{TcO}_4^-$  (130 MBq) in 2 mL of saline

was added by syringe, and the solution was placed in the microwave reactor for 3.5 minutes at 110 °C with 10 seconds of pre-stirring. Once complete, the solution was brought to a pH of 3.5-4 by the addition of 1 M HCl.

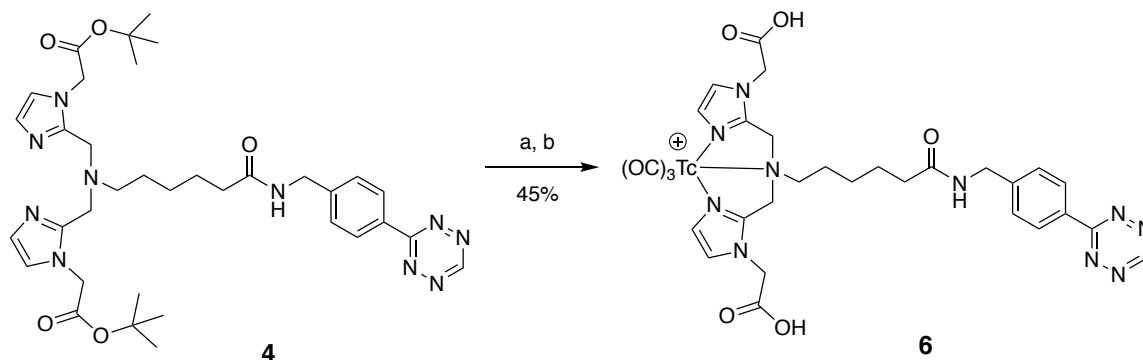


**Figure S2.11** Synthesis of **6** from **4**. a)  $^{99m}\text{Tc}[\text{Tc}(\text{CO})_3(\text{OH}_2)_3]^+$ , MeOH, Saline (0.9%), MW, 60 °C, 20 min. b) DCM, TFA, MW, 60 °C, 6 min.

***tert*-Butyl {2-[{{{1-(*tert*-butoxycarbonylmethyl)-1*H*-imidazol-2-yl}methyl}[6-oxo-6-({[*p*-(1,2,4,5-tetrazin-3-yl)phenyl]methyl}amino)hexyl]amino)methyl]-1*H*-imidazol-1-yl}acetate technetium-99m tricarbonyl complex (**6**).** To a solution of 259  $\mu\text{L}$  of  $^{99m}\text{Tc}[\text{Tc}(\text{CO})_3(\text{OH}_2)_3]^+$  in saline (111 MBq), **4** was added at a concentration of  $10^3$  M (Scheme 6) in 241  $\mu\text{L}$  MeOH in a vial. The vial was sealed and heated in a microwave for 20 minutes at 60°C. Upon cooling, the mixture was analyzed for purity by analytical HPLC (Method 1). After cooling and evaporation of solvent, the *tert*-butyl ester protecting groups were removed by treatment with 1:1 TFA and DCM and heated in a microwave for 6 minutes at

60°C. Upon completion of the deprotection, the reaction was dried and re-suspended in ACN/H<sub>2</sub>O (1:1 v/v) and purified by HPLC resulting **6** with no impurities (1). The radiochemical yield of compound **6** was 45% (n = 22).

**Tetrazine-TCO reaction with 6.** To a solution of **6** and PBS (500 µL), transcyclooctene-4-ol (27 µL (50 mg/mL in DMSO)) was added, and the solution left to incubate at room temperature for 10 minutes. The reaction was monitored by HPLC (method 2).

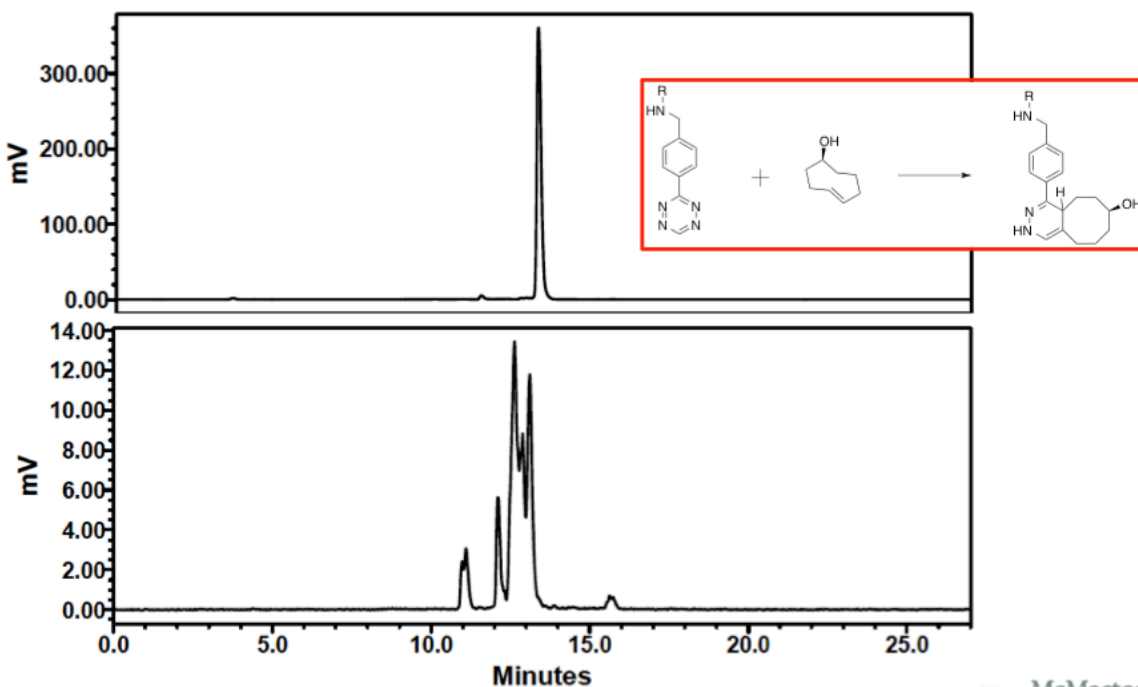


**Figure S2.12** Gamma HPLC traces of reaction between **6** and TCO.

**Stability testing of 7 in PBS.** Compound **6** was added to PBS at formulation concentration (200 µCi/mL) and incubated at 37 °C for 3 hours. The reaction was monitored by HPLC (see figure S10).

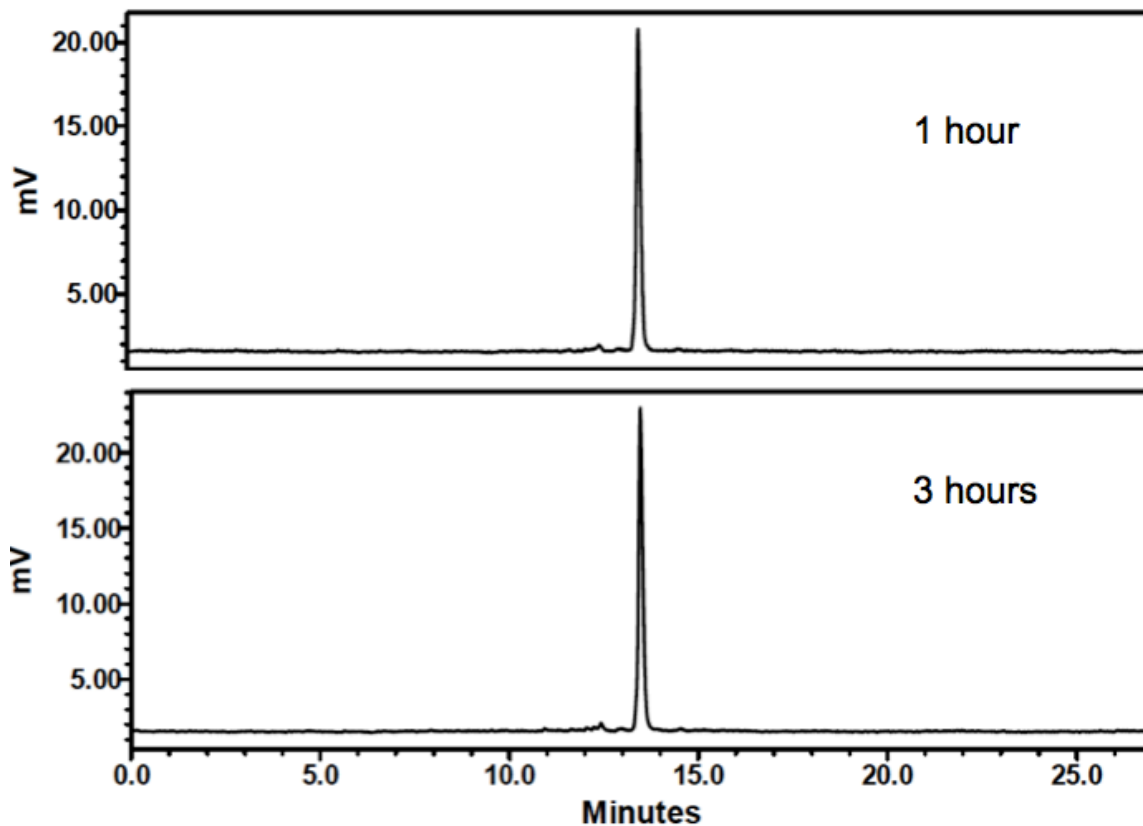


**Figure S2.13** Gamma HPLC traces of **6** after incubation in PBS for 1 and 3 hours.

**Cysteine and Histidine challenge experiments.** Compound **6** was incubated with three concentrations of cysteine (100 mM, 2mM and 100  $\mu$ M), 100 mM histidine, and a PBS standard at 37 °C for 1, 3, and 6 hours. Stability of the **6** was monitored by HPLC (Figures S2.14-2.16).

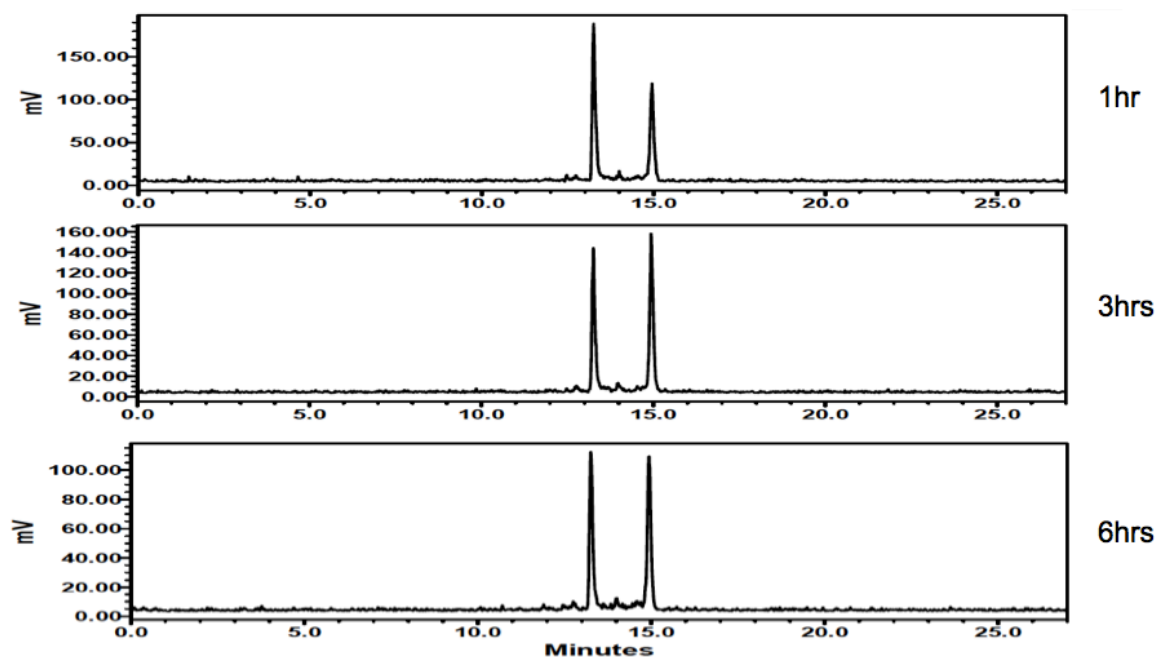


**Figure S2.14** Gamma HPLC traces of **6** upon incubation at 37 °C with 100 mM L-cysteine for 1, 3 and 6 hours.

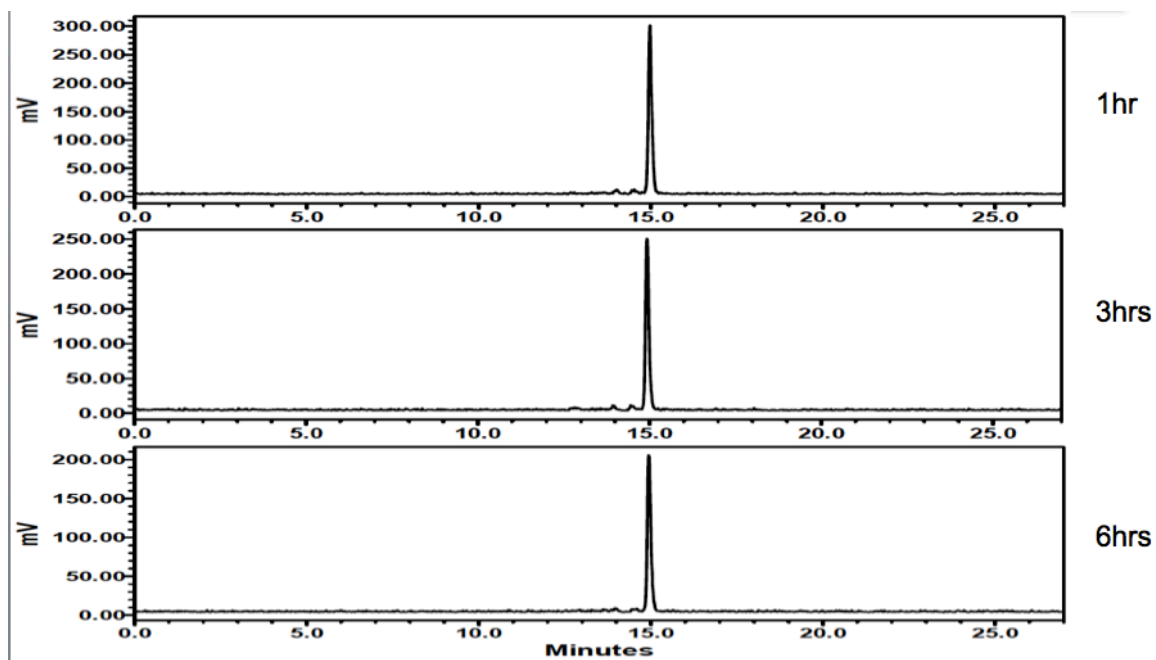


**Figure S2.15** Gamma HPLC traces of **6** upon incubation at 37 °C with 100 mM Histidine for 1, 3 and 6 hours.

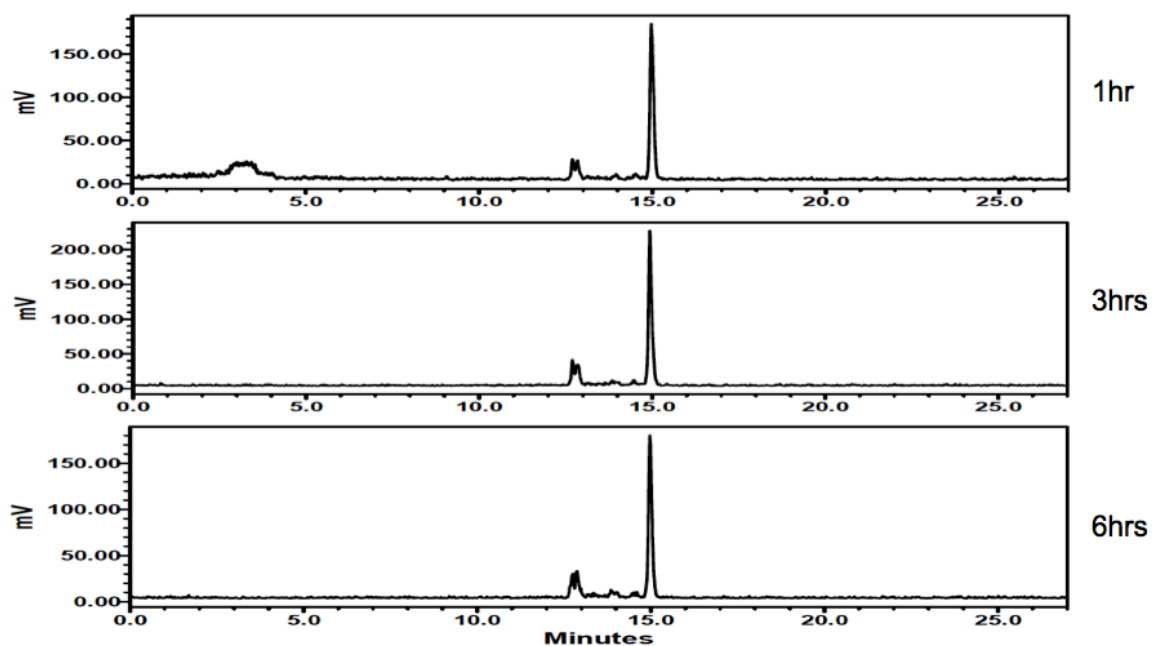


**Figure S2.16** Gamma HPLC traces of **6** upon incubation at 37 °C in PBS for 1, 3 and 6 hours.

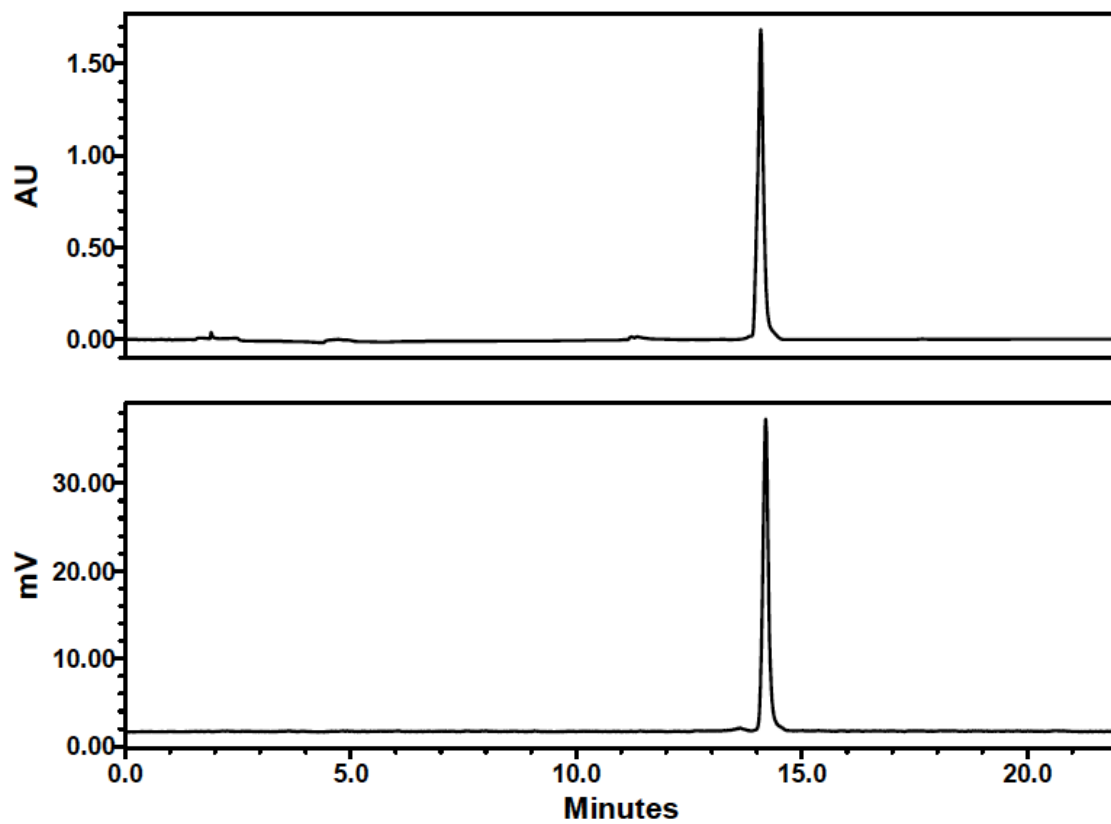


**Figure S2.17** HPLC chromatograms (UV and  $\gamma$ ) of compound **5** (UV) (top) co-injected with compound **6** ( $\gamma$ )(bottom).



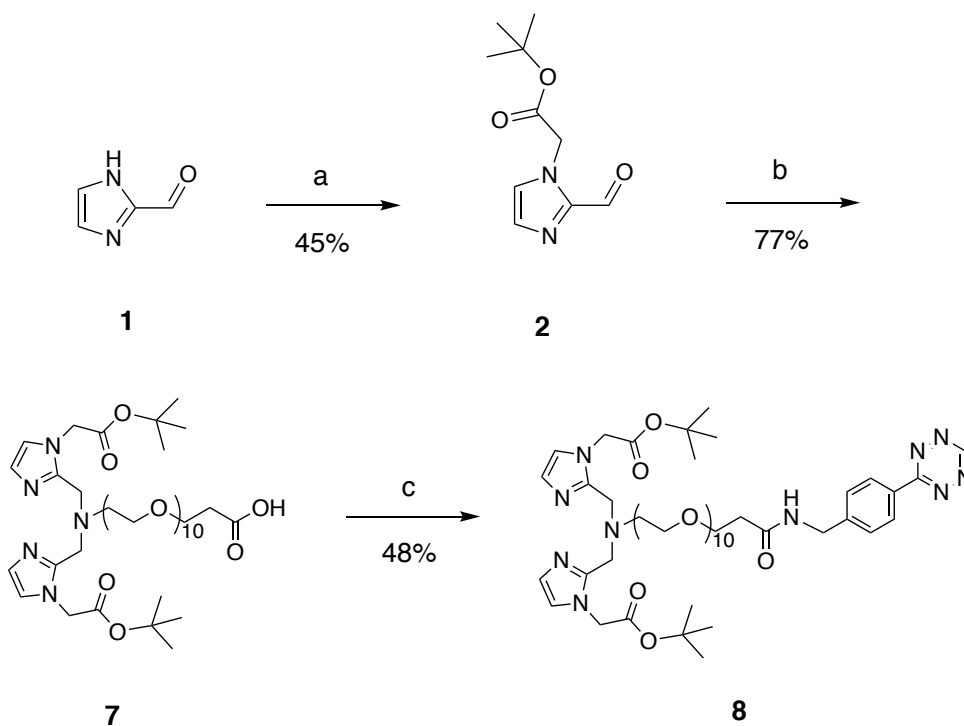


**Figure S2.18** Synthesis of Compound **8** from Compound **2**. a) DMF, DIPEA, *t*-butylbromoacetate, 80 °C, 4 h. b) DCE, NaBH(OAc)<sub>3</sub>, NH<sub>2</sub>-PEG<sub>10</sub>-CH<sub>2</sub>CH<sub>2</sub>COOH, 50 °C, 12 h. c) PyBOP, DIPEA, DMF, ((4-tetrazine-3-yl)phenyl)methanamine hydrochloride, rt, 12 h.

**3-[2-(2-{2-[2-(2-{2-[2-(2-{2-[2-(Bis{[1-(*tert*-butoxycarbonylmethyl)-1*H*-imidazol-2-yl]methyl}amino)ethoxy]ethoxy}ethoxy)ethoxy]ethoxy}ethoxy)ethoxy]propionic acid (**7**).** To a solution of compound **2** (0.23 g, 1.09 mmol) in anhydrous DCE (7.00 mL) was added NH<sub>2</sub>-PEG<sub>10</sub>-CH<sub>2</sub>CH<sub>2</sub>COOH (0.28 g, 0.53 mmol). The reaction mixture was stirred for 1.5 hours at room temperature under argon. Sodium triacetoxyborohydride (0.35 g, 1.64 mmol) was then added and stirred for an additional 12 hours at 50 °C. The

solvent was evaporated under reduced pressure yielding a yellow oil. The desired product was isolated by column chromatography 5-25% MeOH/DCM), which, following evaporation yielded a **2** as a yellow oil (0.24 g, 48%). TLC  $R_f$  = 0.18 (10% MeOH/DCM);  $^1\text{H}$  NMR (600 MHz,  $\text{CDCl}_3$ ):  $\delta$  7.27 (s, 1H), 6.93 (s, 2H), 6.84 (d, 2H), 4.61 (s, 4H), 2.76 (t,  $J$  = 6 Hz, 2H), 2.54 (t,  $J$  = 6 Hz, 2H), 1.38 (s, 18H).  $^{13}\text{C}$  NMR (150 MHz,  $\text{CDCl}_3$ ):  $\delta$  175.5, 167.2, 145.5, 127.3, 121.4, 82.8, 70.6, 70.6, 70.5, 70.4, 70.4, 70.3, 70.2, 70.1, 69.8, 67.6, 53.2, 50.5, 48.0, 36.2, 28.1. HRMS ( $\text{ES}^+$ )  $m/z$  calculated for  $\text{C}_{42}\text{H}_{76}\text{N}_5\text{O}_{16}$  [ $\text{M}+\text{H}^+$ ] 918.5260, found 918.5287.

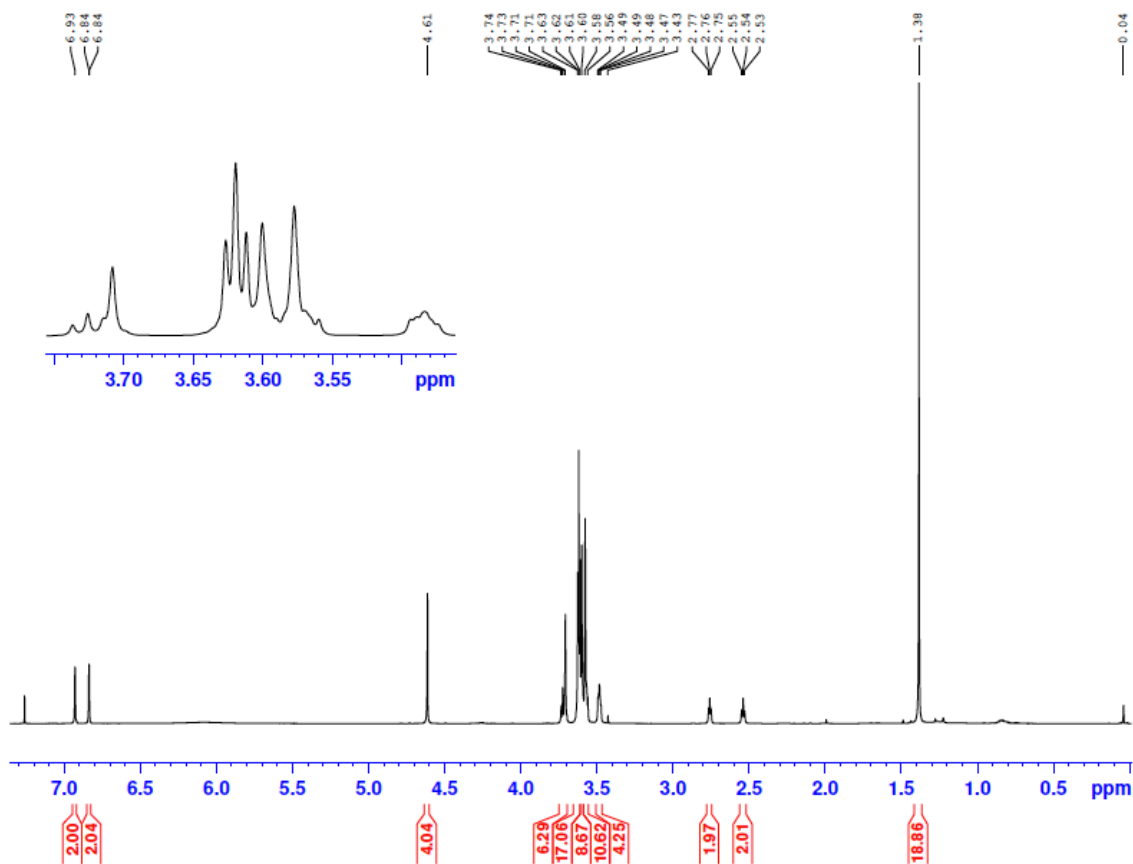


Figure S2.19  $^1\text{H}$  NMR (600 MHz,  $\text{CDCl}_3$ ) of **7**.

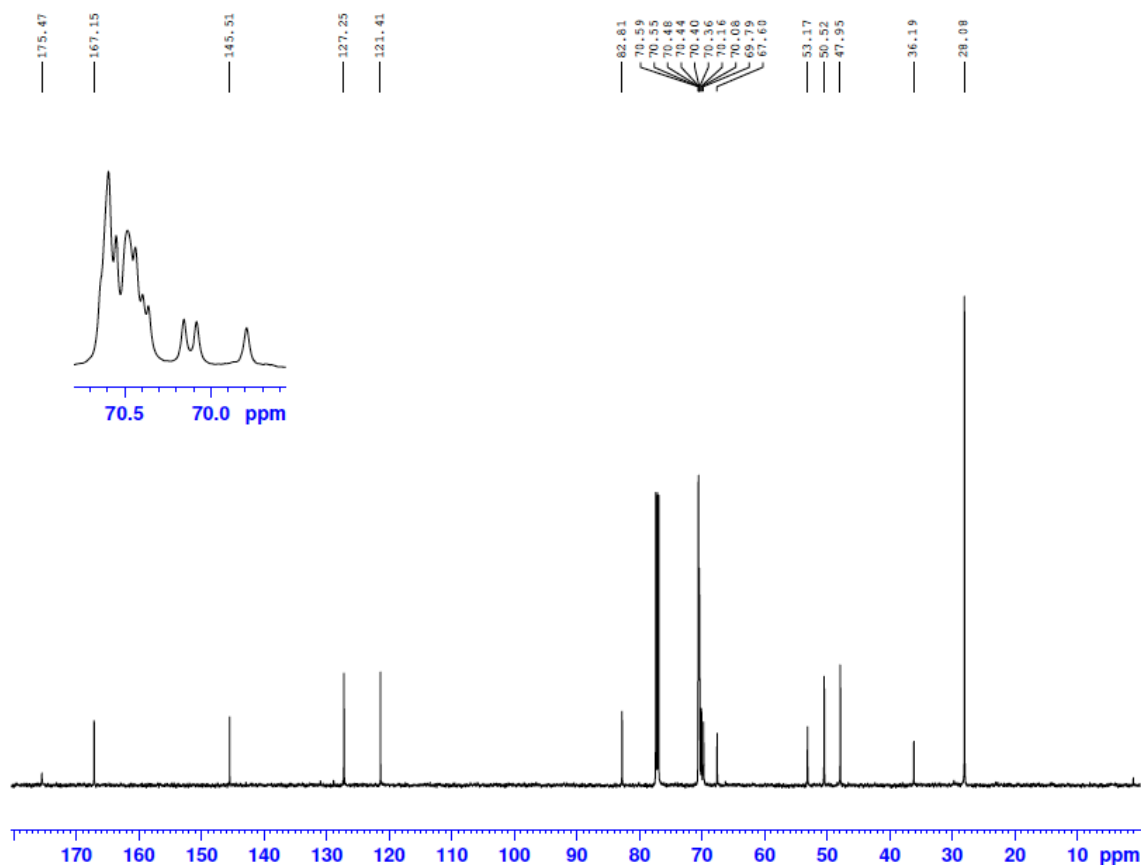
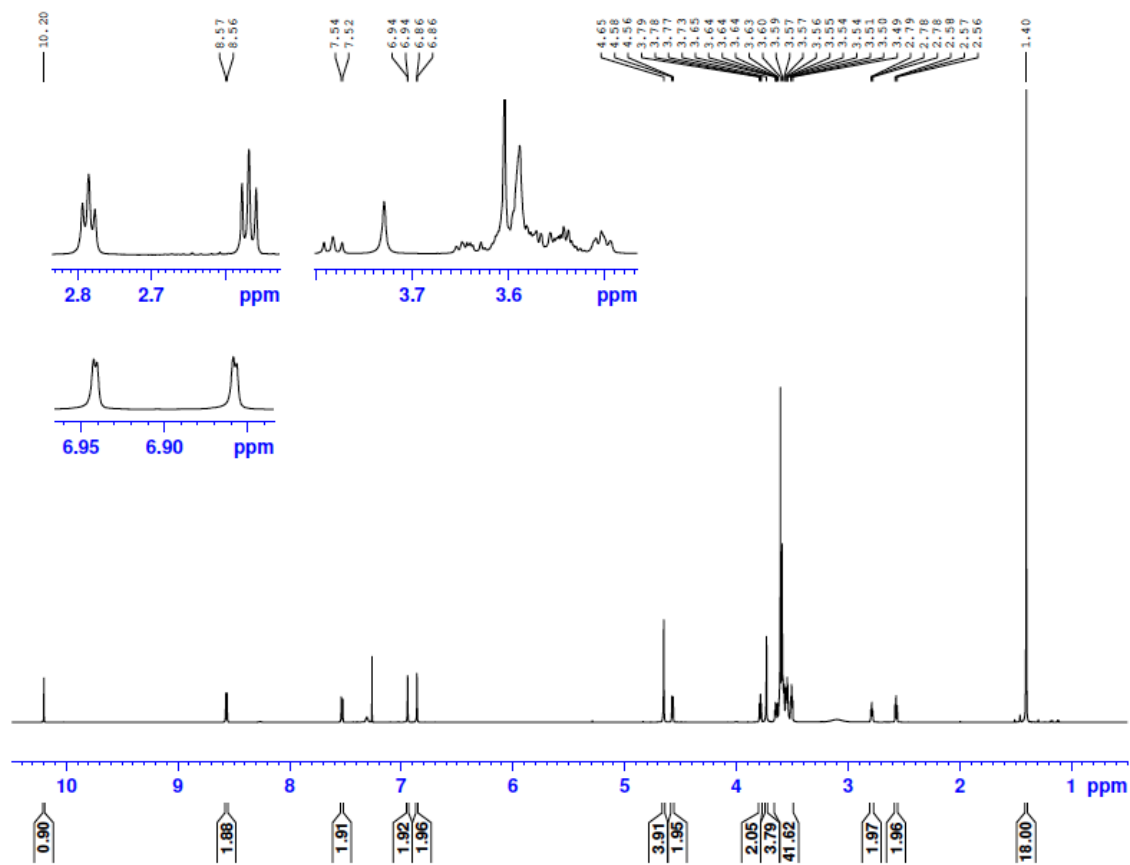


Figure S2.20  $^{13}\text{C}$  NMR (150 MHz,  $\text{CDCl}_3$ ) of **7**.

***tert*-Butyl {2-[[[1-(*tert*-butoxycarbonylmethyl)-1*H*-imidazol-2-yl]methyl]{2-[2-(2-{2-[2-(2-{2-[2-(2-{2-[3-oxo-3-({[*p*-(1,2,4,5-tetrazin-3-yl)phenyl]methyl} amino)propoxy]ethoxy}ethoxy)ethoxy]ethoxy}ethoxy)ethoxy]ethoxy}ethoxy]ethyl}amino)methyl]-1*H*-imidazol-1-yl}acetate (**8**).** To a stirring solution of compound **7** (0.12 g, 0.13 mmol) in DMF (15.0 mL), PyBOP (0.21 g, 0.41 mmol) was added and stirred for 15 min. In a separate reaction vessel, ((4-tetrazine-3-yl)phenyl)methanamine hydrochloride (0.03 g, 0.15 mmol) in , DIPEA

(0.62 mL, 6.41 mmol) and DMF (15.0 mL) were combined. After 15 minutes of stirring at room temperature, the two separate reaction mixtures were combined. The reaction was allowed to stir for 12 hours at room temperature under argon. Upon completion, solvents were evaporated under reduced pressure. The desired product was isolated by column chromatography 1-15% MeOH/DCM, followed by semi-preparative HPLC (Method 1). The solvents were evaporated under reduced pressure, yielding a bright pink oil (0.07 g, 44%). TLC  $R_f$  = 0.16 (10% MeOH/DCM).  $^1\text{H}$  NMR (600 MHz,  $\text{CDCl}_3$ ):  $\delta$  10.20 (s, 1H), 8.57 (d,  $J$  = 6 Hz, 2H), 7.53 (d,  $J$  = 12 Hz, 2H), 6.94 (d, 2H), 6.86 (d, 2H), 4.65 (t, 4H), 4.57 (d,  $J$  = 12 Hz, 2H), 3.78 (t,  $J$  = 6 Hz, 2H), 3.73 (s, 4H), PEG MESS, 2.78 (t,  $J$  = 6 Hz, 2H), 2.57 (t,  $J$  = 6 Hz, 2H), 1.40 (s, 18H).  $^{13}\text{C}$  NMR (150 MHz,  $\text{CDCl}_3$ ):  $\delta$  172.2, 167.2, 166.5, 158.0, 145.6, 144.9, 130.6, 128.7, 128.5, 127.3, 121.6, 82.9, 70.7, 70.5, 70.4, 70.2, 69.9, 67.5, 55.3, 50.7, 48.1, 43.1, 37.2, 28.2.



**Figure S2.21**  $^1\text{H}$  NMR (600 MHz,  $\text{CDCl}_3$ ) of **8**.

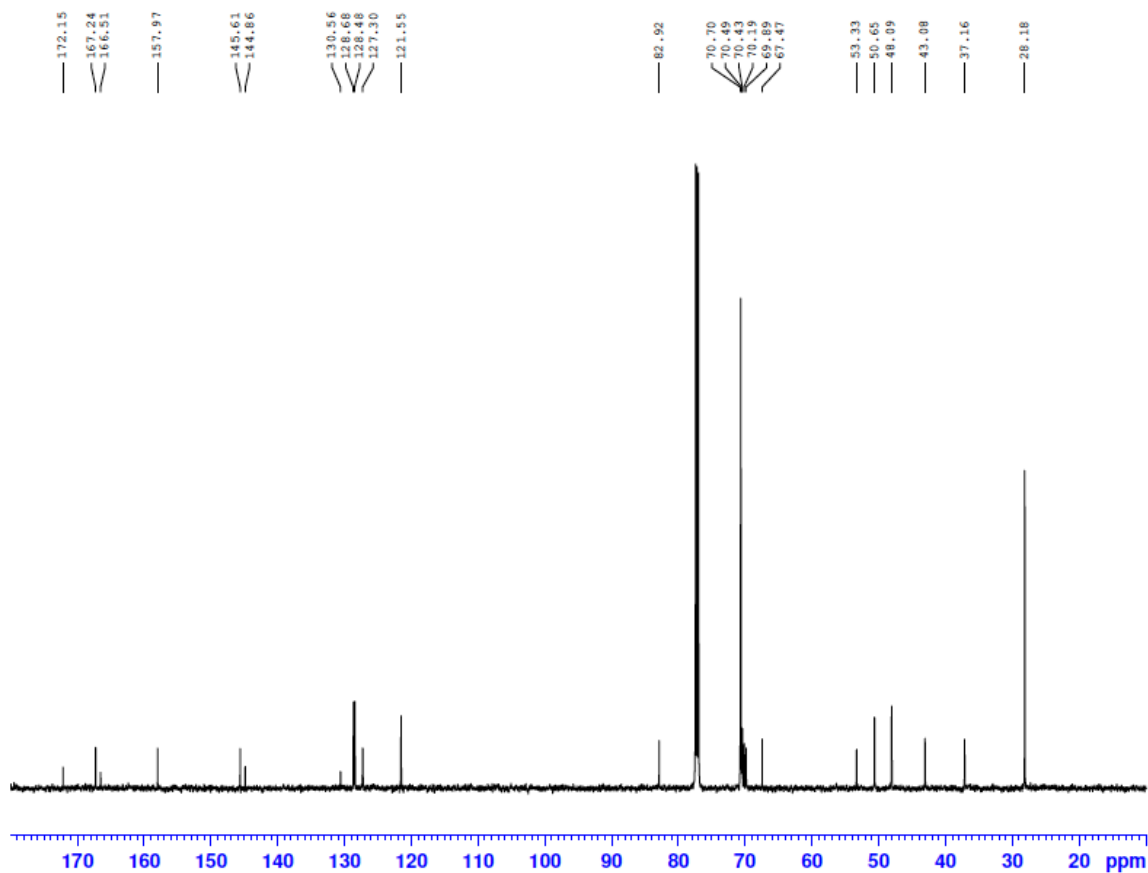


**Figure S2.22**  $^{13}\text{C}$  NMR (150 MHz,  $\text{CDCl}_3$ ) of **8**.

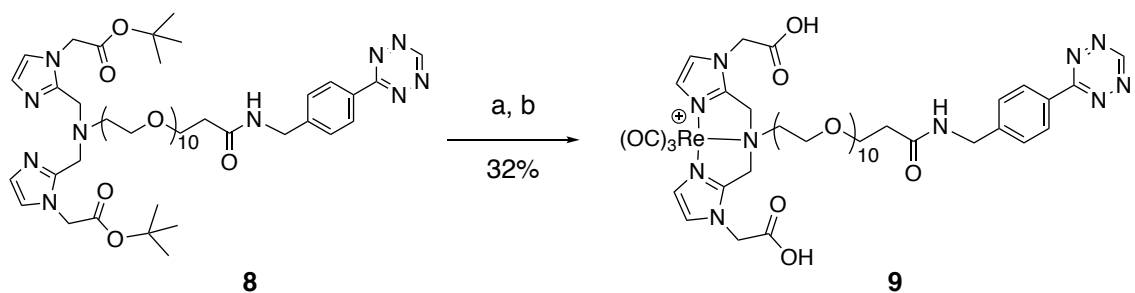


**Figure S2.23** Synthesis of compound **9** from **8**. a)  $\text{Re}(\text{CO})_3(\text{OH}_2)_3\text{Br}$ , ACN, MW, 60 °C, 20 min. b) DCM, TFA, MW, 60 °C, 6 min.

To a solution of compound **8** (0.01 g, 0.01 mmol) in ACN (3 mL),  $\text{Re}(\text{CO})_3(\text{H}_2\text{O})_3\text{Br}$  was added (0.005 g, 0.01 mmol). After a microwave reaction for 20 minutes at 60 °C, solvents were removed under reduced pressure, and dissolved in a 1:1 solution of DCM:TFA. A second microwave reaction was performed for 6 minutes at 60°C to remove the *tert*-butyl ester protecting groups. Solvents were removed under reduced pressure, and the desired product was isolated using semi-preparative HPLC (Method 1) yielding compound **9** as a bright pink oil (0.004, 32%). TLC  $R_f$  = 0.11 (10% MeOH/DCM).  $^1\text{H}$  NMR (600 MHz, MeOD):  $\delta$  10.23 (s, 1H), 8.47 (d,  $J$  = 6 Hz, 2H), 7.49 (d,  $J$  = 3 Hz, 2H), 6.92 (d,  $J$  = 3 Hz, 4H), 4.56-4.29 (PEG mess), 3.56 (s, 6H), 2.28 (t,  $J$  = 12 Hz, 2H), 1.84 (m, 2H), 1.70 (m, 2H), 1.36 (m, 2H), 1.04 (t, 1H).  $^{13}\text{C}$  NMR (150 MHz,  $\text{CDCl}_3$ ):  $\delta$  197.8, 176.0, 167.7, 159.3, 152.7, 145.8, 132.4, 129.5, 129.4, 128.1, 124.7, 71.4, 70.1, 60.2, 43.8, 36.7, 27.3, 26.7, 26.3. HRMS ( $\text{ES}^+$ )  $m/z$  calculated for  $\text{C}_{47}\text{H}_{66}\text{N}_{10}\text{O}_{18}\text{Re}$  [ $\text{M}+\text{H}^+$ ] 1245.4067, found 1245.2114.

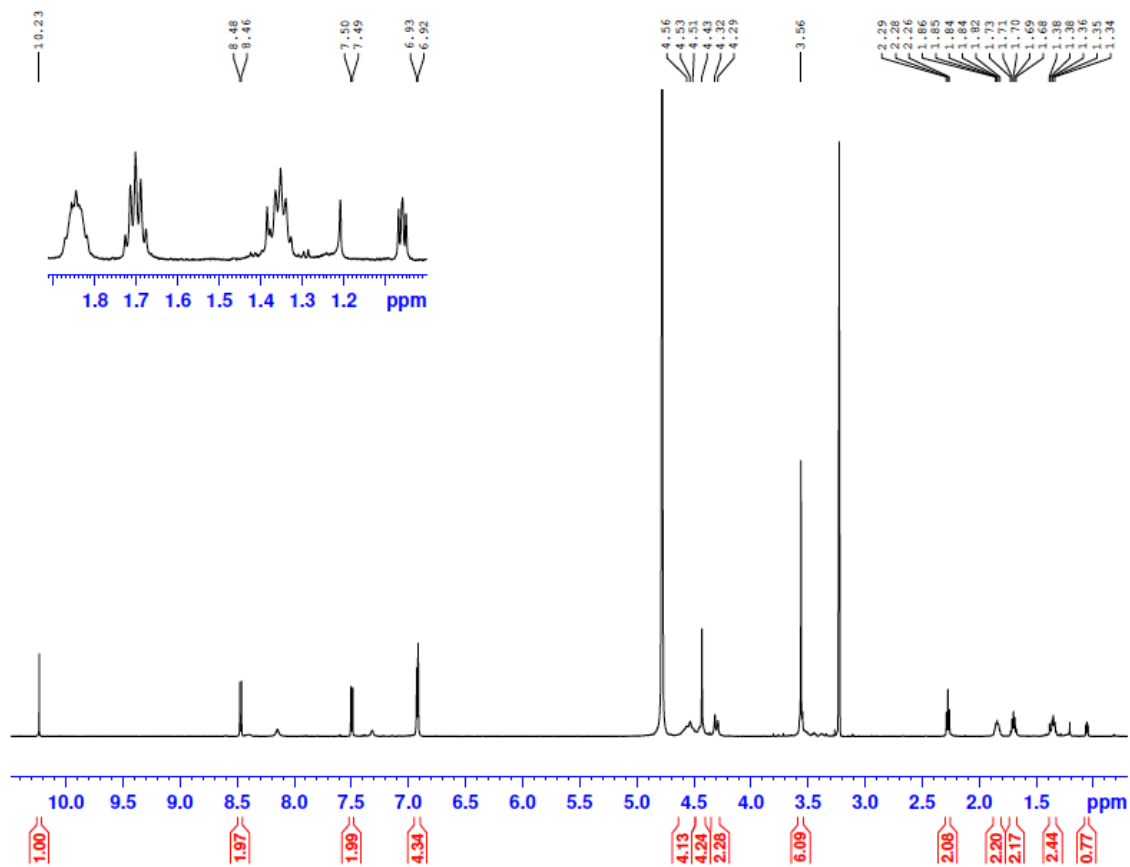


**Figure S2.24**  $^1\text{H}$  NMR (600 MHz, MeOD) of **9**.



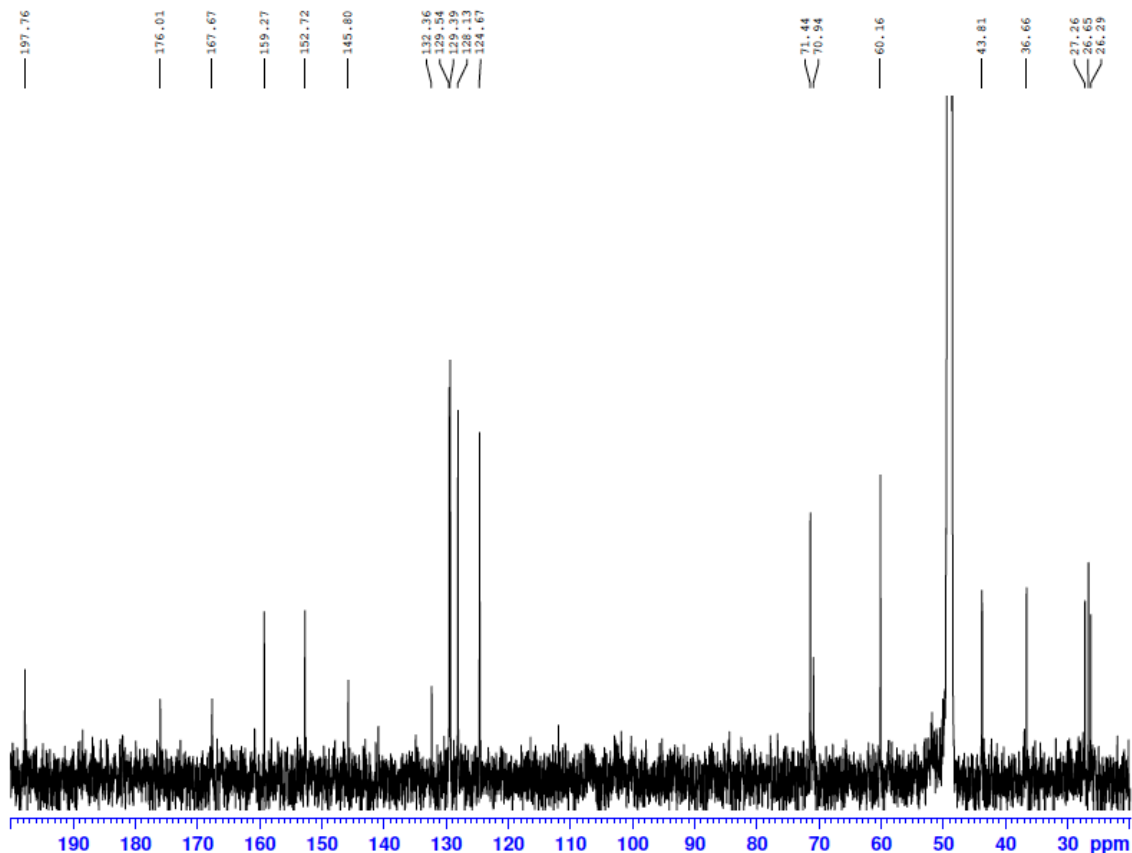


**Figure S2.25**  $^{13}\text{C}$  NMR (150 MHz, MeOD) of **9**.

**Preparation of  $^{99\text{m}}\text{Tc}[\text{Tc}(\text{CO})_3(\text{OH}_2)_3]^+$ .** A sealed 0.5-2 mL microwave vial containing  $\text{K}_2[\text{BH}_3\text{CO}_2]$  (10.0 mg, 73.5  $\mu\text{mol}$ ),  $\text{Na}_2\text{CO}_3$  (15.0 mg, 141  $\mu\text{mol}$ ),  $\text{Na}_2\text{B}_4\text{O}_7 \cdot 10\text{H}_2\text{O}$  (20.0 mg, 52.4  $\mu\text{mol}$ ), and Na/K-tartrate (25.0 mg, 88.6  $\mu\text{mol}$ ) was flushed with Argon gas for 15 minutes.  $^{99\text{m}}\text{TcO}_4^-$  (130 MBq) in 2 mL of saline was added by syringe, and the solution was placed in the microwave reactor for 3.5 minutes at 100 °C with 10 seconds of pre-stirring. Once complete, the solution was brought to a pH of 3.5-4 by the addition of 1M HCl.

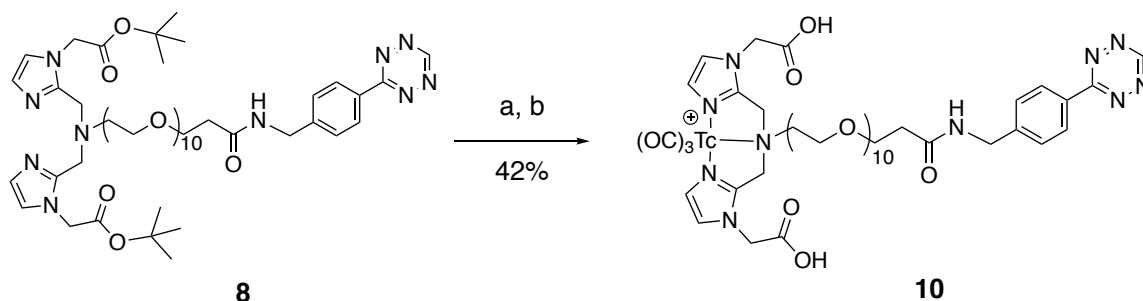


**Figure S2.26** Synthesis of **10** from **8**. a)  $^{99\text{m}}\text{Tc}[\text{Tc}(\text{CO})_3(\text{OH}_2)_3]^+$ , MeOH, Saline (0.9%), MW, 60 °C, 20 min. b) DCM, TFA, MW, 60 °C, 6 min.

**Preparation of compound 10 from 8.** To a solution of 250  $\mu\text{L}$  of  $^{99\text{m}}\text{Tc}[\text{Tc}(\text{CO})_3(\text{OH}_2)_3]^+$  in saline (111 MBq) was then added to **8** at  $10^3$  M in 250  $\mu\text{L}$  MeOH in a vial. The vial was sealed and heated in a microwave for 20 minutes at 60 °C. Upon cooling, the mixture was analyzed for purity by analytical HPLC (Method 1). After cooling and evaporation of solvent, the *tert*-butyl ester protecting groups were removed by treatment with 1 mL of 1:1 DCM:TFA, followed by a microwave reaction for 6 minutes at 60 °C. Upon completion of the deprotection, the reaction was dried and re-suspended in ACN/ $\text{H}_2\text{O}$  (1:1 v/v) and purified by HPLC resulting **10** with no impurities (Method 1). The radiochemical yield of compound **10** was 42% ( $n = 18$ ).

**Validation of 10 with Co-injection with 9.** To a solution of **10** (37 MBq) in PBS (1 mL), **9** (0.25 mg, 0.0002 mmol) in Methanol (50  $\mu$ L) was added. Confirmation of the compound was analyzed by analytical HPLC (Method 1).

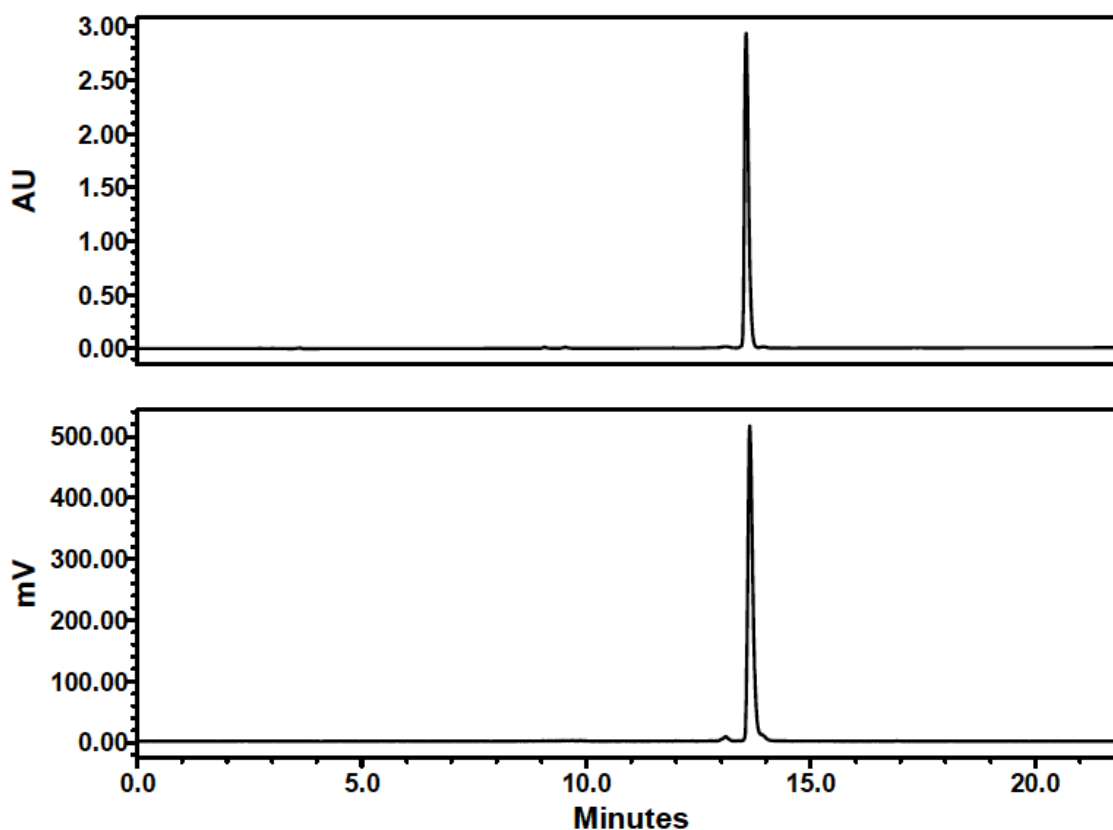


**Figure S2.27** Co-injection of **9** (UV) (top) with **10** (bottom) (gamma).

**Stability of 10 in PBS.** Compound **10** was dissolved in PBS (185 MBq/mL) and incubated at 37 °C for 6 hours. The reaction was monitored periodically by analytical HPLC (see Figure 10).

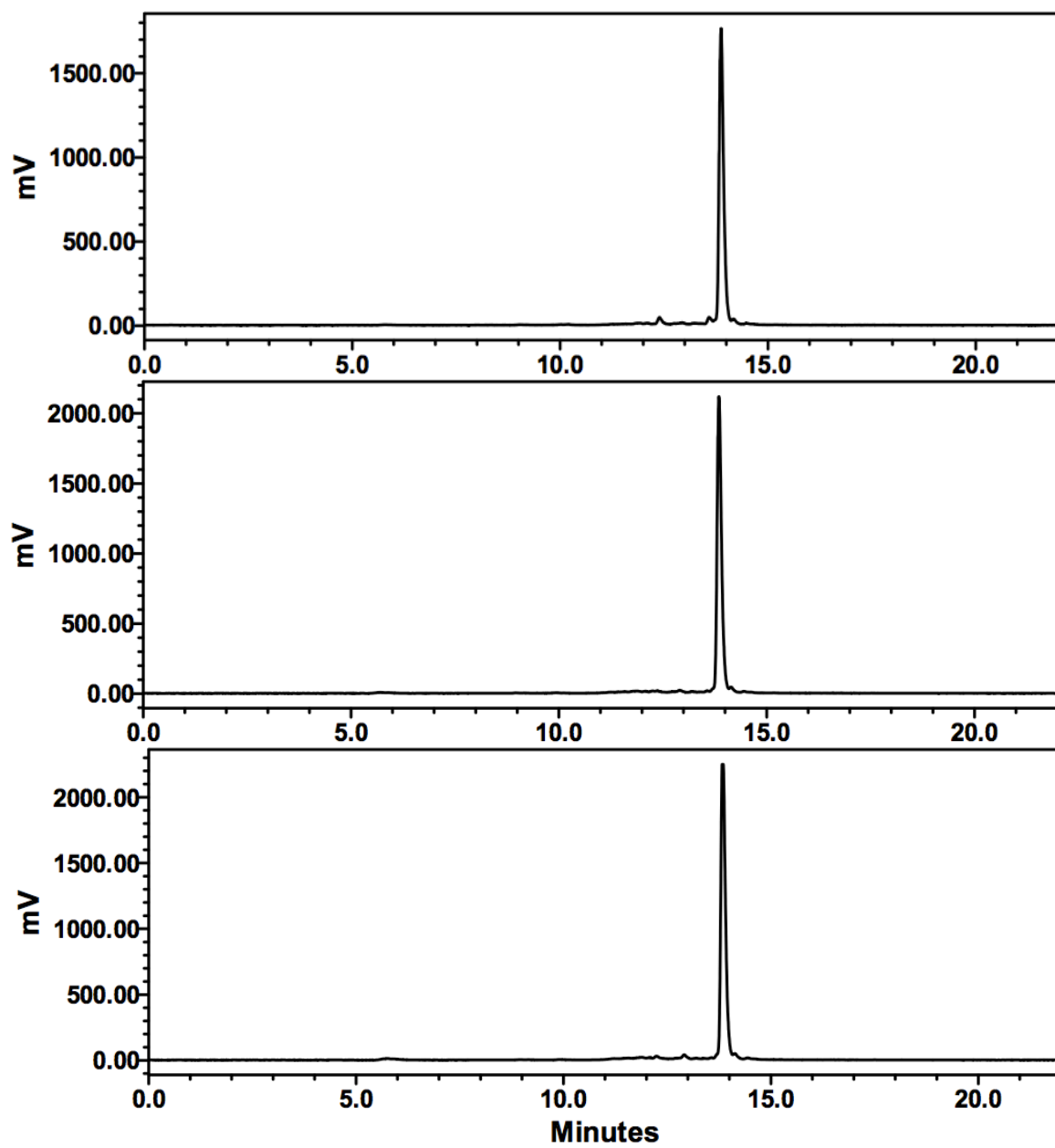


**Figure S2.28** Stability of **10** in PBS at 1 (top), 4 (middle) and 6 hours (bottom).

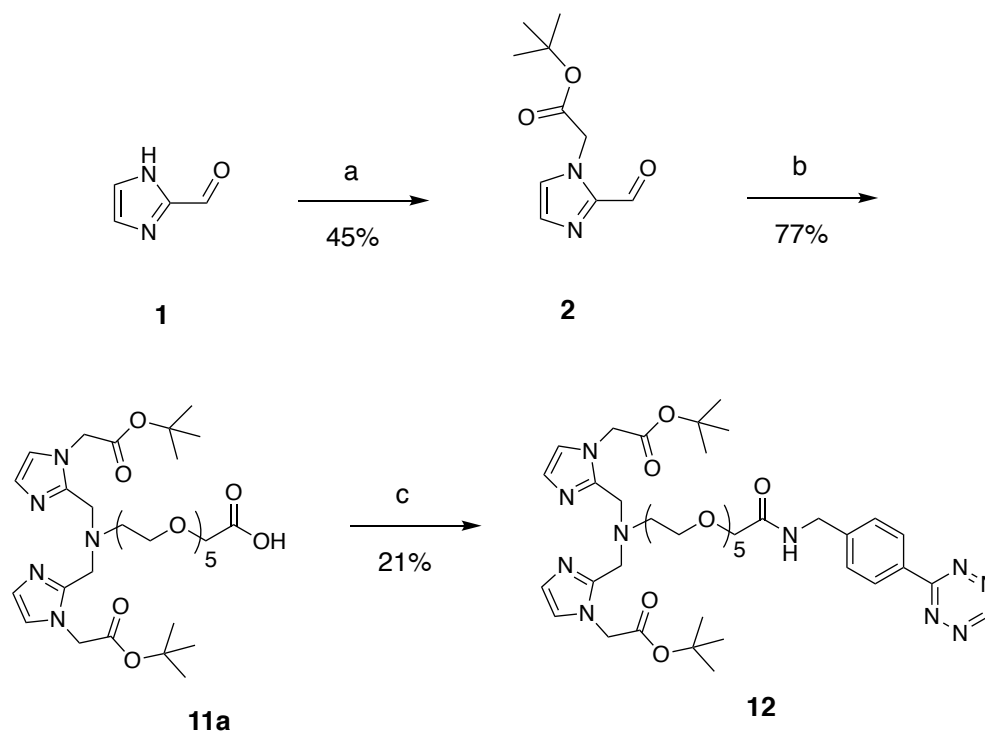


**Figure S2.29** Synthesis of **12** from **2**. a) DMF, DIPEA, t-butylbromoacetate, 80 °C, 4 h. b) DCE, NaBH(OAc)<sub>3</sub>, NH<sub>2</sub>-PEG<sub>5</sub>-CH<sub>2</sub>COOH, 50 °C, 12 h. c) PyBOP, DIPEA, DMF, ((4-tetrazine-3-yl)phenyl)methanamine hydrochloride, rt, 12 h.

***tert*-butoxycarbonylmethyl-1*H*-imidazol-2-yl[methyl}amino)ethoxy]ethoxy}ethoxy)ethoxy]ethoxy}acetic acid (**11a**)**. To a solution of compound **2** (313 mg, 1.49 mmol) in anhydrous DCE (4.00 mL), NH<sub>2</sub>PEG<sub>5</sub>COOH (217 mg, 0.734 mmol) was added. The reaction mixture was stirred for 1.5 h at room temperature under argon. Sodium triacetoxyborohydride (465 mg, 2.20 mmol) was then added and the mixture stirred for an additional 12 h. The solvent was evaporated under reduced pressure yielding a clear, pale yellow oil. The desired product was isolated semi-preparative HPLC (method 1, 4 mL/min), which, following

evaporation yielded a **11a** as a colourless oil (422 mg, 0.618 mmol, 84%). TLC  $R_f$  = 0.43 (10% MeOH/DCM);  $^1\text{H}$  NMR (600 MHz,  $\text{CDCl}_3$ ):  $\delta$  8.28 (s, 1H), 6.97 (d, 2H), 6.88 (d, 2H), 4.66 (s, 2H), 4.00 (s, 2H), 3.78 (s, 4H), 3.63 (m, 2H), 3.57 (m, 2H), 3.52 (m, 10H), 3.43 (m, 4H), 2.68 (t,  $J$  = 6 Hz, 2H), 1.34 (s, 18H).  $^{13}\text{C}$  NMR (150 MHz,  $\text{CDCl}_3$ ):  $\delta$  181.8, 173.7, 166.5, 165.1, 145.0, 131.2, 127.2, 124.9, 121.9, 116.5, 83.1, 70.4, 70.4, 70.3, 69.9, 69.2, 69.2, 53.2, 49.6, 48.0, 27.9, 1.8. HRMS ( $\text{ES}^+$ )  $m/z$  calculated for  $\text{C}_{32}\text{H}_{53}\text{N}_5\text{O}_{11}$   $[\text{M}+\text{H}^+]$  684.3823, found 684.3820.

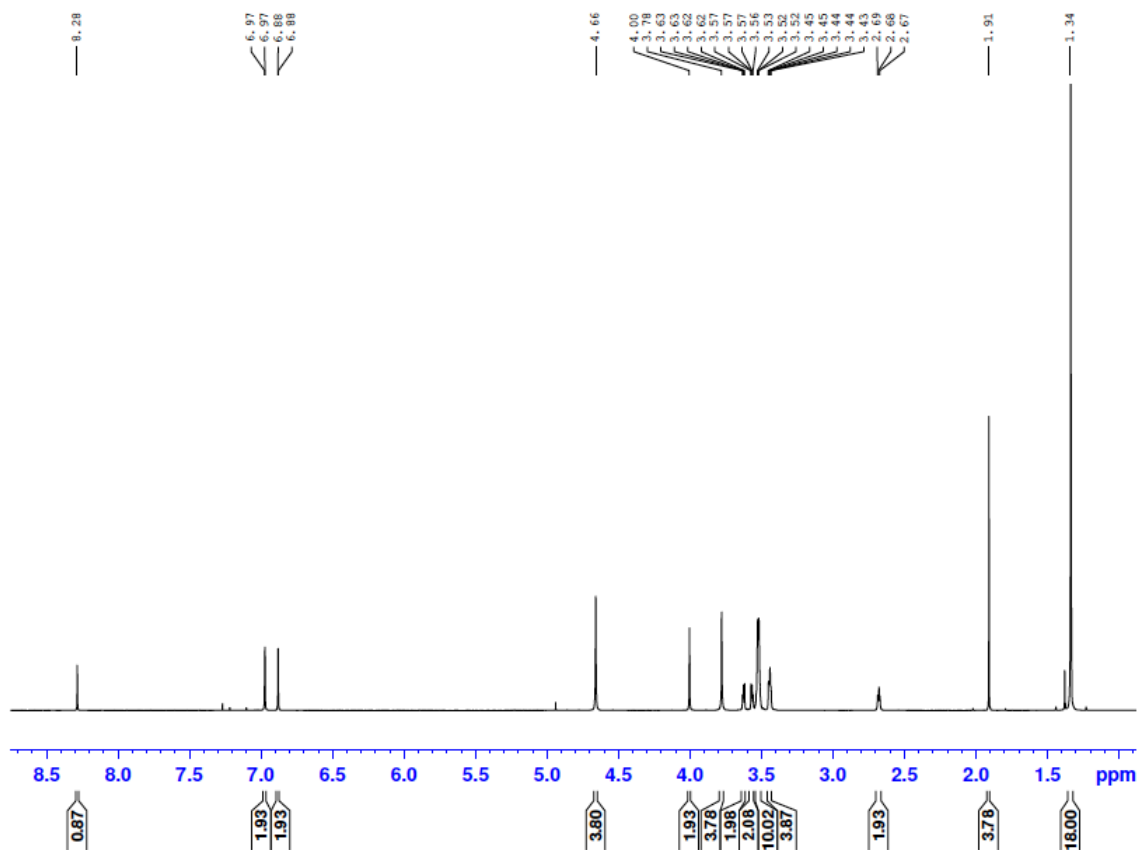


**Figure S2.30**  $^1\text{H}$  NMR (600 MHz,  $\text{CDCl}_3$ ) of **11a**.

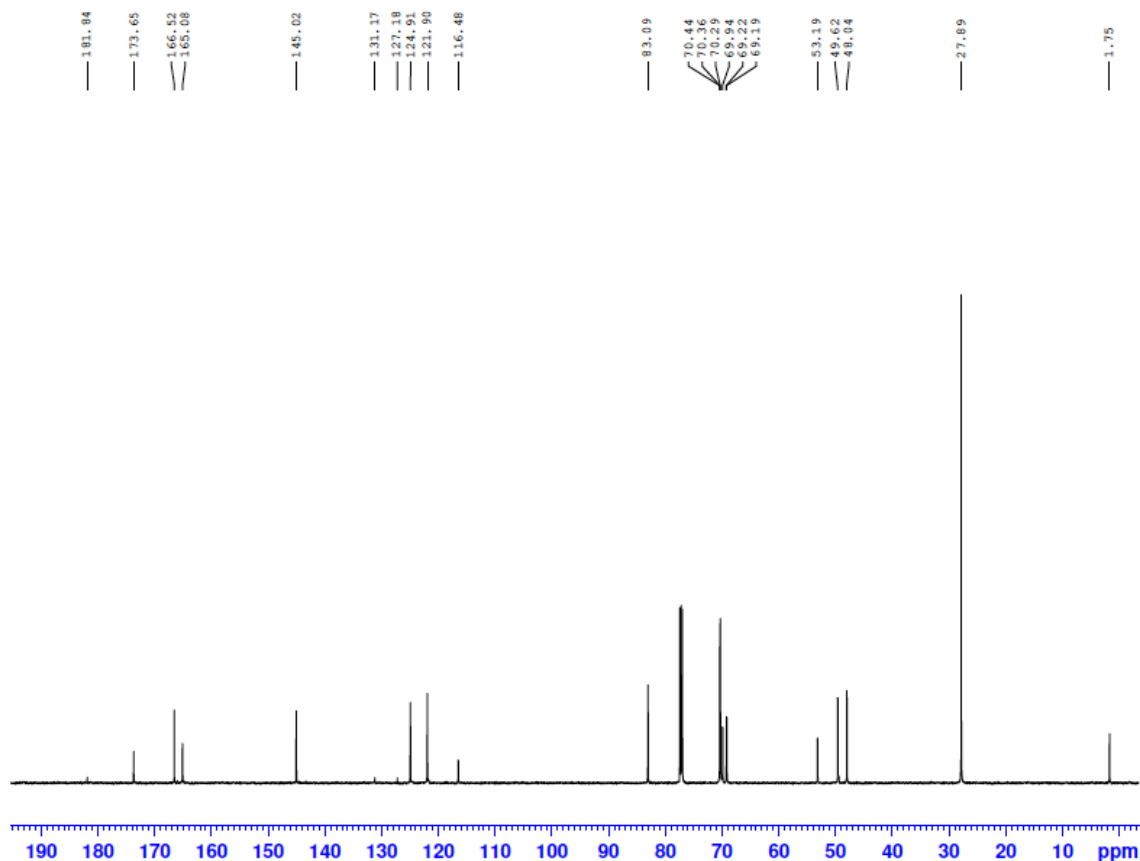


**Figure S2.31**  $^{13}\text{C}$  NMR (150 MHz,  $\text{CDCl}_3$ ) of **11a**.

***tert*-Butyl {2-[[[1-(*tert*-butoxycarbonylmethyl)-1H-imidazol-2-yl]methyl](2-{2-[2-(2-{2-[2-oxo-2-([p-(1,2,4,5-tetrazin-3-yl)phenyl]methyl)amino]ethoxy]ethoxy}ethoxy)ethoxy]ethyl)amino)methyl]-1H-imidazol-1-yl]acetate (**12**).** In one vial, compound **11a** (191 mg, 0.280 mmol), benzotriazol-1-yl-oxytripyrrolidinophosphonium hexafluorophosphate (PyBOP) (437 mg, 0.84 mmol) and N,N-dimethylformamide (DMF) (15 mL) were combined and stirred at room temperature under argon for 15 min. In a separate vial, ((4-tetrazine-3-yl)phenyl)methanamine hydrochloride (76.1 mg, 0.34 mmol), N,N-

diisopropylethylamine (DIPEA) (1.30 mL, 7.46 mmol) and DMF (15 mL) were combined and stirred at room temperature under argon for 15 min. The two vials were then combined, and allowed to stir at room temperature under argon gas for 12 h, where the solvent was then removed under reduced pressure. The desired product was isolated by semi-preparative HPLC (method 1, 4 mL/min), yielding **12** as a bright pink oil (50.1 mg, 21%). TLC  $R_f$  = 0.26 (10% MeOH/DCM);  $^1\text{H}$  NMR (600 MHz,  $\text{CDCl}_3$ ):  $\delta$  10.20 (s, 1H), 8.54 (d,  $J$  = 6 Hz, 2H), 7.77 (s, 1H), 7.51 (d,  $J$  = 12 Hz, 2H), 7.39 (s, 2H), 7.16 (s, 2H), 4.93 (s, 4H), 4.58 (d,  $J$  = 6 Hz, 2H), 4.23 (s, 4H), 4.15 (s, 2H), 3.69 (d,  $J$  = 6 Hz, 2H), 3.64 (d, 2H), 3.60 (d,  $J$  = 6 Hz, 2H), 3.54 (m, 6H), 3.52 (m, 4H), 3.45 (d,  $J$  = 6 Hz, 2H), 2.77 (t, 2H), 1.47 (s, 18H).  $^{13}\text{C}$  NMR (150 MHz,  $\text{CDCl}_3$ ):  $\delta$  171.9, 166.4, 165.1, 158.0, 146.4, 143.4, 131.0, 128.8, 128.7, 123.4, 119.5, 116.8, 114.9, 85.4, 70.8, 70.3, 70.2, 70.0, 69.8, 68.9, 54.0, 49.5, 46.6, 43.0, 28.0, 26.6, 26.5. HRMS ( $\text{ES}^+$ )  $m/z$  calculated for  $\text{C}_{41}\text{H}_{60}\text{N}_{10}\text{O}_{10}$  [ $\text{M}+\text{H}^+$ ] 853.4581, found 853.4572.



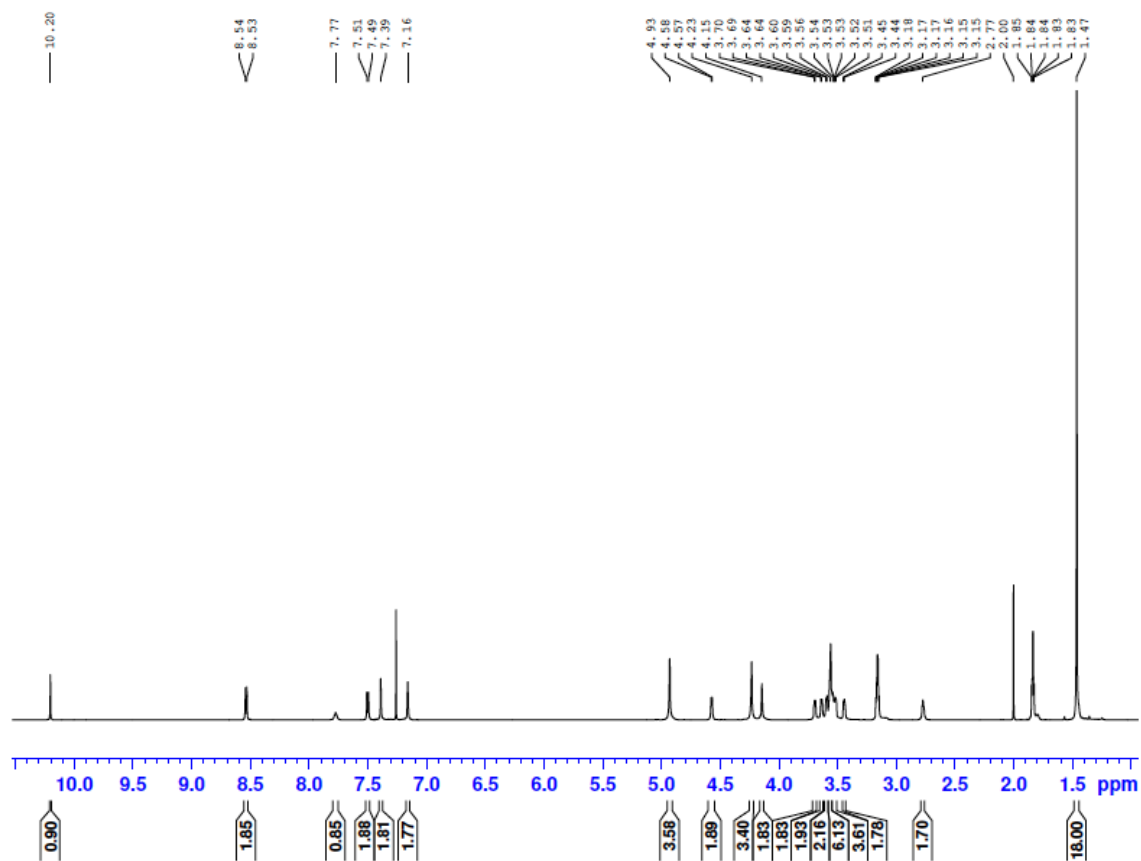


**Figure S2.32** <sup>1</sup>H NMR (600 MHz, CDCl<sub>3</sub>) of **12**.

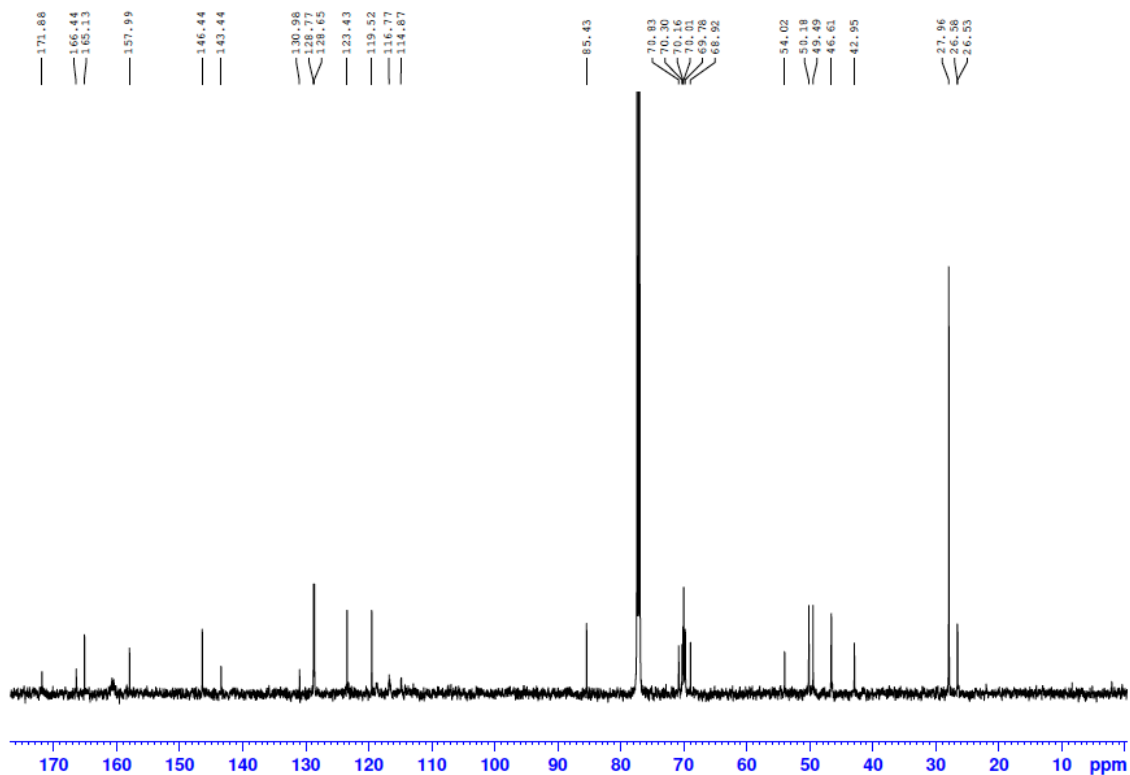


**Figure S2.33**  $^{13}\text{C}$  NMR (150 MHz,  $\text{CDCl}_3$ ) of **12**.

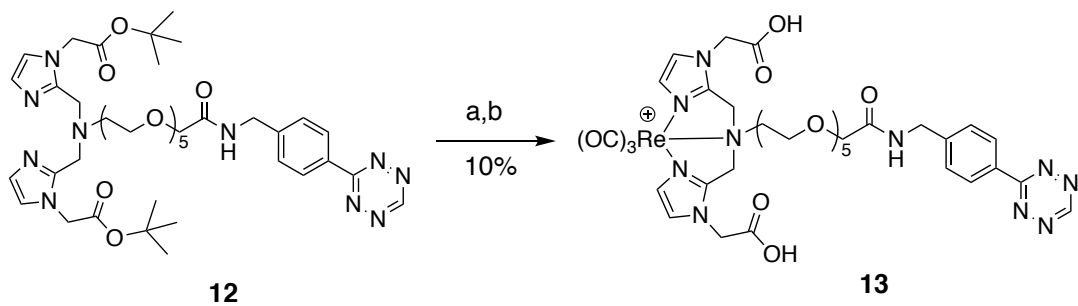


**Figure S2.34** Synthesis of **13** from **12**. a)  $\text{Re}(\text{CO})_3(\text{OH}_2)_3\text{Br}$ , ACN, 60 °C, 20 min.

b) DCM, TFA, 60 °C, 6 min.

***tert*-Butyl {2-[[[1-(*tert*-butoxycarbonylmethyl)-1H-imidazol-2-yl]methyl](2-{2-[2-(2-{2-[2-oxo-2-([p-(1,2,4,5-tetrazin-3-yl)phenyl]methyl)amino)ethoxy]ethoxy}ethoxy)ethoxy]ethyl)amino) methyl]-1H-imidazol-1-yl} acetate rhenium tricarbonyl complex (**13**).** To a microwave vial, compound **12** (30.5 mg, 0.04 mmol),  $\text{Re}(\text{CO})_3(\text{H}_2\text{O})_3\text{Br}$  (20.2 mg, 0.05 mmol) and acetonitrile (ACN) (3 mL) were combined. The vial was sealed and heated in a microwave for 20 min at 60 °C. Solvent was removed under reduced pressure. Next, the crude product was dissolved in a 1:1 solution of DCM:TFA (1 mL) and added to a microwave vial. The vial was sealed and heated in a microwave for 6 min at 60 °C. Solvent was removed under reduced pressure. The desired product was isolated by semi-preparative HPLC (method 1, 4 mL/min), yielding **13** as a bright pink oil (4.1 mg, 10%). TLC  $R_f = 0.18$  (10% MeOH/DCM); HRMS ( $\text{ES}^+$ )  $m/z$  calculated for  $\text{C}_{36}\text{H}_{44}\text{N}_{10}\text{O}_{13}\text{Re}^+ [\text{M}+\text{H}^+]$  1011.2629, found 1011.2660.

**Preparation of  $^{99\text{m}}\text{Tc}[\text{Tc}(\text{CO})_3(\text{H}_2\text{O})_3]^+$ .** A sealed 0.5-2 mL microwave vial containing  $\text{K}_2[\text{BH}_3\text{CO}_2]$  (10.0 mg, 73.5  $\mu\text{mol}$ ),  $\text{Na}_2\text{CO}_3$  (15.0 mg, 141  $\mu\text{mol}$ ),  $\text{Na}_2\text{B}_4\text{O}_7 \cdot 10\text{H}_2\text{O}$  (20.0 mg, 52.4  $\mu\text{mol}$ ), and Na/K-tartrate (25.0 mg, 88.6  $\mu\text{mol}$ ) was flushed with argon gas for 10 min.  $^{99\text{m}}\text{TcO}_4^-$  (130 MBq) in 2 mL of saline was added by syringe, and the solution was placed in the microwave reactor for 3.5 min at 110 °C with 10 s of pre-stirring. Once complete, the solution was brought to a pH of 3.5-4 by the addition of 1 M HCl.

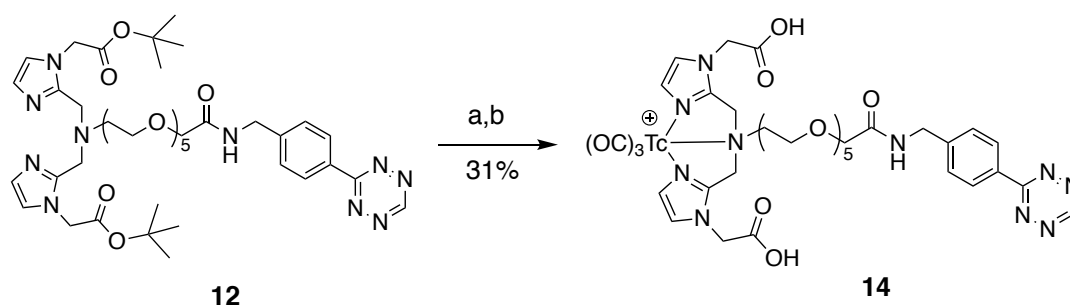


**Figure S2.35** Synthesis of **14** from **12**. a)  $^{99m}\text{Tc}[\text{Tc}(\text{CO})_3(\text{OH}_2)_3]^+$ , MeOH, Saline (0.9%), MW, 60 °C, 20 min. b) DCM, TFA, 60 °C, 6 min.

***tert*-Butyl {2-[[[1-(*tert*-butoxycarbonylmethyl)-1H-imidazol-2-yl]methyl](2-{2-[2-(2-{2-[2-oxo-2-([p-(1,2,4,5-tetrazin-3-yl)phenyl]methyl)amino]ethoxy]ethoxy}ethoxy)ethyl)amino)methyl]-1H-imidazol-1-yl]acetate technetium-99m tricarbonyl complex (**14**).** To a solution of  $^{99m}\text{Tc}[\text{Tc}(\text{CO})_3(\text{OH}_2)_3]^+$  in saline (259  $\mu\text{L}$ , 111 MBq), **12** dissolved in methanol was added ( $10^{-3}$  M in 241  $\mu\text{L}$ ). The vial was sealed and heated in a microwave for 20 min at 60°C. Upon cooling, the mixture was analyzed for purity by analytical HPLC (method 1, 1 mL/min). After cooling and evaporation of solvent, the *tert*-butyl ester protecting groups were removed by treatment with 1:1 TFA in DCM for 2.5 h at room temperature. Upon completion of the deprotection, the reaction was dried and re-suspended in ACN/H<sub>2</sub>O (1:1 v/v) and purified by HPLC resulting **14** with no impurities. The radiochemical yield of compound **14** was 31% (n = 10).

**Validation of 14 with co-injection with 13.** To a solution of **14** (9.25 MBq) in PBS (500 mL), **13** (0.25 mg, 0.25  $\mu$ mol) in methanol (50  $\mu$ L) was added. Confirmation of the compound was analyzed by analytical HPLC (Method 1).

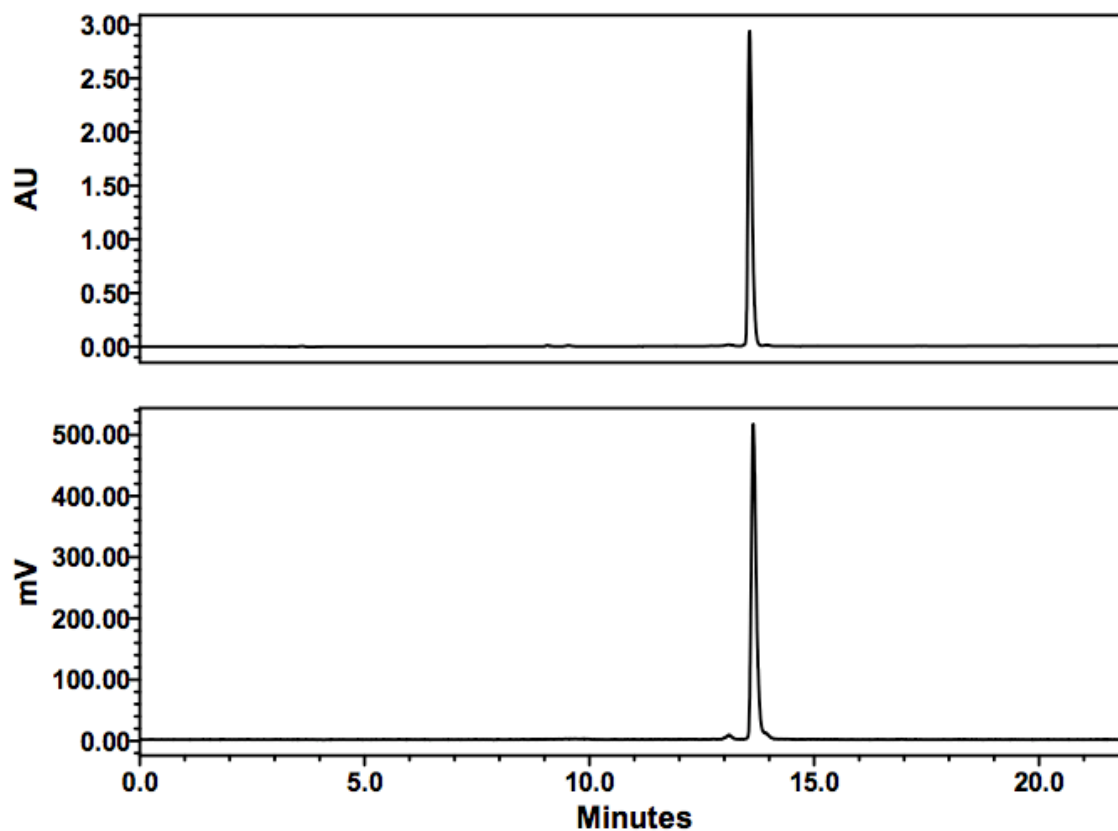


**Figure S2.36** HPLC chromatograms (UV and gamma) of compound **13** (UV - top) co-injected with compound **14** (gamma - bottom).

## APPENDIX II

### Supplemental Information for Chapter 5

Synthesis of *tert*-butoxycarbonylmethyl)-1*H*-imidazol-2-yl)methyl}amino)ethoxy}ethoxy}ethoxy}ethoxy}ethoxy}acetic acid *technetium-99m tricarboxyl complex (11b)*. To a solution of 259  $\mu\text{L}$  of  $^{99\text{m}}\text{Tc}[\text{Tc}(\text{CO})_3(\text{OH}_2)_3]^+$  in saline (111 MBq), **11a** was added at a concentration of  $10^3$  M (Scheme 6) in 241  $\mu\text{L}$  MeOH in a vial. The vial was sealed and heated in a microwave for 20 minutes at 60°C. Upon cooling, the mixture was analyzed for purity by analytical HPLC (Method 2). After cooling and evaporation of solvent, the *tert*-butyl ester protecting groups were removed by treatment with 1:1 TFA and DCM and heated in a microwave for 6 minutes at 60°C. Upon completion of the deprotection, the reaction was dried and re-suspended in ACN/H<sub>2</sub>O (1:1 v/v) and purified by HPLC resulting **11b** with no impurities. The radiochemical yield of compound **11b** was 35% (n = 3).

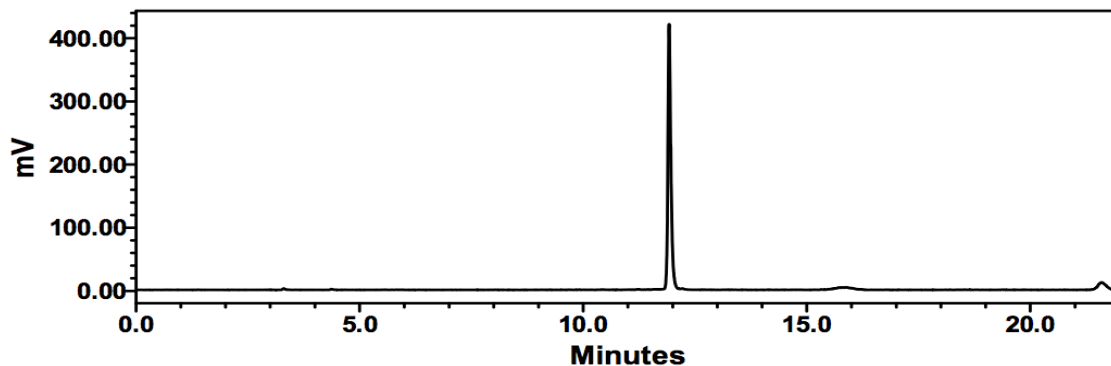


**Figure S5.1** Gamma HPLC trace of  $^{99m}\text{Tc}$  labeling of **11b**.

**Synthesis of 6-{4-[(2R)-2-Carboxy-2-(tert-butoxycarbonylamino)ethyl]-1H-1,2,3-triazol-1-yl}-2-[(9H-fluoren-9-yl)methoxycarbonylamino]hexanoic acid (21).** Compound **21** was prepared using a literature procedure.<sup>3</sup> To a solution of Fmoc-Lys(N<sub>3</sub>)-OH (50 mg,  $1.3 \times 10^{-1}$  mmol) in 3.0 mL of 2/1 t-BuOH/H<sub>2</sub>O), Boc-L-propargylglycine·DCHA was added (50 mg, 0.13 mmol). Sodium ascorbate was then added (1.0 mg,  $5.0 \times 10^{-3}$  mmol in 0.50 mL water), followed by Cu(OAc)<sub>2</sub>·H<sub>2</sub>O (0.6 mg,  $2.6 \times 10^{-3}$  mmol in 0.50 mL water). The mixture was stirred at 30 °C for 12 hours under argon. Quadrapure-IDA resin (10 mg) was added to the solution and gently shaken at room temperature for 2 hours to remove Cu(II). The solution was filtered through a Celite bed and evaporated to dryness. The light yellow solid obtained was then extracted between EtOAc and water (3 × 20 mL). All organic phases were combined and dried over a bed of Na<sub>2</sub>SO<sub>4</sub>. The crude product was then purified by HPLC (Method 2, 4 mL/min), resulting in a clear, colourless oil (35 mg,  $5.7 \times 10^{-2}$  mmol, 45%). <sup>1</sup>H NMR (600 MHz, Acetone-d<sub>6</sub>): δ 7.85 (d, 2H),

7.80 (s, 1H), 7.71 (t, 2H), 7.41 (t, 2H), 7.33 (t, 2H), 4.50 (t, 1H), 4.41 (t, 2H), 4.34 (d, 2H), 4.23 (m, 2H), 3.18 (m, 2H), 2.64 (s, 1H), 2.07 (m, 1H), 2.07 (s, 2H), 1.95 (m, 2H), 1.80 (m, 1H), 1.48, d, 2H), 1.38 (s, 9H).  $^{13}\text{C}$  NMR (150 MHz, Acetone- $\text{d}_6$ ):  $\delta$ 174.6, 173.8, 157.7, 156.9, 145.7, 145.6, 144.5, 142.7, 129.2, 128.6, 126.8, 124.1, 121.4, 80.1, 67.8, 55.1, 54.6, 51.0, 48.6, 41.1, 32.4, 31.2, 31.1, 31.0, 29.2, 24.1. HRMS ( $\text{ES}^+$ )  $m/z$  calculated for  $\text{C}_{31}\text{H}_{38}\text{N}_5\text{O}_8$   $[\text{M}+\text{H}^+]$  608.272, found 608.2708.

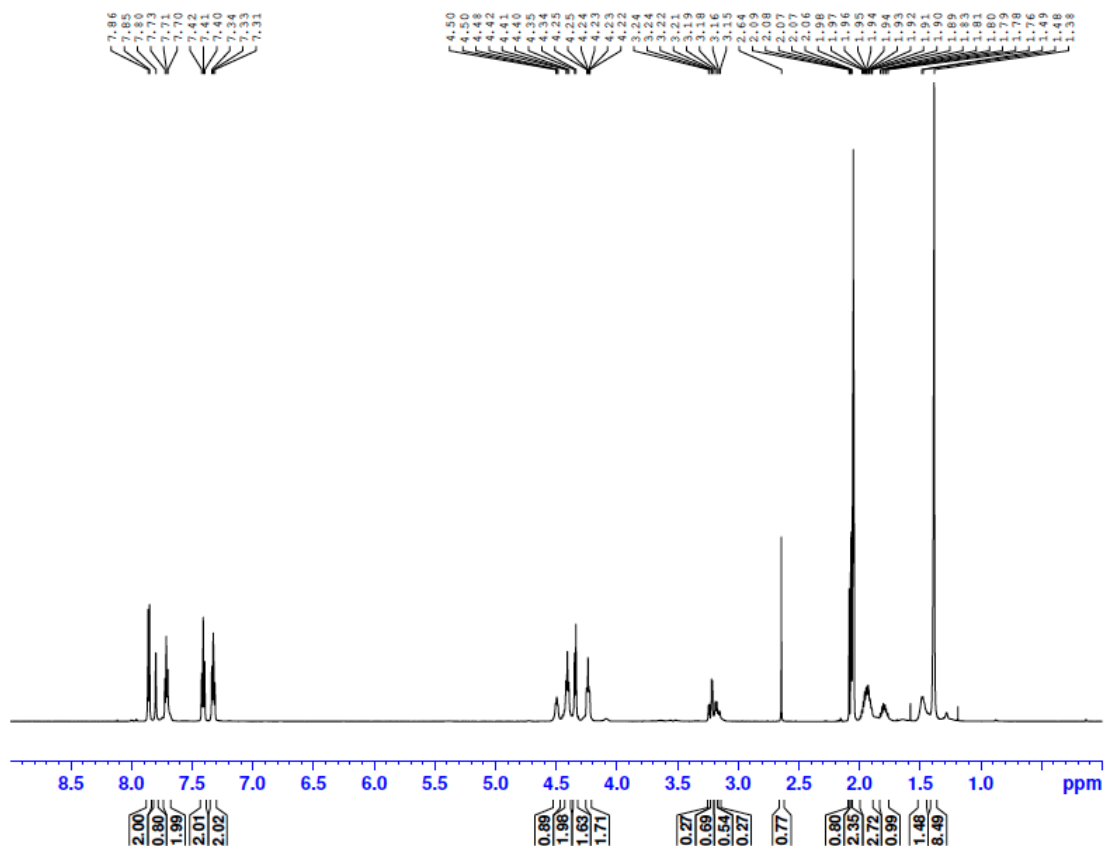


**Figure S5.2**  $^1\text{H}$  NMR (600 MHz, Acetone- $\text{d}_6$ ) of **21**.



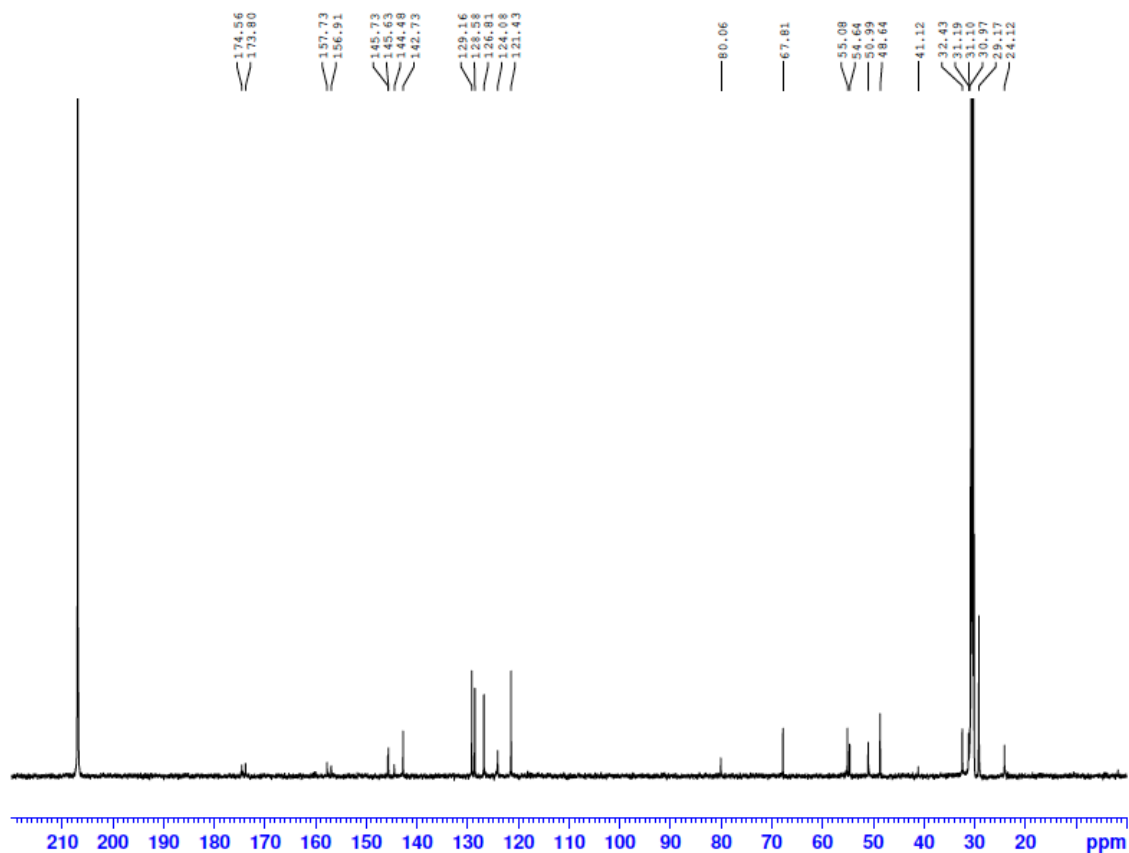


**Figure S5.3**  $^{13}\text{C}$  NMR (150 MHz, Acetone- $\text{d}_6$ ) of **21**.

**6-{4-[(2R)-2-Carboxy-2-(tert-butoxycarbonylamino)ethyl]-1H-1,2,3-triazol-1-yl}-2-aminohexanoic acid (**22**)**. To a solution of **21** (30 mg, 0.05 mmol) in DMF (0.8 mL), piperazine was added (0.2 mL). The reaction was allowed to stir for 2 hours at room temperature, before being evaporated to dryness. The reaction mixture was then dissolved in a 1:1 solution of DCM/TFA (1 mL) and heated in the microwave for 10 minutes at 60 °C. The deprotected product was used for labeling without further purification.

**Preparation of  $^{99m}\text{Tc}[\text{Tc}(\text{CO})_3(\text{OH}_2)_3]^+$ .** A sealed 0.5-2 mL microwave vial containing  $\text{K}_2[\text{BH}_3\text{CO}_2]$  (10 mg, 74  $\mu\text{mol}$ ),  $\text{Na}_2\text{CO}_3$  (15 mg, 140  $\mu\text{mol}$ ),  $\text{Na}_2\text{B}_4\text{O}_7 \cdot 10\text{H}_2\text{O}$  (20 mg, 52  $\mu\text{mol}$ ), and Na/K-tartrate (25 mg, 89  $\mu\text{mol}$ ) was flushed with Argon gas for 10 minutes.  $^{99m}\text{TcO}_4^-$  (130 MBq) in 2 mL of saline was added by syringe, and the solution was placed in the microwave reactor for 3.5 minutes at 110°C with 10 seconds of pre-stirring. Once complete, the solution was brought to a pH of 7 by the addition of 1M HCl.

**Synthesis of 6-{4-[(2R)-2-Amino-2-carboxyethyl]-1H-1,2,3-triazol-1-yl}-2-aminohexanoic acid technetium-99m tricarbonyl complex (23a).** To a solution of 1/1 DCM/TFA (1 mL), **21** was added (1 mg,  $3 \times 10^{-3}$  mmol). The reaction was heated to 60 °C in the microwave for 10 minutes, before being evaporated to dryness. The deprotected product was confirmed by analytical HPLC (Method 2, 1 mL/min). To a solution of 500  $\mu\text{L}$  of  $^{99m}\text{Tc}[\text{Tc}(\text{CO})_3(\text{OH}_2)_3]^+$  in saline (930 MBq), 200  $\mu\text{g}$  of deprotected **22** was added in 100  $\mu\text{L}$  MeOH in a vial, followed by 100  $\mu\text{L}$  of PBS. The vial was sealed and heated in a microwave for 15 minutes at 60 °C. Upon cooling, the mixture was analyzed for purity by analytical HPLC (Method 2) resulting **23a** with no gamma impurities. The reaction mixture was dried and dissolved in PBS at a concentration of 0.74 MBq/ $\mu\text{L}$ .

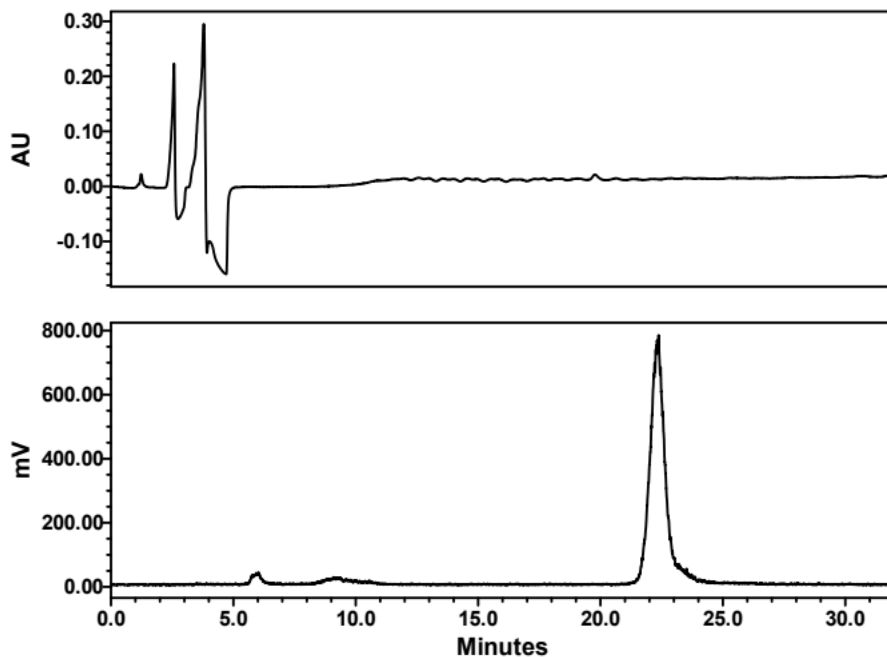


**Figure S5.4** HPLC trace of  $^{99\text{m}}\text{Tc}$  labeling of **23a** (UV – top, Gamma – bottom).

**Stability testing of 23a in PBS.** Compound **23a** was dissolved in PBS (7.4 MBq/mL) and incubated at 37 °C for 6 hours. At 1 and 6 hours a sample, 200  $\mu\text{L}$  was taken from the mixture and diluted to 500  $\mu\text{L}$  with  $\text{H}_2\text{O}$  and analyzed by analytical HPLC (Method 1, 1 mL/min) to assess stability.

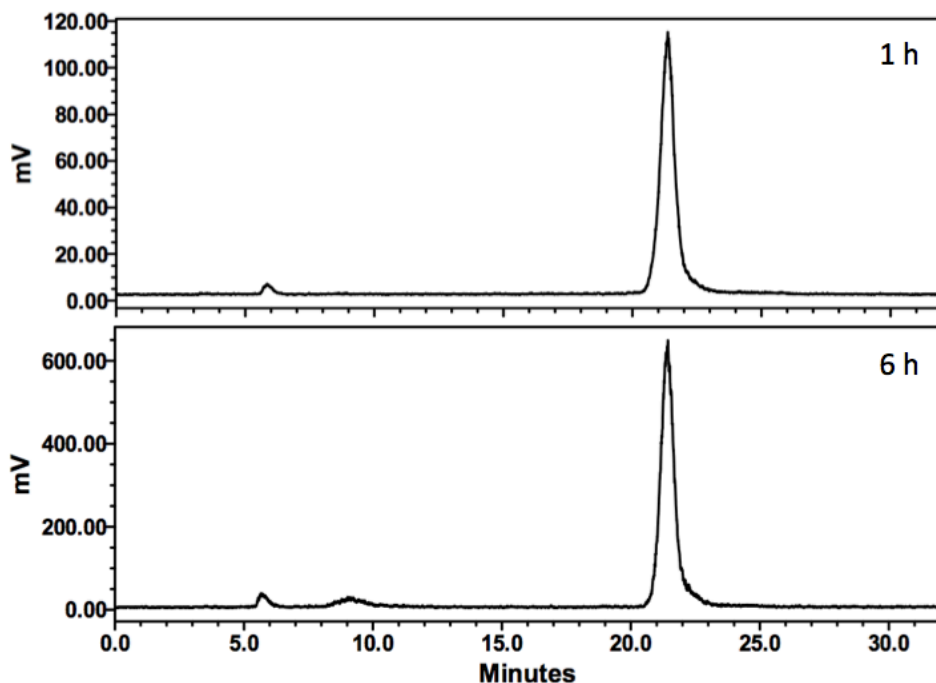


**Figure S5.5** Gamma HPLC traces of **23a** upon incubation at 37 °C in PBS for 1 and 6 hours.

**Synthesis of 5-Oxo-5-([p-(1,2,4,5-tetrazin-3-yl)phenyl]methyl)amino)valeric acid (**26**).** To a stirring solution of tetrazine (52 mg, 0.23 mmol) in 6.0 mL DCM, triethylamine was added (162  $\mu$ L, 1.16 mmol), followed by glutaric anhydride (132.4 mg, 1.16 mmol). The mixture was stirred at room temperature under argon for 18 hours. The crude product was purified by HPLC (Method 1, 4 mL/min), resulting in a pink oil (61 mg, 0.20 mmol, 89%). TLC  $R_f$  (DCM + 10% MeOH)= 0.49.  $^1\text{H}$  NMR (600 MHz,  $\text{CD}_3\text{OD}$ ):  $\delta$ 10.32 (s, 1H), 8.56 (d, 2H), 7.56 (d, 2H), 4.50 (s, 2H), 2.35 (t, 4H), 1.95 (m, 2H).  $^{13}\text{C}$  NMR (150 MHz,  $\text{CD}_3\text{OD}$ ):  $\delta$ 177.1, 175.6,

167.7, 159.4, 145.7, 132.4, 129.5, 129.4, 43.9, 36.2, 34.4, 34.2, 22.5, 21.6.

HRMS (ES<sup>-</sup>) m/z calculated for C<sub>14</sub>H<sub>15</sub>N<sub>5</sub>O<sub>3</sub> [M-H<sup>+</sup>] 300.1102, found 300.1098.

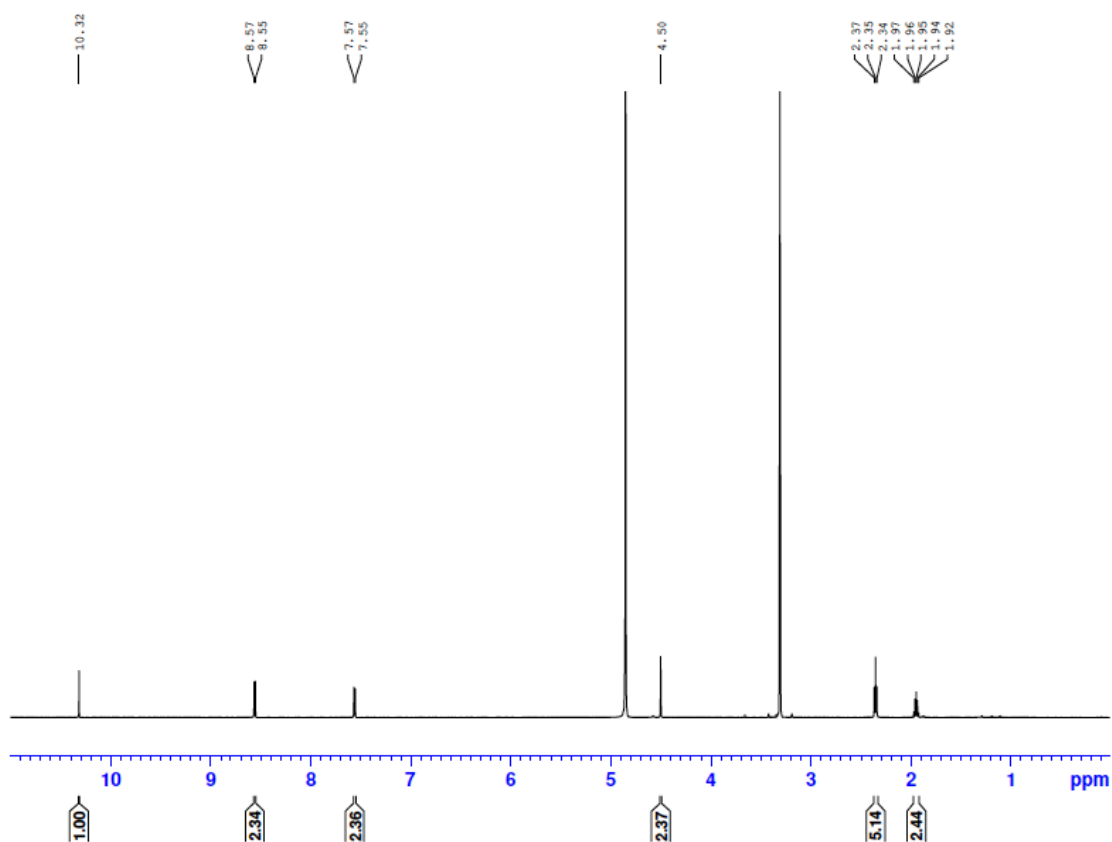


**Figure S5.6** <sup>1</sup>H NMR (600 MHz, CD<sub>3</sub>OD) of **26**.

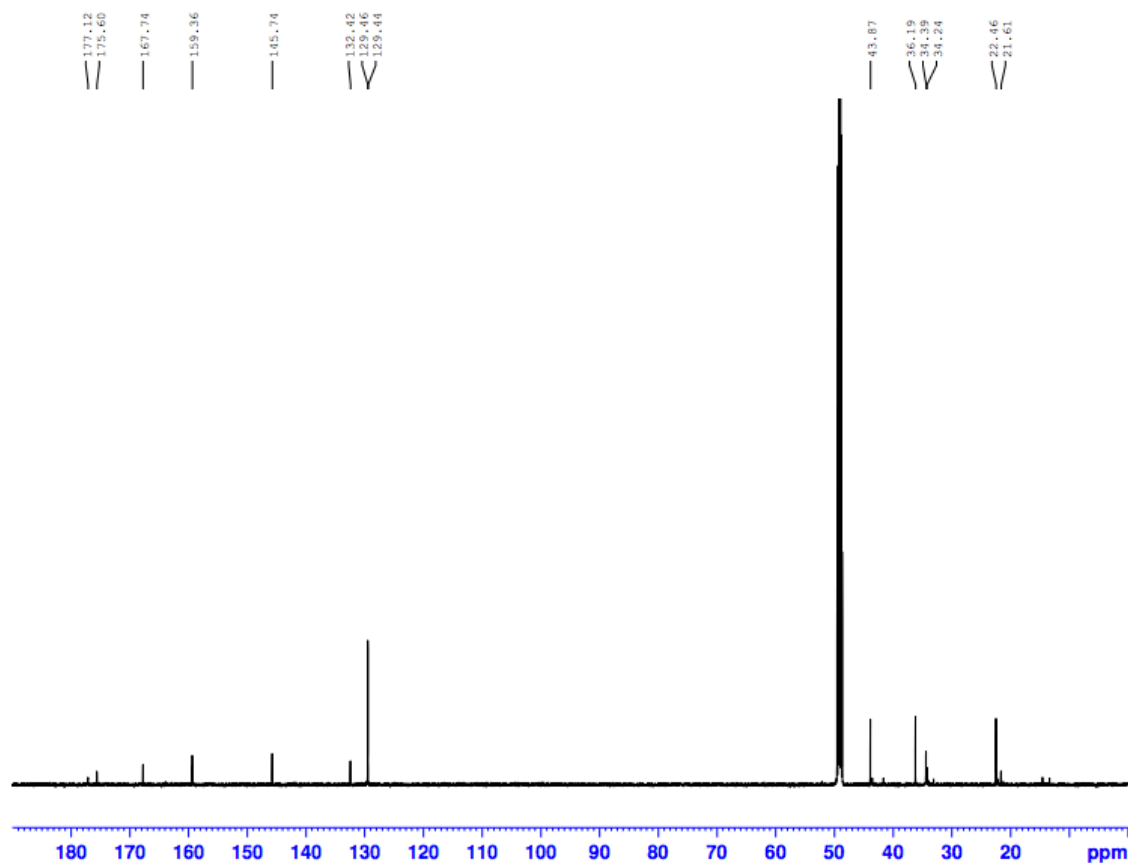


**Figure S5.7**  $^{13}\text{C}$  NMR (150 MHz,  $\text{CD}_3\text{OD}$ ) of **26**.

**Synthesis of *p*-(1,2,4,5-tetrazin-3-yl)phenyl[methyl]amino)valerate (**27**).** To a solution of **26** (20 mg, 0.066 mmol) in 1.3 mL DMF, N-hydroxysuccinimide (38.2 mg, 0.33 mmol) and 1-Ethyl-3-(3-dimethylaminopropyl)carbodiimide (63.4 mg, 0.33 mmol) was added. The mixture was stirred at room temperature under argon for 18 hours. The crude reaction was purified by Biotage flash chromatography (DCM with 1-5% MeOH over 15 CV), yielding a pink solid (22 mg, 0.055 mmol, 85%). TLC  $R_f$  (DCM + 5% MeOH) = 0.57.  $^1\text{H}$  NMR (600 MHz,  $\text{CDCl}_3$ ):  $\delta$  10.21 (s, 1H), 8.59 (d, 2H), 7.53 (d, 2H), 4.57 (d, 2H), 3.01 (s, 3H), 2.94 (s, 3H), 2.69 (s,

1H), 2.43 (t, 2H), 2.39 (t, 2H), 2.01 (m, 2H). <sup>13</sup>C NMR (150 MHz, CDCl<sub>3</sub>): δ171.9, 169.5, 169.1, 168.5, 167.9, 166.4, 158.0, 144.1, 130.8, 128.8, 128.7, 43.4, 34.5, 30.1, 29.8, 25.8, 21.1, 19.8. HRMS (ES<sup>+</sup>) m/z calculated for C<sub>14</sub>H<sub>15</sub>N<sub>5</sub>O<sub>3</sub> [M-H<sup>+</sup>] 399.1400, found 399.1000.

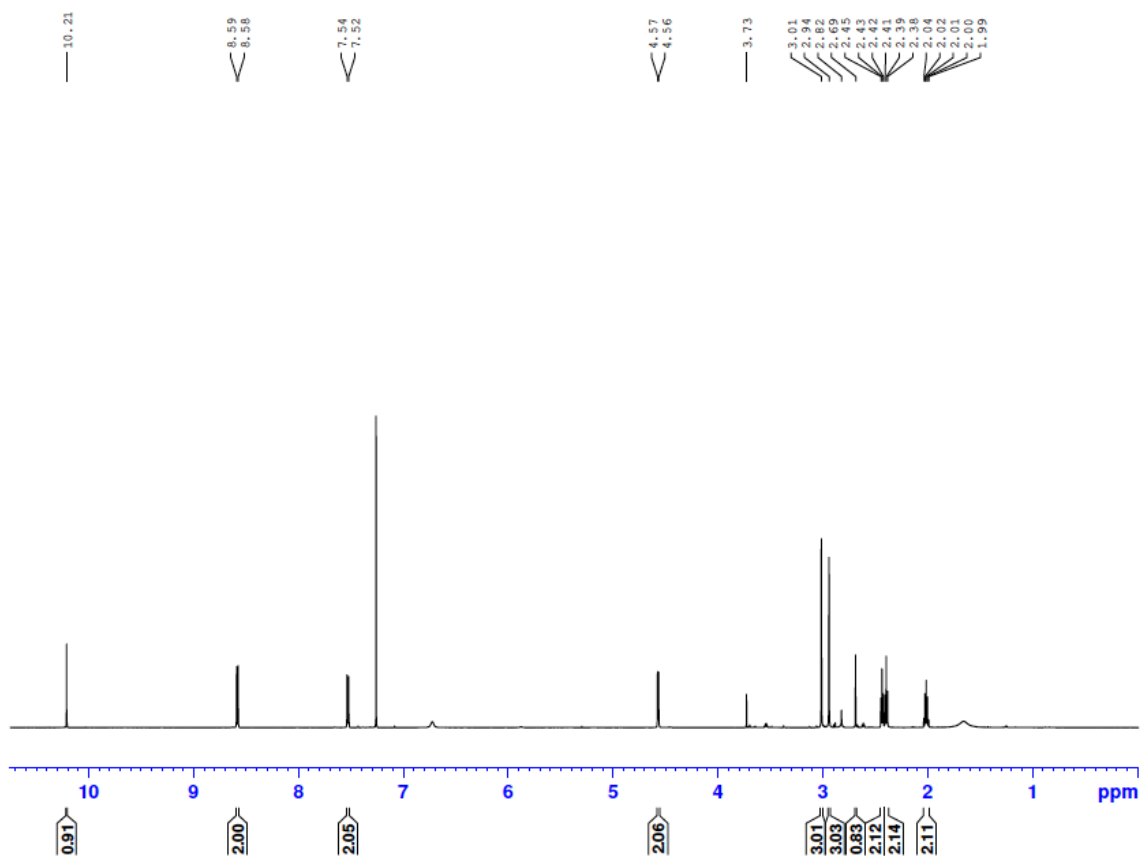


**Figure S5.8** <sup>1</sup>H NMR (600 MHz, CDCl<sub>3</sub>) of 27.

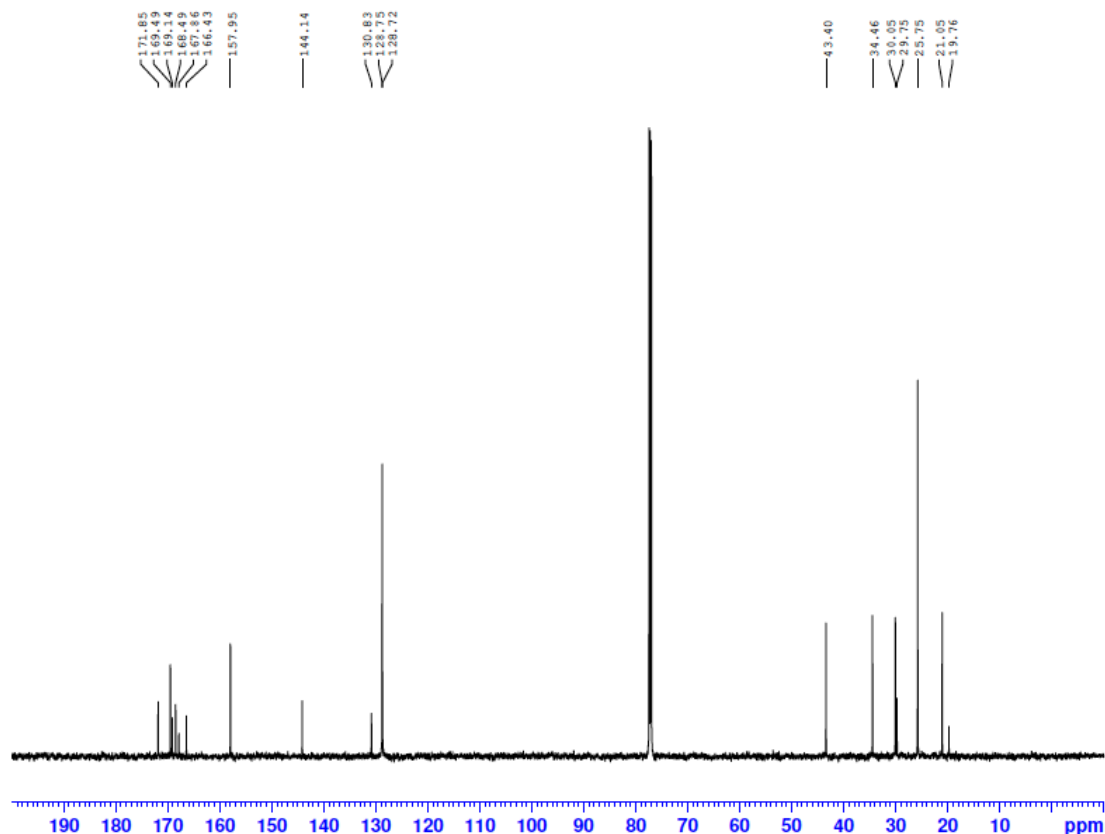


**Figure S5.9**  $^{13}\text{C}$  NMR (150 MHz,  $\text{CDCl}_3$ ) of **27**.

**Synthesis of H-1,2,3-triazol-4-yl]-2-(tert-butoxycarbonylamino)propionic acid (30).** Compound **30** was prepared using a literature procedure.<sup>3</sup> To a solution of 3-azido-1-propanamine (10.4 mg, 0.10 mmol) in 1.0 mL of 2/1 t-BuOH/ $\text{H}_2\text{O}$ ), Boc-L-propargylglycine-DCHA was added (43.2 mg, 0.11 mmol). Sodium ascorbate was then added (0.83 mg,  $4.2 \times 10^{-3}$  mmol in 0.2 mL water), followed by  $\text{Cu}(\text{OAc})_2 \cdot \text{H}_2\text{O}$  (0.42 mg,  $2.1 \times 10^{-3}$  mmol in 0.20 mL water). The mixture was stirred at 30 °C for 12 hours under argon. Quadrapure-IDA resin (~10 mg) was added to the solution and gently shaken at room temperature for 2 hours



to remove Cu(II). The solution was filtered through a Celite bed and evaporated to dryness. The crude product was purified by HPLC (Method 1, 4 mL/min), resulting in a clear, colourless oil (23 mg,  $7.3 \times 10^{-2}$  mmol, 71%).  $^1\text{H}$  NMR (600 MHz,  $\text{CDCl}_3$ ):  $\delta$ 7.48 (s, 1H), 4.15 (t, 2H), 4.04 (m, 1H), 2.89 (dd, 1H), 2.72 (dd, 2H), 1.90 (m, 2H), 1.03 (s, 9H).  $^{13}\text{C}$  NMR (150 MHz,  $\text{CDCl}_3$ ):  $\delta$ 175.5, 171.6, 162.6, 162.4, 162.1, 158.7, 145.9, 143.5, 126.1, 125.5, 81.6, 55.7, 54.5, 49.1, 49.0, 38.9, 30.0, 29.9, 29.5, 29.4, 28.0. HRMS ( $\text{ES}^+$ )  $m/z$  calculated for  $\text{C}_{13}\text{H}_{23}\text{N}_5\text{O}_4$   $[\text{M}+\text{H}^+]$  314.1823, found 314.1821.

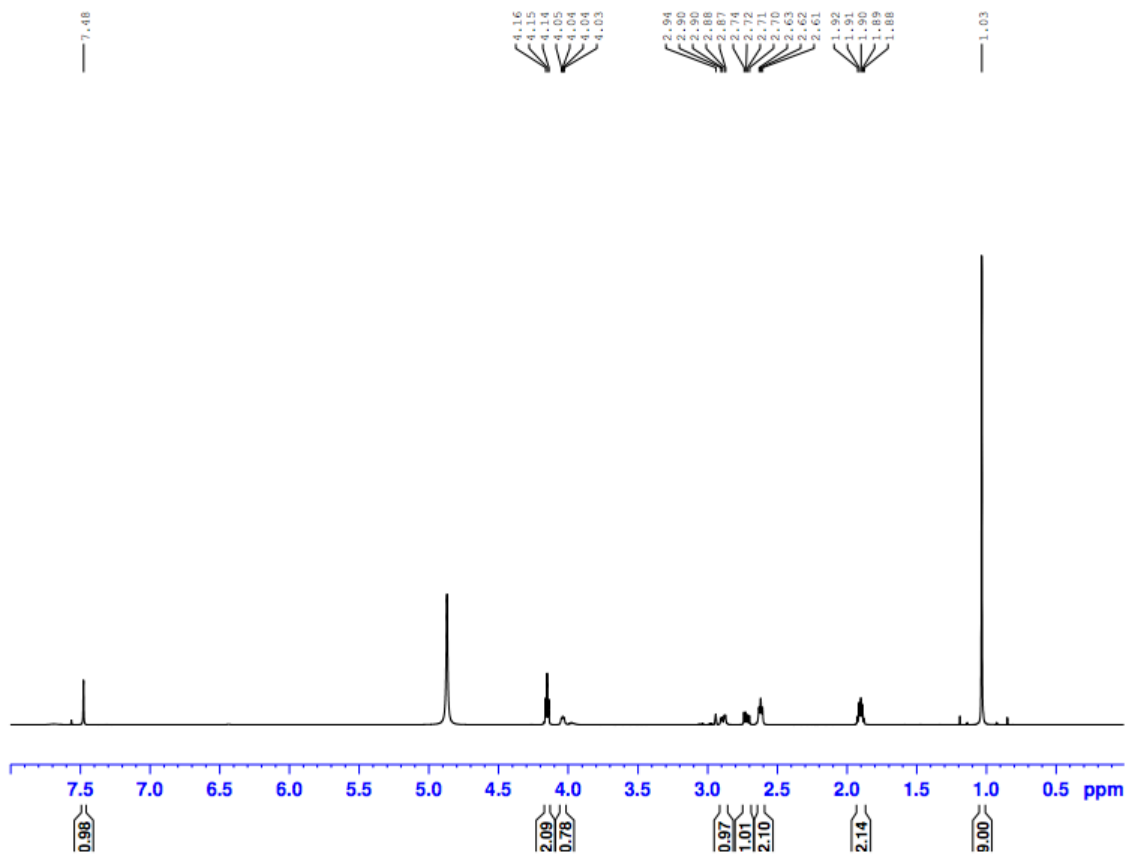


**Figure S5.10**  $^1\text{H}$  NMR (600 MHz,  $\text{CD}_3\text{OD}$ ) of **30**.

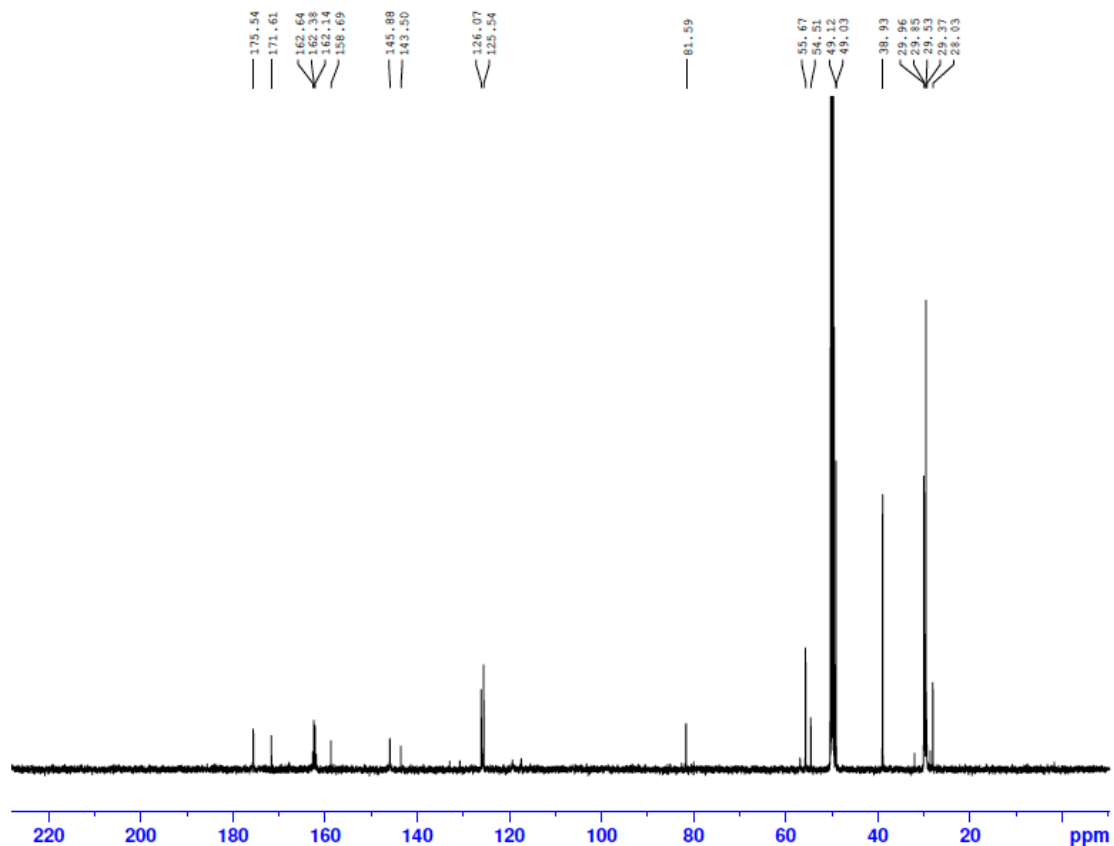


**Figure S5.11**  $^{13}\text{C}$  NMR (150 MHz,  $\text{CDCl}_3$ ) of **30**.

**Synthesis of *p*-(1,2,4,5-tetrazin-3-yl)phenyl[methyl]amino)valeryl amino] propyl} -1*H*-1,2,3-triazol-4-yl)-2-(tert-butoxycarbonylamino)propionic acid (**31**).** To a stirring solution of **30** (23 mg, 0.073 mmol) in 1.5 mL of DMF, triethylamine was added (13  $\mu\text{L}$ , 0.092 mmol) followed by **27** (28.5 mg, 0.071 mmol). The reaction mixture was stirred under argon at room temperature for 3 hours. The crude reaction was purified by HPLC (Method 1, 4 mL/min) yielding a pink oil (3.8 mg, 0.0064 mmol, 9%). TLC  $R_f$  (DCM + 5% MeOH) = 0.13.  $^1\text{H}$  NMR

(600 MHz, CD<sub>3</sub>OD):  $\delta$ 10.32 (s, 1H), 8.56 (d, 2H), 7.80 (s, 1H), 7.56 (d, 2H), 4.50 (s, 2H), 4.40 (t, 3H), 3.24 (dd, 1H), 3.19 (t, 2H), 3.06 (dd, 1H), 2.33 (t, 2H), 2.26 (t, 2H), 2.07 (m, 2H), 1.95 (m, 2H), 1.40 (s, 9H). <sup>13</sup>C NMR (150 MHz, CD<sub>3</sub>OD):  $\delta$ 175.7, 175.6, 174.8, 159.4, 145.8, 144.9, 132.5, 129.6, 129.5, 124.7, 80.8, 54.9, 43.9, 37.5, 36.3, 31.3, 29.1, 28.8, 23.3. HRMS (ES<sup>-</sup>) m/z calculated for C<sub>27</sub>H<sub>36</sub>N<sub>10</sub>O<sub>6</sub> [M-H<sup>+</sup>] 596.2809, found 595.2747.

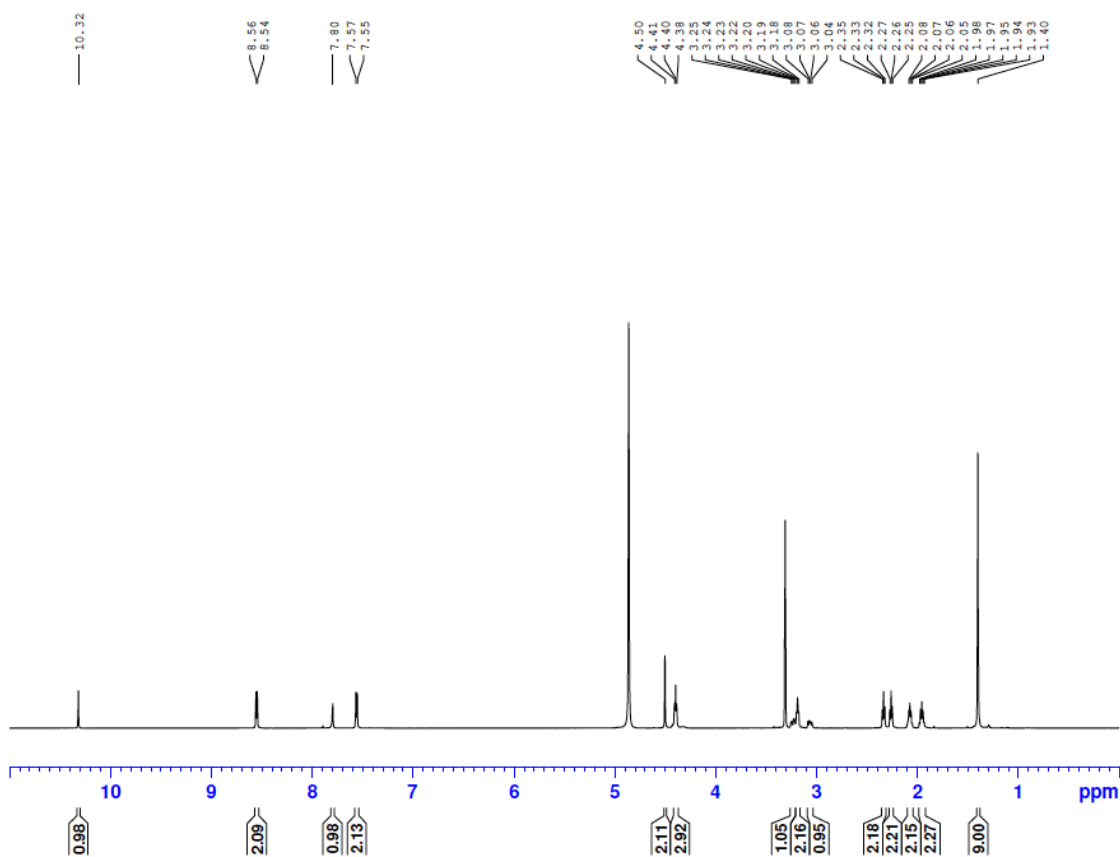


**Figure S5.12** <sup>1</sup>H NMR (600 MHz, CD<sub>3</sub>OD) of **31**.

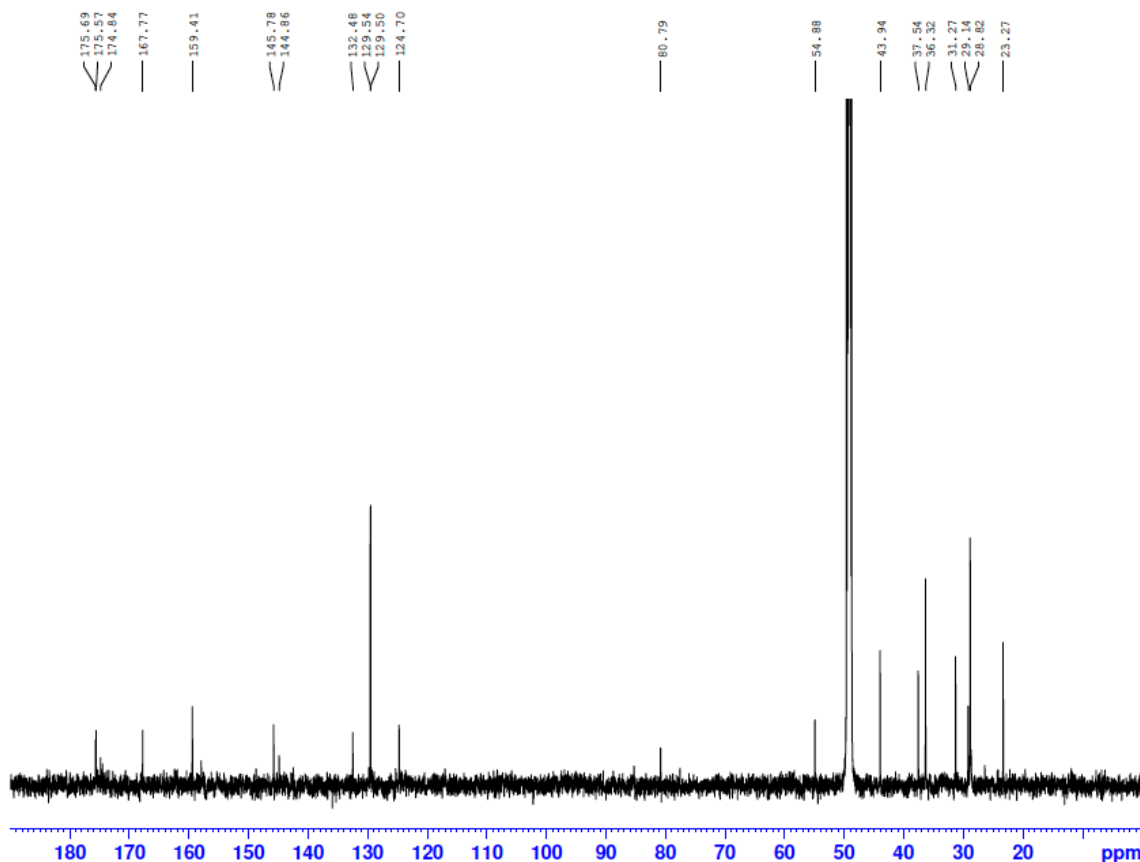


**Figure S5.13**  $^{13}\text{C}$  NMR (150 MHz,  $\text{CD}_3\text{OD}$ ) of **31**.

**Synthesis of *p*-(1,2,4,5-tetrazin-3-yl)phenyl[methyl]amino)valerylamino]propyl}-1*H*-1,2,3-triazol-4-yl)propionic acid technetium-99m tricarbonyl complex (**32**).** To a solution of 1/1 DCM/TFA (1 mL), **31** was added (0.2 mg,  $3.4 \times 10^{-4}$  mmol). The reaction was heated to 60 °C in the microwave for 10 minutes, before being evaporated to dryness. To a solution of 500  $\mu\text{L}$  of  $^{99\text{m}}\text{Tc}[\text{Tc}(\text{CO})_3(\text{H}_2\text{O})_3]^+$  in saline (930 MBq) pH adjusted to 5.5 by 0.1 M HCl, 200  $\mu\text{g}$  of deprotected **7** was added in 100  $\mu\text{L}$  MeOH in a vial. The vial was sealed and heated in a microwave for 15 minutes at 60 °C. Upon cooling, the mixture

was purified by analytical HPLC (Method 1, 1 mL/min) resulting **32** (15% RCY).

The reaction mixture was dried and dissolved in PBS at a concentration of 0.74 MBq/ $\mu$ L.

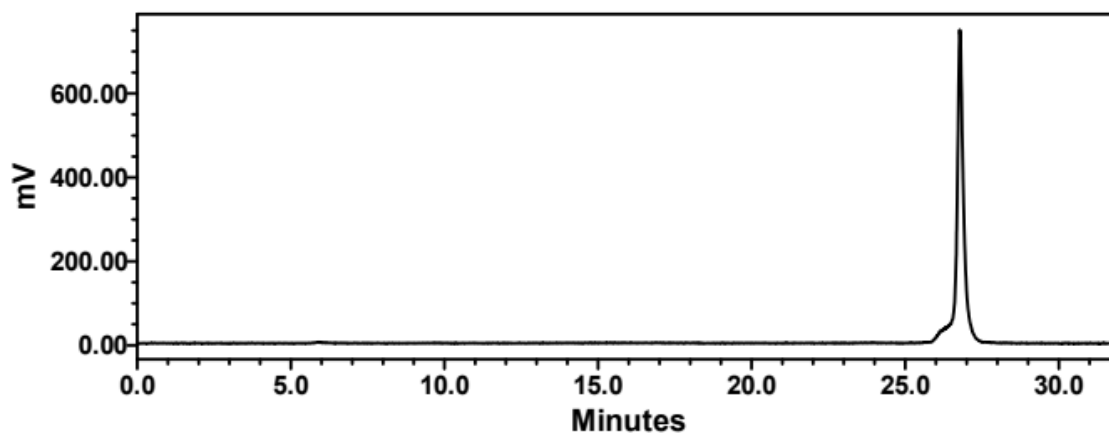


**Figure S5.14** Purified gamma HPLC trace of **32**.